frontiers | Research Topics

Catalysis rising stars in china

Edited by
Yulian He, Haifeng Xiong and Liuqingqing Yang

Published in
Frontiers in Chemistry

ISSN 1664-8714
ISBN 978-2-83251-772-7
DOI 10.3389/978-2-83251-772-7

About Frontiers

Frontiers is more than just an open access publisher of scholarly articles: it is a pioneering approach to the world of academia, radically improving the way scholarly research is managed. The grand vision of Frontiers is a world where all people have an equal opportunity to seek, share and generate knowledge. Frontiers provides immediate and permanent online open access to all its publications, but this alone is not enough to realize our grand goals.

Frontiers journal series

The Frontiers journal series is a multi-tier and interdisciplinary set of open-access, online journals, promising a paradigm shift from the current review, selection and dissemination processes in academic publishing. All Frontiers journals are driven by researchers for researchers; therefore, they constitute a service to the scholarly community. At the same time, the *Frontiers journal series* operates on a revolutionary invention, the tiered publishing system, initially addressing specific communities of scholars, and gradually climbing up to broader public understanding, thus serving the interests of the lay society, too.

Dedication to quality

Each Frontiers article is a landmark of the highest quality, thanks to genuinely collaborative interactions between authors and review editors, who include some of the world's best academicians. Research must be certified by peers before entering a stream of knowledge that may eventually reach the public - and shape society; therefore, Frontiers only applies the most rigorous and unbiased reviews. Frontiers revolutionizes research publishing by freely delivering the most outstanding research, evaluated with no bias from both the academic and social point of view. By applying the most advanced information technologies, Frontiers is catapulting scholarly publishing into a new generation.

What are Frontiers Research Topics?

Frontiers Research Topics are very popular trademarks of the *Frontiers journals series*: they are collections of at least ten articles, all centered on a particular subject. With their unique mix of varied contributions from Original Research to Review Articles, Frontiers Research Topics unify the most influential researchers, the latest key findings and historical advances in a hot research area.

Find out more on how to host your own Frontiers Research Topic or contribute to one as an author by contacting the Frontiers editorial office: frontiersin.org/about/contact

Catalysis rising stars in china

Topic editors

Yulian He — Shanghai Jiao Tong University, China

Haifeng Xiong — Xiamen University, China

Liuqingqing Yang — Shanghai Jiao Tong University, China

Citation

He, Y., Xiong, H., Yang, L., eds. (2023). *Catalysis rising stars in china*. Lausanne: Frontiers Media SA. doi: 10.3389/978-2-83251-772-7

Table of contents

frontiers | Frontiers in Chemistry

TYPE Editorial
PUBLISHED 13 February 2023
DOI 10.3389/fchem.2023.1158203

OPEN ACCESS

EDITED AND REVIEWED BY
Tomas Ramirez Reina,
University of Surrey, United Kingdom

*CORRESPONDENCE
Yulian He,
yulian.he@sjtu.edu.cn

SPECIALTY SECTION
This article was submitted to Catalytic Reactions and Chemistry, a section of the journal Frontiers in Chemistry

RECEIVED 03 February 2023
ACCEPTED 07 February 2023
PUBLISHED 13 February 2023

CITATION
Yang L, He Y and Xiong H (2023), Editorial: Catalysis rising stars in China. *Front. Chem.* 11:1158203. doi: 10.3389/fchem.2023.1158203

Editorial: Catalysis rising stars in China

Liuqingqing Yang[1], Yulian He[1,2]* and Haifeng Xiong[3]

[1]University of Michigan—Shanghai Jiao Tong University Joint Institute, Shanghai, China, [2]Department of Chemical Engineering, Shanghai Jiao Tong University, Shanghai, China, [3]State Key Laboratory of Physical Chemistry of Solid Surfaces, Collaborative Innovation Center of Chemistry for Energy Materials, College of Chemistry and Chemical Engineering, Xiamen University, Xiamen, China

KEYWORDS

catalysis and biocatalysis, DFT, density functional theory, C1 catalysis, single atom catalysis, electrocatalysis

Editorial on the Research Topic
Catalysis rising stars in China

Catalysis Rising Stars in China is devoted to bringing together high-quality works from outstanding Chinese researchers in the early stages of their independent careers in order to advance our understanding of the design, synthesis, characterization, and application of catalysts. Indeed, catalysts are applied in various situations, from industrial chemical processes to biochemical reactions in the human body, to facilitate the important chemical transformation of one set of molecules into another. In this sense, catalysts play important roles in both our lives and our lifestyles. Over the decades, researchers in the catalysis field have been actively designing and synthesizing novel catalytic systems and exploring the role of catalysis in many different sectors of industry, energy, health, the environment, *etc.* Therefore, this Research Topic highlights the latest progress in the research field of catalysis, working across China.

Widely found in the natural environment and food, BaP is regulated as a Group I human carcinogen, and its degradation is of great importance. Long et al. discovered that the degradation of BaP to hydroxybenzo [a]pyrene by Mn-corrolazine can be simplified from a three-step process to one step with the aid of the oriented external electronic field *via* DFT calculations. In this way, the production of toxic epoxide intermediates in the conventional three-step process can be avoided.

Metal-support interaction (MSI) has been a research hotspot since it was first discovered in 1978. This interaction was found to be central to governing the catalytic performance of supported systems. Through systematic investigations on Cu_XO/ZnO catalysts, Lyu et al. were able to regulate the MSI and reveal that the electron transfer from ZnO to CuO leads to the formation of an electron-rich interface, which is favorable for the adsorption of oxygen and CO oxidation reaction.

Electrocatalytic alkaline water splitting is considered an environmentally friendly technology for the production of green hydrogen. To overcome energy barriers and accelerate reaction kinetics, Li et al. have successfully developed the Ru-doped CoS_2 catalyst for highly efficient HER. The high crystallinity of Ru-doped CoS_2 materials was obtained with rich heterogeneous interfaces between Ru-CoS_2 and Ru-doped MoS_{2-X}. Characterization results show that this synthesized strategy could regulate the concentration of S-vacancy (CS-vacancy) precisely by the synergistic engineering of Ru doping and compositing with CoS_2. Overall, the typical sample, which has 17.1% CS-

vacancy, demonstrated the highest alkaline HER activity, with a low overpotential of 170 mV at 100 mA/cm^2 and a TOF of 4.29 s^{-1} at −0.2 V.

Biomass holds great promise as a sustainable alternative to fossil fuel resources. Hu et al. reported an Mo, Mg co-modified Sn-β catalyst for the catalytic transformation of glucose and fructose into alkyl lactate at moderate temperatures. The results show that both the Mo species and the synergetic effect between Mo and neighboring Mg species are important in enabling the retro-aldol condensation of fructose. The selection of solvent was also found to be important for both product yield and selectivity.

The conversion of carbon dioxide (CO_2) into value-added products is an urgent research field aimed at not only curbing carbon emissions but also realizing circular carbon economy. Zhang et al. summarize the recent metal-organic frameworks (MOFs)-based catalysts for the process of hydrogenation of CO_2 to methanol, methane, and other C_{2+} products. The design strategies of MOF materials are also provided in order to boost the overall efficiency of CO_2 conversion and utilization processes.

Single-atom catalysts (SACs) have attracted significant attention in the research field of heterogeneous catalysis. However, the rational design of well-performed SACs still remains challenging. Zhai et al. discuss a rational design of a Pd_1-Pd NPs hybrid structure on a 2,6-pyridinedicarbonitrile-derived covalent triazine framework. This synthesized strategy allows for the regulation of the ratio of Pd_1 and Pd NPs, and the typical sample presents the optimal catalytic activity with a formate formation rate of 3.66 $mol_{HCOOM} \cdot mol_{Pd^{-1}} \cdot h^{-1}$.

Atomically precise gold nanoclusters (Au NCs) have highly specific surface areas and many unsaturated active sites, such that they are widely explored in the development of new heterogeneous catalysts. Hu et al. summarize the photophysical properties of several Au NCs and discuss their application in different photocatalytic reactions. The typical properties, including discrete energy levels; tunable photophysical and electrochemical properties, including visible to near-infrared absorption; microsecond long-lived excited-state lifetime; and redox chemistry are highlighted.

Methane is the cleanest fossil fuel resource with low carbon emissions; in the pursuit of carbon neutrality, catalytic methane combustion (CMC) has attracted significant attention in the efforts to curb unwanted automobile emissions as well as in green energy generation. Gao et al. focus on the transition metal oxide catalysts applied in CMC due to their comparable catalytic performance with that of precious metals. The authors also comprehensively summarize four different kinetic reaction models that have been proposed for CMC and future research prospects in this reaction field.

As mentioned, SACs catalysts constitute a research Frontier in heterogeneous catalysts. Liu et al. summarize SAC materials from the unique angle of their stability and activity at high temperatures. The authors collected the latest efforts in the development of thermally-stable SACs at elevated temperatures through the reverse-Ostwald ripening mechanism, especially for the approaches of atom trapping and vapor-phase self-assembly strategies. Other factors that can affect the thermal stability of SACs catalysts at high temperatures are also summarized, including the loading upper limit, the location of the metal single atom, the reducibility of lattice oxygen, and so on.

We are thankful to all authors for their meaningful works and to all the reviewers for their constructive suggestions and opinions. We expect that this Research Topic will encourage more researchers to discover and design novel catalysts in the future, as well as promote the in-depth development of well-performed catalytic applications.

Author contributions

LY, YH and HX cowrote the editorial draft.

Conflict of interest

The authors declare that the research was conducted in the absence of any commercial or financial relationships that could be construed as a potential conflict of interest.

The handling editor TR declared a past co-authorship with the authors LY and YH.

Publisher's note

frontiers | Frontiers in Chemistry

ORIGINAL RESEARCH
published: 13 May 2022
doi: 10.3389/fchem.2022.912550

Electronic Metal-Support Interactions Between Cu_xO and ZnO for Cu_xO/ZnO Catalysts With Enhanced CO Oxidation Activity

Shuai Lyu[1†], Yuhua Zhang[1†], Zhe Li[1], Xinyue Liu[1], Zhenfang Tian[2], Chengchao Liu[1], Jinlin Li[1] and Li Wang[1*]*

[1]Key Laboratory of Catalysis and Energy Materials Chemistry of Ministry of Education & Hubei Key Laboratory of Catalysis and Materials Science, South-Central Minzu University, Wuhan, China, [2]Hubei Key Laboratory of Processing and Application of Catalytic Materials, Huanggang Normal University, Huanggang, China

Metal-support interaction has been one of the main topics of research on supported catalysts all the time. However, many other factors including the particle size, shape and chemical composition can have significant influences on the catalytic performance when considering the role of metal-support interaction. Herein, we have designed a series of Cu_xO/ZnO catalysts as examples to quantitatively investigate how the metal-support interaction influences the catalytic performance. The electronic metal-support interactions between Cu_xO and ZnO were regulated successfully without altering the structure of Cu_xO/ZnO catalyst. Due to the lower work function of ZnO, electrons would transfer from ZnO to CuO, which is favorable for the formation of higher active Cu species. Combined experimental and theoretical calculations revealed that electron-rich interface result from interaction was favorable for the adsorption of oxygen and CO oxidation reaction. Such strategy represents a new direction to boost the catalytic activity of supported catalysts in various applications.

Keywords: metal-support interactions, Cu species, CO oxidation, ZnO, supported catalysts

OPEN ACCESS

Edited by:
Haifeng Xiong,
Xiamen University, China

Reviewed by:
Sen Linq,
Fuzhou University, China
Yang Lou,
Jiangnan University, China

***Correspondence:**
Yuhua Zhang
poale_zhang@aliyun.com
Li Wang
li.wang@scuec.edu.cn

[†]These authors have contributed equally to this work

Specialty section:
This article was submitted to Catalytic Reactions and Chemistry, a section of the journal Frontiers in Chemistry

Received: *05 April 2022*
Accepted: *25 April 2022*
Published: *13 May 2022*

Citation:
Lyu S, Zhang Y, Li Z, Liu X, Tian Z, Liu C, Li J and Wang L (2022) Electronic Metal-Support Interactions Between Cu_xO and ZnO for Cu_xO/ZnO Catalysts With Enhanced CO Oxidation Activity. Front. Chem. 10:912550. doi: 10.3389/fchem.2022.912550

INTRODUCTION

For decades, the Cu/ZnO system has attracted fundamental interest concerning its unique performance in CH_3OH synthesis, CO_2 conversion, steam reforming reactions, and oxidation reactions (Behrens et al., 2012; Kuld et al., 2016; Jia et al., 2017; Ye et al., 2018; Jiang et al., 2020). However, the role of the interaction between the two species on the catalytic performance is still not fully understood (Kniep et al., 2004; Liao et al., 2011; Bikaljevic et al., 2019; Zhang et al., 2021). The investigation of this key feature for the performance of Cu/ZnO catalysts has often led to different conclusions. For example, the interface in Cu/ZnO catalysts is crucial for CH_3OH synthesis via CO_2 hydrogenation reaction. Although the exact nature of the interfacial sites is still under debate, two possible active sites are generally proposed: Cu-ZnO synergistic sites at the interface and Cu-Zn surface alloy sites (Nakamura et al., 1996; Fujitani and Nakamura, 2000; Kattel et al., 2017a). In other reactions having different activation and reaction conditions, the reconstruction of Cu and Zn species during the reaction is nonnegligible as well. The active species and valence states at the interface are different. Due to the complexity of the catalytic reaction mechanism, there is no unified

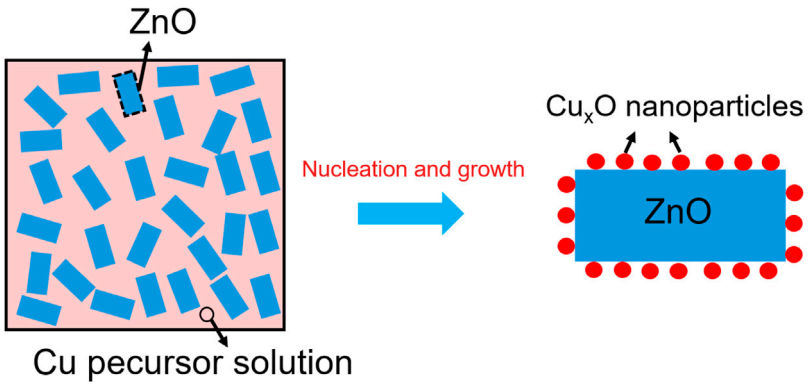

Scheme 1 | Illustration of the preparation of CuxO/ZnO supported catalysts.

opinion on the interaction between the two components in Cu/ZnO catalysts (Whittle et al., 2002; Kattel et al., 2017b; Yang et al., 2017).

In fact, revealing the specific structure-activity relationship of supported catalysts is a challenging task because their performance is affected by numerous factors, including the composition, specific surface area, and pore structure of the support, particle size, crystal structure, and morphology of the active metal, and the interaction between the support and the active metal (Li et al., 2018a; Lou et al., 2020a; Lou et al., 2020b; Song et al., 2021). Moreover, these factors generally affect each other. Therefore, to study the effect of one of these parameters while maintaining the other factors constant is not an easy task. For example, to study the pore structure of Al_2O_3 on the

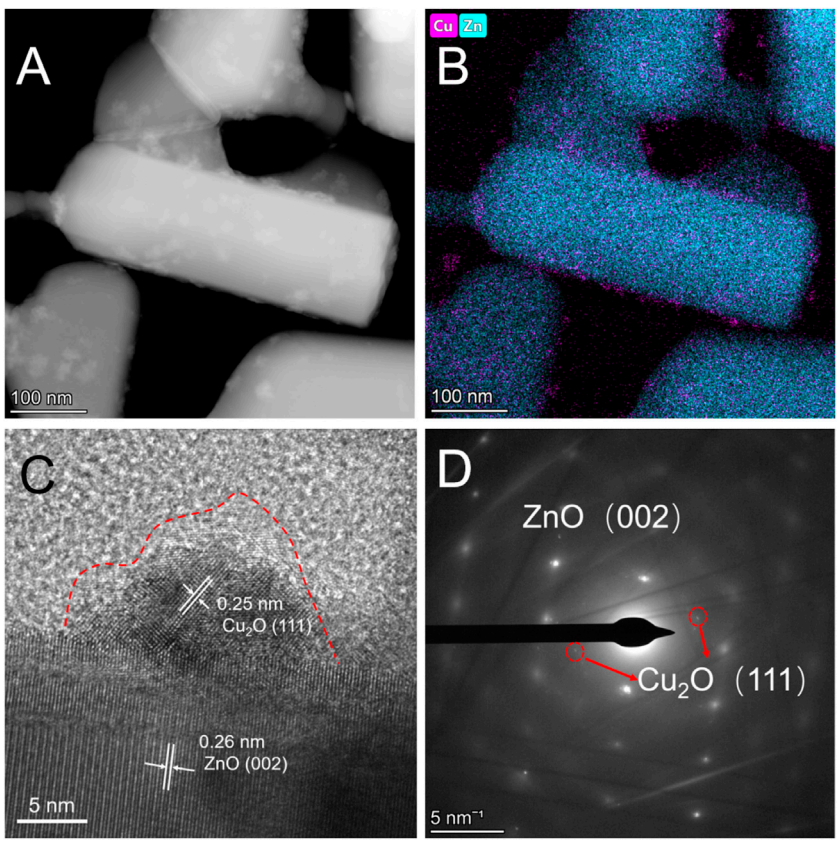

FIGURE 1 | (A) High-angle annular dark-field scanning transmission electron microscopy images, **(B)** energy dispersive X-ray mapping, **(C)** high-resolution transmission electron microscopy, and **(D)** selected-area electron diffraction patterns of Cu_xO/ZnO-12 catalyst.

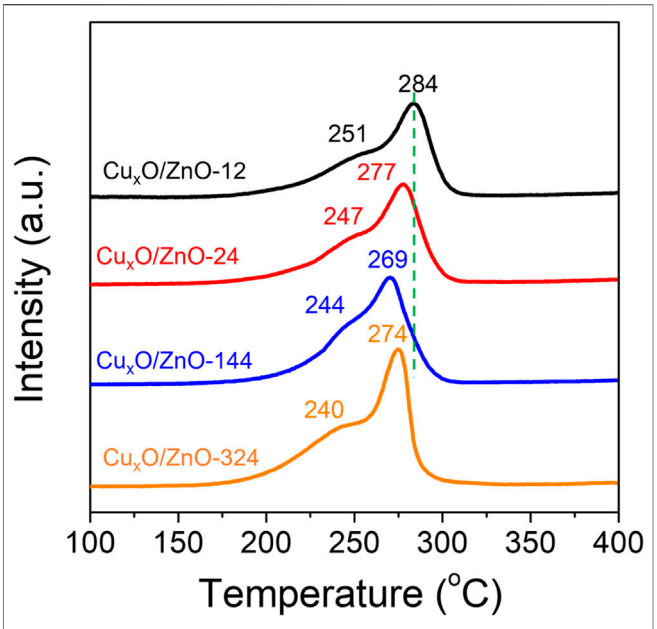

FIGURE 2 | H_2 Temperature-programmed reduction profiles of the as-synthesized Cu_xO/ZnO catalysts.

performance in the Fischer-Tropsch synthesis reaction of a Co/Al_2O_3 catalyst, a series of Al_2O_3 materials with different pore structures need to be synthesized for the first. However, Al_2O_3 supports with different specific surface area or external exposed surface were obtained, which could affect the dispersion degree and size of the Co particles, as well as the interaction between Co having different particle sizes and the Al_2O_3 support (Xiong et al., 2005; Liu et al., 2017). Too many influencing factors were introduced during the research, leading to a controversial result. Thus, well-defined catalytic materials and well-designed experiments are essential to obtain a reliable result (Zhang et al., 2014; Yang et al., 2018).

One of the best studied catalytic reactions from a fundamental scientific viewpoint is the CO oxidation reaction, which constitutes an effective pathway to remove exhaust gas (Doherty et al., 2020; Jing et al., 2020). For this reaction, Cu-based materials have been preferentially employed as primary catalysts due to their variable valence state, low temperature reducibility, and low cost (Jernigan and Somorjai, 1994). Although pristine ZnO catalysts lack substantial oxygen vacancy defects to facilitate an efficient CO oxidation, its strong metal-support interaction (SMSI) with expensive noble metals can improve the reaction performance effectively (Liu et al., 2012; Liu et al., 2018). In this context, the combination of ZnO with Cu can be envisaged as a low-cost alternative to catalyze the CO oxidation reaction. However, the role of the interaction between both components in the catalytic performance is still unclear. Thermal decomposition is one of the most effective methods to obtain highly homogeneous nanomaterials (Park et al., 2004). In this paper, a well-defined Cu_xO/ZnO catalyst was synthesized via a thermal decomposition method. By performing simple efficient treatments, the interaction between Cu_xO and ZnO was regulated successfully without altering the structure of the catalyst. Using these well-defined catalysts and a series of advanced characterization methods, the role of the interaction between Cu_xO and ZnO on the CO oxidation performance was investigated thoroughly.

EXPERIMENTAL

Chemicals and Reactant Gases

$Cu(acac)_2$ (98%; acac = acetylacetonate), benzylamine (98%), and the ZnO support (99%, 100–500 nm) were purchased from Aladdin Chemical Reagent Co., Ltd. Ethanol was purchased from Sinopharm.

CO (99.999% purity), Ar (99.999% purity), O_2 (99.999% purity), and 10% O_2/90% Ar gas mixture were purchased from Sichuan Tianyi Science and Technology Co., Ltd.

Preparation of Catalysts

The Cu_xO/ZnO catalysts were synthesized via a thermal decomposition method, according to which Cu_xO

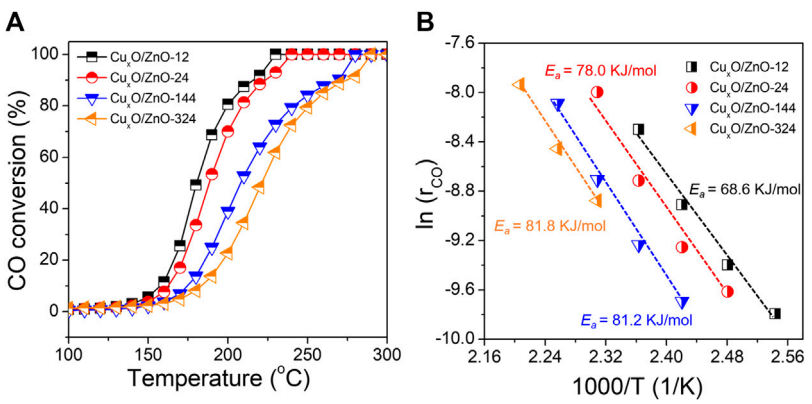

FIGURE 3 | (A) CO conversion over the catalyst series as a function of the reaction temperature; **(B)** Arrhenius plots of the different catalysts.

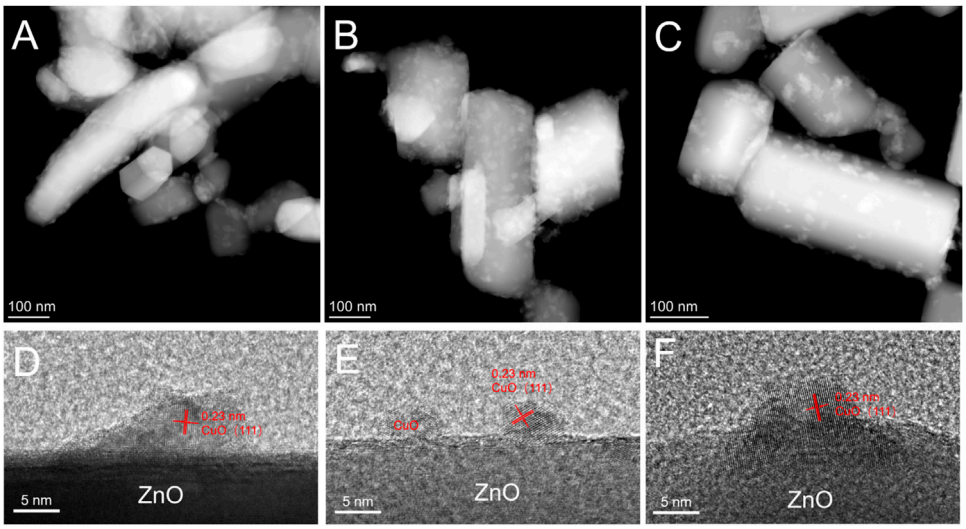

FIGURE 4 | High-angle annular dark-field scanning transmission electron microscopy images of **(A)** used Cu_xO/ZnO-12 catalyst, **(B)** used Cu_xO/ZnO-24 catalyst, and **(C)** used Cu_xO/ZnO-144 catalyst; high-resolution transmission electron microscopy images of **(D)** used Cu_xO/ZnO-12 catalyst, **(E)** used Cu_xO/ZnO-24 catalyst, and **(F)** used Cu_xO/ZnO-144 catalyst.

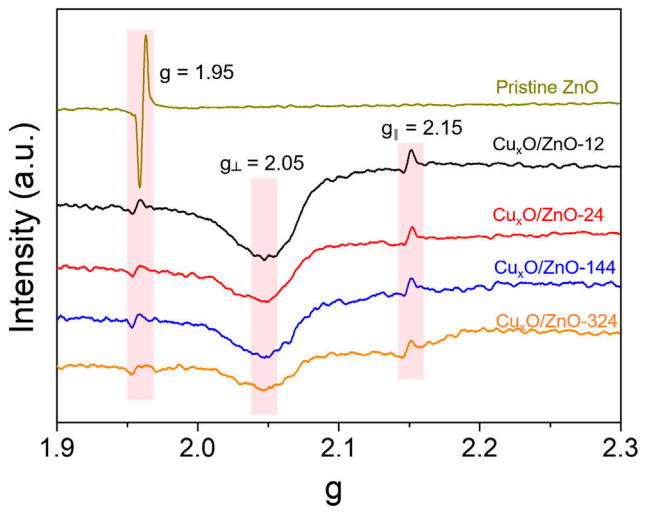

FIGURE 5 | Electron paramagnetic resonance profiles of the as-synthesized Cu_xO/ZnO catalysts and pristine ZnO support.

nanoparticles were allowed to nucleate and grow on the ZnO surface as presented in **Scheme 1**. In a typical synthesis, 0.626 g of $Cu(acac)_2$ (2.4 mmol), 1.8 g of ZnO, and 100 g of benzylamine were suspended in a round-bottomed flask equipped with a reflux condenser. The mixture was ultrasonically dispersed under vigorous stirring for 0.5 h. Subsequently, the obtained solution was heated to 190°C with stirring in an oil bath and refluxed for 2 h. After cooling down to room temperature, the sample was centrifuged and washed with ethanol five times. The obtained catalyst was divided into four equal parts, followed by drying at 200°C for 12, 24, 144, and 324 h in a vacuum drying oven, respectively. The obtained catalyst samples were denoted as Cu_xO/ZnO-12, Cu_xO/ZnO-24, Cu_xO/ZnO-144, and Cu_xO/ZnO-324 depending on the drying time.

Materials Characterization

X-ray powder diffraction (XRD) was performed on a Bruker D8 powder diffractometer using Cu Kα radiation (1.5404 Å), operated at 40 kV and 40 mA and a Vantec −1 detector. The size and morphology of the catalysts was investigated using a Tecnai G2 20 S-TWIN transmission electron microscope (TEM) equipped with an energy dispersive X-ray (EDX) spectroscope operated at 200 kV. H2 Temperature-programmed reduction (TPR) was conducted using a Zeton Altamira AMI-300 instrument equipped with a thermal conductivity detector. Prior to the measurement, the catalyst (0.05 g) was flushed with high-purity Ar at 150°C for 1 h and then cooled to 50°C. Then, the temperature was raised to 800°C (ramp rate 10°C min^{-1}) by applying a flow of 10% H_2/Ar at a flow rate of 30 ml min^{-1}. Finally, the temperature was held at 800°C for 30 min. X-ray photoelectron spectroscopy (XPS) measurements were performed on a Thermal Electron VG multilab 2000 with an Al K α X-ray source under vacuum at 2×10^{-6} Pa (the binding energies were corrected using the C 1 s peak at 284.6 eV of the surface adventitious carbon). Electron paramagnetic resonance (EPR) spectra were recorded on a Bruker EMX spectrometer. The EPR experiments were conducted with a center field of 3507.815 G and a frequency of 9.83 GHz using an Elexsys probe head with 15 mg of sample placed in a 4 mm tube. *In situ* diffuse reflectance infrared Fourier transform (DRIFT) spectra of catalysts were collected on a Nicolet Fourier transform infrared spectrometer (NEXUS 470). Before data collection, the catalyst was pretreated with a 10% O_2/Ar flow rate of 100 ml min^{-1} at 300°C for 1 h to remove absorbed residues and then cooled to 30°C. Pure Ar was introduced to remove O_2 before CO adsorption experiments.

DFT Calculations

Density functional theory calculations were performed by PBE (Perdew–Burke–Ernzerhof) method with PAW (projected-augmentation wave) potentials in Vienna ab-initio simulation package program. Plane-wave energy cutoff was set to 400 eV with Gaussian smearing scheme (sigma = 0.05 eV) suitable for semi-conduntor. Total energy and residual atomic force were converged to 10^-4 and 0.03 eV/A.

Catalytic Test

The CO oxidation reaction was conducted in an atmospheric pressure fixed-bed flow quartz reactor. To prevent temperature gradients, 30 mg of catalyst was diluted with inert SiC powder (0.3 g). The catalyst was pretreated with a 10% O_2/Ar flow rate of 100 ml min^{-1} at 300 °C for 1 h to remove any absorbed residues and then cooled to room temperature. For the CO oxidation reaction, the reaction temperature was ramped up from 25 to 400°C with a heating rate of 2°C min^{-1}. A total flow rate of 100 ml min^{-1} was used, and the space velocity was 200,000 ml $(g_{cat}\ h)^{-1}$. The outlet gas composition was measured using a gas chromatograph Agilent 7890 BGC equipped with a thermal conductivity detector. The CO conversion was calculated as follows:

$$CO\ conversion\ (\%) = \frac{CO_{inlet} - CO_{outlet}}{CO_{inlet}} * 100\%$$

RESULTS AND DISCUSSION

The Cu_xO/ZnO-12 catalyst was synthesized *via* a previously reported thermal decomposition approach (Lyu et al., 2019) and dried in a vacuum drying oven at 200°C for 12 h. In the XRD pattern, characteristic diffraction peaks attributed to ZnO (JCPDS # 36-1451) were observed, whereas no peaks corresponding to Cu_xO appeared (**Supplementary Figure S1**). This indicates that Cu_xO particles were well dispersed on the ZnO support. Scanning transmission electron microscopy (STEM) and EDX mapping was used to investigate the morphology and element distribution of the catalysts. The high-angle annular dark-field STEM (HAADF-STEM) images displayed in **Figures 1A,B** show that Cu_xO particles with an irregular morphology and broad size distribution were distributed uniformly on the ZnO surface. The selected-area electron diffraction (SEAD) results show that the catalyst was composed of Cu_2O and ZnO (**Figure 1D**). Thus, the lattice fringes with a d-spacing of 0.26 nm correspond to the (002) planes of ZnO, and the 0.25 nm lattice fringes can be ascribed to the (111) planes of Cu_2O. **Figure 1C** also reveals a distinct oxide layer on the surface of the particles resulting from the formation of CuO after exposure to air and a distinct interface between Cu_xO and ZnO.

To modify the interaction between the Cu_xO and ZnO components without affecting the structure of the catalyst, other three Cu_xO/ZnO samples were prepared using the same procedure described for Cu_xO/ZnO-12 except that the

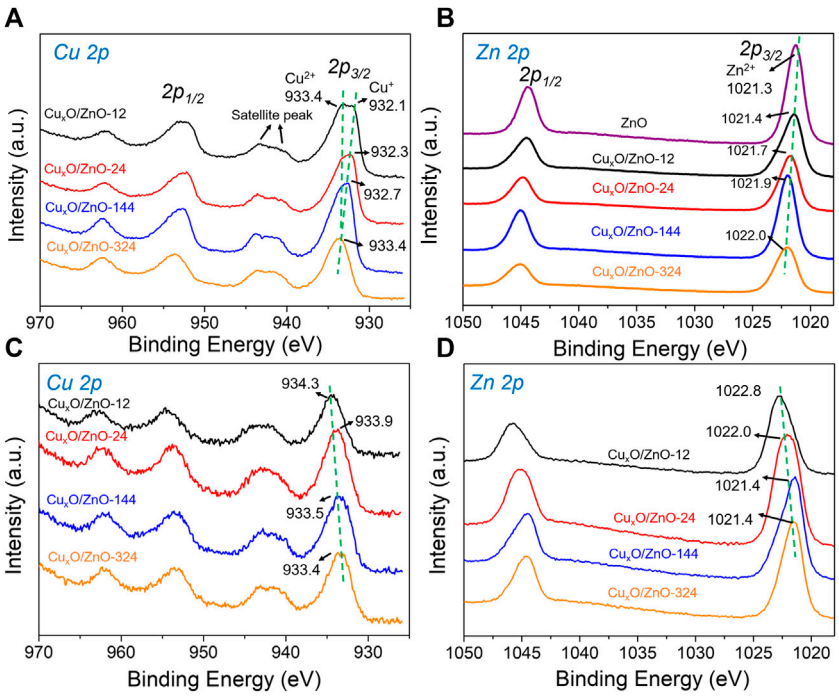

FIGURE 6 | X-ray photoelectron spectra of the catalysts: **(A)** Cu 2p spectra of the fresh catalyst; **(B)** Zn 2p spectra of the fresh catalyst; **(C)** Cu 2p spectra of the used catalyst; **(D)** Zn 2p spectra of the used catalyst.

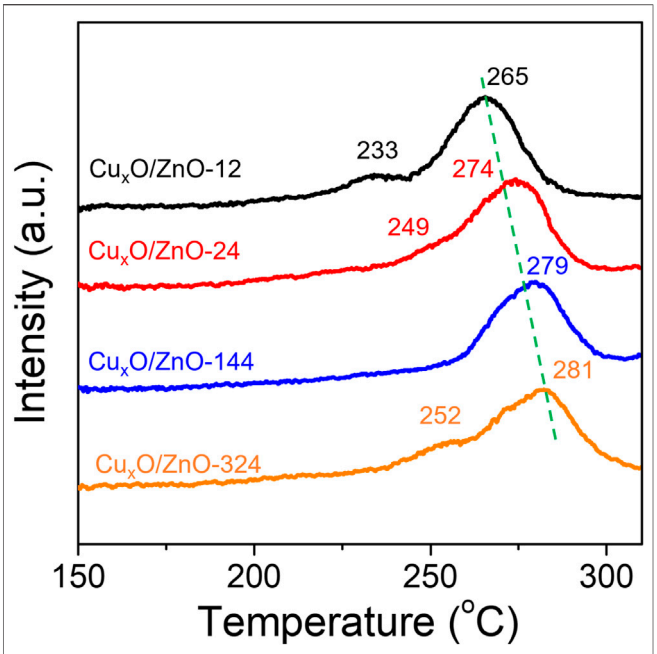

FIGURE 7 | H_2 temperature-programmed reduction profiles of the used Cu_xO/ZnO catalysts.

heating in the vacuum drying oven at 200°C and 0.08 MPa was conducted for 24, 144, and 324 h, respectively. According to Fick's second law, a concentration gradient due to the different degree of doping with time would cause diffusion of the atoms of the two components into the lattices of each other. The surface reconstruction of the catalyst would be minimized under vacuum. Besides, since the temperature is much lower than the Tammann temperature of Cu_xO, the agglomeration of Cu_xO particles would be reduced (Imtiaz et al., 2016). As confirmed by the STEM images of Cu_xO/ZnO-24, Cu_xO/ZnO-144, and Cu_xO/ZnO-324 presented in **Supplementary Figure S2–4**, the dispersion of Cu_xO particles was not affected by the treatment time. The change in Cu loading and pore structure was negligible under the present mild treatment conditions.

To confirm whether the interaction between the two components in the catalysts was tuned after treatment, the catalysts were characterized by H_2-TPR. As shown in **Figure 2**, all the catalysts exhibited two distinct peaks at 220°C–300°C, which are related to the reduction of different Cu_xO species. The main TPR peak at about 260–300°C can be ascribed to the reduction of bulk Cu_xO, and a smaller shoulder peak at about 220°C–250°C is attributable to the reduction of Cu_xO interacting with ZnO, which confirms the existence of a Cu_xO-ZnO interaction that facilitates the reduction of Cu_xO species in all the catalysts (Jun et al., 1998; Kniep et al., 2005). Interestingly, the TPR profiles of the whole series of catalysts exhibit similar peak shapes, but the peak position shifts to lower temperature upon increasing the heat treatment time, indicating that the strong interaction with ZnO can promote the reduction of Cu_xO effectively. This suggests strongly that the Cu_xO-ZnO interaction was regulated successfully. Thus, a batch of well-defined Cu_xO/ZnO catalysts with different interactions between components was obtained. It should be pointed out that other structural differences between these catalysts were negligible.

The CO oxidation reaction was conducted on a fix-bed reactor under a gas hourly space velocity of 200,000 ml g_{cat}^{-1} h^{-1} (g_{cat}, grams of catalyst), which matches standard vehicle exhaust conditions. The light-off curves of the CO conversions are shown in **Figure 3**. Overall, although the activity of the Cu_xO/ZnO catalysts was limited, significant differences between the catalysts were observed. Thus, the temperature at which CO conversion is 100% (T_{100}) was 230°C for Cu_xO/ZnO-12, whereas it increased gradually with increasing the heat treatment time. The Arrhenius plots of the CO oxidation rates and the activation energies (E_a) are presented in **Figure 3B**. The Cu_xO/ZnO-324 sample showed the highest E_a (81.8 kJ/mol), which was much higher than that of Cu_xO/ZnO-12 (68.6 kJ/mol). The E_a increased monotonously with the drying time.

The different catalytic performance can be ascribed to the structural differences of the catalysts, which are exclusively due to the interaction between the two components, as described above. Although the "metal-support interaction" is a relatively broad concept because the interaction between the two components can be expressed in many forms, it is known to affect the catalytic performance. In a recent review, de Jong et al. (van Deelen et al., 2019) described that several catalyst characteristics such as nanoparticle morphology, charge transfer, interfacial perimeter, chemical composition, and SMSI have a profound effect on the catalytic performance in different reactions. These phenomena are often related to each other and influence the catalytic performance in different degrees, depending on the catalyst and the reaction.

The adhesion energy at the metal-support interface has been reported to affect the shape of the nanoparticles, which has a strong influence on their catalytic performance because different shapes expose certain facets (Bratlie et al., 2007; Xie et al., 2009; Zhou and Li, 2012). Recently, Zhang at al. explored the active sites of a Cu_2O catalyst in CO oxidation using a series of Cu_2O particles with regular morphology as model materials, since cubic Cu_2O particles with different sizes possess different face sites and edge sites (Zhang et al., 2019). Herein, high-resolution TEM (HRTEM) was used to investigate the morphology of the Cu_xO particles in each catalyst. As shown in **Figure 1**, the Cu_xO particles in the Cu_xO/ZnO-12 catalyst exhibited no special morphology, and no morphological changes were observed upon extending the treatment time (**Supplementary Figure S2–4**). Therefore, the Cu_xO morphology is not the reason for the different performance of the catalysts. The STEM result also allows excluding the influence of the interface perimeter between Cu_xO and ZnO because the size of the Cu_xO particles is similar in the whole catalyst series. This was also confirmed by the surface element composition data obtained by XPS, according to which the surface Cu

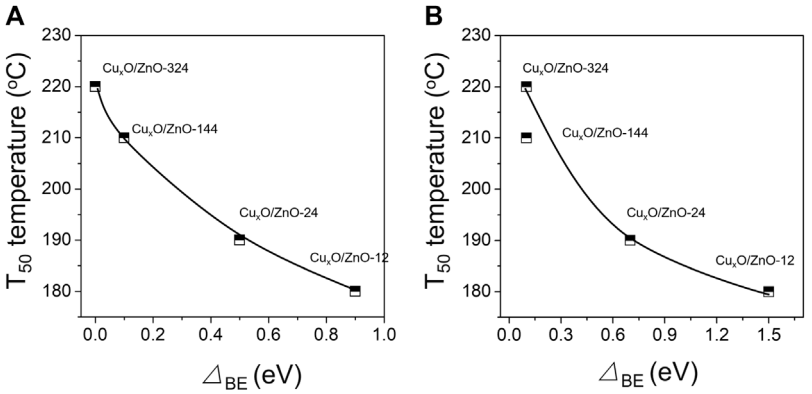

FIGURE 8 | (A) Dependence of the T_{50} temperature and the difference between the Cu $2p_{2/3}$ peak position of the used catalyst and the peak position for Cu^{2+} (933.4 eV); **(B)** dependence of the T_{50} temperature and the difference between the Zn $2p_{2/3}$ peak position of the used catalyst and the peak position for Zn^{2+} (1021.3 eV).

content and Cu/ZnO ratio of all the catalysts were almost the same (**Supplementary Table S1**).

The term strong metal-support interaction refers to the coverage of metal nanoparticles by suboxides, which are generated from the support under reducing conditions as a result of the surface reconstruction of the catalyst in a specific atmosphere (Liu et al., 2015; Tang et al., 2017; Dong et al., 2020). In the present study, HRTEM was used to examine whether the Cu_xO particles in the used catalyst were covered by ZnO (**Figure 4**). After the reaction, the structure of the Cu_xO-ZnO interface remained virtually unchanged, and no covering was observed. Recently, Luo et al. studied the surface reconstruction of a Cu catalyst during CO oxidation using *in situ* aberration-corrected environmental TEM under O_2 atmosphere (Luo et al., 2020). However, this nonreducing atmosphere may not be conducive to the formation of SMSI in current case (Yang et al., 2021).

A solid-state reaction occurring between metal nanoparticles and the support results in the formation of new phases (Chaika et al., 2020). For Cu/ZnO catalysts, the formation of a Cu-Zn compound induced by hydrogen or a reducing atmosphere often occurs in hydrogenation reactions (Grunwaldt et al., 2000). Meanwhile, the Cu-Zn alloy was reported to be the active center in CO_2 hydrogenation. In this study, the Cu_xO/ZnO compound was fabricated according to Fick's law (Van Milligen et al., 2005), and its formation was confirmed via EPR spectroscopy. As presented in **Figure 5**, the spectra of all the catalysts exhibited a resonance at g = 1.953, which is attributable to shallow donor centers caused by interstitial Zn and surface O vacancies (Wen et al., 2020). This peak of Cu_xO/ZnO catalysts was relatively weaker than that of pristine ZnO and decreased slightly with increasing the heat treatment time. Meanwhile, an anisotropic hyperfine structure was observed in all the catalysts. A resonance parameter $g_{//}$ of 2.15 indicates that Cu^{2+} replaced the cation sites of ZnO. Moreover, a broad peak at around $g_{\perp} = 2.05$ was detected for each sample, which can be ascribed to adsorbed oxygen radicals associated with oxygen vacancies, according to previous studies (Li et al., 2018b). Thus, the EPR results confirm that Cu^{2+} was successfully doped into the ZnO lattice. Notably, the signal assigned to the anisotropic hyperfine structure of Cu^{2+} decreased mildly with increasing the heating time due to the increase of the long-range dipolar interaction between Cu^{2+} ions as the Cu doping amount increased.

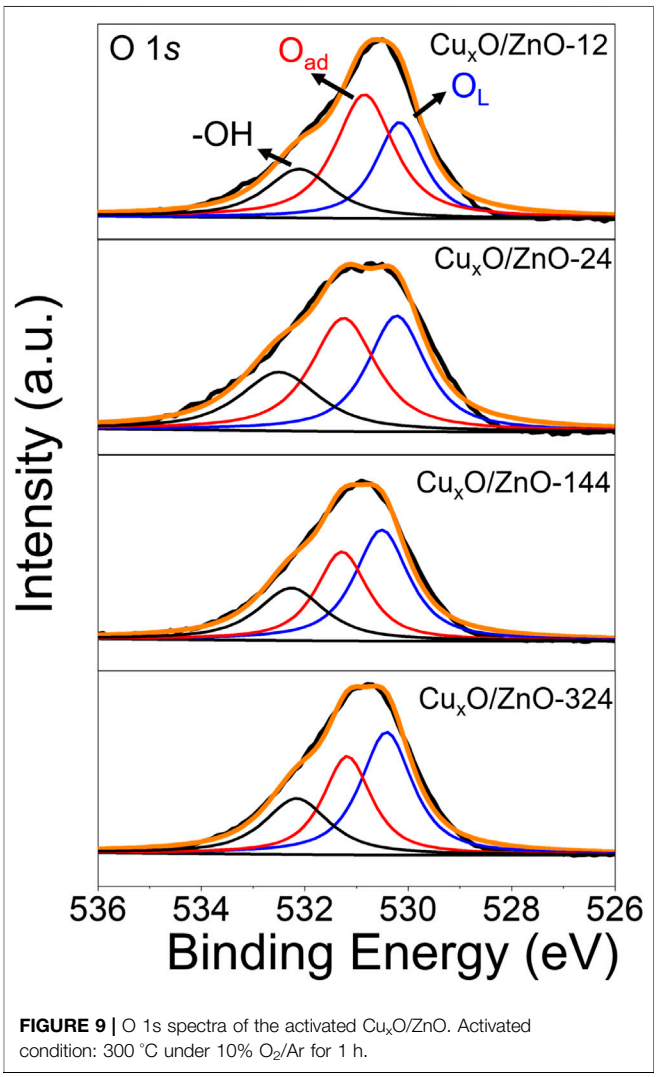

FIGURE 9 | O 1s spectra of the activated Cu_xO/ZnO. Activated condition: 300 °C under 10% O_2/Ar for 1 h.

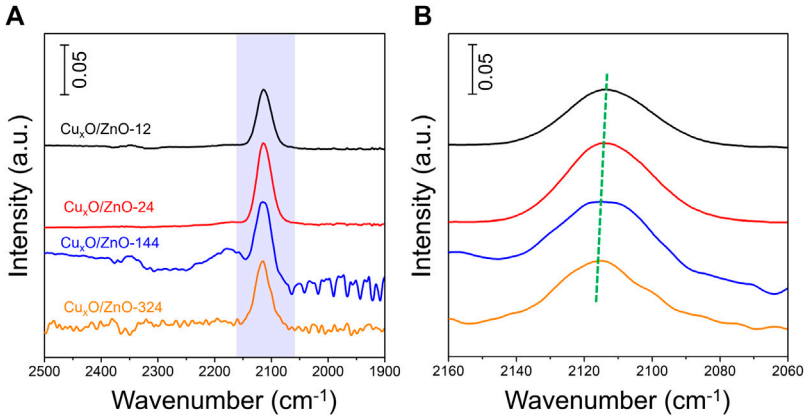

FIGURE 10 | (A): *In-situ* DRIFTS spectra of different Cu_xO/ZnO catalyst. **(B)**: Spectroscopic data between 2060 and 2160 cm^{-1}.

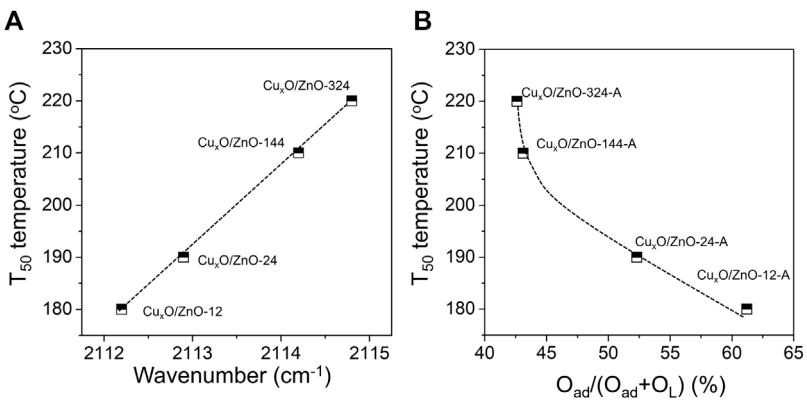

FIGURE 11 | (A) Dependence of the T_{50} temperature and the adsorption position of CO molecular; **(B)** dependence of the T_{50} temperature and relative O_{ad} concentration.

To investigate the electronic states of the different catalysts, XPS measurements were performed. **Figure 6A** shows the Cu 2p spectra of the catalysts, in which some differences in the peak shape of Cu $2p_{2/3}$ can be observed. Thus, the Cu $2p_{2/3}$ peak for Cu_xO/ZnO-12, Cu_xO/ZnO-24, and Cu_xO/ZnO-144 was clearly split into two peaks: a peak at higher binding energy (933.4 eV) that can be assigned to Cu^{2+} and another peak at ca. 931.9 eV corresponding to Cu^{+}. In contrast, only one peak at 933.4 eV was observed in the spectrum of Cu_xO/ZnO-344 (Svintsitskiy et al., 2013). Interestingly, the Cu^{+} peak shifted gradually toward the high binding energy region as the heat treatment time increased. For Cu_xO/ZnO-144, the Cu^{+} peak shifted to 932.6 eV. This is a strong indication of the change in the Cu electron state in the catalyst. The electronic state of Zn in the catalyst is also worthy of note.

As shown in **Figures 6A,B** peak at 1021.4 eV attributable to Zn^{2+} appeared in the spectra of Cu_xO/ZnO-12 (Zhu et al., 2018). This peak shifted gradually to higher binding energies with increasing the treatment time, indicating that the interaction between the two components changed and the electronic structure of the components was affected simultaneously.

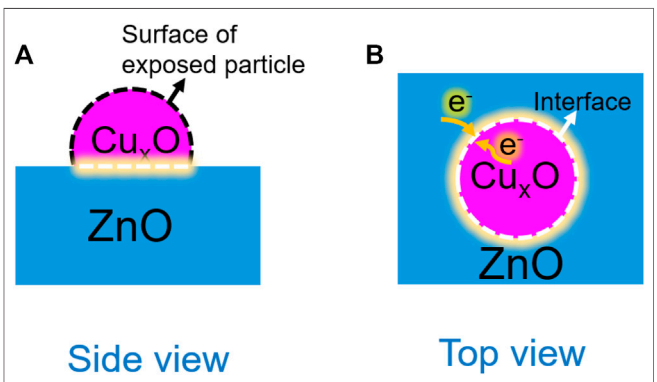

FIGURE 12 | Schematic of the interaction between Cu_xO and ZnO during the CO oxidation reaction. **(A)**: Side view; **(B)** TOP view.

Next, considering that the interaction between the active component and the support of a catalyst is sensitive to the atmosphere (Dong et al., 2018), the electronic property of the used

catalysts was investigated by XPS to study the changes in the catalysts during the reaction. An interesting "reverse behavior" of the interaction was observed. As shown in **Figure 6C**, the surface Cu species of all the catalysts presented characteristic of Cu^{2+} after reaction, in line with the previous studies (Zhang et al., 2019). For the Cu_xO/ZnO-12 catalyst, the peak corresponding to Cu^{2+} shifted by 0.9 eV to higher binding energy (934.3 eV) compared with that of fresh Cu_xO/ZnO-12. For Cu_xO/ZnO-24, the peak shifted by 0.6 eV, for Cu_xO/ZnO-144 by 0.1 eV, and for Cu_xO/ZnO-144 by 0 eV. The Zn 2p spectra of the catalysts were also found to change dramatically after the reaction (**Figure 6D**). Thus, for Cu_xO/ZnO-12, the binding energy of the Zn $2p_{2/3}$ peak shifted from 1021.4 to 1022.8 eV. For Cu_xO/ZnO-24, this shift was 0.7 eV. Meanwhile, the Zn $2p_{2/3}$ peak shifted to lower binding energy after the reaction for Cu_xO/ZnO-144 and Cu_xO/ZnO-324. Taking the Zn $2p_{2/3}$ peak of pristine ZnO as a reference, the shift value to higher binding energy decreased with increasing the treatment time. In other words, the interaction between Cu_xO and ZnO in Cu_xO/ZnO-12 was the strongest among the catalysts after the reaction, whereas that of Cu_xO/ZnO-324 was the weakest, opposite to the trend for the fresh catalysts.

The used catalysts were further characterized by TPR to confirm the change in the interaction for all the catalysts. As shown in **Figure 7**, the main peak position of used Cu_xO/ZnO-12 shifted to lower temperature from 284 to 265°C. The reducibility of the catalysts decreased with the treatment time, following an opposite trend to that of the fresh catalysts. Considering that the strong interaction between Cu_xO and ZnO facilitated the reduction of Cu_xO, it can be concluded that the interaction between Cu_xO and ZnO in Cu_xO/ZnO-12 was the strongest in the series of catalysts after the reaction, which is in line with the XPS results. This suggests a dramatic reconstruction of the catalysts during the reaction. However, the initial strong interactions between Cu_xO and ZnO impeded the reconstruction process. Therefore, the Cu_xO/ZnO-12 sample, which had a weaker interaction at the beginning, underwent to a greater extent the reconstruction phenomenon compared with the other catalysts.

The electron transfer between the two components was predicted according to the work functions. The work functions calculated by the energy difference between the vacuum and Fermi levels are 5.51, 7.65, 4.57 eV for ZnO(100), CuO(100) and Cu_2O(111) surfaces respectively, which indicates the shuttling charge transfer between ZnO and CuO/Cu_2O. In other words, the electrons in Cu^+ will be transferred to ZnO, which explains the shifting of the Cu^+ peak in the XPS data toward higher binding energy (**Figure 6A**). Meanwhile, CuO accepts electrons from ZnO. For the used catalyst, since ZnO is a typical p-typ semiconductor, part of the electrons in the ZnO conduction band are trapped by the adsorbed surface oxygen to form oxygen species, and part of the electrons diffuse into the interface (Yin et al., 2016), which is consistent with the XPS results. After the reaction, the binding energy of the Zn $2p_{2/3}$ peak of Cu_xO/ZnO-12 shifted by 1.0 eV compared with that of pristine ZnO, indicating that the strong interaction causes ZnO to release a considerable amount of electrons. The shift value of the Cu $2p_{2/3}$ and Zn $2p_{2/3}$ peaks was negatively correlated with the T_{50} temperature (**Figure 8**). Electron transfer between metal and oxide support is a key step in CO oxidation reaction. In previous studies, White et al. (White et al., 2006) revealed that surface Cu^{2+} was an unlikely candidate for oxidation or O2 dissociation. The active catalyst state was confirmed to be Cu^+ (in a Cu_2O lattice) which is either present from the onset or formed by reduction of Cu^{2+} by adsorbed CO. Jernigan et al. (Jernigan and Somorjai, 1994) found that reaction rates for CO oxidation decreased with increasing copper oxidation state (Cu > Cu_2O > CuO). Huang et al. (Huang and Tsai, 2003) also found that the activity of CuO will be significantly enhanced when non-stoichiometric copper oxides are formed. Thus, it is documented that electrons transfer could contribute to the formation of active Cu species with higher activity, revealing that the strong interaction between Cu_xO and ZnO is favorable for CO oxidation.

It has been demonstrated that the electron-rich interface would promote the adsorption of oxygen on catalyst (Hayyan et al., 2016; Zeng et al., 2017), which was favorable for CO oxidation reaction. **Figure 9** presented the O 1s spectra of activated Cu_xO/ZnO catalysts. It can be seen that three characteristic peaks could be fitted from the original curve. The peak at around 530.1 eV is assigned to lattice oxygen (O_L) of catalysts, peak around 531.5 eV is attributed to the adsorbed oxygen (O_{ad}) species including O^{2-} and O^{2-} on the surface, the weaker peak at 532.4 eV was the oxygen in hydroxyl groups on the surface. The relative O_{ad} concentration [$O_{ad}/(O_L + O_{ad})$] was related to the oxygen storage capacity of catalysts. It can be seen that the activated Cu_xO/ZnO-12 possess a highest O_{ad} concentration of 61.2% (**Supplementary Table S2**) and the O_{ad} concentration of Cu_xO/ZnO catalysts decreased with the treatment time. Thus, the electron-rich interface was favorable for the adsorption of oxygen and CO oxidation reaction.

To confirmed further the electronic metal-support interaction between two components. *In situ* DRIFTs experiment was conducted to revealed CO adsorbates behavior on surface of catalysts. Before data collection, the catalyst was pretreated with a 10% O_2/Ar flow rate of 100 ml min^{-1} at 300 °C for 1 h to remove any absorbed residues and then cooled to 30°C. **Supplementary Figure S8** present the spectrum evolution of Cu_xO/ZnO-12 catalyst at different stage. The peaks appear at 2120 and 2177 cm^{-1} after CO inlet are assigned to the vibrations of gaseous CO. After purging with Ar for 15 min, most gaseous CO in the cell was blew out, a surviving peak at ~2113 cm^{-1} was assigned to the vibrations of linearly CO species adsorbed on Cu^+ (Sarkodie et al., 2021). All the catalysts present a distinct CO absorption peak at ~2113 cm^{-1}, as shown in **Figure 10A**. Moreover, **Figure 10B** present the detailed absorption peak position of the catalysts, revealing that the absorption peak shift slightly to lower wavenumbers. As established in literature, strong M-C bonds are favored by electron-rich metal centers due to π back-bonding, high d-electron density leads to the formation of strong bond between Cu^+ and CO *via* π-back bonding contributions (Li et al., 2017; Sarkodie et al., 2021). The ZnO support acts as an electronic donor to Cu species would increase the π^* back-donation from Cu^+ to adsorbed CO and hence decrease the carbonyl stretching frequency.

Furthermore, *in situ* CO-DRIFTs date and relative O_{ad} concentration data were correlated with activity data of catalyst. As shown in **Figure 11A**, the T_{50} temperature of catalyst decreased with position of CO adsorption peak, indicating that the activity of Cu_xO/ZnO catalyst decreases with the decreasing interfacial electron density. From **Figure 11B**, one can see that the catalytic activity increases with the relative O_{ad} concentration of Cu_xO/ZnO catalyst.

On the basis of the experimental and theoretical results, the effect of the interaction between Cu_xO and ZnO on the oxidation performance of CO can be described as depicted in **Figure 12**. The active sites of the catalysts can be divided into two types: exposed Cu_xO particles (**Figure 12A**) and the heterojunction at the interface (**Figure 12B**). The particle size of the catalysts before and after the reaction was almost unchanged, and the difference in the contribution of exposed Cu_xO particles on the activity among all the catalysts was negligible. Thus, the electronic structure at the catalyst interface can be considered the main factor affecting the catalytic activity. The strong interaction between the two components promotes the enrichment of electrons at the interface and the activation and dissociation of oxygen molecules. Nevertheless, the catalyst reconstruction during the reaction is an important factor in the formation of a strong catalyst interaction.

CONCLUSION

In this study, a well-defined Cu_xO/ZnO catalyst was synthesized via a typical thermal decomposition method. By adjusting the drying time of the catalyst under vacuum, the Cu_xO-ZnO interaction was regulated successfully. The interaction between Cu_xO and ZnO was altered by the reconstruction of the catalyst during the CO oxidation reaction. For catalysts with a weak interaction, the reconstruction process enhanced the interaction between the two components, which was conducive to the electron transfer and the overall activity. In contrast, for the catalysts with a strong interaction, the reconstruction process is blocked. After a restructuring procedure, the strong interaction between Cu_xO and ZnO is favorable for the CO oxidation reaction.

DATA AVAILABILITY STATEMENT

The raw data supporting the conclusions of this article will be made available by the authors, without undue reservation.

AUTHOR CONTRIBUTIONS

SL, YZ, and XL: validation, investigation, data curation, visualization, writing—original draft. ZL: DFT calculation. Z T: data curation. CL: writing—editing. JL: methodology, resources, supervision. LW: conceptualization, methodology, resources, supervision, writing—review and editing.

FUNDING

This work was supported by the National Natural Science Foundation of China (No. 22072184 and 22102220), the Young Top-notch Talent Cultivation Program of Hubei Province and Hubei Key Laboratory of Processing and Application of Catalytic materials (202023604).

SUPPLEMENTARY MATERIAL

The Supplementary Material for this article can be found online at: https://www.frontiersin.org/articles/10.3389/fchem.2022.912550/full#supplementary-material

REFERENCES

Behrens, M., Studt, F., Kasatkin, I., Kühl, S., Hävecker, M., Abild-Pedersen, F., et al. (2012). The Active Site of Methanol Synthesis over Cu/ZnO/Al 2 O 3 Industrial Catalysts. *Science* 336, 893–897. doi:10.1126/science.1219831

Bikaljevic, D., Rameshan, R., Köpfle, N., Götsch, T., Mühlegger, E., Schlögl, R., et al. (2019). Structural and Kinetic Aspects of CO Oxidation on ZnOx-Modified Cu Surfaces. *Appl. Catal. A General* 572, 151–157. doi:10.1016/j.apcata.2018.12.032

Bratlie, K. M., Lee, H., Komvopoulos, K., Yang, P., and Somorjai, G. A. (2007). Platinum Nanoparticle Shape Effects on Benzene Hydrogenation Selectivity. *Nano Lett.* 7, 3097–3101. doi:10.1021/nl0716000

Chaika, M. A., Mancardi, G., and Vovk, O. M. (2020). Influence of CaO and SiO2 Additives on the Sintering Behavior of Cr,Ca:YAG Ceramics Prepared by Solid-State Reaction Sintering. *Ceram. Int.* 46, 22781–22786. doi:10.1016/j.ceramint.2020.06.045

Doherty, F., Wang, H., Yang, M., and Goldsmith, B. R. (2020). Nanocluster and Single-Atom Catalysts for Thermocatalytic Conversion of CO and CO2. *Catal. Sci. Technol.* 10, 5772–5791. doi:10.1039/D0CY01316A

Dong, J., Fu, Q., Jiang, Z., Mei, B., and Bao, X. (2018). Carbide-Supported Au Catalysts for Water-Gas Shift Reactions: A New Territory for the Strong Metal-Support Interaction Effect. *J. Am. Chem. Soc.* 140, 13808–13816. doi:10.1021/jacs.8b08246

Dong, J., Fu, Q., Li, H., Xiao, J., Yang, B., Zhang, B., et al. (2020). Reaction-induced Strong Metal-Support Interactions between Metals and Inert Boron Nitride Nanosheets. *J. Am. Chem. Soc.* 142, 17167–17174. doi:10.1021/jacs.0c08139

Fujitani, T., and Nakamura, J. (2000). The Chemical Modification Seen in the Cu/ZnO Methanol Synthesis Catalysts. *Appl. Catal. A General* 191, 111–129. doi:10.1016/S0926-860X(99)00313-0

Grunwaldt, J.-D., Molenbroek, A. M., Topsøe, N.-Y., Topsøe, H., and Clausen, B. S. (2000). *In Situ* investigations of Structural Changes in Cu/ZnO Catalysts. *J. Catal.* 194, 452–460. doi:10.1006/jcat.2000.2930

Hayyan, M., Hashim, M. A., and AlNashef, I. M. (2016). Superoxide Ion: Generation and Chemical Implications. *Chem. Rev.* 116, 3029–3085. doi:10.1021/acs.chemrev.5b00407

Huang, T.-J., and Tsai, D. H. (2003). CO Oxidation Behavior of Copper and Copper Oxides. *Catal. Lett.* 87, 173–178. doi:10.1023/A:1023495223738

Imtiaz, Q., Abdala, P. M., Kierzkowska, A. M., Van Beek, W., Schweiger, S., Rupp, J. L. M., et al. (2016). Na+ Doping Induced Changes in the Reduction and Charge Transport Characteristics of Al2O3-Stabilized, CuO-Based Materials for CO2 Capture. *Phys. Chem. Chem. Phys.* 18, 12278–12288. doi:10.1039/C6CP00257A

Jernigan, G. G., and Somorjai, G. A. (1994). Carbon Monoxide Oxidation over Three Different Oxidation States of Copper: Metallic Copper, Copper (I) Oxide, and Copper (II) Oxide - A Surface Science and Kinetic Study. *J. Catal.* 147, 567–577. doi:10.1006/jcat.1994.1173

Jia, J., Qian, C., Dong, Y., Li, Y. F., Wang, H., Ghoussoub, M., et al. (2017). Heterogeneous Catalytic Hydrogenation of CO2by Metal Oxides: Defect Engineering - Perfecting Imperfection. *Chem. Soc. Rev.* 46, 4631–4644. doi:10.1039/C7CS00026J

Jiang, X., Nie, X., Guo, X., Song, C., and Chen, J. G. (2020). Recent Advances in Carbon Dioxide Hydrogenation to Methanol via Heterogeneous Catalysis. *Chem. Rev.* 120, 7984–8034. doi:10.1021/acs.chemrev.9b00723

Jing, P., Gong, X., Liu, B., and Zhang, J. (2020). Recent Advances in Synergistic Effect Promoted Catalysts for Preferential Oxidation of Carbon Monoxide. *Catal. Sci. Technol.* 10, 919–934. doi:10.1039/C9CY02073J

Jun, K.-W., Shen, W.-J., Rama Rao, K. S., and Lee, K.-W. (1998). Residual Sodium Effect on the Catalytic Activity of Cu/ZnO/Al2O3 in Methanol Synthesis from CO2 Hydrogenation. *Appl. Catal. A General* 174, 231–238. doi:10.1016/S0926-860X(98)00195-1

Kattel, S., Liu, P., and Chen, J. G. (2017a). Tuning Selectivity of CO2 Hydrogenation Reactions at the Metal/Oxide Interface. *J. Am. Chem. Soc.* 139, 9739–9754. doi:10.1021/jacs.7b05362

Kattel, S., Ramírez, P. J., Chen, J. G., Rodriguez, J. A., and Liu, P. (2017b). Active Sites for CO 2 Hydrogenation to Methanol on Cu/ZnO Catalysts. *Science* 355, 1296–1299. doi:10.1126/science.aal3573

Kniep, B., Girgsdies, F., and Ressler, T. (2005). Effect of Precipitate Aging on the Microstructural Characteristics of Cu/ZnO Catalysts for Methanol Steam Reforming. *J. Catal.* 236, 34–44. doi:10.1016/j.jcat.2005.09.001

Kniep, B. L., Ressler, T., Rabis, A., Girgsdies, F., Baenitz, M., Steglich, F., et al. (2004). Rational Design of Nanostructured Copper-Zinc Oxide Catalysts for the Steam Reforming of Methanol. *Angew. Chem. Int. Ed.* 43, 112–115. doi:10.1002/anie.200352148

Kuld, S., Thorhauge, M., Falsig, H., Elkjaer, C. F., Helveg, S., Chorkendorff, I., et al. (2016). Quantifying the Promotion of Cu Catalysts by ZnO for Methanol Synthesis. *Science* 352, 969–974. doi:10.1126/science.aaf0718

Li, W., Hu, Y., Jiang, H., Jiang, N., Bi, W., and Li, C. (2018b). Litchi-peel-like Hierarchical Hollow Copper-Ceria Microspheres: Aerosol-Assisted Synthesis and High Activity and Stability for Catalytic CO Oxidation. *Nanoscale* 10, 22775–22786. doi:10.1039/C8NR04642E

Li, W., Wang, H., Jiang, X., Zhu, J., Liu, Z., Guo, X., et al. (2018a). A Short Review of Recent Advances in CO2 Hydrogenation to Hydrocarbons over Heterogeneous Catalysts. *RSC Adv.* 8, 7651–7669. doi:10.1039/C7RA13546G

Li, Z., Zhong, L., Yu, F., An, Y., Dai, Y., Yang, Y., et al. (2017). Effects of Sodium on the Catalytic Performance of CoMn Catalysts for Fischer-Tropsch to Olefin Reactions. *ACS Catal.* 7, 3622–3631. doi:10.1021/acscatal.6b03478

Liao, F., Huang, Y., Ge, J., Zheng, W., Tedsree, K., Collier, P., et al. (2011). Morphology-Dependent Interactions of ZnO with Cu Nanoparticles at the Materials' Interface in Selective Hydrogenation of CO2 to CH3OH. *Angew. Chem. Int. Ed.* 50, 2162–2165. doi:10.1002/ange.20100710810.1002/anie.201007108

Liu, C., Zhang, Y., Zhao, Y., Wei, L., Hong, J., Wang, L., et al. (2017). The Effect of the Nanofibrous Al2O3aspect Ratio on Fischer-Tropsch Synthesis over Cobalt Catalysts. *Nanoscale* 9, 570–581. doi:10.1039/C6NR07529K

Liu, J., Qiao, B., Song, Y., Huang, Y., and Liu, J. (2015). Hetero-epitaxially Anchoring Au Nanoparticles onto ZnO Nanowires for CO Oxidation. *Chem. Commun.* 51, 15332–15335. doi:10.1039/C5CC03353E

Liu, M.-H., Chen, Y.-W., Lin, T.-S., and Mou, C.-Y. (2018). Defective Mesocrystal ZnO-Supported Gold Catalysts: Facilitating CO Oxidation via Vacancy Defects in ZnO. *ACS Catal.* 8, 6862–6869. doi:10.1021/acscatal.8b0491310.1021/acscatal.8b01282

Liu, X., Liu, M.-H., Luo, Y.-C., Mou, C.-Y., Lin, S. D., Cheng, H., et al. (20122012). Strong Metal-Support Interactions between Gold Nanoparticles and ZnO Nanorods in CO Oxidation. *J. Am. Chem. Soc.* 134 (24), 10251–10258. doi:10.1021/ja3033235

Lou, Y., Cai, Y., Hu, W., Wang, L., Dai, Q., Zhan, W., et al. (2020a). Identification of Active Area as Active Center for CO Oxidation over Single Au Atom Catalyst. *ACS Catal.* 10, 6094–6101. doi:10.1021/acscatal.0c01303

Lou, Y., Xu, J., Zhang, Y., Pan, C., Dong, Y., and Zhu, Y. (2020b). Metal-support Interaction for Heterogeneous Catalysis: from Nanoparticles to Single Atoms. *Mater. Today Nano* 12, 100093. doi:10.1016/j.mtnano.2020.100093

Luo, L., Nian, Y., Wang, S., Dong, Z., He, Y., Han, Y., et al. (2020). Real-Time Atomic-Scale Visualization of Reversible Copper Surface Activation during the CO Oxidation Reaction. *Angew. Chem. Int. Ed.* 59, 2505–2509. doi:10.1002/ange.20191502410.1002/anie.201915024

Lyu, S., Peng, B., Kuang, T., Rappé, K. G., Zhang, Y., Li, J., et al. (2019). Supported Cobalt Nanoparticles with a Single Active Phase for Fischer-Tropsch Synthesis. *ACS Appl. Nano Mat.* 2, 2266–2272. doi:10.1021/acsanm.9b00187

Milligen, B. P. v., Bons, P. D., Carreras, B. A., and Sánchez, R. (2005). On the Applicability of Fick's Law to Diffusion in Inhomogeneous Systems. *Eur. J. Phys.* 26, 913–925. doi:10.1088/0143-0807/26/5/023

Nakamura, J., Uchijima, T., Kanai, Y., and Fujitani, T. (1996). The Role of ZnO in Cu/ZnO Methanol Synthesis Catalysts. *Catal. Today* 28, 223–230. doi:10.1016/0920-5861(95)00240-5

Park, J., An, K., Hwang, Y., Park, J.-G., Noh, H.-J., Kim, J.-Y., et al. (2004). Ultra-large-scale Syntheses of Monodisperse Nanocrystals. *Nat. Mater* 3 (12), 891–895. doi:10.1038/nmat1251

Sarkodie, B., Hu, Y., Bi, W., Jiang, J., and Li, C. (2021). Promotional Effects of Cu O on the Activity of Cu/ZnO Catalyst toward Efficient CO Oxidation. *Appl. Surf. Sci.* 548, 149241. doi:10.1016/j.apsusc.2021.149241

Song, T., Dong, J., Li, R., Xu, X., Hiroaki, M., Yang, B., et al. (2021). Oxidative Strong Metal-Support Interactions between Metals and Inert Boron Nitride. *J. Phys. Chem. Lett.* 12, 4187–4194. doi:10.1021/acs.jpclett.1c00934

Svintsitskiy, D. A., Kardash, T. Y., Stonkus, O. A., Slavinskaya, E. M., Stadnichenko, A. I., Koscheev, S. V., et al. (2013). *In Situ* XRD, XPS, TEM, and TPR Study of Highly Active in CO Oxidation CuO Nanopowders. *J. Phys. Chem. C* 117, 14588–14599. doi:10.1021/jp403339r10.1021/jp403339r

Tang, H., Su, Y., Zhang, B., Lee, A. F., Isaacs, M. A., Wilson, K., et al. (2017). Classical Strong Metal-Support Interactions between Gold Nanoparticles and Titanium Dioxide. *Sci. Adv.* 3, e1700231. doi:10.1126/sciadv.1700231

van Deelen, T. W., Hernández Mejía, C., and de Jong, K. P. (2019). Control of Metal-Support Interactions in Heterogeneous Catalysts to Enhance Activity and Selectivity. *Nat. Catal.* 2, 955–970. doi:10.1038/s41929-019-0364-x

Wen, J., Huang, C., Sun, Y., Liang, L., Zhang, Y., Zhang, Y., et al. (2020). The Study of Reverse Water Gas Shift Reaction Activity over Different Interfaces: The Design of Cu-Plate ZnO Model Catalysts. *Catalysts* 10, 533. doi:10.3390/catal10050533

White, B., Yin, M., Hall, A., Le, D., Stolbov, S., Rahman, T., et al. (2006). Complete CO Oxidation over Cu2O Nanoparticles Supported on Silica Gel. *Nano Lett.* 6, 2095–2098. doi:10.1021/nl061457v

Whittle, D. M., Mirzaei, A. A., Hargreaves, J. S. J., Joyner, R. W., Kiely, C. J., Taylor, S. H., et al. (2002). Co-precipitated Copper Zinc Oxide Catalysts for Ambient Temperature Carbon Monoxide Oxidation: Effect of Precipitate Ageing on Catalyst Activity. *Phys. Chem. Chem. Phys.* 4, 5915–5920. doi:10.1039/B207691H

Xie, X., Li, Y., Liu, Z.-Q., Haruta, M., and Shen, W. (2009). Low-temperature Oxidation of CO Catalysed by Co3O4 Nanorods. *Nature* 458, 746–749. doi:10.1038/nature07877

Xiong, H., Zhang, Y., Wang, S., and Li, J. (2005). Fischer-Tropsch Synthesis: the Effect of Al2O3 Porosity on the Performance of Co/Al2O3 Catalyst. *Catal. Commun.* 6, 512–516. doi:10.1016/j.catcom.2005.04.018

Yang, F., Zhao, H., Wang, W., Wang, L., Zhang, L., Liu, T., et al. (2021). Atomic Origins of the Strong Metal-Support Interaction in Silica Supported Catalysts. *Chem. Sci.* 12, 12651–12660. doi:10.1039/D1SC03480D

Yang, X., Chen, H., Meng, Q., Zheng, H., Zhu, Y., and Li, Y. W. (2017). Insights into Influence of Nanoparticle Size and Metal-Support Interactions of Cu/ZnO Catalysts on Activity for Furfural Hydrogenation. *Catal. Sci. Technol.* 7, 5625–5634. doi:10.1039/C7CY01284E

Yang, Y., Luo, M., Zhang, W., Sun, Y., Chen, X., and Guo, S. (2018). Metal Surface and Interface Energy Electrocatalysis: Fundamentals, Performance Engineering, and Opportunities. *Chem* 4, 2054–2083. doi:10.1016/j.chempr.2018.05.019

Ye, R.-P., Lin, L., Li, Q., Zhou, Z., Wang, T., Russell, C. K., et al. (2018). Recent Progress in Improving the Stability of Copper-Based Catalysts for Hydrogenation of Carbon-Oxygen Bonds. *Catal. Sci. Technol.* 8, 3428–3449. doi:10.1039/C8CY00608C

Yin, M., Wang, F., Fan, H., Xu, L., and Liu, S. (2016). Heterojunction CuO@ZnO Microcubes for Superior P-type Gas Sensor Application. *J. Alloys Compd.* 672, 374–379. doi:10.1016/j.jallcom.2016.02.197

Zeng, Y., Wang, T., Zhang, S., Wang, Y., and Zhong, Q. (2017). Sol-gel Synthesis of CuO-TiO 2 Catalyst with High Dispersion CuO Species for Selective Catalytic Oxidation of NO. *Appl. Surf. Sci.* 411, 227–234. doi:10.1016/j.apsusc.2017.03.107

Zhang, Z.-c., Xu, B., and Wang, X. (2014). Engineering Nanointerfaces for Nanocatalysis. *Chem. Soc. Rev.* 43, 7870–7886. doi:10.1039/C3CS60389J

Zhang, Z., Chen, X., Kang, J., Yu, Z., Tian, J., Gong, Z., et al. (2021). The Active Sites of Cu-ZnO Catalysts for Water Gas Shift and CO Hydrogenation Reactions. *Nat. Commun.* 12, 4331–4339. doi:10.1038/s41467-021-24621-8

Zhang, Z., Wu, H., Yu, Z., Song, R., Qian, K., Chen, X., et al. (2019). Site-Resolved Cu 2 O Catalysis in the Oxidation of CO. *Angew. Chem. Int. Ed.* 58, 4276–4280. doi:10.1002/anie.201814258

Zhou, K., and Li, Y. (2012). Catalysis Based on Nanocrystals with Well-Defined Facets. *Angew. Chem. Int. Ed.* 51, 602–613. doi:10.1002/anie.201102619

Zhu, Y., Kong, X., Zheng, H., and Zhu, Y. (2018). Strong Metal-Oxide Interactions Induce Bifunctional and Structural Effects for Cu Catalysts. *Mol. Catal.* 458, 73–82. doi:10.1016/j.mcat.2018.07.023

Conflict of Interest: The authors declare that the research was conducted in the absence of any commercial or financial relationships that could be construed as a potential conflict of interest.

Publisher's Note: All claims expressed in this article are solely those of the authors and do not necessarily represent those of their affiliated organizations, or those of the publisher, the editors and the reviewers. Any product that may be evaluated in this article, or claim that may be made by its manufacturer, is not guaranteed or endorsed by the publisher.

frontiers | Frontiers in Chemistry

ORIGINAL RESEARCH
published: 02 June 2022
doi: 10.3389/fchem.2022.884105

The High-Effective Catalytic Degradation of Benzo[a]pyrene by Mn-Corrolazine Regulated by Oriented External Electric Field: Insight From DFT Study

Tairen Long[1], Haiyan Wan[1], Jianqiang Zhang[2], Jie Wu[1], Jin-Xia Liang[1] and Chun Zhu[1]**

[1]School of Chemistry and Chemical Engineering, Guizhou University, Guiyang, China, [2]Guizhou Fukangren Pharmaceutical Co., Ltd, Guiyang, China

The degradation of BaP into hydroxybenzo[a]pyrene by Mn-corrolazine and its regulation by an oriented external electronic field (OEEF) were systematically studied using first-principle calculations. Extensive density function calculations showed that the degradation of BaP into hydroxybenzo[a]pyrene by Mn-corrolazine occurs *via* a three-step process in the absence of OEEF, in which a more toxic and stable epoxide intermediate is generated. However, upon application of OEEF along the intrinsic Mn-O reaction axis, the degradation of BaP into hydroxybenzo[a]pyrene is greatly simplified. The negative charge on the terminal O atom of Mn-OO corrolazine increases with an increase in the OEEF intensity. As the intensity of the OEEF increases over 0.004 a.u., the negatively charged terminal O atom has the ability to directly abstract the positively charged H atom of BaP and the degradation of BaP into hydroxybenzo[a]pyrene can be completed *via* a one-step process, avoiding the production of more toxic epoxide intermediates.

Keywords: benzo[a]pyrene, Mn-corrolazine, catalytic oxidation, density functional theory calculations, oriented external electric field

OPEN ACCESS

Edited by:
Liuqingqing Yang,
Shanghai Jiao Tong University, China

Reviewed by:
Ke Yang,
Yale University, United States
Pengfei Tian,
East China University of Science and Technology, China

****Correspondence:***
Jin-Xia Liang
liangjx2009@163.com
Chun Zhu
czhu2014@163.com

Specialty section:
This article was submitted to Theoretical and Computational Chemistry, a section of the journal Frontiers in Chemistry

Received: *28 February 2022*
Accepted: *16 May 2022*
Published: *02 June 2022*

Citation:
Long T, Wan H, Zhang J, Wu J, Liang J-X and Zhu C (2022) The High-Effective Catalytic Degradation of Benzo[a]pyrene by Mn-Corrolazine Regulated by Oriented External Electric Field: Insight From DFT Study. Front. Chem. 10:884105. doi: 10.3389/fchem.2022.884105

1 INTRODUCTION

With the development of modern industry, the use of fossil fuels and discharge of soot, flue gas and industrial wastewater have resulted in serious environmental pollution from polycyclic aromatic hydrocarbons (PAHs) (Paulik et al., 2016; Poater et al., 2018; Wu et al., 2018; Yan et al., 2021). As a representative of carcinogenic PAHs, benzo[a]pyrene (BaP) bearing five fused aromatic rings, which is classified as a Group I "human carcinogen" by the World Health Organization (WHO) International Agency for Research on Cancer IARC (2021), has caused irreversible damage to air, water and soil (Lemieux et al., 2015; Strobel et al., 2015; Roberts et al., 2016). Moreover, BaP is persistent organic pollutant, which poses a serious threat to global food security (Średnicka et al., 2021). Seafood with increasing BaP content increases the risk of cancer (Wang et al., 2020) and BaP in roast meat, smoked meat and fried foods will cause serious damage to animals and human organs, such as the liver and kidneys (Takeshita and kanaly, 2019; Iko Afé et al., 2020; Cunha et al., 2021; Goedtke et al., 2021; Mertens et al., 2021; Ge et al., 2022). Very recent studies (Kostoff et al., 2020) have indicated that people exposed to increased levels of BaP will lead to degradation or dysfunction of the immune system and people will become more susceptible to 2019-nCoV. Therefore, to eliminate the toxicity of BaP, it is essential to study its degradation.

BaP is mainly degraded *via* chemical oxidation, photo-oxidation, microbial degradation and bioaccumulation in the natural environment (Wilson and Jones, 1993; Rubio-Clemente et al., 2018). Among them, the use of bacteria or fungi to biodegrade BaP has received a lot of research attention (Kou et al., 2009; Kuppusamy et al., 2016; Ping et al., 2017; Qin et al., 2017; Delsarte et al., 2018; Gan et al., 2018; Harry-Asobara and Kamei, 2019; Ostrem Loss et al., 2019; Sampaio et al., 2019; Tian et al., 2019), but this approach has a series of drawbacks, such as low catalytic efficiency and difficulty in cultivating suitable bacteria (Wang et al., 2012; Wongwongsee et al., 2013). From the perspective of utilizing solar energy, photocatalysis is one of the most attractive BaP degradation methods reported to date (Kou et al., 2009). BaP can be directly photodegraded upon adsorbing solar energy (Miller and Olejnik, 2001) or degraded using sensitized photochemical reactions (Mill et al., 1981; Fasnacht and Blough, 2002). Recently, the group Luo et al. (2015); Luo et al. (2018) has reported for the first time that natural porphyrins can promote the photoconversion of BaP in water into quinones using singlet oxygen generated *via* a photocatalytic detoxification reaction (Zang et al., 2007). In addition, the possible oxidative degradation mechanisms and pathways of BaP in the atmosphere have been explored by Dang et al. (2015). However, despite the involvement of transition metals in many catalytic processes (Fujihara and Tsuji, 2019; Lin et al., 2021; Parmar et al., 2021; Sánchez-López et al., 2021; Yang et al., 2021; Zhou et al., 2021; Zhou et al., 2022), the use of transition metal complexes as non-sacrificial oxidants for the degradation of BaP has not been reported in the literature.

Our group has recently reported that Mn-corrolazine can activate oxygen in the air *via* an electron spin-flip mechanism under visible light irradiation, which forms a singlet [Mn]-O-O species with terminal radical characteristics (Zhu et al., 2018). In fact, corrole has been widely used in many fields (Zhu and Liang, 2015; Zhu et al., 2016; Li and Cao, 2018; Lvova et al., 2018; Liang et al., 2019; Zheng et al., 2020; Dedic et al., 2021; Li et al., 2021). Very recently, oriented external electric fields (OEEFs) have been extensively studied as a 'smart agent' by Shaik et al. (2016); (Ramanan et al., 2018; Wang et al., 2018); Shaik et al. (2020). They found that the interaction between OEEFs and dipole moments can change the electron transfer process and enhance the ionicity in the direction of the "reaction axis", resulting in the regioselectivity of the reaction. Furthermore, our group has also found that OEEFs can effectively regulate the catalytic activity of metal-corrolazines (Wang et al., 2021; Zhu et al., 2021). Therefore, in order to discover a new effective and environmentally-friendly strategy for the degradation of BaP, we have explored the degradation mechanism of BaP to form hydroxybenzo[a]pyrene using Mn-corrolazine involving a [Mn]-O-O species. We further studied the regulation of OEEF on the degradation process. Based on considerable theoretical calculations, we have discovered the reasonable reaction process and OEEF regulation mechanism, which provide a theoretical foundation for further experimental research on the degradation of BaP using Mn-corrolazine regulated by OEEF.

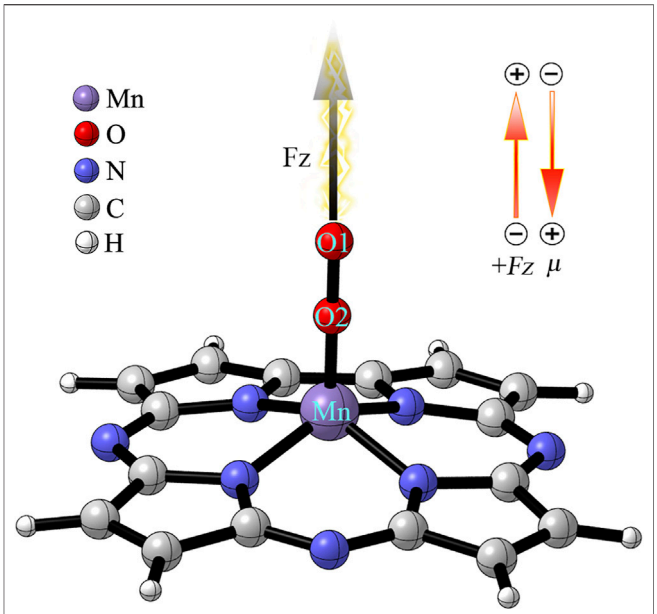

SCHEME 1 | Definitions of the OEEF. F_Z is along the intrinsic Mn-O reaction axis perpendicular to the corrolazine ring. The inset indicates the definition of a positive OEEF (Fz > 0) and the stabilizing orientation of the dipole moment (μ_z).

2 COMPUTATIONAL METHODS

The B3LYP density functional method (Lee et al., 1988; Stephens et al., 1994) in combination with an effective core pseudopotential basis set (LANL2DZ) for the Mn atom and 6-31G(d) basis set for all other atoms (B1) was used for all geometry optimizations and frequency calculations performed in the Gaussian 16 package (Frisch et al., 2016). The energies were refined using single-point calculations (Stuyver et al., 2020) utilizing the B3LYP functional with D3BJ dispersion correction (Grimme et al., 2011) coupled with 6-311+G (d,p) (Andersson and Uvdal, 2005) and aug-cc-pVQZ (Mn) (Kendall and Harrison, 1992), i.e., B3LYP-D3(BJ)/6-311+G (d,p), aug-cc-pVQZ (Mn) level of theory (B2). Zero-point energy (ZPE) corrections were taken from the B3LYP/6-31G(d), LANL2DZ (Mn) level of theory. Twelve structures formed by [Mn]-O-O adsorbing different H atoms from BaP were fully optimized to obtain the most stable structure. Based on this structure, the degradation of BaP was studied in which the reactant complexes (RC), transition states (TS), intermediates (IM), and products (P) were fully optimized without any symmetry constraints. Frequency calculations were carried out at the same level of theory in order to assess the nature of a stable point on the potential energy surface and estimate the thermodynamic properties. Moreover, intrinsic reaction coordinate (IRC) analysis was used to further confirm the TS correlating to their corresponding RC and P.

To investigate the effect of OEEF on the reaction, the OEEF Fz along the intrinsic Mn-O reaction axis perpendicular to the corrolazine ring was applied using the keyword "field = M ±

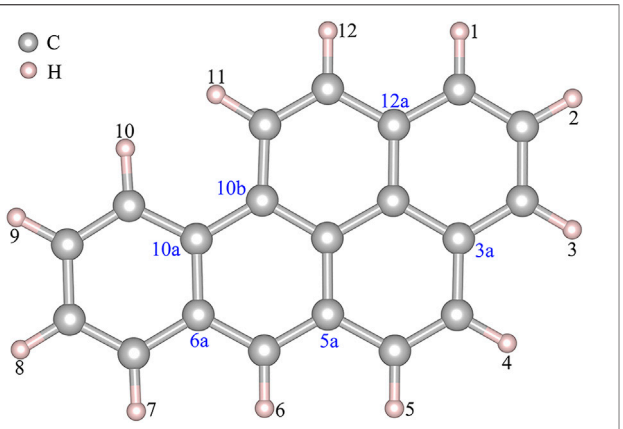

FIGURE 1 | Partial atomic numbers of BaP.

N", as shown in **Scheme 1**. The positive direction of the electric field vector in **Scheme 1** follows the Gaussian 16 convention. In addition, the electric field strength of Fz was in the range of 0.001–0.01 a.u. (1 a.u. = 51.4 V/Å).

3 RESULTS AND DISCUSSION

3.1 Reactive Site Screening

Figure 1 shows that BaP has 12 H atoms in different chemical environments and in order to find the most reasonable reaction site, we optimized the different RC formed by these 12 different H atoms in BaP and the [Mn]-O-O corrolazines, respectively. **Figure 2** and **Table 1** show that BaP and [Mn]-O-O corrolazine form weak interaction complexes, in which the bond lengths of $d_{O1\text{-}HX}$ (X = 1, 2, 3, ..., 12), where the numbers refer to the serial numbers of the H atom, are very similar in the range from 2.537 to 2.845 Å, and the bond length of $d_{O1\text{-}H11}$ was the smallest, indicating its interaction was the strongest. Similarly, the energies of these structures are very similar, in which the difference between the highest energy and the lowest energy was only 1.07 kcal/mol, which originates from the weak interaction formed between BaP and [Mn]-O-O corrolazine. In addition, the energy of structure **11** was the lowest, again proving that it was the most stable. Furthermore, **Table 1** shows the bond lengths of Mn-O and O-O were 1.617 and1.265 Å, respectively, which are similar to the results obtained in

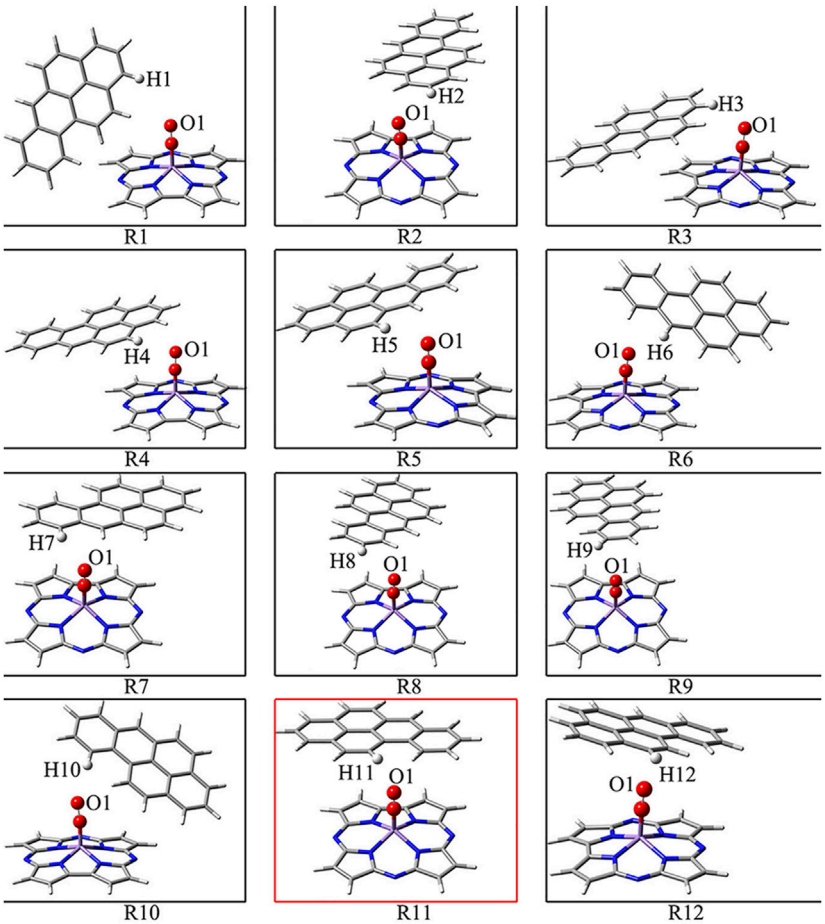

FIGURE 2 | Optimized structures of the different reactant complexes.

TABLE 1 | |O1-HX (X = 1, 2, 3, ..., 12), Mn-O, O-O bond lengths (Å), relative electronic energies and zero-point energies (ΔE, ΔE_0, kcal/mol).

Structure	$d_{O1-HX(X=1, 2, 3, ...,12)}$	d_{Mn-O}	d_{O-O}	ΔE	ΔE_0
R1	2.697	1.617	1.264	0.218	0.166
R2	2.776	1.617	1.262	0.792	0.683
R3	2.671	1.617	1.264	0.319	0.263
R4	2.599	1.617	1.263	1.015	0.907
R5	2.608	1.618	1.264	0.953	0.838
R6	2.703	1.619	1.263	0.945	0.809
R7	2.648	1.617	1.264	0.342	0.288
R8	2.845	1.617	1.262	0.725	0.604
R9	2.778	1.617	1.261	0.802	0.684
R10	2.676	1.617	1.263	0.705	0.647
R11	2.537	1.617	1.265	0	0
R12	2.563	1.618	1.264	1.068	0.958

our previous study (Zhu et al., 2018), indicating that the [Mn]-O-O moiety in structure **11** has strong oxidation ability. Therefore, we chose structure **11** as the RC to further explore the degradation of BaP.

3.2 Reaction Mechanism of [Mn]-O-O Catalysed Oxidation of BaP Into 11-OH-BaP

Figure 3 shows [Mn]-O-O corrolazine catalyses the degradation BaP into 11-hydroxybenzo[a]pyrene (11-OH-BaP) *via* three steps: 1) epoxidation, 2) hydrogen transfer and 3) rearrangement. The first epoxidation step in which 11,12-epoxybenzopyrene (IM1) was generated from BaP. The O-O bond in the [Mn]-O-O moiety was tilted and its terminal O1 attacks the C12 atom in the BaP moiety. The BaP moiety then rotates and its C11 atom attacks the terminal O1 atom to form 11,12-epoxybenzopyrene with a reaction activation energy of 23.3 kcal/mol. During this step, the hybridization of C11 and C12 changes from sp^2 to sp^3. Following the epoxidation step, IM2 was formed *via* a hydrogen transfer step. In this step, the C11-O1 bond was broken and at the same time, the C11-H11 was broken with H11 being transferred to C12 and C11 returns to sp^2 hybridization. The activation energy of this step was up to 37.98 kcal/mol. The third step was an H atom rearrangement to form 11-OH-BaP (P), in which one H atom on C12 is transferred to O1, followed by a rebound reaction to form P with C12 returning to sp^2 hybridization. In addition, the activation energy in this step was even higher (up to 53.47 kcal/mol). Using whole process analysis, P was the most stable with the lowest energy compared to RC, IM1 and IM2. However, as the activation energies in step 2 and step 3 are very high (37.98 and 53.47 kcal/mol respectively), it is difficult to reach the final product (P) *via* TS2 and TS3. Thus, the reaction will stop at the intermediate product, 11,12-epoxybenzopyrene, which is a carcinogen and even more toxic than BaP. Therefore, it is necessary to seek an efficient way to degrade BaP into the final non-toxic product, 11-OH-BaP.

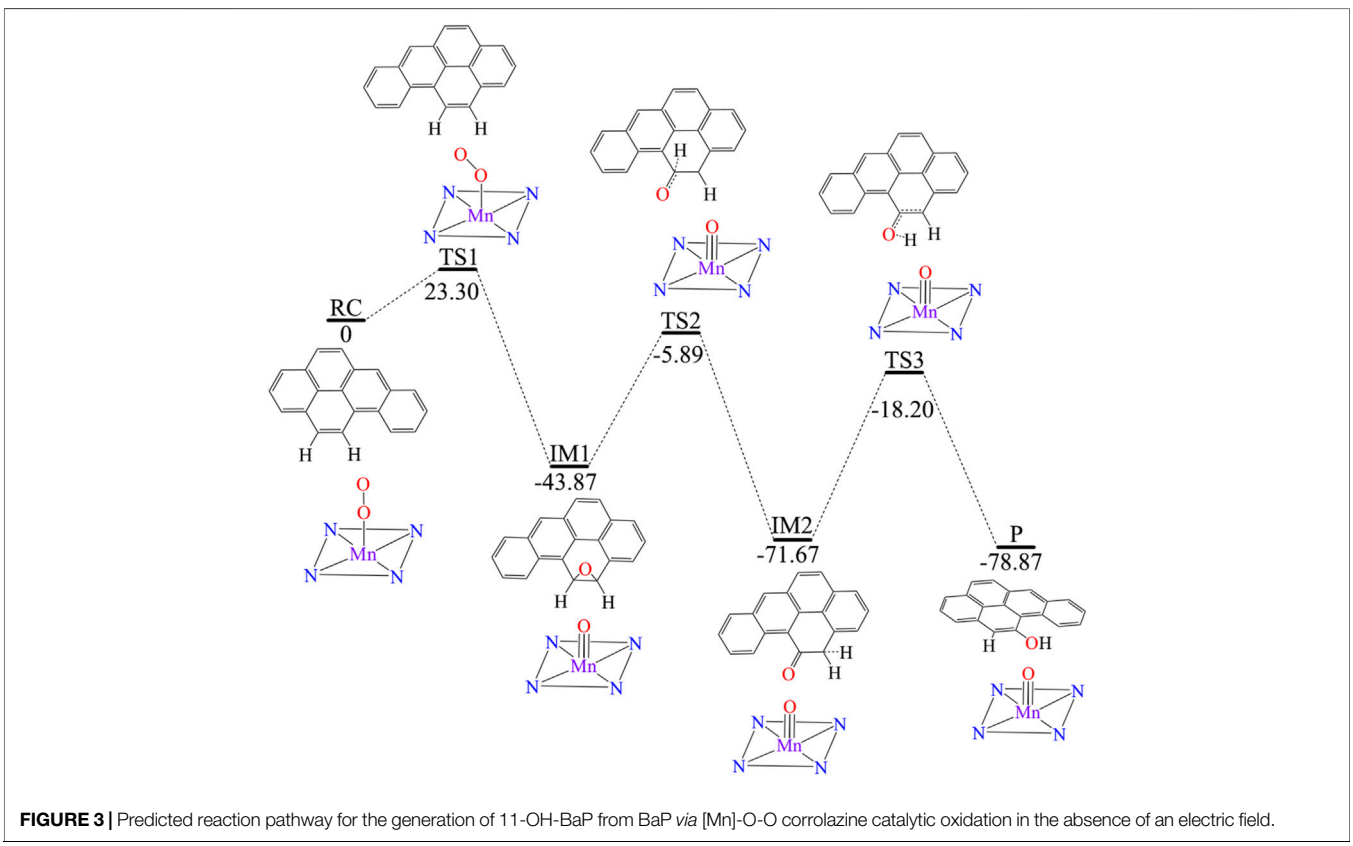

FIGURE 3 | Predicted reaction pathway for the generation of 11-OH-BaP from BaP *via* [Mn]-O-O corrolazine catalytic oxidation in the absence of an electric field.

TABLE 2 | | Variation in the relative electronic energy and dipole moment on the z-axis for the reactants (RC) and transition states (TS) under different electric field strengths in the range of 0–0.01 a.u. Units: ΔE, kcal/mol and μ_z, D.

F_Z (10^{-4}) (a.u.)	Complex (ΔE, μ_z)			
	RC (ΔE)	RC (μ_z)	TS (ΔE)	TS (μ_z)
0	0	−2.19	0	5.07
10	0.26	−4.94	1.89	2.27
20	−1.86	−6.46	3.06	2.24
30	−2.51	−7.92	3.47	−1.35
40	−5.53	−10.98	3.32	−6.38
50	−8.84	−12.56	10.58	−9.68
60	−11.53	−13.51	8.28	−11.16
70	−15.14	−15.15	5.27	−13.02
80	−19.17	−16.81	1.81	−14.89
90	−23.52	−18.41	−2.05	−16.67
100	−28.19	−20.05	−6.50	−18.61

3.3 One-step Degradation Mechanism Regulated by OEEF

3.3.1 The Effect of OEEF on the RC and TS

To simplify the reaction process so that BaP can be degraded into 11-OH-BaP in one-step, thereby avoiding the production of highly toxic epoxybenzopyrene, we applied an OEEF Fz along the z-axis, which is the intrinsic Mn-O bond reaction axis perpendicular to the corrolazine ring, in order to regulate the degradation reaction process, as shown in **Scheme 1**.

We first considered the effect of the Fz on the stability of RC in the range of 0–0.01 a.u. **Table 2** and **Figure 4A** show the application of the Fz increases the stability of the RC, in which the relative electronic energy increases upon increasing the electric field intensity. To further explore the reason why the stability of the RC becomes stronger due to the application of the Fz, we analysed the change in the dipole moment in the z-orientation of the RC upon changing the Fz. **Table 2** shows the dipole moment in the z-orientation of the RC increases from |−2.19| D without OEEF to |−20.05| D in Fz = 0.01 a.u. Thus, the enhanced stability of the RC originates from the interaction between the increased dipole moment in the z-orientation and the Fz.

For the TS, the effect of the OEEF becomes complex, in which different Fz strengths exhibit different behaviour. **Table 2** shows for Fz < 0.008 a.u., the OEEF destabilizes the TS upon increasing its relative electronic energy. However, further increasing the intensity of Fz to more than 0.008 a.u., the OEEF stabilizes the TS upon decreasing its relative electronic energy, as shown in the insert of **Figure 4B**. The change in the stabilization can be attributed to the repulsion between the OEEF and increasing dipole moment in the z-orientation of the TS, from 5.07 D without an electric field to 2.24 D in Fz = 0.002 a.u. However, further increasing with dipole moment results in the dipole moment in z-orientation flipping its direction at the critical Fz value of 0.003 a.u., and the repulsion between the OEEF and molecular dipole moment in the z-orientation becomes attractive. Thus, the OEEF stabilizes the TS.

3.3.2 The Effect of the OEEF on the Reaction Mechanism

We further investigated the effect of the OEEF on the mechanism of the degradation of BaP into 11-OH-BaP and discovered a very significant phenomenon. The reaction mechanism changes upon increasing the OEEF intensity, i.e., the degradation of BaP into 11-OH-BaP was simplified from a three-step process to a one-step process in which the H11 atom in BaP was directly transferred to the terminal O1 atom in [Mn]-O-O, followed by a rebound reaction of the resulting OH group back to BaP to form 11-OH-BaP, as shown in **Figure 5**. To further explore the reason for the change in the BaP degradation mechanism, we calculated the Mulliken charges of the atoms in the TS involved the H11 atom transfer step. **Table 3** shows the Mulliken charge at O1 was −0.203 |e| without the OEEF. As the Fz strength increases from 0 to 0.004 a.u., the Mulliken charge of the O1 atom increases from −0.21 |e| to −0.30 |e|, increasing its attraction to the positively charged H11 atom. However, the BaP moiety in

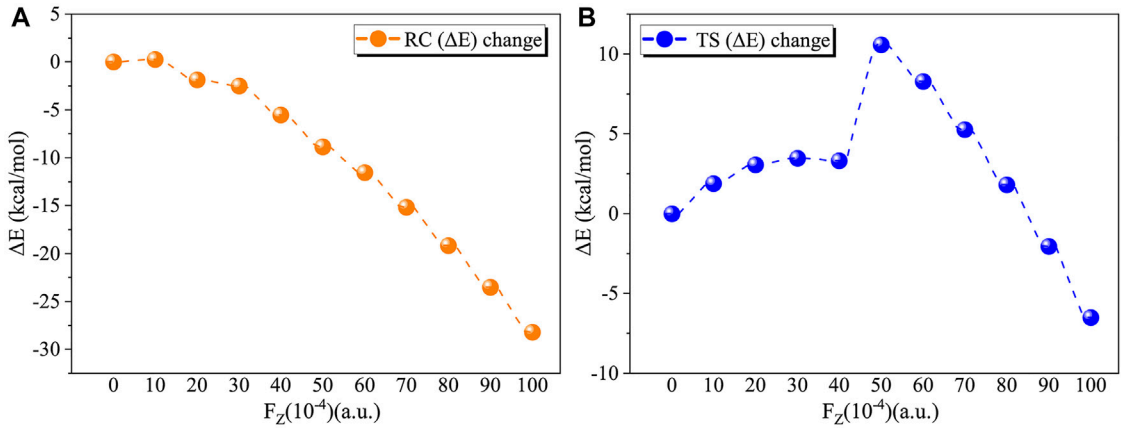

FIGURE 4 | (A) Variation in the relative electron energy of the reactants (RC) with the electric field strength. **(B)** Variation in the relative electron energy of the transition states (TS) with the electric field strength.

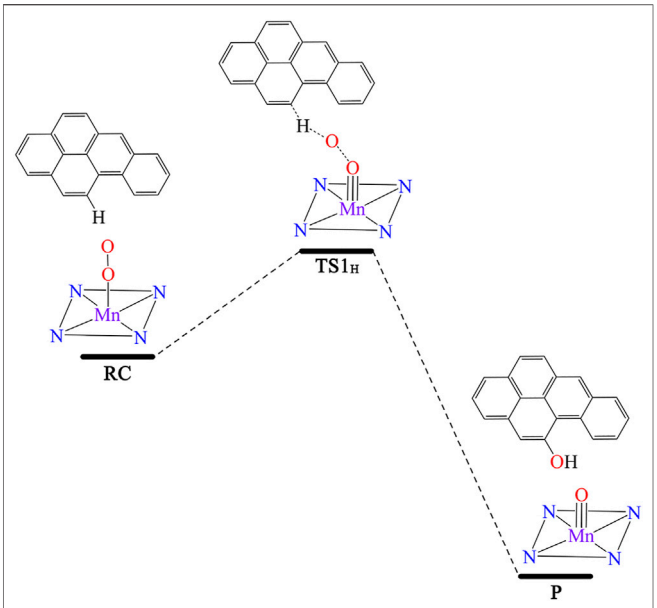

FIGURE 5 | The one-step reaction process converting BaP into 11-OH-BaP.

the reactant complex rotates continuously in this process, from almost parallel to the Mn-O bond to almost perpendicular to the Mn-O bond, so that the effect of the OEEF parallel to the Mn-O bond on BaP initially increases and then decreases. Therefore, the Mulliken charge on the H11 atom first increases from 0.175 |e| at Fz = 0 to 0.179 |e| at Fz = 0.002 a.u., and then decreases to 0.144 |e| at Fz = 0.004 a.u., which is the minimum value. In addition, the attraction of the negatively charged terminal O1 atom to the positively charged H11 atom was also weakened. Therefore, the reaction mechanism remains a three-step process, in which the terminal O1 atom is attracts to the C12 atom to form an epoxybenzopyrene intermediate. However, further increasing the OEEF intensity increases the negative charge on the terminal O1 atom to be more than 0.3 |e|. At the same time, the BaP moiety further rotates and deviates from direction parallel to the Mn-O bond, so the effect of the OEEF on BaP moiety was significantly strengthened and the positive charge on the H11 atom increases sharply. Moreover, as the positive charge of H11 exceeds that of C12, the interaction between H11 and the terminal O1 atom is stronger than that between C12 and O1, resulting in the TS to change from O1 attacking C12 to O1 attacking H11. Due to the change in the TS, the H11 atom can be directly transferred to the O1 atom to form 11-OH-BaP *via* a subsequent rebound reaction. Thus, the degradation of BaP into 11-OH-BaP was greatly simplified from a one-step to three-step process. Moreover, the simplified degradation reaction of BaP avoids the production of toxic epoxybenzopyrene.

Analysis of the reaction activation energy of the degradation reaction of BaP into 11-OH-BaP upon the application of the OEEF shows its effect on the RC and TS was similar in the first step with the reaction activation energy varying slightly from Fz = 0 to Fz = 0.004 a.u. When the Fz was increased from 0.004 to 0.005 a.u., the reaction activation energy increases sharply from 17.03 to 28.80 kcal/mol due to the fundamental change in the TS. However, further increasing the OEEF from Fz = 0.005 to Fz = 0.01 a.u., the reaction activation increases slightly because the structure of the TS remains unchanged. Analysis of the whole reaction process shows that the reaction activation energy of the one-step process in Fz > 0.005 a.u. was higher than that in the first step of the three-step process and the activation energy of the one-step process was significantly less than those of the second and third step in the three-step process. Therefore, the regulation of the OEEF significantly simplifies the degradation reaction of BaP to an effective and environmentally-friendly process, which is of great significance to the food industry.

TABLE 3 | | Mulliken charges (|e|) of some atoms in the reactive centre of the transition state and activation energies ΔE_0 (electronic energies + ZPE: kcal/mol) under an electric field.

F_Z (10^{-4}) (a.u.)	O1	H11	C12	Activation energy
0	−0.203	0.175	−0.170	23.30
10	−0.216	0.171	−0.160	17.32
20	−0.210	0.179	−0.168	21.37
30	−0.230	0.166	−0.151	21.42
40	−0.300	0.144	−0.164	17.03
50	−0.357	0.276	−0.179	28.80
60	−0.362	0.280	−0.181	29.07
70	−0.368	0.285	−0.183	29.58
80	−0.374	0.291	−0.184	30.07
90	−0.379	0.294	−0.185	30.50
100	−0.386	0.299	−0.185	30.92

4 CONCLUSION

BaP is widely found in the natural environment and food, etc., and its degradation is of great significance for biosafety because of its carcinogenicity as a Group I "human carcinogen". We have used Mn-OO corrolazine to degrade BaP into 11-OH-BaP in order to detoxify it. The degradation process occurs *via* a three-step process under field-free condition, i.e., epoxidation, hydrogen transfer and rearrangement, in which a more toxic epoxide intermediate is produced. Due to the high stability of the epoxide intermediate with an activation energy of up to 53.47 kcal/mol for further reaction, BaP is difficult to degrade into 11-OH-BaP using [Mn]-O-O corrolazine. However, the application of an OEEF along the intrinsic Mn-O reaction axis, which is more easily aligned in practical applications, greatly simplified the degradation of BaP into 11-OH-BaP. As the OEEF can effectively regulate the charge on the terminal O atom in [Mn]-O-O corrolazine, the H atom in BaP can be directly attracted by the terminal O atom to generate 11-OH-BaP *via* a subsequent rebound reaction. Thus, the complex

three-step degradation process of BaP into 11-OH-BaP has been simplified into a one-step process, avoiding the generation of the more toxic and stable epoxide intermediate. This effective and environmentally-friendly degradation process will have a far-reaching impact on areas such as the environment and food industry.

DATA AVAILABILITY STATEMENT

The original contributions presented in the study are included in the article/supplementary material, further inquiries can be directed to the corresponding authors.

AUTHOR CONTRIBUTIONS

TL: investigation, Writing-original draft. HW: investigation. JZ: investigation. JW: investigation, discussed the data. J-XL: investigation, supervision, writing-review and editing, project. CZ: supervision, writing-review and editing, project administration, funding acquisition.

FUNDING

This work was supported by the National Science Foundation of China (No. 21963005 and 21763006), Natural Science Foundation of Guizhou University [No. (2021)40 and (2020)32].

REFERENCES

Andersson, M. P., and Uvdal, P. (2005). New Scale Factors for Harmonic Vibrational Frequencies Using the B3LYP Density Functional Method with the Triple-ζ Basis Set 6-311+G(d,p). *J. Phys. Chem. A* 109, 2937–2941. doi:10.1021/jp045733a

Cunha, S. C., Siminel, D., Guàrdia, M. D., de Alda, M. L., López-Garcia, E., Muñoz, I., et al. (2021). Effect of Processing Smoked Salmon on Contaminant Contents. *Food Chem. Toxicol.* 153, 112276. doi:10.1016/j.fct.2021.112276

Dang, J., Shi, X., Hu, J., Chen, J., Zhang, Q., and Wang, W. (2015). Mechanistic and Kinetic Studies on OH-initiated Atmospheric Oxidation Degradation of Benzo [α]pyrene in the Presence of O2 and NOx. *Chemosphere* 119, 387–393. doi:10.1016/j.chemosphere.2014.07.001

Dedic, D., Dorniak, A., Rinner, U., and Schöfberger, W. (2021). Recent Progress in (Photo-)-Electrochemical Conversion of CO2 with Metal Porphyrinoid-Systems. *Front. Chem.* 9, 685619. doi:10.3389/fchem.2021.685619

Delsarte, I., Rafin, C., Mrad, F., and Veignie, E. (2018). Lipid Metabolism and Benzo[a]pyrene Degradation by Fusarium Solani: an Unexplored Potential. *Environ. Sci. Pollut. Res.* 25, 12177–12182. doi:10.1007/s11356-017-1164-y

Fasnacht, M. P., and Blough, N. V. (2002). Aqueous Photodegradation of Polycyclic Aromatic Hydrocarbons. *Environ. Sci. Technol.* 36, 4364–4369. doi:10.1021/es025603k

Frisch, M. J., Trucks, G. W., Schlegel, H. B., Scuseria, G. E., Robb, M. A., Cheeseman, J. R., et al. (2016). *Gaussian 16, Revision B.01*. Wallingford, CT: Gaussian, Inc.

Fujihara, T., and Tsuji, Y. (2019). Carboxylation Reactions Using Carbon Dioxide as the C1 Source via Catalytically Generated Allyl Metal Intermediates. *Front. Chem.* 7, 430. doi:10.3389/fchem.2019.00430

Gan, X., Teng, Y., Zhao, L., Ren, W., Chen, W., Hao, J., et al. (2018). Influencing Mechanisms of Hematite on Benzo(a)pyrene Degradation by the PAH-Degrading Bacterium Paracoccus Sp. Strain HPD-2: Insight from Benzo(a) pyrene Bioaccessibility and Bacteria Activity. *J. Hazard. Mater.* 359, 348–355. doi:10.1016/j.jhazmat.2018.07.070

Ge, J., Hao, R., Rong, X., Dou, Q. P., Tan, X., Li, G., et al. (2022). Secoisolariciresinol Diglucoside Mitigates Benzo[a]pyrene-Induced Liver and Kidney Toxicity in Mice via miR-101a/MKP-1-Mediated P38 and ERK Pathway. *Food Chem. Toxicol.* 159, 112733. doi:10.1016/j.fct.2021.112733

Goedtke, L., John, A., Lampen, A., Seidel, A., Braeuning, A., and Hessel-Pras, S. (2021). Mixture Effects of Food-Relevant Polycyclic Aromatic Hydrocarbons on the Activation of Nuclear Receptors and Gene Expression, Benzo[a]pyrene Metabolite Profile and DNA Damage in HepaRG Cells. *Food Chem. Toxicol.* 147, 111884. doi:10.1016/j.fct.2020.111884

Grimme, S., Ehrlich, S., and Goerigk, L. (2011). Effect of the Damping Function in Dispersion Corrected Density Functional Theory. *J. Comput. Chem.* 32, 1456–1465. doi:10.1002/jcc.21759

Harry-Asobara, J. L., and Kamei, I. (2019). Growth Management of White-Rot Fungus Phlebia Brevispora Improved Degradation of High-Molecular-Weight Polycyclic Aromatic Hydrocarbons. *3 Biotech.* 9, 403. doi:10.1007/s13205-019-1932-0

IARC (2021). Monographs on the Evaluation of Carcinogenic Risks to Humans. Avilable at: http://monographs.iarc.fr/ENG/Classification/ (accessed December 8, 2021).

Iko Afé, O. H., Douny, C., Kpoclou, Y. E., Igout, A., Mahillon, J., Anihouvi, V., et al. (2020). Insight about Methods Used for Polycyclic Aromatic Hydrocarbons Reduction in Smoked or Grilled Fishery and Meat Products for Future Re-engineering: A Systematic Review. *Food Chem. Toxicol.* 141, 111372. doi:10.1016/j.fct.2020.111372

Kendall, R. A., Jr., Dunning, T. H., and Harrison, R. J. (1992). Electron Affinities of the First-row Atoms Revisited. Systematic Basis Sets and Wave Functions. *J. Chem. Phys.* 96, 6796–6806. doi:10.1063/1.462569

Kostoff, R. N., Briggs, M. B., Porter, A. L., Hernández, A. F., Abdollahi, M., Aschner, M., et al. (2020). The Under-reported Role of Toxic Substance Exposures in the COVID-19 Pandemic. *Food Chem. Toxicol.* 145, 111687. doi:10.1016/j.fct.2020.111687

Kou, J., Li, Z., Yuan, Y., Zhang, H., Wang, Y., and Zou, Z. (2009). Visible-Light-Induced Photocatalytic Oxidation of Polycyclic Aromatic Hydrocarbons over Tantalum Oxynitride Photocatalysts. *Environ. Sci. Technol.* 43, 2919–2924. doi:10.1021/es802940a

Kuppusamy, S., Thavamani, P., Megharaj, M., Lee, Y. B., and Naidu, R. (2016). Kinetics of PAH Degradation by a New Acid-Metal-Tolerant Trabulsiella Isolated from the MGP Site Soil and Identification of its Potential to Fix Nitrogen and Solubilize Phosphorous. *J. Hazard. Mater.* 307, 99–107. doi:10.1016/j.jhazmat.2015.12.068

Lee, C., Yang, W., and Parr, R. G. (1988). Development of the Colle-Salvetti Correlation-Energy Formula into a Functional of the Electron Density. *Phys. Rev. B* 37, 785–789. doi:10.1103/PhysRevB.37.785

Lemieux, C. L., Long, A. S., Lambert, I. B., Lundstedt, S., Tysklind, M., and White, P. A. (2015). Cancer Risk Assessment of Polycyclic Aromatic Hydrocarbon Contaminated Soils Determined Using Bioassay-Derived Levels of Benzo[a] pyrene Equivalents. *Environ. Sci. Technol.* 49, 1797–1805. doi:10.1021/es504466b

Li, P., and Cao, Z. (2018). Catalytic Preparation of Cyclic Carbonates from CO2 and Epoxides by Metal-Porphyrin and −Corrole Complexes: Insight into Effects of Cocatalyst and Meso-Substitution. *Organometallics* 37, 406–414. doi:10.1021/acs.organomet.7b00830

Li, X., Zhang, X.-P., Guo, M., Lv, B., Guo, K., Jin, X., et al. (2021). Identifying Intermediates in Electrocatalytic Water Oxidation with a Manganese Corrole Complex. *J. Am. Chem. Soc.* 143, 14613–14621. doi:10.1021/jacs.1c05204

Liang, J.-X., Wu, Y., Deng, H., Long, C., and Zhu, C. (2019). Theoretical Investigation on the Electronic Structure of One Dimensional Infinite Monatomic Gold Wire: Insights into Conducting Properties. *RSC Adv.* 9, 1373–1377. doi:10.1039/C8RA08286C

Lin, K., Shi, A., Shi, C., Lin, J., and Lin, H. (2021). Catalytic Asymmetric Amino Acid and its Derivatives by Chiral Aldehyde Catalysis. *Front. Chem.* 9, 687817. doi:10.3389/fchem.2021.687817

Luo, L., Lai, X., Chen, B., Lin, L., Fang, L., Tam, N. F. Y., et al. (2015). Chlorophyll Catalyse the Photo-Transformation of Carcinogenic Benzo[a]pyrene in Water. *Sci. Rep.* 5, 12776. doi:10.1038/srep12776

Luo, L., Xiao, Z., Chen, B., Cai, F., Fang, L., Lin, L., et al. (2018). Natural Porphyrins Accelerating the Phototransformation of Benzo[a]pyrene in Water. *Environ. Sci. Technol.* 52, 3634–3641. doi:10.1021/acs.est.7b05854

Lvova, L., Caroleo, F., Garau, A., Lippolis, V., Giorgi, L., Fusi, V., et al. (2018). A Fluorescent Sensor Array Based on Heteroatomic Macrocyclic Fluorophores for the Detection of Polluting Species in Natural Water Samples. *Front. Chem.* 6, 258. doi:10.3389/fchem.2018.00258

Mertens, B., Van Heyst, A., Demaegdt, H., Boonen, I., Van Den Houwe, K., Goscinny, S., et al. (2021). Assessment of Hazards and Risks Associated with Dietary Exposure to Mineral Oil for the Belgian Population. *Food Chem. Toxicol.* 149, 112034. doi:10.1016/j.fct.2021.112034

Mill, T., Mabey, W. R., Lan, B. Y., and Baraze, A. (1981). Photolysis of Polycyclic Aromatic Hydrocarbons in Water. *Chemosphere* 10, 1281–1290. doi:10.1016/0045-6535(81)90045-X

Miller, J. S., and Olejnik, D. (2001). Photolysis of Polycyclic Aromatic Hydrocarbons in Water. *Water Res.* 35, 233–243. doi:10.1016/S0043-1354(00)00230-X

Ostrem Loss, E. M., Lee, M.-K., Wu, M.-Y., Martien, J., Chen, W., Amador-Noguez, D., et al. (2019). Cytochrome P450 Monooxygenase-Mediated Metabolic Utilization of Benzo[a]Pyrene by Aspergillus Species. *Mbio* 10, e00558–00519. doi:10.1128/mBio.00558-19

Parmar, S. V., Avasare, V., and Pal, S. (2021). Unraveling the Effect of Aromatic Groups in Mn(I)NNN Pincer Complexes on Carbon Dioxide Activation Using Density Functional Study. *Front. Chem.* 9, 778718. doi:10.3389/fchem.2021.778718

Paulik, L. B., Donald, C. E., Smith, B. W., Tidwell, L. G., Hobbie, K. A., Kincl, L., et al. (2016). Emissions of Polycyclic Aromatic Hydrocarbons from Natural Gas Extraction into Air. *Environ. Sci. Technol.* 50, 7921–7929. doi:10.1021/acs.est.6b02762

Ping, L., Guo, Q., Chen, X., Yuan, X., Zhang, C., and Zhao, H. (2017). Biodegradation of Pyrene and Benzo[a]pyrene in the Liquid Matrix and Soil by a Newly Identified Raoultella Planticola Strain. *3 Biotech.* 7, 56. doi:10.1007/s13205-017-0704-y

Poater, J., Duran, M., and Solà, M. (2018). Aromaticity Determines the Relative Stability of Kinked vs. Straight Topologies in Polycyclic Aromatic Hydrocarbons. *Front. Chem.* 6, 561. doi:10.3389/fchem.2018.00561

Qin, W., Zhu, Y., Fan, F., Wang, Y., Liu, X., Ding, A., et al. (2017). Biodegradation of Benzo(a)pyrene by Microbacterium Sp. Strain under Denitrification: Degradation Pathway and Effects of Limiting Electron Acceptors or Carbon Source. *Biochem. Eng. J.* 121, 131–138. doi:10.1016/j.bej.2017.02.001

Ramanan, R., Danovich, D., Mandal, D., and Shaik, S. (2018). Catalysis of Methyl Transfer Reactions by Oriented External Electric Fields: Are Gold-Thiolate Linkers Innocent? *J. Am. Chem. Soc.* 140, 4354–4362. doi:10.1021/jacs.8b00192

Roberts, S. M., Munson, J. W., Ruby, M. V., and Lowney, Y. (2016). Effects of Source and Concentration on Relative Oral Bioavailability of Benzo(a)pyrene from Soil. *Environ. Sci. Technol.* 50, 11274–11281. doi:10.1021/acs.est.6b01534

Rubio-Clemente, A., Chica, E., and Peñuela, G. A. (2018). Photovoltaic Array for Powering Advanced Oxidation Processes: Sizing, Application and Investment Costs for the Degradation of a Mixture of Anthracene and Benzo[a]pyrene in Natural Water by the UV/H2O2 System. *J. Environ. Chem. Eng.* 6, 2751–2761. doi:10.1016/j.jece.2018.03.046

Sampaio, C. J. S., de Souza, J. R. B., Damião, A. O., Bahiense, T. C., and Roque, M. R. A. (2019). Biodegradation of Polycyclic Aromatic Hydrocarbons (PAHs) in a Diesel Oil-Contaminated Mangrove by Plant Growth-Promoting Rhizobacteria. *3 Biotech.* 9, 155. doi:10.1007/s13205-019-1686-8

Sánchez-López, P., Kotolevich, Y., Yocupicio-Gaxiola, R. I., Antúnez-García, J., Chowdari, R. K., Petranovskii, V., et al. (2021). Recent Advances in Catalysis Based on Transition Metals Supported on Zeolites. *Front. Chem.* 9, 716745. doi:10.3389/fchem.2021.716745

Shaik, S., Danovich, D., Joy, J., Wang, Z., and Stuyver, T. (2020). Electric-Field Mediated Chemistry: Uncovering and Exploiting the Potential of (Oriented) Electric Fields to Exert Chemical Catalysis and Reaction Control. *J. Am. Chem. Soc.* 142, 12551–12562. doi:10.1021/jacs.0c05128

Shaik, S., Mandal, D., and Ramanan, R. (2016). Oriented Electric Fields as Future Smart Reagents in Chemistry. *Nat. Chem.* 8, 1091–1098. doi:10.1038/nchem.2651

Średnicka, P., Juszczuk-Kubiak, E., Wójcicki, M., Akimowicz, M., and Roszko, M. Ł. (2021). Probiotics as a Biological Detoxification Tool of Food Chemical Contamination: A Review. *Food Chem. Toxicol.* 153, 112306. doi:10.1016/j.fct.2021.112306

Stephens, P. J., Devlin, F. J., Chabalowski, C. F., and Frisch, M. J. (1994). Ab Initio Calculation of Vibrational Absorption and Circular Dichroism Spectra Using Density Functional Force Fields. *J. Phys. Chem.* 98, 11623–11627. doi:10.1021/j100096a001

Strobel, A., Burkhardt-Holm, P., Schmid, P., and Segner, H. (2015). Benzo(a)pyrene Metabolism and EROD and GST Biotransformation Activity in the Liver of Red- and White-Blooded Antarctic Fish. *Environ. Sci. Technol.* 49, 8022–8032. doi:10.1021/acs.est.5b00176

Stuyver, T., Ramanan, R., Mallick, D., and Shaik, S. (2020). Oriented (Local) Electric Fields Drive the Millionfold Enhancement of the H-Abstraction Catalysis Observed for Synthetic Metalloenzyme Analogues. *Angew. Chem. Int. Ed.* 59, 7915–7920. doi:10.1002/anie.201916592

Takeshita, T., and Kanaly, R. A. (2019). *In Vitro* DNA/RNA Adductomics to Confirm DNA Damage Caused by Benzo[a]pyrene in the Hep G2 Cell Line. *Front. Chem.* 7, 491. doi:10.3389/fchem.2019.00491

Tian, F., Guo, G., Ding, K., Wang, L., Liu, T., and Yang, F. (2019). Effect of Bioaugmentation by Bacterial Consortium and Methyl-β-Cyclodextrin on Soil Functional Diversity and Removal of Polycyclic Aromatic Hydrocarbons. *Polycycl. Aromat. Compd.* 39, 353–362. doi:10.1080/10406638.2017.1326952

Wang, H., Huang, W., Gong, Y., Chen, C., Zhang, T., and Diao, X. (2020). Occurrence and Potential Health Risks Assessment of Polycyclic Aromatic Hydrocarbons (PAHs) in Different Tissues of Bivalves from Hainan Island, China. *Food Chem. Toxicol.* 136, 111108. doi:10.1016/j.fct.2019.111108

Wang, S., Li, X., Liu, W., Li, P., Kong, L., Ren, W., et al. (2012). Degradation of Pyrene by Immobilized Microorganisms in Saline-Alkaline Soil. *J. Environ. Sci.* 24, 1662–1669. doi:10.1016/s1001-0742(11)60963-7

Wang, X., Wang, H., Zheng, L., Zhu, C., and Liang, J. X. (2021). Oriented External Electric Fields Regulating the Oxidation Reaction of CH 4 Catalyzed by Mn-corrolazine. *Int. J. Quantum Chem.* 121, e26443. doi:10.1002/qua.26443

Wang, Z., Danovich, D., Ramanan, R., and Shaik, S. (2018). Oriented-External Electric Fields Create Absolute Enantioselectivity in Diels-Alder Reactions: Importance of the Molecular Dipole Moment. *J. Am. Chem. Soc.* 140, 13350–13359. doi:10.1021/jacs.8b08233

Wilson, S. C., and Jones, K. C. (1993). Bioremediation of Soil Contaminated with Polynuclear Aromatic Hydrocarbons (PAHs): a Review. *Environ. Pollut.* 81, 229–249. doi:10.1016/0269-7491(93)90206-4

Wongwongsee, W., Chareanpat, P., and Pinyakong, O. (2013). Abilities and Genes for PAH Biodegradation of Bacteria Isolated from Mangrove Sediments from the Central of Thailand. *Mar. Pollut. Bull.* 74, 95–104. doi:10.1016/j.marpolbul.2013.07.025

Wu, D., Li, Q., Ding, X., Sun, J., Li, D., Fu, H., et al. (2018). Primary Particulate Matter Emitted from Heavy Fuel and Diesel Oil Combustion in a Typical Container Ship: Characteristics and Toxicity. *Environ. Sci. Technol.* 52, 12943–12951. doi:10.1021/acs.est.8b04471

Yan, X., Wang, Y., Meng, T., and Yan, H. (2021). Computational Insights into the Influence of Substitution Groups on the Inclusion Complexation of β-Cyclodextrin. *Front. Chem.* 9, 668400. doi:10.3389/fchem.2021.668400

Yang, L., Pastor-Pérez, L., Villora-Pico, J. J., Sepúlveda-Escribano, A., Tian, F., Zhu, M., et al. (2021). Highly Active and Selective Multicomponent Fe-Cu/CeO2-Al2O3 Catalysts for CO2 Upgrading via RWGS: Impact of Fe/Cu Ratio. *ACS Sustain. Chem. Eng.* 9, 12155–12166. doi:10.1021/acssuschemeng.1c03551

Zang, S.-y., Li, P.-j., Yu, X.-c., Shi, K., Zhang, H., and Chen, J. (2007). Degradation of Metabolites of Benzo[a]pyrene by Coupling Penicillium chrysogenum with KMnO4. *J. Environ. Sci.* 19, 238–243. doi:10.1016/S1001-0742(07)60039-4

Zheng, L., Meng, Y., Wang, X., Zhu, C., and Liang, J.-X. (2020). Screening Metal-Dicorrole-Based Dyes with Excellent Photoelectronic Properties for Dye-Sensitized Solar Cells by Density Functional Calculations. *J. Porphyr. Phthalocyanines* 24, 1003–1012. doi:10.1142/s1088424620500145

Zhou, C., Zhang, H., Yang, L., Wu, D., He, S., Yang, H., et al. (2022). Methane-selective Oxidation to Methanol and Ammonia Selective Catalytic Reduction of

NOx over Monolithic Cu/SSZ-13 Catalysts: Are Hydrothermal Stability and Active Sites Same? *Fuel* 309, 122178. doi:10.1016/j.fuel.2021.122178

Zhou, J., Zhao, Z., and Shibata, N. (2021). Silylboronate-Mediated Defluorosilylation of Aryl Fluorides with or without Ni-Catalyst. *Front. Chem.* 9, 771473. doi:10.3389/fchem.2021.771473

Zhu, C., Liang, J.-X., and Cao, Z. (2018). Mn-O-O Electron Spin Flip Mechanism Triggered by the Visible-Light Irradiation for the Generation of an Active Mn(V)-Oxo Complex from O2: Insight from Density Functional Calculations. *J. Phys. Chem. C* 122, 20781–20786. doi:10.1021/acs.jpcc.8b05531

Zhu, C., Liang, J.-X., Meng, Y., Lin, J., and Cao, Z. (2021). Mn-corrolazine-based 2D-Nanocatalytic Material with Single Mn Atoms for Catalytic Oxidation of Alkane to Alcohol. *Chin. J. Catal.* 42, 1030–1039. doi:10.1016/S1872-2067(20)63707-X

Zhu, C., and Liang, J.-X. (2015). Theoretical Insight into the Interaction between Gallium Di-corrole Dyes and Iodine in Dye-Sensitized Solar Cells (DSCs). *J. Power Sources* 283, 343–350. doi:10.1016/j.jpowsour.2015.02.136

Zhu, C., Liang, J.-X., and Wei, G. (2016). Theoretical Investigation of an Ultrastable One Dimensional Infinite Monatomic Mixed Valent Gold Wire with Excellent Electronic Properties. *Phys. Chem. Chem. Phys.* 18, 12338–12343. doi:10.1039/c6cp00787b

Conflict of Interest: Author JZ is employed by Guizhou Fukangren Pharmaceutical Co., LTD.

The remaining authors declare that the research was conducted in the absence of any commercial or financial relationships that could be construed as a potential conflict of interest.

frontiers | Frontiers in Chemistry

ORIGINAL RESEARCH
published: 08 June 2022
doi: 10.3389/fchem.2022.915468

Synergistic Regulation of S-Vacancy of MoS_2-Based Materials for Highly Efficient Electrocatalytic Hydrogen Evolution

Xiao-Yun Li[1], Shao-Ju Zhu[2], Yi-Long Wang[3], Tian Lian[2], Xiao-yu Yang[2], Cui-Fang Ye[4], Yu Li[2], Bao-Lian Su[2] and Li-Hua Chen[2]**

[1]State Key Laboratory of Silicate Materials for Architectures, Wuhan University of Technology, Wuhan, China, [2]State Key Laboratory of Advanced Technology for Materials Synthesis and Processing, Wuhan University of Technology, Wuhan, China, [3]School of Chemistry, Chemical Engineering and Life Science, Wuhan University of Technology, Wuhan, China, [4]Department of Histology and Embryology, Tongji Medical College, Huazhong University of Science and Technology, Wuhan, China

OPEN ACCESS

Edited by:
Liuqingqing Yang,
Shanghai Jiao Tong University, China

Reviewed by:
Guigao Liu,
Nanjing University of Science and Technology, China
Dafeng Yan,
Huazhong University of Science and Technology, China

***Correspondence:**
Yi-Long Wang
wangyilong@whut.edu.cn
Li-Hua Chen
chenlihua@whut.edu.cn

Specialty section:
This article was submitted to Catalytic Reactions and Chemistry, a section of the journal Frontiers in Chemistry

Received: 08 April 2022
Accepted: 02 May 2022
Published: 08 June 2022

Citation:
Li X-Y, Zhu S-J, Wang Y-L, Lian T, Yang X-y, Ye C-F, Li Y, Su B-L and Chen L-H (2022) Synergistic Regulation of S-Vacancy of MoS_2-Based Materials for Highly Efficient Electrocatalytic Hydrogen Evolution. Front. Chem. 10:915468. doi: 10.3389/fchem.2022.915468

Low or excessively high concentration of S-vacancy ($C_{S\text{-vacancy}}$) is disadvantageous for the hydrogen evolution reaction (HER) activity of MoS_2-based materials. Additionally, alkaline water electrolysis is most likely to be utilized in the industry. Consequently, it is of great importance for fine-tuning $C_{S\text{-vacancy}}$ to significantly improve alkaline hydrogen evolution. Herein, we have developed a one-step Ru doping coupled to compositing with CoS_2 strategy to precisely regulate $C_{S\text{-vacancy}}$ of MoS_2-based materials for highly efficient HER. In our strategy, Ru doping favors the heterogeneous nucleation and growth of CoS_2, which leads to a high crystallinity of Ru-doped CoS_2 (Ru-CoS_2) and rich heterogeneous interfaces between Ru-CoS_2 and Ru-doped MoS_{2-x} (Ru-MoS_{2-x}). This facilitates the electron transfer from Ru-CoS_2 to Ru-MoS_{2-x}, thereby increasing $C_{S\text{-vacancy}}$ of MoS_2-based materials. Additionally, the electron injection effect increases gradually with an increase in the mass of Co precursor (m_{Co}), which implies more S^{2-} leaching from MoS_2 at higher m_{Co}. Subsequently, $C_{S\text{-vacancy}}$ of the as-synthesized samples is precisely regulated by the synergistic engineering of Ru doping and compositing with CoS_2. At $C_{S\text{-vacancy}}$ = 17.1%, a balance between the intrinsic activity and the number of exposed Mo atoms (EMAs) to boost highly active EMAs should be realized. Therefore, the typical samples demonstrate excellent alkaline HER activity, such as a low overpotential of 170 mV at 100 mA cm^{-2} and a TOF of 4.29 s^{-1} at -0.2 V. Our results show promise for important applications in the fields of electrocatalysis or energy conversion.

Keywords: S-vacancy of MoS_2, heterogeneous interfaces, exposed Mo atoms, electrocatalysis, hydrogen evolution reaction

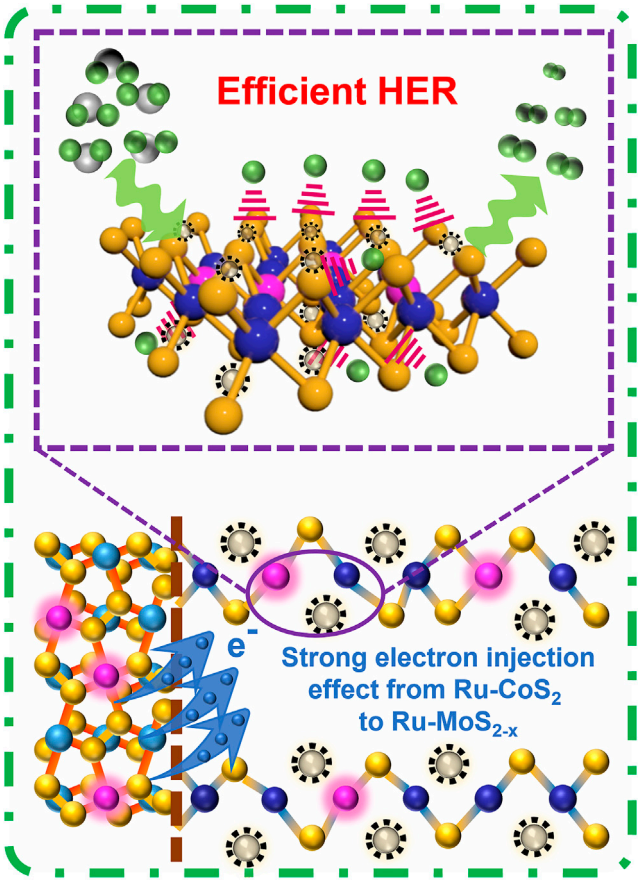

Graphical Abstract |

INTRODUCTION

The rapid development of the economy has made the fast consumption of fossil energy, resulting in the energy crisis and severe environmental pollution (Xie et al., 2013b; Xu et al., 2017; Jiang et al., 2022). Hydrogen energy, as one of the clean and renewable energies, has received extensive attention around the world (Huang et al., 2019; Venkateshwaran and Senthil Kumar, 2019; Zhu et al., 2019; Wang F. et al., 2020). Electrocatalytic water splitting (Lin et al., 2017; Lin et al., 2019; Djara et al., 2020; Liu L. et al., 2022) is regarded as an eco-friendly technology for hydrogen (H_2) production. So far, platinum-based materials are still the best electrocatalysts for acidic water electrolysis (Chen et al., 2020). Nevertheless, the high cost and low abundance seriously restrict the wide applications of such precious metals (Li et al., 2011; Qi et al., 2019; Jing et al., 2020). On the other hand, alkaline water electrolysis is most likely to be utilized in the industry, owing to the unrestricted reactant availability, desirable safety, and satisfactory output (Yin et al., 2015). However, the sluggish dynamics of hydrogen evolution reaction (HER) in alkaline environments results in excessive energy consumption (Yin et al., 2015). Therefore, it is of great significance for the development of highly efficient and low-cost electrocatalysts to overcome energy barriers for accelerating kinetics and to decrease overpotential during the hydrogen evolution reaction (HER) process.

It is well known that molybdenum disulfide (MoS_2) can be designed as an alternative to Pt due to the excellent H* adsorption–desorption properties, special layered structures, good stability, and low cost (Hinnemann et al., 2005; Deng et al., 2017; Wang Y. et al., 2019; Gao et al., 2020). However, the pristine 2H-MoS_2 tends to aggregate under van der Waals forces, resulting in poor edge active sites (Kibsgaard et al., 2012; Wang et al., 2017; Wang et al., 2021b). More importantly, there remain a lot of active sites from the vast basal planes of such MoS_2 to be developed (Kibsgaard et al., 2012; Wang et al., 2017; Wang et al., 2021b). To address these drawbacks, defect-rich, double-gyroid, and amorphous structures have been introduced into such MoS_2 nanosheets to increase the unsaturated sulfur atoms as active sites for HER (Kibsgaard et al., 2012; Xie et al., 2013a; Liu et al., 2018). Doping transition metals (TMs) into MoS_2 is another important method for the advancement of electrocatalysis. This is because doping TMs not only increases the number of unsaturated sulfur atoms but also regulates the adsorption free

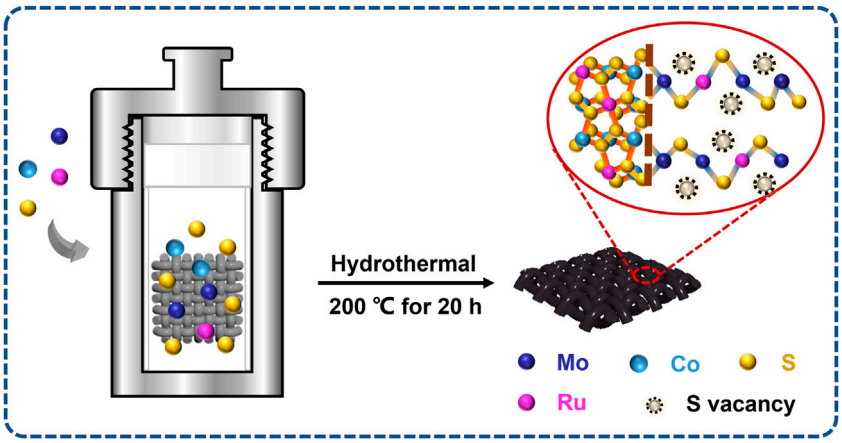

FIGURE 1 | Schematic representation of the fabrication of Ru-MoS_2-CoS_2/CC samples.

energy of hydrogen atoms (ΔG_H) of active sites to favor HER (Wang et al., 2015; Wang D. et al., 2019; Wang et al., 2021b). Among these TMs, ruthenium (Ru) belongs to the Pt group, but its price is as low as about 5% of Pt (Zhang J. et al., 2019). A quintessential example demonstrates that ΔG_H at the Ru-doped in-plane sulfur sites decreases to approximately 0.19 eV (Zhang X. et al., 2019). This indicates that doping Ru can efficiently modulate the electronic features of the adjacent sulfur atoms, thereby leading to the optimal H atom binding energy (Yan et al., 2018). On the other hand, after doping Ru into 2H-MoS_2 (Li J. et al., 2021) or 2H-WS_2 (Li J. et al., 2022), these Ru sites can significantly accelerate the water dissociation in alkaline environments. For example, the energy barrier of the H–OH cleavage (E) is as high as 2.42 eV before doping Ru. Remarkably, E of such Ru sites decreases to 2.02 eV, which is advantageous for water dissociation to OH and H intermediates.

Modulating S-vacancy into MoS_2-based materials has been developed as an efficient strategy (Tsai et al., 2017; Park et al., 2018; Li Y. et al., 2021) to activate inert basal planes because the exposed Mo atoms can be tailored into newborn active sites (Wang X. et al., 2020). Following this opinion, much effort has so far been devoted to introducing S-vacancy into the basal planes of monolayered or multi-layered 2H-MoS_2 nanosheets (Li et al., 2016b; Tsai et al., 2017; Park et al., 2018; Li et al., 2019; Wang X. et al., 2020). Among these strategies, chemical vapor deposition coupled to plasma has been developed to modulate S-vacancy into MoS_2 (Li et al., 2016b). In this case, S atoms escape from the MoS_2 lattice more easily than Mo atoms due to the lower formation energy of S-vacancy compared to that of the Mo interstitial (Li et al., 2016b). Subsequently, the controllable electrochemical preparation of S-vacancy for multi-layered MoS_2 has been proposed by simply adjusting desulfurization parameters, such as desulfurization potential and time (Tsai et al., 2017). More recently, the single Ru atom doping technology promotes the phase transition of 2H-MoS_2 and the formation of S-vacancy, which greatly enhances its HER activity (Zhang J. et al., 2019). Nevertheless, a low or excessively high concentration of S-vacancy ($C_{S\text{-vacancy}}$) is disadvantageous for the hydrogen evolution reaction (HER) activity of MoS_2-based materials. Consequently, it is of great importance for the development of a novel approach to fine-tuning $C_{S\text{-vacancy}}$ to significantly improve alkaline hydrogen evolution. In addition, the aforementioned electrocatalysts based on S-vacancy only consist of a single component (that is, MoS_2) rather than hybrid catalysts. As one of the traditional semiconductor materials, MoS_2 suffers from another drawback of unsatisfactory charge-transfer resistance (R_{CT}), leading to low HER activity (Li Y. et al., 2021; Wang et al., 2021b; Wang et al., 2021c). Hence, compositing with the metallic phase will favor fast electrode kinetics, realizing synergistically regulating $C_{S\text{-vacancy}}$ and R_{CT} of MoS_2-based electrocatalysts for highly efficient HER.

Herein, we develop a one-step Ru doping coupled to compositing with the CoS_2 strategy to synergistically regulate $C_{S\text{-vacancy}}$ of MoS_2-based materials for highly efficient alkaline HER. Ru doping is advantageous for the formation of S-vacancy in the basal planes of MoS_2. On the other hand, Ru doping favors heterogeneous nucleation and growth of CoS_2, which leads to rich heterogeneous interfaces between Ru-doped CoS_2 (Ru-CoS_2) and Ru-doped $MoS_{2\text{-}x}$ (Ru-$MoS_{2\text{-}x}$). This facilitates the electron transfer from Ru-CoS_2 to Ru-$MoS_{2\text{-}x}$, thereby increasing $C_{S\text{-vacancy}}$ of MoS_2-based materials. At fixed Ru dopant, the electron injection effect increases gradually with an increase in the mass of Co precursor, which means more S^{2-} escaping from Ru-MoS_2 nanosheets. Therefore, synergistically regulating $C_{S\text{-vacancy}}$ of the as-synthesized samples, from 2.1 to 27.5%, is realized by a new one-step Ru doping coupled to compositing with the CoS_2 strategy. On regulating $C_{S\text{-vacancy}}$ to 17.1%, a balance between the intrinsic activity and the number of exposed Mo atoms (EMAs) to boost highly active EMAs should be realized. As a consequence, the typical samples demonstrate the optimal alkaline HER activity among all samples, such as a low overpotential of 170 mV at 100 mA cm^{-2}, a large specific alkaline HER current density of 77.6 μA cm^{-2}, and a turnover frequency of 4.29 s^{-1} at -0.2 V as well as excellent long-term stability. Our results pave a novel approach to unlocking the potential of inert basal planes in MoS_2-based materials for highly efficient HER and promise important applications in the field of electrocatalytic hydrogen evolution.

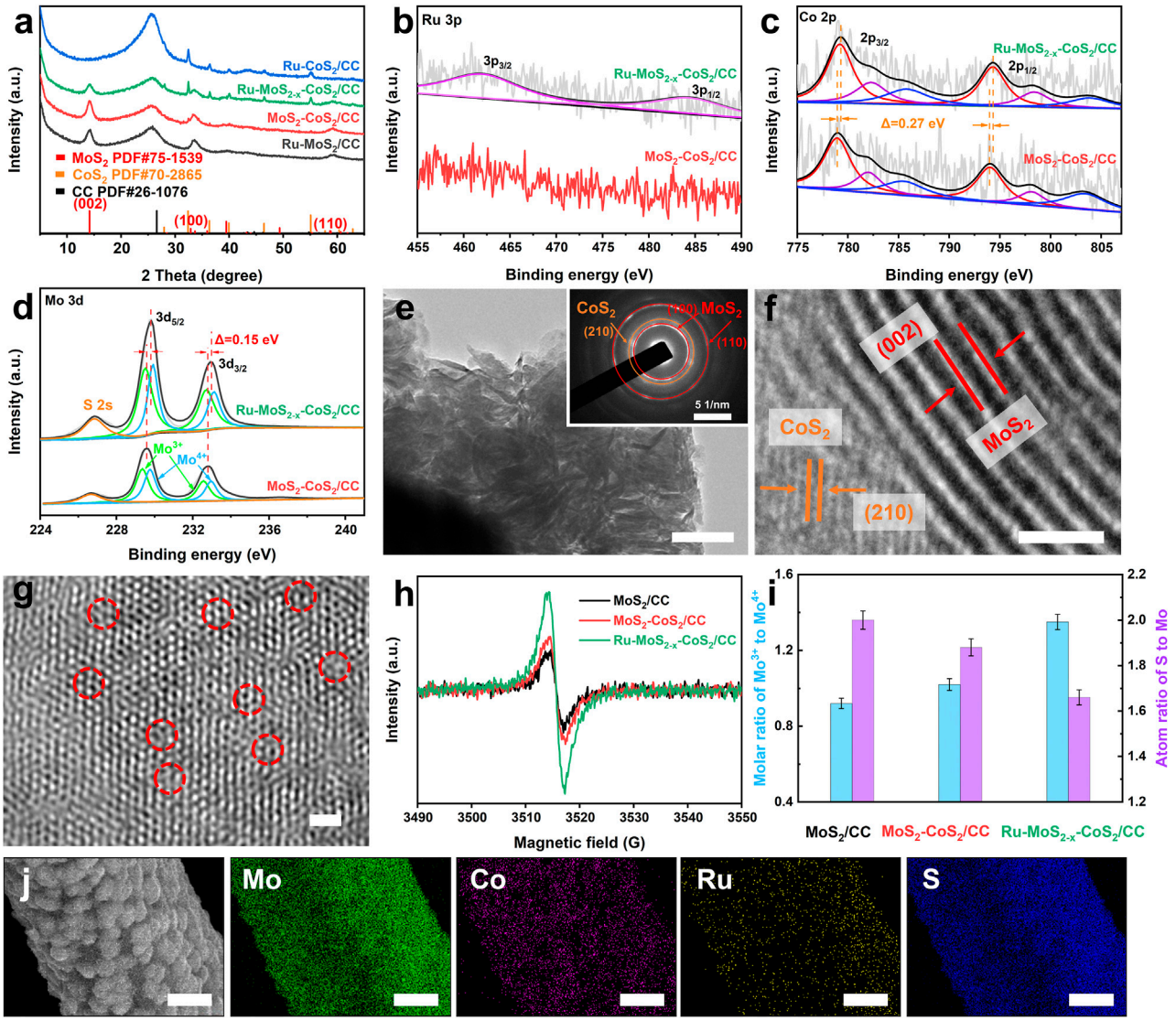

FIGURE 2 | (A) XRD patterns of Ru-MoS_2/CC, MoS_2-CoS_2/CC, Ru-CoS_2/CC, and the typical samples; **(B)** Ru 3p, **(C)** Co 2p, and **(D)** Mo3d high-resolution XPS spectra of the typical samples and MoS_2-CoS_2/CC; **(E)** TEM image and **(F,G)** HR-TEM images of the typical samples; **(H)** EPR spectra, and **(I)** molar ratio of Mo^{3+} to Mo^{4+}, and the atom ratio of S to Mo of MoS_2/CC, MoS_2-CoS_2/CC, and the typical samples. **(J)** EDX mapping profiles of Mo, Co, Ru, and S over the typical samples. The inset of panel **(E)** is the SAED pattern of the typical samples. Scale bars of panels **(E)**, **(F)**, **(G)**, and **(J)** are 100 nm, 2 nm, 2 nm, and 2 μm, respectively.

EXPERIMENTAL SECTION

Fabrication of the Typical Samples (Ru-MoS_{2-X}-CoS_2/CC)

The typical samples were synthesized by a one-pot hydrothermal strategy using the following precursors such as $Na_2MoO_4.2H_2O$, CH_4N_2S, and $Co(NO_3)_2{\cdot}6H_2O$. In the typical experiments, 160 mg $Co(NO_3)_2{\cdot}6H_2O$, 160 mg $Na_2MoO_4.2H_2O$, and 600 mg CH_4N_2S were dissolved in 46.0 ml deionized water under magnetic stirring. Subsequently, 4.0 ml $RuCl_3$ solution (5 mmol L^{-1}) was introduced into the above cobalt salt solution under magnetic stirring for 0.5 h. Carbon cloth (CC, 4 cm^2) was pretreated according to the related literature (Yu et al., 2015). Then, the above solution and the pretreated CC were transferred into a 100.0 ml Teflon-lined stainless-steel autoclave and heated to 200°C for 20 h. After the hydrothermal reaction, the mixture was cooled to room temperature. The typical samples were harvested after being washed with water thoroughly and vacuum-dried at 60 °C for 12.0 h and abbreviated as Ru-MoS_{2-x}-CoS_2/CC.

Fabrications of Other Ru-MoS_{2-X}-CoS_2/CC Samples

Other Ru-MoS_{2-x}-CoS_2/CC samples were synthesized at various volumes of $RuCl_3$ solution (5 mmol L^{-1}) of 1.0, 7.0, 10.0, and

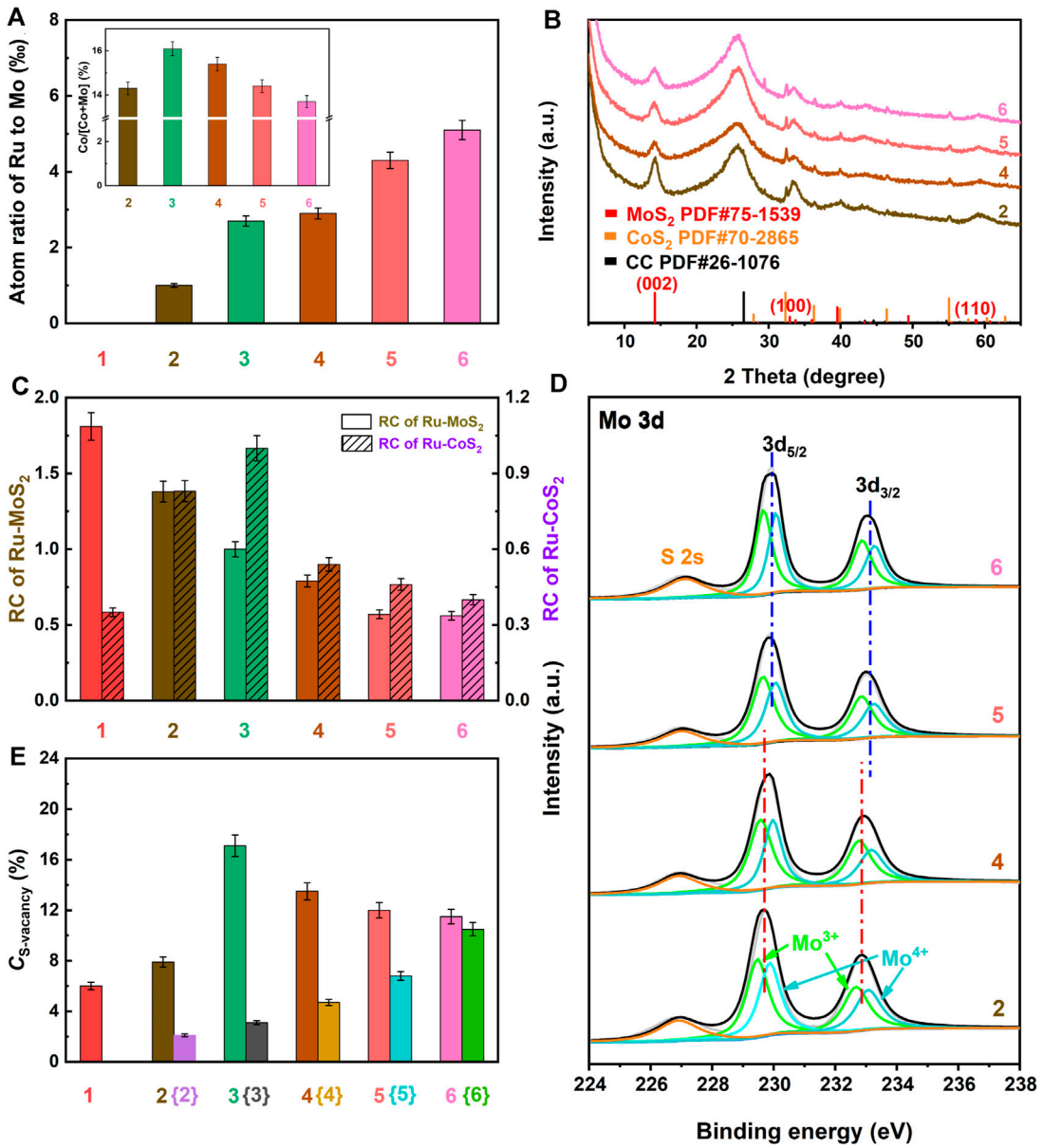

FIGURE 3 | (A) Atom ratio of Ru to Mo based on ICP-OES, **(B)** XRD patterns, **(C)** RC of Ru-MoS_{2-x} and Ru-CoS_2, **(D)** Mo3d high-resolution XPS spectra, and **(E)** $C_{S\text{-vacancy}}$ of the related samples. Meanwhile, 1, 2, 3, 4, 5 and 6 are denoted as MoS_2-CoS_2/CC, Ru-MoS_{2-x}-CoS_2/CC-1.0, the typical samples, Ru-MoS_{2-x}-CoS_2/CC-7.0, Ru-MoS_{2-x}-CoS_2/CC-10.0, and Ru-MoS_{2-x}-CoS_2/CC-30.0, respectively. Fabrications of {2}, {3}, {4}, {5}, and {6} are the same as those of Ru-MoS_{2-x}-CoS_2/CC-1.0, the typical samples, Ru-MoS_{2-x}-CoS_2/CC-7.0, Ru-MoS_{2-x}-CoS_2/CC-10.0, and Ru-MoS_{2-x}-CoS_2/CC-30.0 except for the absence of $Co(NO_3)_2$, to be denoted as Ru-MoS_2/CC-1.0, Ru-MoS_2/CC, Ru-MoS_2/CC-7.0, Ru-MoS_2/CC-10.0, and Ru-MoS_2/CC-30.0, respectively. The inset of panel **(A)** is the atom ratio of Co to (Co + Mo) of the related samples based on ICP-OES.

30.0 ml under otherwise similar conditions as the typical experiments. These Ru-MoS_{2-x}-CoS_2/CC samples are denoted as Ru-MoS_{2-x}-CoS_2/CC-1.0, Ru-MoS_{2-x}-CoS_2/CC-7.0, Ru-MoS_{2-x}-CoS_2/CC-10.0, and Ru-MoS_{2-x}-CoS_2/CC-30.0.

In addition, Ru-MoS_{2-x}-CoS_2/CC-80, Ru-MoS_{2-x}-CoS_2/CC-240, Ru-MoS_{2-x}-CoS_2/CC-280, and Ru-MoS_{2-x}-CoS_2/CC-320 were synthesized at various masses of $Co(NO_3)_2{\cdot}6H_2O$ of 80, 240, 280, and 320 mg under otherwise similar conditions of the typical experiments, respectively.

Figure 1 displays a schematic representation of the fabrication of all Ru-MoS_{2-x}-CoS_2/CC samples.

Fabrications of Ru-MoS_2/CC, MoS_2/CC, MoS_2-CoS_2/CC, and Ru-CoS_2/CC

Ru-doped MoS_2 nanosheets assembled on CC are abbreviated as Ru-MoS_2/CC. Fabrication of Ru-MoS_2/CC is almost the same as the typical samples except for the absence of $Co(NO_3)_2$.

MoS_2 nanosheets assembled on CC are abbreviated as MoS_2/CC. Fabrication of MoS_2/CC is almost the same as Ru-MoS_2/CC except for the absence of $RuCl_3$ solution.

MoS_2 nanosheets coated with CoS_2 assembled on CC are abbreviated as MoS_2-CoS_2/CC. Fabrication of MoS_2-CoS_2/CC is almost the same as the typical samples except for the absence of $RuCl_3$ solution.

Ru-doped CoS_2 assembled on CC are abbreviated as Ru-CoS_2/CC. Fabrication of Ru-CoS_2/CC is almost similar to the typical samples except for the absence of $Na_2MoO_4.2H_2O$.

Other experimental details about materials, characterization, and performance measurements are supplied in **Supplementary Material S1**.

RESULTS AND DISCUSSION

Characterization of the Typical Samples

Scanning electron microscopic (SEM) images display the morphology of the typical samples in **Supplementary Figures SJ–L**. From these figures, it can be observed that lots of nanosheets are grown on the smooth surface of CC (**Supplementary Figure S2**). Powder X-ray diffraction (XRD) pattern of Ru-MoS_{2-x}-CoS_2/CC (**Figure 2A**) shows the diffraction peaks located at $2\theta = 14.1^\circ$, 32.7°, and 58.8°, matching well with the (002), (100), and (110) planes of 2H-MoS_2 (PDF#75-1539) (Nguyen et al., 2021), respectively. Other sharp diffraction peaks of Ru-MoS_{2-x}-CoS_2/CC, such as 32.4° and 55.1°, are attributed to the (200) and 311) planes of CoS_2 (PDF#70-2865) (Yao et al., 2019), respectively, suggesting the presence of highly crystallized CoS_2 besides 2H-MoS_2. From **Figure 2A**, we also observe the diffraction peak at 26.2° originating from CC. The Raman spectrum of Ru-MoS_{2-x}-CoS_2/CC (**Supplementary Figure S3**) displays the typical E^1_{2g} and A_{1g} vibration models of the Mo-S bonds, further verifying the phase structure of 2H-MoS_2 in Ru-MoS_{2-x}-CoS_2/CC. As shown in **Figure 2B**, the Ru 3p high-resolution X-ray photoelectron spectroscopy (XPS) spectrum of Ru-MoS_{2-x}-CoS_2/CC is divided into two characteristic peaks at the binding energies of 462.4 and 484.7 eV, corresponding to Ru $3p_{3/2}$ and Ru $3p_{1/2}$ (Ge et al., 2022). Nevertheless, no peak of Ru is detected in MoS_2 nanosheets coated with CoS_2 assembled on CC (MoS_2-CoS_2/CC) in **Figure 2B**. Furthermore, **Figures 2C, D** exhibit Co 2p and Mo 3 day XPS spectra of Ru-MoS_{2-x}-CoS_2/CC, respectively. It is seen that Co 2p and Mo 3 day peaks positively shift by about 0.27 and 0.15 eV compared to those of MoS_2-CoS_2/CC (Hao et al., 2017), respectively. Additionally, the characteristic peaks about Ru_2S_3 or $RuCl_3$ are not observed in the XRD pattern of Ru-MoS_{2-x}-CoS_2/CC (**Figure 2A**). Therefore, these data confirm the successful doping of Ru into the following two phases of Ru-MoS_{2-x}-CoS_2/CC, 2H-MoS_2, and CoS_2.

Nanosheets of Ru-MoS_{2-x}-CoS_2/CC are also clearly observed from transmission electron microscopic (TEM) image (**Figure 2E**), which is consistent with the results of SEM images. According to the high-resolution TEM (HR-TEM) image (**Figure 2F**), the lattice spacings of 0.625 and 0.245 nm that are seen in Ru-MoS_{2-x}-CoS_2/CC correspond to the (002) plane of MoS_2 and the (210) plane of CoS_2 (He et al., 2020; Liu X. et al., 2022), respectively. These also conform to the results of XRD. As we know, MoS_2 is regarded as one of the traditional semiconductor materials, and CoS_2 is a metallic phase due to its high Fermi level. Therefore, there are lots of Schottky heterojunctions among Ru-MoS_{2-x}-CoS_2/CC. In addition, the inset of **Figure 2E** (selected area electron diffraction, SAED) pattern indicates that Ru-doped MoS_2 (Ru-MoS_2) and Ru-doped CoS_2 (Ru-CoS_2) of Ru-MoS_{2-x}-CoS_2/CC are polycrystalline (Huang et al., 2015). We can clearly observe that many defects exist in such Ru-MoS_2 from **Figure 2G** due to lattice distortion by Ru doping (Zhang J. et al., 2019) and the electron injection effect (Gan et al., 2018; Zhang J. et al., 2019). Energy-dispersive X-ray (EDX) spectroscopy mapping (**Figure 2J**) profiles further confirm the uniform distribution of Mo, Co, Ru, and S elements throughout Ru-MoS_{2-x}-CoS_2/CC. Considering that Ru-MoS_2 assembled on CC (Ru-MoS_2/CC) and Ru-CoS_2 assembled on CC (Ru-CoS_2/CC) tend to form nanosheets (**Supplementary Figures S1B, C**) and nanoparticles (**Supplementary Figures SH, I**), respectively, and that Ru-CoS_2 nucleates and grows prior to Ru-MoS_2 (**Figures 4A–F**), we can reasonably deduce as follows: during the hydrothermal process, Ru-CoS_2 nanoparticles are firstly assembled on CC; then, Ru-CoS_2/CC are densely coated by Ru-MoS_2 nanosheets to construct the typical samples, Ru-MoS_{2-x}-CoS_2/CC.

According to XPS data in **Figure 2D** and **Supplementary Figure S4**, we characterize molar ratios of Mo^{3+} to Mo^{4+} of MoS_2/CC, MoS_2-CoS_2/CC, and Ru-MoS_{2-x}-CoS_2/CC in **Figure 2I**. The presence of Mo^{3+} can induce S-vacancy of the basal planes in Ru-MoS_2 (Ma et al., 2020) of Ru-MoS_{2-x}-CoS_2/CC. From **Figure 2I**, Ru-MoS_{2-x}-CoS_2/CC exhibits a higher value of about the molar ratio of Mo^{3+} to Mo^{4+} than MoS_2/CC or MoS_2-CoS_2/CC, reaching 1.35. To confirm such defective structures, electron paramagnetic resonance (EPR) (Liu et al., 2017; Gong et al., 2020; Wang J. et al., 2021) is further employed to estimate the S-vacancy of all samples. As expected, Ru-MoS_{2-x}-CoS_2/CC demonstrates the highest EPR signal at g = ~ 2.002 among all samples (**Figure 2H**). Moreover, the EPR signal of MoS_2-CoS_2/CC is higher than that of MoS_2/CC. These data straightforwardly indicate that the formation of S-vacancy might be closely related to both Ru doping into MoS_2 and compositing with CoS_2.

Doping Ru Coupled to Compositing With CoS_2 to Regulate Microstructures of the As-synthesized Samples

First, a series of Ru-MoS_2/CC samples were synthesized at the various volumes of $RuCl_3$ solution (V) of 1.0, 4.0, 7.0, 10.0, and 30.0 ml under otherwise similar conditions of the typical experiments except for the absence of $Co(NO_3)_2$. These Ru-MoS_2/CC samples are denoted as Ru-MoS_2/CC-1.0, Ru-MoS_2/CC-7.0, Ru-MoS_2/CC-10.0, and Ru-MoS_2/CC-30.0. Similar Ru 3p XPS spectra to the typical samples are observed in **Supplementary Figure S5A**, which is responsible for successfully doping Ru into all Ru-MoS_2/CC samples. In addition, the atom ratios of Ru to Mo (A) of all Ru-MoS_2/CC samples are characterized by XPS in **Supplementary Figure S5B**. From this figure, A increases with increasing V, indicating that

more Ru will be doped into the Ru-MoS_2/CC samples at higher *V*. In this work, the atomic ratio of S to Mo (S: Mo) of MoS_2/CC is firstly measured (**Supplementary Table S1**) and is normalized to 2.00. Then, it is employed as a reference to confirm the normalized S: Mo of MoS_{2-x} in all Ru-MoS_2/CC samples in terms of XPS data (Xu et al., 2016; Wang J. et al., 2021). Here, the measured S: Mo for all Ru-MoS_2/CC samples are the atom ratios of S minus double Ru to Mo, which is abbreviated as [(S–2Ru)/Mo]. Therefore, the normalized S: Mo of MoS_{2-x} in all samples are listed in **Supplementary Table S2**. From **Figure 3E**, $C_{S\text{-vacancy}}$ of Ru-MoS_2/CC samples increases with the increase in Ru dopants. For example, $C_{S\text{-vacancy}}$ of Ru-MoS_2/CC-30.0 increases to 10.5% at *V* = 30.0 ml. That is to say, doping Ru can regulate $C_{S\text{-vacancy}}$ of Ru-MoS_2/CC samples varying from 2.1 to 10.5%.

Density functional theory (DFT) calculation reveals that the Ru-S bonding energy (about 0.92 eV) decreases by 0.87 eV compared to the Mo-S bonding energy (about 1.79 eV) (Luo et al., 2020), which is advantageous for the formation of S-vacancy in the basal planes of MoS_2. In this work, Ru atoms substituting for Mo atoms in MoS_2 are abbreviated as $Ru_{(Mo)}$. According to the previously reported literature (Zhang J. et al., 2019; Zhang X. et al., 2019), Ru doping results in an increase in $C_{S\text{-vacancy}}$ due to the strong attractive interaction between $Ru_{(Mo)}$ and the adjacent S-vacancy. Furthermore, S-vacancy is exclusively stable around $Ru_{(Mo)}$ (Kang, 2021).

To investigate the synergistic effect of doping Ru coupled to compositing with CoS_2 on the microstructure, other Ru-MoS_{2-x}-CoS_2/CC samples are further synthesized at various *V* of 1.0, 7.0, 10.0, and 30.0 ml under otherwise similar conditions of the typical experiments to be denoted as Ru-MoS_{2-x}-CoS_2/CC-1.0, Ru-MoS_{2-x}-CoS_2/CC-7.0, Ru-MoS_{2-x}-CoS_2/CC-10.0, and Ru-MoS_{2-x}-CoS_2/CC-30.0, respectively. According to **Supplementary Figure S6**, these Ru-MoS_{2-x}-CoS_2/CC samples almost display the same Ru 3p XPS spectra as the typical samples, indicating a successful doping of Ru into them as well. The values of *A* of all samples are characterized by inductively coupled plasma-optical emission spectroscopy (ICP-OES). In terms of **Figure 3A**, the values of *A* of these samples increase with the increase in *V*. Moreover, other Ru-MoS_{2-x}-CoS_2/CC samples also exhibit the same phase structure as the typical samples, since the XRD pattern of each sample is similar to that of the typical samples (**Figure 3B**). **Figure 3C** further presents the relative crystallinity (RC) of Ru-MoS_{2-x} and Ru-CoS_2 for all Ru-MoS_{2-x}-CoS_2/CC samples based on the corresponding XRD data such as the (002) plane for molybdenum disulfide and (200) (210), (211) (220), and 311) planes for cobalt disulfide. From this figure, the RC of Ru-MoS_{2-x} decreases with the increase in *V*, which implies that more defective structures or S-vacancy would be modulated into the basal planes of Ru-MoS_{2-x} at higher *V*. However, the influence of *V* on RC of Ru-CoS_2 is not coincident with the trend of the former. Initially, the RC of Ru-CoS_2 gradually increases with increasing *V*. At *V* = 4.0 ml, the RC of Ru-CoS_2 of the typical samples exhibits the highest value among all samples. However, further increasing *V* leads to a decrease in the RC of Ru-CoS_2.

In addition, Mo^{3+} can be observed in Mo 3 day XPS spectra of all Ru-MoS_{2-x}-CoS_2/CC samples (**Figure 3D**), implying the formation of S-vacancy of the basal planes in Ru-MoS_{2-x}. Taking into account that MoS_2-CoS_2/CC and other Ru-MoS_{2-x}-CoS_2/CC samples (**Supplementary Figures S1E, F**; **Supplementary Figure S7**) are almost similar to the morphology of the typical samples (**Supplementary Figures S1K, L**), such core–shell structure, Ru-MoS_{2-x} nanosheets densely coated Ru-CoS_2 composites, facilitates to correctly reflect the S: Mo of Ru-MoS_{2-x} in all samples by XPS analysis. As mentioned above, the S: Mo of MoS_2/CC is also employed as a reference to confirm the normalized S: Mo of Ru-MoS_{2-x} in all Ru-MoS_{2-x}-CoS_2/CC samples (Li et al., 2016a; Xu et al., 2016) based on XPS data (**Supplementary Figure S8**). Here, the measured S: Mo for all Ru-MoS_{2-x}-CoS_2/CC samples is the atom ratio of S minus double (Co + Ru) to Mo, which is abbreviated as [(S–2Co–2Ru)/Mo]. Subsequently, we further calculate the related $C_{S\text{-vacancy}}$, as shown in **Figure 3E**; **Supplementary Table S1**. From **Figure 3E**, $C_{S\text{-vacancy}}$ of Ru-MoS_{2-x}-CoS_2/CC increases to 7.9% compared to that of MoS_2-CoS_2/CC (about 6.0%). Out of expectation, $C_{S\text{-vacancy}}$ of the typical samples rather than Ru-MoS_{2-x}-CoS_2/CC-30.0 reaches the highest value among all samples, about 17.1% from **Figure 3E**. At the same time, Ru-MoS_{2-x}-CoS_2/CC-30.0 exhibits a lower EPR signal than the typical samples (**Supplementary Figure S9**), further confirming fewer S-vacancy for Ru-MoS_{2-x}-CoS_2/CC-30.0 in comparison with the typical samples. In other words, at a fixed mass of Co precursor, $C_{S\text{-vacancy}}$ of Ru-MoS_{2-x} can be precisely regulated from 7.9 to 17.1% by synergistic Ru doping and compositing with CoS_2 engineering. As a consequence, we can infer that compositing with CoS_2 should be another key factor to regulate $C_{S\text{-vacancy}}$ of Ru-MoS_{2-x} nanosheets in Ru-MoS_{2-x}-CoS_2/CC samples. This is because Ru doping also affects the microstructure of CoS_2, which may have a significant influence on $C_{S\text{-vacancy}}$ of Ru-MoS_{2-x} nanosheets in Ru-MoS_{2-x}-CoS_2/CC samples in turn.

Following this viewpoint, we deeply investigate the influence of doping Ru on the microstructure of cobalt disulfide. As mentioned above, CoS_2 nucleates and grows prior to MoS_2. To eliminate the effect of MoS_2 as much as possible during the characterization of microstructures of CoS_2, the related samples such as [MoS_2-CoS_2/CC], [1] [Ru-MoS_{2-x}-CoS_2/CC], [2], [3], and [4] are synthesized at *t* = 6 h (**Figures 4A–F**) rather than 20 h. Fabrications of [MoS_2-CoS_2/CC], [1] [Ru-MoS_{2-x}-CoS_2/CC], [2], [3], and [4] are the same as those of MoS_2-CoS_2/CC, Ru-MoS_{2-x}-CoS_2/CC-1.0, the typical samples, Ru-MoS_{2-x}-CoS_2/CC-7.0, Ru-MoS_{2-x}-CoS_2/CC-10.0, and Ru-MoS_{2-x}-CoS_2/CC-30.0 except for *t*, respectively. Their SEM images and XRD patterns are displayed in **Figures 4A–G**, respectively. Besides the diffraction peak at 26.2° of CC, other peaks are indexed to CoS_2 without the signal of MoS_2 for all samples (**Figure 4G**), further confirming the heterogeneous nucleation and growth of CoS_2 prior to MoS_2. As shown in **Figure 4A**, a small number of spherical CoS_2 nanoparticles are grown on CC for [MoS_2-CoS_2/CC]. Moreover, the similar phenomena are observed for Ru-doped samples from **Figures 4B–F**. Interestingly, with an increase in *V*, the size and number of Ru-CoS_2 nanoparticles gradually increase (**Figure 4B**). At *V* = 4.0 ml, both the size and number of Ru-CoS_2 nanoparticles for [Ru-MoS_{2-x}-CoS_2/CC] reach up to the maximum value (**Figure 4C**). However, further increasing *V* leads to a decrease in both the size and number of Ru-CoS_2

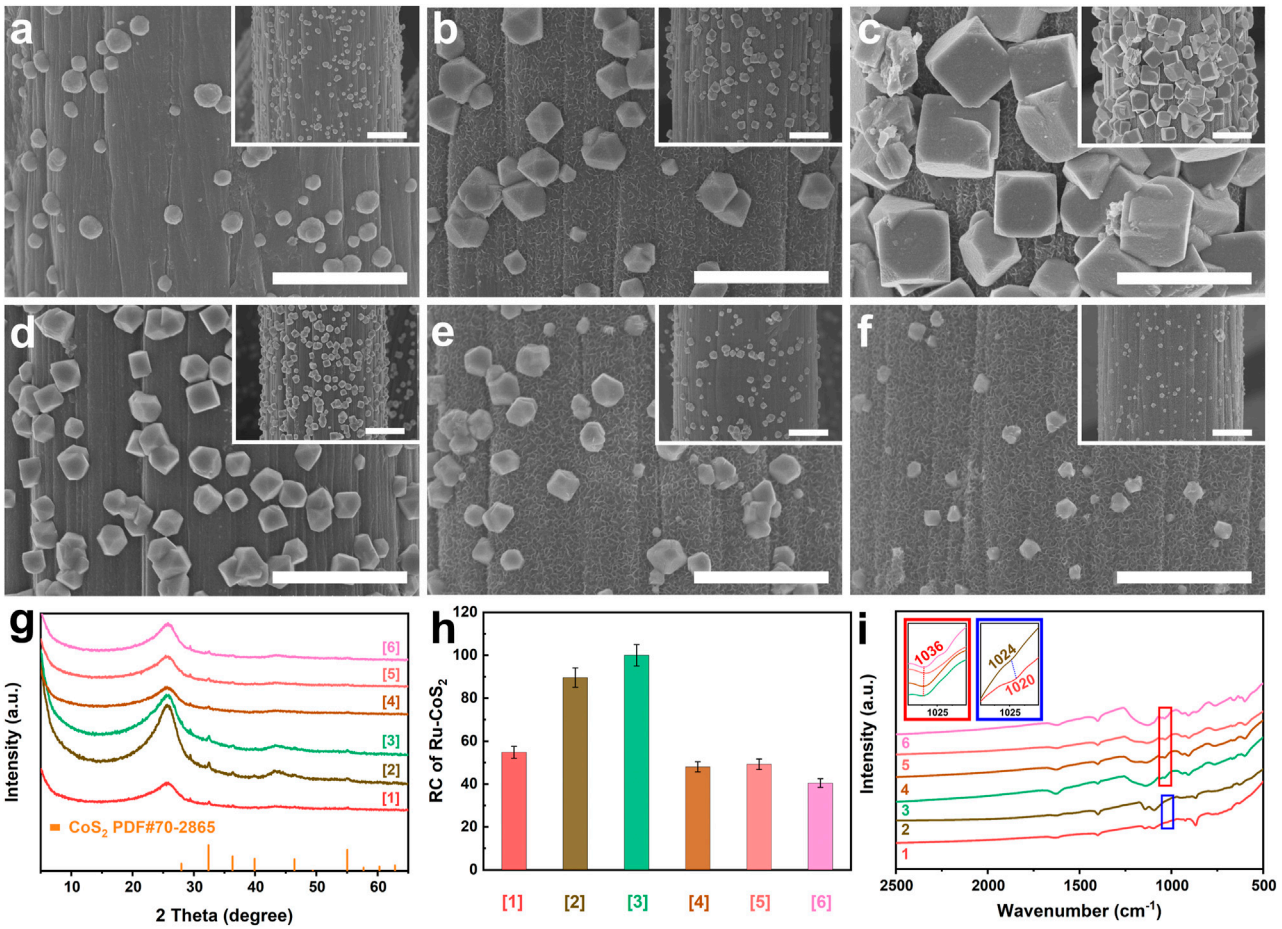

FIGURE 4 | SEM images of **(A)** [MoS_2-CoS_2/CC] ([1]), **(B)** [Ru-MoS_{2-x}-CoS_2/CC-1.0] ([2]), **(C)** [the typical samples] ([3]), **(D)** [Ru-MoS_{2-x}-CoS_2/CC-7.0] ([4]), **(E)** [Ru-MoS_{2-x}-CoS_2/CC-10.0] ([5]), and **(F)** [Ru-MoS_{2-x}-CoS_2/CC-30.0] ([6]); **(G)** XRD patterns and **(H)** RC of Ru-CoS_2 of the corresponding samples; and **(I)** FT-IR spectra of the related samples. Meanwhile, 1, 2, 3, 4, 5, and 6 are MoS_2-CoS_2/CC, Ru-MoS_{2-x}-CoS_2/CC-1.0, the typical samples, Ru-MoS_{2-x}-CoS_2/CC-7.0, Ru-MoS_{2-x}-CoS_2/CC-10.0, and Ru-MoS_{2-x}-CoS_2/CC-30.0, respectively. Additionally, [1], [2], [3], [4], [5], and [6] are the corresponding samples synthesized at t = 6 h rather than 20 h. The insets of panels **(A–F)** are the low-magnified SEM images of the corresponding samples. The insets in red and blue solid lines of panel **(I)** are the high-magnified images of panel **(I)** indicated in red and blue solid frames, respectively. Scale bars of panels **(A–F)** and their insets are 2 and 5 μm.

for other [Ru-MoS_{2-x}-CoS_2/CC] (**Figures 4D–F**). Next, we characterize the RC of Ru-CoS_2 for all samples synthesized at 6 h according to XRD data such as (200) (210), (211) (220), and (311) planes of cobalt disulfide, as shown in **Figure 4H**. Impressively, their trend in the variation is almost consistent with that of the RC of Ru-CoS_2 of Ru-MoS_{2-x}-CoS_2/CC samples synthesized at 20 h (**Figure 3C**). This confirms that doping Ru can improve the crystallinity of CoS_2 under certain conditions. To find out the reason for this issue, we investigate the Fourier-transforming infrared (FT-IR) spectrum of MoS_2-CoS_2/CC in **Figure 4I**. The peak located at 1020 cm^{-1} straightforwardly indicates the formation of CoS_2 (Chakraborty et al., 2006) at V = 0.0 ml. At V increasing to 1.0 ml, the peak of Ru-MoS_{2-x}-CoS_2/CC-1.0 located at 1024 cm^{-1} shows a blue-shift of about 4 cm^{-1} compared to that of MoS_2-CoS_2/CC. At V = 4.0 ml, the related peak blue-shifts to about 1036 cm^{-1}, as shown in **Figure 4I**. This indicates that doping Ru into CoS_2 can decrease the Co–S bond length and enhance the bonding energy (Feng et al., 2018), which favors the formation of Ru-CoS_2. However, a decrease in both the size and number of CoS_2 with further increasing V (**Figures 4D–F**) can be explained as follows: introducing excessive Ru into the lattice of CoS_2 may induce an increase in the oxidation state of neighboring Co ions to maintain the charge neutrality. The similar result has been observed for other transition metal compounds, such as NiO (Smyth, 2000; Ge et al., 2022). This implies that excessive dopant will hinder the formation of CoS_2 in turn.

Possible Formation Mechanism of S-Vacancy in Ru-MoS_{2-x}-CoS_2/CC Samples

Based on these results and discussion, a possible formation mechanism of S-vacancy of the basal planes in Ru-MoS_{2-x} of Ru-MoS_{2-x}-CoS_2/CC samples can be proposed as follows: on the one side, S-vacancy is modulated into the basal planes of MoS_2 due to the strong attractive interaction between $Ru_{(Mo)}$ and the

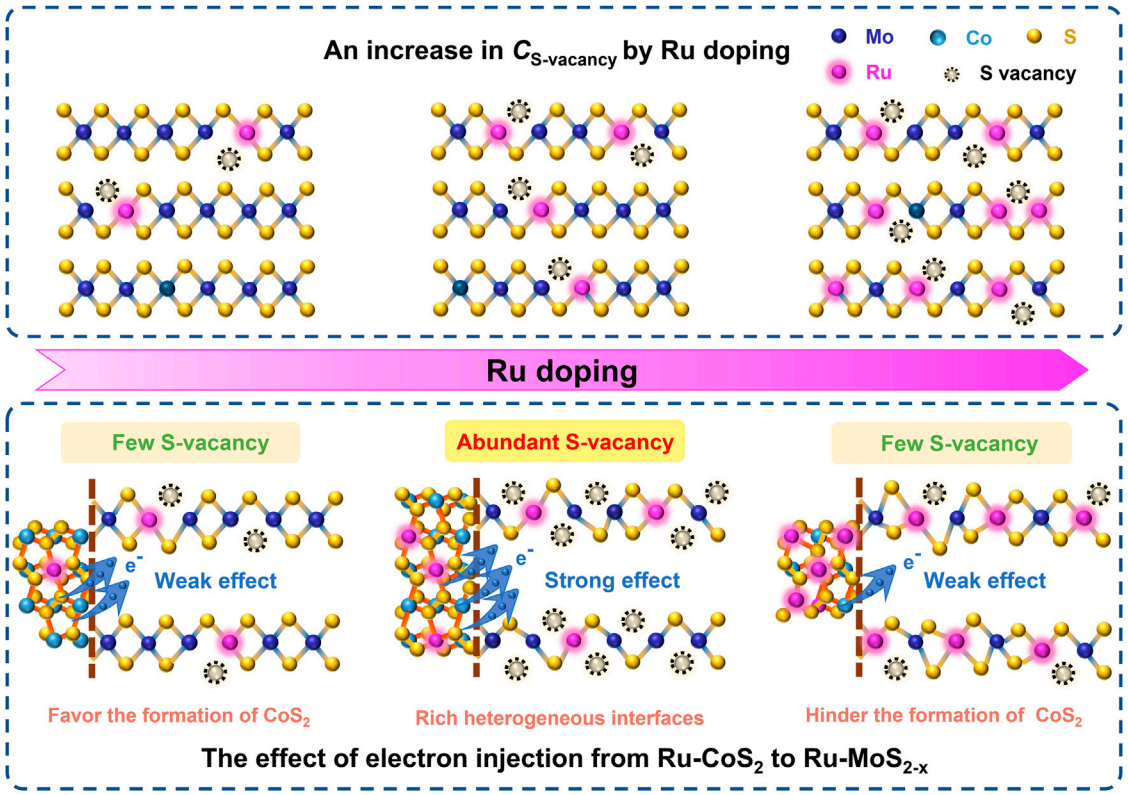

FIGURE 5 | Schematic illustration of the possible formation mechanism of the S-vacancy of the basal planes in Ru-MoS_{2-x} of Ru-MoS_{2-x}-CoS_2/CC samples.

adjacent S-vacancy. Furthermore, S-vacancy is exclusively stable around $Ru_{(Mo)}$. On the other hand, by compositing with CoS_2, Schottky heterojunctions provide a feasible opportunity for the electron transfer from Ru-CoS_2 to Ru-MoS_{2-x} (Li et al., 2018) due to a high Fermi level of CoS_2. This effect can promote S^{2-} escaping from Ru-MoS_{2-x} nanosheets to remain charge neutrality (Liu et al., 2017; Gan et al., 2018), indicating the formation of the positively charged defects, S-vacancy. Subsequently, we further characterize the atom ratios of Co to (Co + Mo) of the related samples by ICP-OES in the inset of **Figure 3A**. From this inset, the atom ratio of Co to (Co + Mo) of the typical samples is as high as about 16.1% at V increasing to 4.0 ml, thereby resulting in more Ru-CoS_2, and rich heterogeneous interfaces between Ru-CoS_2 and Ru-MoS_{2-x} as well. More heterogeneous interfaces favor the electron injection from Ru-CoS_2 to Ru-MoS_{2-x}, which leads to an increase in $C_{S\text{-vacancy}}$ (**Figure 3E**). However, further increasing V results in a decrease in atom ratios of Co to (Co + Mo) (inset of **Figure 3A**) and poor heterojunctions. This could indicate a weaker electron injection effect of Ru-CoS_2 and lower $C_{S\text{-vacancy}}$ at excessively high V. The schematic illustration of the possible formation mechanism of S-vacancy of the basal planes in Ru-MoS_{2-x} of Ru-MoS_{2-x}-CoS_2/CC samples is presented in **Figure 5**.

To confirm this viewpoint, we systematically investigate the effect of compositing with CoS_2 on $C_{S\text{-vacancy}}$ of the as-synthesized samples at fixed V or Ru dopants in **Figure 6**. **Figure 6A** exhibits XRD patterns of Ru-MoS_{2-x}-CoS_2/CC-80, Ru-MoS_{2-x}-CoS_2/CC -240, Ru-MoS_{2-x}-CoS_2/CC-280, and Ru-MoS_{2-x}-CoS_2/CC-320. With an increase in the mass of Co precursor (m_{Co}), the intensity of the diffraction peak of the (002) plane at 14.1° for Ru-MoS_{2-x} greatly decreases, while intensities of peaks of the (200) and 311) planes for Ru-CoS_2 gradually increase (**Figure 6A**), indicating a decrease in the RC of Ru-MoS_{2-x} and an increase in the RC of Ru-CoS_2 (**Supplementary Figure S10**). At m_{Co} increasing to 240 mg, Ru-CoS_2 can be densely coated by Ru-MoS_{2-x} nanosheets (**Supplementary Figure S11B**). Nevertheless, further increasing m_{Co} to 280 or 320 mg leads to incompact Ru-MoS_{2-x} shells (**Supplementary Figures S11C, D**) due to the formation of more Ru-CoS_2 or a decrease in the content of Ru-MoS_{2-x}. These data are in good agreement with the results of **Figure 6D**, which displays atom ratios of Co to (Co + Mo) of the as-synthesized samples by XPS analysis. These atom ratios also increase with increasing m_{Co}. For example, the atom ratio of Co to (Co + Mo) of R Ru-MoS_{2-x}-CoS_2/CC-320 increases up to 10.1%. To further confirm the effect of electron injection from Ru-CoS_2 to Ru-MoS_{2-x}, we characterize Mo3d high-resolution XPS spectra of Ru-MoS_{2-x}-CoS_2/CC-80, Ru-MoS_{2-x}-CoS_2/CC-240, Ru-MoS_{2-x}-CoS_2/CC-280, and Ru-MoS_{2-x}-CoS_2/CC-320 in **Figure 6B**. Mo 3 days in XPS data move to low binding energy (Huang et al., 2019), implying an increase in the electron density

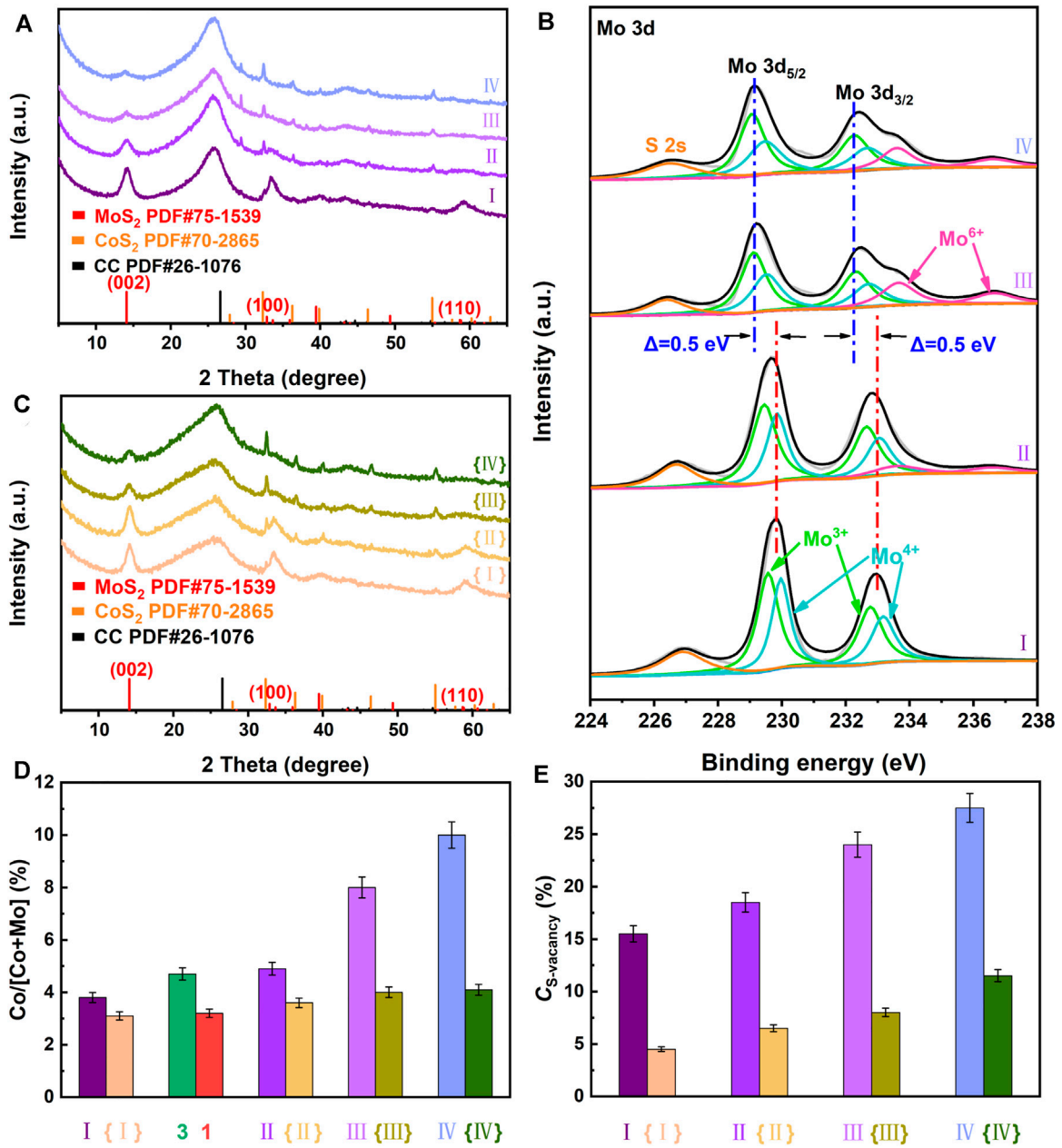

FIGURE 6 | (A) XRD patterns and **(B)** Mo3d high-resolution XPS spectra of Ru-MoS_{2-x}-CoS_2/CC-80 (I), Ru-MoS_{2-x}-CoS_2/CC-240 (II), Ru-MoS_{2-x}-CoS_2/CC-280 (III), and Ru-MoS_{2-x}-CoS_2/CC-320 (IV); **(C)** XRD patterns of MoS_2-CoS_2/CC-80 ({I}), MoS_2-CoS_2/CC-240 ({II}), MoS_2-CoS_2/CC-280 ({III}), and MoS_2-CoS_2/CC-320 ({IV}); **(D)** atom ratios of Co to (Co + Mo) by XPS data, **(E)** $C_{S\text{-vacancy}}$ of the related samples. Meanwhile, fabrications of MoS_2-CoS_2/CC-80, MoS_2-CoS_2/CC-240, MoS_2-CoS_2/CC-280, and MoS_2-CoS_2/CC-320 are almost the same as those of Ru-MoS_{2-x}-CoS_2/CC-80, Ru-MoS_{2-x}-CoS_2/CC-240, Ru-MoS_{2-x}-CoS_2/CC-280, and Ru-MoS_{2-x}-CoS_2/CC-320 except for the absence of $RuCl_3$ solution.

of Ru-MoS_{2-x} of the as-synthesized samples. For example, Mo 3 day peaks of the typical samples negatively shift by about 0.06 eV compared to those of Ru-MoS_{2-x}-CoS_2/CC-80 in terms of **Figure 2D** and **Figure 6B**. After careful investigations, similar results are observed in Mo3d XPS spectra of other Ru-MoS_{2-x}-CoS_2/CC samples (**Figure 6B**), yielding the related data about negative shifts of 0.12 eV for Ru-MoS_{2-x}-CoS_2/CC-240, 0.45 eV for Ru-MoS_{2-x}-CoS_2/CC-280, and 0.50 eV for Ru-MoS_{2-x}-CoS_2/CC-320. It is seen that such an electron injection effect increases gradually with the increase in m_{Co}, which means more S^{2-} escaping from MoS_{2-x} nanosheets (Liu et al., 2017; Gan et al., 2018) at higher m_{Co}. Therefore, the atom ratios of S to Mo for all Ru-MoS_{2-x}-CoS_2/CC samples decrease (**Supplementary Table S3**), and $C_{S\text{-vacancy}}$ increases (**Figure 6E**) with increasing m_{Co}. For instance, Ru-MoS_{2-x}-CoS_2/CC-320 demonstrate the highest $C_{S\text{-vacancy}}$ (about 27.5%) among all samples.

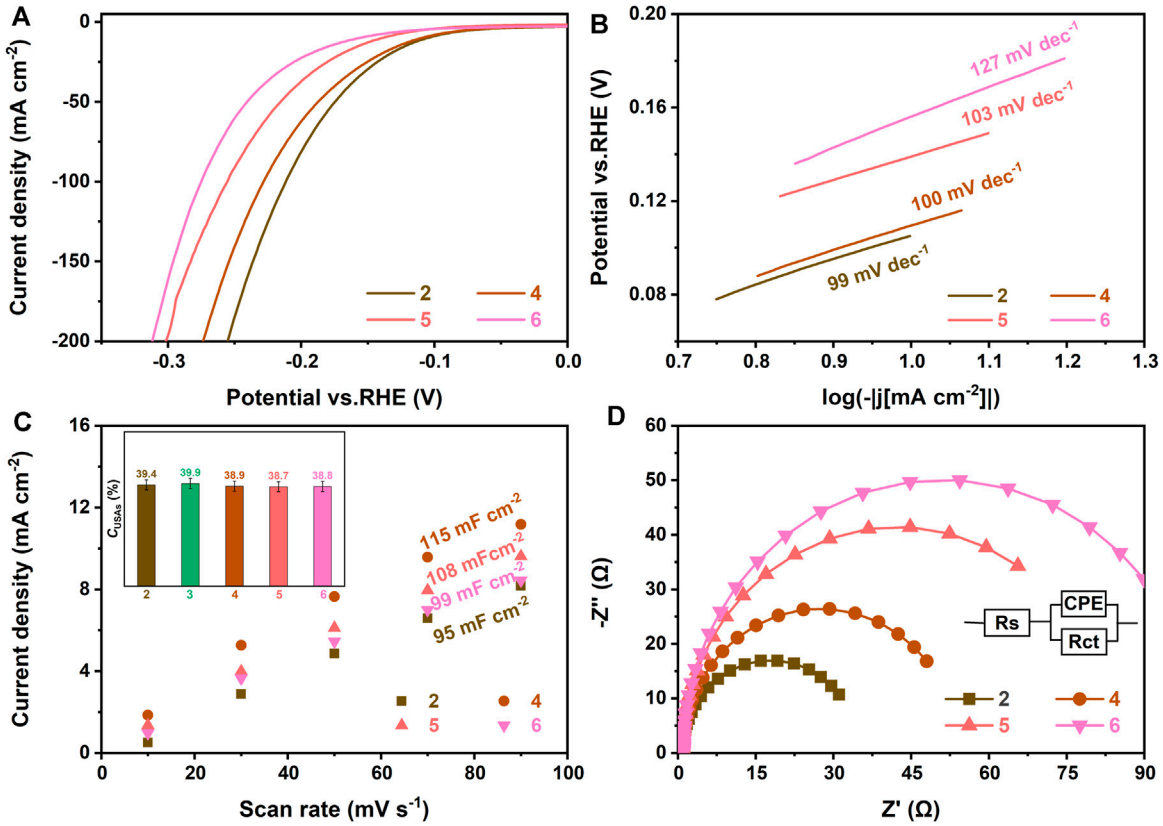

FIGURE 7 | (A) Polarization curves, **(B)** Tafel plots, **(C)** C_{dl} at different scan rates, and **(D)** Nyquist plots of Ru-MoS_{2-x}-CoS_2/CC-1.0 (2), Ru-MoS_{2-x}-CoS_2/CC-7.0 (4), Ru-MoS_{2-x}-CoS_2/CC-10.0 (5), and Ru-MoS_{2-x}-CoS_2/CC-30.0 (6). The inset of panel **(C)** is C_{USAs} of the related samples. The electrolyte is N_2-saturated 1 M KOH.

Additionally, **Figure 6** also demonstrates the influence of compositing with CoS_2 on $C_{S\text{-vacancy}}$ of the as-synthesized samples without Ru dopants. **Figure 6C** shows XRD patterns of MoS_2-CoS_2/CC-80, MoS_2-CoS_2/CC-240, MoS_2-CoS_2/CC-280, and MoS_2-CoS_2/CC-320. The influences of m_{Co} on intensities of the related peaks and RC of MoS_2 and CoS_2 are shown in **Figure 6C** and **Supplementary Figure S12**, suggesting a decline in the crystallinity of MoS_2 and an increase in crystallinity of CoS_2 as well. The trend in the variation of atom ratios of Co to (Co + Mo) of the as-synthesized samples without Ru dopants is the same as that of Ru-doped samples in **Figure 6D**, which implies the formation of more CoS_2 and richer heterojunctions at higher m_{Co}. Similarly, the more heterojunctions are, the stronger electron injection effect from CoS_2 to MoS_{2-x} is obtained. For instance, Mo 3 day peaks of MoS_2-CoS_2/CC-240 display a negative shift of 0.15 eV in comparison with those of MoS_2-CoS_2/CC-80 from **Supplementary Figure S13**. At m_{Co} increasing to 320 mg, Mo 3 day peaks of MoS_2-CoS_2/CC-320 present a negative shift of about 0.36 eV compared to those of MoS_2-CoS_2/CC-80 (**Supplementary Figure S13**). Therefore, the atom ratios of S to Mo for these samples without Ru dopants also decrease with increasing m_{Co} (**Supplementary Table S3**), leading to an increase in $C_{S\text{-vacancy}}$ (**Figure 6E**) as well. Therefore, $C_{S\text{-vacancy}}$ of the basal planes of Ru-MoS_{2-x} can be efficiently regulated by simply changing m_{Co} based on the effect of electron injection from Ru-CoS_2 to Ru-MoS_{2-x}.

Together, either doping Ru or compositing with CoS_2 only regulates $C_{S\text{-vacancy}}$ of the as-synthesized samples within a narrow range, such as between 2.1 and 10.5% for doping Ru (**Figure 3E**) and 4.5 and 11.5% for compositing with CoS_2 (**Figure 6E**). Interestingly, synergistically regulating $C_{S\text{-vacancy}}$ of the as-synthesized samples, from 2.1 to 27.5% (**Figure 6E**), is realized by a new one-step doping-assisted compositing strategy.

HER Activities of Ru-MoS_{2-x}-CoS_2/CC Samples Synthesized at Various *V*

To find out the relationship between the microstructure and HER activity, we carefully investigate a series of electrochemical performances of Ru-MoS_{2-x}-CoS_2/CC samples synthesized at various V under the fixed m_{Co} (160 mg) in **Figures 7**, **8**. According to **Figures 7A–D**, the typical samples exhibit the highest HER activity among these samples, such as an overpotential of about 170 mV at a current density of 100 mA cm^{-2} and a Tafel plot of 71 mV dec^{-1} in alkaline environments (1 M KOH), implying that low or excessive Ru dopant is disadvantageous for the HER activity of Ru-MoS_{2-x}-CoS_2/CC samples.

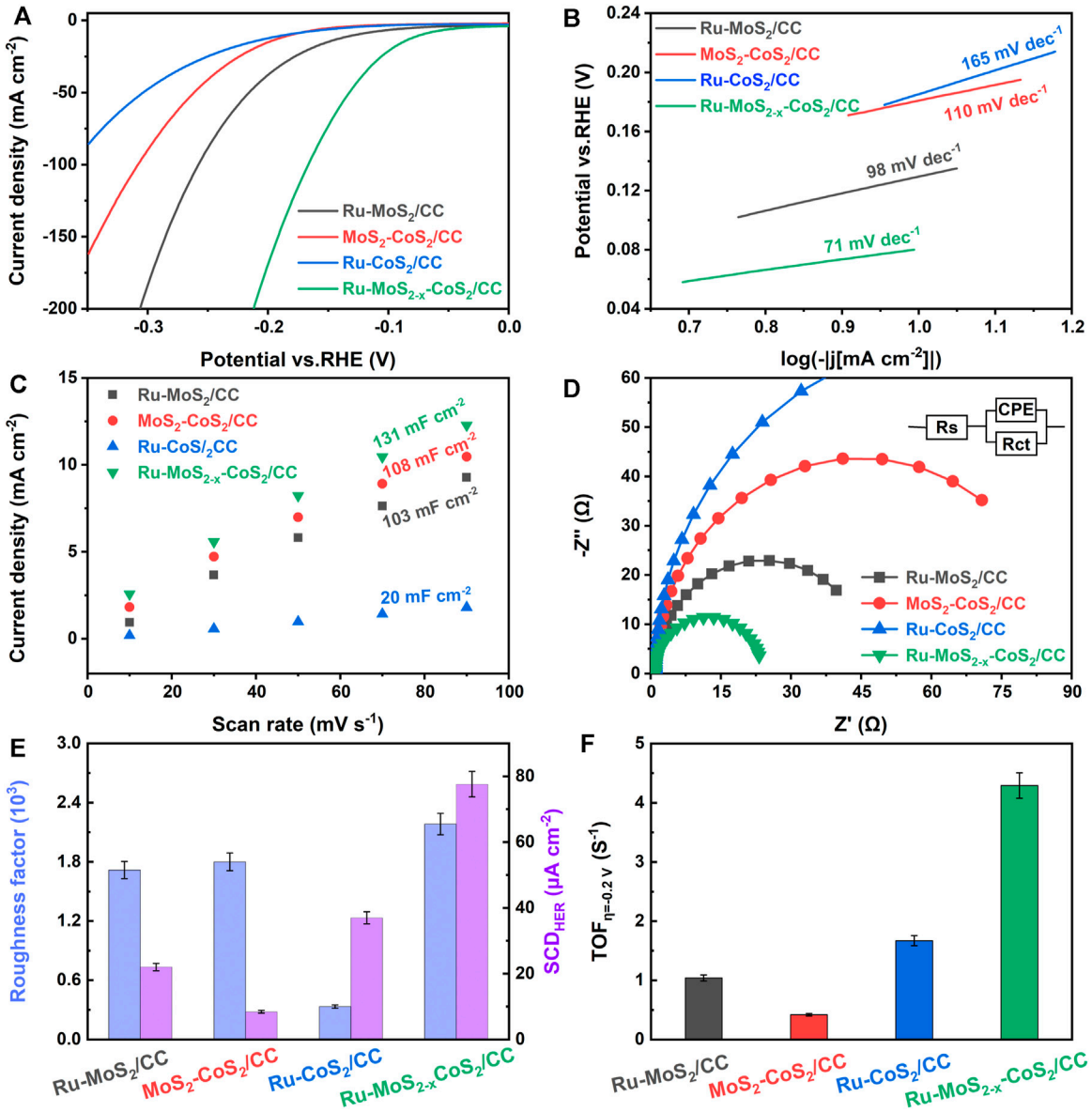

FIGURE 8 | (A) Polarization curves, **(B)** Tafel plots, **(C)** C_{dl} at different scan rates, **(D)** Nyquist plots, **(E)** R_f and SCD_{HER}, and **(F)** TOF at 0.2 V of Ru-MoS_2/CC, MoS_2-CoS_2/CC, Ru-CoS_2/CC, and the typical samles. The electrolyte is N_2-saturated 1 M KOH.

Figure 7C displays double-layer capacitance (C_{dl}) to evaluate electrochemical active surface area (ECSA), which is calculated by cyclic voltammetry (CV) curves in **Supplementary S14, 15**. From **Figure 7C** and **Figure 8C**, the typical samples also demonstrate the highest C_{dl} among all Ru-MoS_{2-x}-CoS_2/CC samples, reaching up to *ca.* 131 mF cm^{-2}. For 2H-MoS_2, its active sites are mainly from unsaturated sulfur atoms (Kibsgaard et al., 2012; Xie et al., 2013a; Liu et al., 2018). This is because the adsorption free energy of hydrogen atom (ΔG_H) of unsaturated sulfur atoms approaches zero (about -0.06 eV), which indicates their excellent H* adsorption–desorption property (Hinnemann et al., 2005). More recently, modulating sulfur vacancy into MoS_2-based materials has been developed as an efficient strategy (Tsai et al., 2017; Park et al., 2018; Li Y. et al., 2021) to activate inert basal planes because EMAs can be tailored into newborn active sites (Wang X. et al., 2020). Therefore, the active sites of these Ru-MoS_{2-x}-CoS_2/CC samples should include unsaturated sulfur atoms and EMAs.

To confirm the difference in active sites for such Ru-MoS_{2-x}-CoS_2/CC samples, the inset of **Figure 7C** further shows the concentration of unsaturated sulfur atoms (USAs) of all samples based on XPS data from **Supplementary Figure S16**. From this inset, there is no significant difference in the concentration of USAs (C_{USAs}) for these samples. This may be closely related to preferentially exposed sulfur-edge atoms of Ru-MoS_{2-x} nanosheet array vertically assembled on CC. At the same

time, this inset implies that USAs are not the essential factor for the most abundant active sites of the typical samples. From **Figure 3E**, $C_{S\text{-vacancy}}$ for Ru-MoS_{2-x}-CoS_2/CC-1.0, the typical samples, Ru-MoS_{2-x}-CoS_2/CC-7.0, Ru-MoS_{2-x}-CoS_2/CC-10.0, and Ru-MoS_{2-x}-CoS_2/CC-30.0 are 7.9, 17.1, 14.0, 12.5, and 12.0%, respectively. It is seen that $C_{S\text{-vacancy}}$ of the typical samples is higher than that of other Ru-MoS_{2-x}-CoS_2/CC samples. Consequently, we can reasonably conclude that the difference in active sites of RCM/CC should be dependent on $C_{S\text{-vacancy}}$. The formation of one S-vacancy means the occurrence of three EMAs at $C_{S\text{-vacancy}}$ < 18% (Li et al., 2016a) because S-vacancy uniformly distributes on the basal planes of 2H-MoS_{2-x}. Obviously, under this situation, the higher $C_{S\text{-vacancy}}$ is obtained, the more EMAs or active sites are achieved. At m_{Co} = 160 mg, Ru doping firstly favors heterogeneous nucleation and growth of CoS_2 (**Figures 4C, I**) besides introducing a certain quantity S-vacancy into the basal planes. For instance, at V increasing to 4.0 ml, the typical samples demonstrate higher $C_{S\text{-vacancy}}$ (**Figure 3E**) than Ru-MoS_{2-x}-CoS_2/CC-1.0, maybe due to more heterogeneous interfaces between Ru-CoS_2 and Ru-MoS_{2-x}. Nevertheless, further increasing V hinders the formation of Ru-CoS_2 (**Figures 4F, I**) and leads to a decline in $C_{S\text{-vacancy}}$. Lower $C_{S\text{-vacancy}}$ could originate from fewer Schottky heterojunctions and a weaker electron injection effect of Ru-CoS_2 at excessively high V.

As another key factor for HER, the R_{CT} of all Ru-MoS_{2-x}-CoS_2/CC samples is investigated in **Figure 7D** and **Figure 8D**. These figures exhibit their Nyquist plots. Each semicircle represents the R_{CT} of the cathode reaction. The charge transfer of Ru-MoS_{2-x}-CoS_2/CC-1.0 or Ru-MoS_{2-x}-CoS_2/CC-7.0 is inferior to that of the typical samples. Moreover, further increasing V results in considerably unsatisfactory R_{CT} from **Figure 7D**. In our viewpoint, rich active sites will promote the occurrence of HER reaction in the cathode, implying efficient charge transfer for the typical samples. On the other hand, compositing with the metallic phase for fast electrode kinetics (He et al., 2020; Li et al., 2020; Zhou G. et al., 2021), such as CoS_2 (Li et al., 2020), carbon nanotube (Huang et al., 2017), and reduced graphene oxide (Wang Y. et al., 2020), is one of the important approaches to improving electrocatalytic HER activity. From **Figure 7D** and **Figure 8D**, Ru-MoS_{2-x}-CoS_2/CC-1.0 demonstrate better charge transfer compared to Ru-MoS_2/CC. Furthermore, the influence of V on R_{CT} is coincident with the trend in the variation of RC of Ru-CoS_2 (**Figure 3C**) and atom ratios of Co to (Co + Mo) (inset of **Figure 3A**) of all Ru-MoS_{2-x}-CoS_2/CC samples. Therefore, the higher crystallinity of cobalt disulfide or the more CoS_2 is obtained, the lower R_{CT} of the as-synthesized samples is achieved.

HER Activities of Ru-MoS_{2-X}-CoS_2/CC Samples Synthesized at Various m_{Co}

We further investigate the HER activity of Ru-MoS_{2-x}-CoS_2/CC samples synthesized at various m_{Co} under the fixed V (4.0 ml) in **Supplementary Figure S17**. From **Supplementary Figures S17A, B**, HER activities of Ru-MoS_{2-x}-CoS_2/CC-80 are an overpotential of about 228 mV at a current density of 100 mA cm^{-2} and a Tafel plot of 102 mV dec^{-1}. At m_{Co} increasing to 160 mg, the typical samples demonstrate higher HER activity than other samples (**Figure 8A**; **Supplementary Figure S17A**). Further increasing m_{Co} leads to unsatisfactory overpotential and sluggish electrode kinetics, yielding the related data of 264 and 123 mV dec^{-1} for Ru-MoS_{2-x}-CoS_2/CC-240, 294 and 130 mV dec^{-1} for Ru-MoS_{2-x}-CoS_2/CC-280, and 301 and 140 mV dec^{-1} for Ru-MoS_{2-x}-CoS_2/CC-320 at the same current density.

TABLE 1 | Comparison of the HER electrocatalytic activity of Ru-MoS_{2-x}-CoS_2/CC with some MoS_2-based HER electrocatalysts recently reported.

Samples	η_{10} (mV)	Ref
Co_3S_4/MoS_2 NRs	−166	Li et al. (2022b)
MoS_2@$CoSe_2$-CC	−101	Yuan et al. (2022)
NiS_2/MoS_2@GNS	−130	Balaji et al. (2022)
N-doped $MoS_2/Ti_3C_2T_x$	−80	Liu et al. (2021)
Co-E_x-MoS_2	−89	Luo et al. (2018)
SA-Ru-MoS_2	−76	Zhang et al. (2019a)
0.2NM ($Ni(OH)_2/MoS_2$)	−227	Zhao et al. (2018)
Co_9S_8-MoS_2@3DC	−177	Diao et al. (2019)
Ru-MoS_2	−98	Geng et al. (2022)
ZnS@C@MoS_2	−118	Liu et al. (2019)
Ru-MoS_{2-x}-CoS_2/CC	−73	This work

To illustrate the reason why excessive m_{Co} is disadvantageous for HER activity, C_{dl} and C_{USAs} of all samples are tested in **Supplementary FIgure S17C** and **Supplementary Figure S18**, respectively. The corresponding CV curves related to **Supplementary FIgure S17C** are shown in **Supplementary Figure S19**. From **Supplementary FIgure S17C**, C_{dl} gradually increases with an increase in m_{Co}. For example, Ru-MoS_{2-x}-CoS_2/CC-80 display low C_{dl} (about 118 mF cm^{-2}) at m_{Co} = 80 mg. At m_{Co} increasing to 320 mg, the C_{dl} of Ru-MoS_{2-x}-CoS_2/CC-320 is as high as 199 mF cm^{-2}. We rationally hypothesize that this is closely related to $C_{S\text{-vacancy}}$, due to the fact that high $C_{S\text{-vacancy}}$ favors abundant EMAs. As we know, the basal planes in 2H-MoS_2 are inert, owing to ΔG_H reaching 2.1 eV (Zhou W. et al., 2021). Impressively, inert basal planes can be efficiently activated by a low concentration of S-vacancy (*ca* 4%) modulating into them because the corresponding ΔG_H closes to zero (Wang X. et al., 2020). It is not difficult to understand that such EMAs should be highly active, but the number is considerably poor.

According to the related literature (Wang X. et al., 2020), ΔG_H negatively shifts with an increase in $C_{S\text{-vacancy}}$, implying that hydrogen atoms do not easily desorb at excessive $C_{S\text{-vacancy}}$. For instance, at excessive m_{Co}, $C_{S\text{-vacancy}}$ of Ru-MoS_{2-x}-CoS_2/CC-320 reaches up to 27.5%. As expected, EMAs are abundant in this case, but the catalytic sites are of low activity, owing to the undesirable ΔG_H (Wang X. et al., 2020). Subsequently, a balance between the intrinsic activity and the number of EMAs to boost highly active EMAs could be realized by precisely regulating $C_{S\text{-vacancy}}$ to 17.1% (Wang X. et al., 2020). Consequently, the typical samples demonstrate the optimal HER activity among all samples. Furthermore, C_{USAs} of all samples except for Ru-MoS_{2-x}-CoS_2/CC-320 is almost the same as that of the typical samples. C_{USAs} of Ru-MoS_{2-x}-CoS_2/CC-320 (about 33.9%) is lower than that of other samples, which is responsible for the incompact Ru-MoS_{2-x} shells (**Supplementary Figure S11D**), and the significant

decrease in the content of molybdenum disulfide (**Figure 6D**). This indicates that sulfur-edge atoms of Ru-MoS_{2-x} nanosheets are not easy to be preferentially exposed for such samples synthesized at excessive m_{Co}.

Last but not least, **Supplementary Figure S17D**and **Figure 8D** further exhibit R_{CT} of all samples. Higher m_{Co} leads to higher R_{CT} of the related samples (**Supplementary Figure S17D**). For example, at m_{Co} reaching up to 320 mg, Ru-MoS_{2-x}-CoS_2/CC-320 display the highest R_{CT} among all Ru-MoS_{2-x}-CoS_2/CC samples. It can be ascribed to insufficient highly active EMAs regardless of the higher RC of Ru-CoS_2 (**Figure 6A**; **Supplementary Figure S10**) for these samples synthesized at higher m_{Co}. Insufficient active sites could not promote redox half-reaction, thereby leading to inefficient charge transfer.

Comparison of HER Activities of the Typical Samples and Other Similar Electrocatalysts

HER activities of Ru-MoS_2/CC, MoS_2-CoS_2/CC, Ru-CoS_2/CC, and the typical samples are shown in **Figure 8A**. Ru-CoS_2/CC display the lowest HER activity among these samples, suggesting that the activity of the typical samples is mainly from Ru-MoS_{2-x} rather than Ru-CoS_2. In addition, Ru-MoS_2/CC exhibit faster electrode kinetics than MoS_2-CoS_2/CC according to **Figure 8B**. In our viewpoint, the Ru-doped sites can significantly accelerate the sluggish water dissociation in alkaline HER (Li J. et al., 2021).

From **Figure 8C**, C_{dl} of Ru-MoS_2/CC is only 103 mF cm^{-2} and lower than that of the typical samples. Furthermore, C_{USAs} of Ru-MoS_2/CC (about 39.3%) is almost the same as that of the typical samples from **Supplementary Figure S18**. Therefore, the difference in active sites between Ru-MoS_2/CC and the typical samples should be closely related to $C_{S\text{-}vacancy}$. Higher $C_{S\text{-}vacancy}$ indicates more highly active EMAs. As shown in **Figure 3E**, $C_{S\text{-}vacancy}$ of Ru-MoS_2/CC is only about 3.1% by doping Ru, implying insufficient active sites. In our strategy, doping Ru coupled to compositing with CoS_2 synergistically regulates $C_{S\text{-}vacancy}$ of the as-synthesized samples from 2.1 to 27.5%. For instance, $C_{S\text{-}vacancy}$ of the typical samples reaches up to 17.1% (**Figure 3E**), which implies that rich highly active sites are successfully introduced into the typical samples. In terms of **Figure 8D**, R_{CT} of the typical samples is lower than that of Ru-MoS_2/CC. Besides rich active sites promoting redox half-reaction, high crystallized Ru-CoS_2 of the typical samples is another important factor to realize the efficient charge transfer during electrocatalysis. Next, the specific activity and turnover frequency (TOF) are further conducted to investigate the intrinsic activity of all samples (**Figures 8E, F**). C_{dl} of an ideal plane electrode is considered as 60 μF cm^{-2} (Levine and Smith, 1971); the roughness factor (R_f) can be calculated by the formula: $R_f = (C_{dl}\ 60^{-1})\times 10^{+3}$. The specific alkaline HER current density (SCD_{HER}) is determined by the formula: $SCD_{HER} = j\ R_f^{-1}$ (Jovic et al., 2015; Jovic et al., 2016), where j is the current density at an overpotential of -0.2 V. From **Figure 8E**, the typical samples have not only the largest R_f ($2.18 \times 10^{+3}$) but also the highest specific activity (about 77.6 μA cm^{-2}) among all samples. In addition, the TOF for these samples is obtained by the formula $TOF = jS\ (2nF)^{-1}$. Here, S is the geometrical surface area in cm^2 and F is the Faraday constant. The value of n is the number of active sites (mol), which is confirmed according to the previously reported literature (Tian et al., 2014). The typical samples also exhibit the highest intrinsic activity among all samples, about 4.29 s^{-1} in **Figure 8F**. Moreover, the comparison between the typical samples and other similar electrocatalysts is provided in **Table 1**. The typical samples exhibit higher HER activity than other similar electrocatalysts listed in **Table 1**, which is ascribed to two factors: abundant active sites and accelerated electrode kinetics during the HER process.

The Long-Term Durability of the Typical Samples

In addition, LSV curves of the typical samples before and after 1000 cycles are recorded to evaluate their durability, and just a 10 mV negative shift at a current density of -100 mA cm^{-2} is seen in **Supplementary Figure S20A, B**; the chronoamperometric response (i ~ t) of the typical samples displays negligible attenuation of the current density for 10 h. Moreover, no significant change is observed in the morphology and phase structure after 1000 cycles (**Supplementary Figures S21, 22**). All results suggest that the typical samples possess remarkable long-term durability for HER in alkaline media.

CONCLUSION

Herein, we develop a one-step Ru doping coupled to compositing with the CoS_2 strategy for the fabrication of Ru-MoS_{2-x}-CoS_2/CC. In our strategy, Ru doping is advantageous for the formation of S-vacancy in the basal planes of MoS_2. More importantly, Ru doping affects microstructures of CoS_2, which has a significant influence on $C_{S\text{-}vacancy}$ of Ru-MoS_{2-x} nanosheets in Ru-MoS_{2-x}-CoS_2/CC samples in turn. At the fixed m_{Co} (160 mg), Ru doping favors the heterogeneous nucleation and growth of CoS_2 at V increasing to 4.0 ml, which leads to a high crystallinity of Ru-CoS_2 and rich heterogeneous interfaces between Ru-CoS_2 and Ru-MoS_{2-x}. This facilitates the electron transfer from Ru-CoS_2 to Ru-MoS_{2-x}, indicating an increase in $C_{S\text{-}vacancy}$, thereby increasing $C_{S\text{-}vacancy}$ of the MoS_2-based materials. However, further increasing V results in a low crystallinity of Ru-CoS_2 and poor heterojunctions, implying a weaker electron injection effect of Ru-CoS_2 and low $C_{S\text{-}vacancy}$. At fixed V (4.0 ml of $RuCl_3$ solution), the electron injection effect increases gradually with the increase in m_{Co}, which means more S^{2-} escaping from Ru-MoS_2 nanosheets at higher m_{Co}. Therefore, synergistically regulating $C_{S\text{-}vacancy}$ of the as-synthesized samples, from 2.1 to 27.5%, is realized by a new one-step Ru doping coupled to compositing with the CoS_2 strategy. High $C_{S\text{-}vacancy}$ indicates abundant EMAs. Impressively, inert basal planes can be efficiently activated by modulating low $C_{S\text{-}vacancy}$ into Ru-MoS_{2-x}-CoS_2/CC samples. However, the number is considerably poor. Additionally, hydrogen atoms do not easily desorb at excessive $C_{S\text{-}vacancy}$. This is because EMAs are abundant in this case, but the catalytic sites are of low activity, owing to the undesirable ΔG_H. By precisely regulating $C_{S\text{-}vacancy}$ to 17.1%, a balance

between the intrinsic activity and the number of EMAs to boost highly active EMAs should be realized. Consequently, the typical samples demonstrate the optimal alkaline HER activity among all samples, such as a low overpotential of 170 mV at 100 mA cm^{-2}, a large SCD_{HER} of 77.6 μA cm^{-2}, and a TOF of 4.29 s^{-1} at - 0.2 V as well as excellent long-term stability. The results pave a new approach to activating inert basal planes in MoS_2 for efficient hydrogen evolution and promise important applications in the fields of electrocatalysis or energy conversion.

DATA AVAILABILITY STATEMENT

The original contributions presented in the study are included in the article/**Supplementary Material**; further inquiries can be directed to the corresponding authors.

AUTHOR CONTRIBUTIONS

X-YL has made substantial contributions to the design of this work and has drafted the work. S-JZ has made substantial contributions to the acquisition, analysis, and interpretation of data for the work. YW has revised the work critically for the important intellectual content and has approved the final version to be published. TL, X-YY, and C-FY have made some contributions to the analysis and interpretation of data for the work. YL has given some important suggestions for this revised article. BS has given some suggestions on preparing this article. L-HC has provided some important ideas for the design of this work and has approved the final version to be published.

FUNDING

This work was also financially supported by the National Natural Science Foundation of China (No. U20A20122).

ACKNOWLEDGMENTS

L-HC acknowledges the Hubei Provincial Department of Education for the "Chutian Scholar" program. Y-LW acknowledges the Fundamental Research Funds for the Central Universities (WUT: 2020-IB-028). The authors deeply thank the 111 Projects (Grant No. B20002) and the International Science and Technology Cooperation Program of China (2021YFE0115800) for supporting this work.

SUPPLEMENTARY MATERIAL

The Supplementary Material for this article can be found online at: https://www.frontiersin.org/articles/10.3389/fchem.2022.915468/full#supplementary-material

REFERENCES

Balaji, D., Madhavan, J., Vinesh, V., Neppolian, B., AlSalhi, M. S., and Prasad, S. (2022). Graphene Supported Flower-like NiS2/MoS2 Mixed Phase Nano-Composites as a Low Cost Electrode Material for Hydrogen Evolution Reaction in Alkaline Media. *Mater. Chem. Phys.* 280, 125839. doi:10.1016/j.matchemphys.2022.125839

Chakraborty, I., Malik, P. K., and Moulik, S. P. (2006). Preparation and Characterisation of CoS2 Nanomaterial in Aqueous Cationic Surfactant Medium of Cetyltrimethylammonium Bromide (CTAB). *J. Nanopart. Res.* 8 (6), 889–897. doi:10.1007/s11051-005-9032-y

Chen, T.-T., Wang, R., Li, L.-K., Li, Z.-J., and Zang, S.-Q. (2020). MOF-derived Co9S8/MoS2 Embedded in Tri-doped Carbon Hybrids for Efficient Electrocatalytic Hydrogen Evolution. *J. Energy Chem.* 44, 90–96. doi:10.1016/j.jechem.2019.09.018

Deng, J., Li, H., Wang, S., Ding, D., Chen, M., Liu, C., et al. (2017). Multiscale Structural and Electronic Control of Molybdenum Disulfide Foam for Highly Efficient Hydrogen Production. *Nat. Commun.* 8 (1), 14430. doi:10.1038/ncomms14430

Diao, L., Zhang, B., Sun, Q., Wang, N., Zhao, N., Shi, C., et al. (2019). An In-Plane Co9S8@MoS2 Heterostructure for the Hydrogen Evolution Reaction in Alkaline Media. *Nanoscale* 11 (44), 21479–21486. doi:10.1039/C9NR06609H

Djara, R., Holade, Y., Merzouki, A., Lacour, M.-A., Masquelez, N., Flaud, V., et al. (2020). Nanostructured Carbon-Nitrogen-Sulfur-Nickel Networks Derived from Polyaniline as Bifunctional Catalysts for Water Splitting. *Front. Chem.* 8, 22. doi:10.3389/fchem.2020.00385

Feng, J.-X., Wu, J.-Q., Tong, Y.-X., and Li, G.-R. (2018). Efficient Hydrogen Evolution on Cu Nanodots-Decorated Ni3S2 Nanotubes by Optimizing Atomic Hydrogen Adsorption and Desorption. *J. Am. Chem. Soc.* 140 (2), 610–617. doi:10.1021/jacs.7b08521

Gan, X., Lee, L. Y. S., Wong, K.-y., Lo, T. W., Ho, K. H., Lei, D. Y., et al. (2018). 2H/1T Phase Transition of Multilayer MoS2 by Electrochemical Incorporation of S Vacancies. *ACS Appl. Energy Mat.* 1 (9), 4754–4765. doi:10.1021/acsaem.8b00875

Gao, B., Du, X., Li, Y., Ding, S., Xiao, C., and Song, Z. (2020). Deep Phase Transition of MoS2 for Excellent Hydrogen Evolution Reaction by a Facile C-Doping Strategy. *ACS Appl. Mat. Interfaces* 12 (1), 877–885. doi:10.1021/acsami.9b18940

Ge, R., Wang, Y., Li, Z., Xu, M., Xu, S. M., Zhou, H., et al. (2022). Selective Electrooxidation of Biomass-Derived Alcohols to Aldehydes in a Neutral Medium: Promoted Water Dissociation over a Nickel-Oxide-Supported Ruthenium Single-Atom Catalyst. *Angew. Chem. Int. Ed.* 61. doi:10.1002/anie.202200211

Geng, S., Tian, F., Li, M., Liu, Y., Sheng, J., Yang, W., et al. (2022). Activating Interfacial S Sites of MoS2 Boosts Hydrogen Evolution Electrocatalysis. *Nano Res.* 15 (3), 1809–1816. doi:10.1007/s12274-021-3755-7

Gong, F., Ye, S., Liu, M., Zhang, J., Gong, L., Zeng, G., et al. (2020). Boosting Electrochemical Oxygen Evolution over Yolk-Shell Structured O-MoS2 Nanoreactors with Sulfur Vacancy and Decorated Pt Nanoparticles. *Nano Energy* 78, 105284. doi:10.1016/j.nanoen.2020.105284

Hao, J., Yang, W., Peng, Z., Zhang, C., Huang, Z., and Shi, W. (2017). A Nitrogen Doping Method for CoS2 Electrocatalysts with Enhanced Water Oxidation Performance. *ACS Catal.* 7 (6), 4214–4220. doi:10.1021/acscatal.7b00792

He, S., Du, H., Wang, K., Liu, Q., Sun, J., Liu, Y., et al. (2020). Low-temperature Molten Salt Synthesis of MoS2@CoS2 Heterostructures for Efficient Hydrogen Evolution Reaction. *Chem. Commun.* 56 (41), 5548–5551. doi:10.1039/D0CC01726D

Hinnemann, B., Moses, P. G., Bonde, J., Jørgensen, K. P., Nielsen, J. H., Horch, S., et al. (2005). Biomimetic Hydrogen Evolution: MoS2 Nanoparticles as Catalyst for Hydrogen Evolution. *J. Am. Chem. Soc.* 127 (15), 5308–5309. doi:10.1021/ja0504690

Huang, H., Huang, W., Yang, Z., Huang, J., Lin, J., Liu, W., et al. (2017). Strongly Coupled MoS2 Nanoflake-Carbon Nanotube Nanocomposite as an Excellent Electrocatalyst for Hydrogen Evolution Reaction. *J. Mat. Chem. A* 5 (4), 1558–1566. doi:10.1039/C6TA09612C

Huang, J., Hou, D., Zhou, Y., Zhou, W., Li, G., Tang, Z., et al. (2015). MoS2 Nanosheet-Coated CoS2 Nanowire Arrays on Carbon Cloth as Three-Dimensional Electrodes for Efficient Electrocatalytic Hydrogen Evolution. *J. Mat. Chem. A* 3 (45), 22886–22891. doi:10.1039/C5TA07234D

Huang, N., Ding, Y., Yan, S., Yang, L., Sun, P., Huang, C., et al. (2019). Ultrathin MoS2 Nanosheets Vertically Grown on CoS2 Acicular Nanorod Arrays: A Synergistic Three-Dimensional Shell/Core Heterostructure for High-Efficiency Hydrogen Evolution at Full pH. *ACS Appl. Energy Mat.* 2 (9), 6751–6760. doi:10.1021/acsaem.9b01219

Jiang, J., Cong, H., Huang, X., Sun, R., Li, Y., Xu, W., et al. (2022). Three-dimensional ZnCo/MoS2-Co3S4/NF Heterostructure Supported on Nickel Foam as Highly Efficient Catalyst for Hydrogen Evolution Reaction. *Int. J. Hydrogen Energy* 47 (5), 2947–2957. doi:10.1016/j.ijhydene.2021.10.217

Jing, Y., Lei, Q., Hu, G., He, J., Lei, X., Wang, F., et al. (2020). PVP/ZIF-8-derived Zn, Ni Co-loaded N-Doped Porous Carbon as a Catalyst for an Efficient Hydrogen Evolution Reaction. *Front. Chem.* 8, 6. doi:10.3389/fchem.2020.00723

Jović, B. M., Jović, V. D., Lačnjevac, U. Č., Gajić-Krstajić, L., and Krstajić, N. V. (2015). Ni-(Ebonex-supported Ir) Composite Coatings as Electrocatalysts for Alkaline Water Electrolysis. Part I: Hydrogen Evolution. *Int. J. Hydrogen Energy* 40 (33), 10480–10490. doi:10.1016/j.ijhydene.2015.06.127

Jović, B. M., Jović, V. D., Lačnjevac, U. Č., Stevanović, S. I., Kovač, J., Radović, M., et al. (2016). Ru Layers Electrodeposited onto Highly Stable Ti2AlC Substrates as Cathodes for Hydrogen Evolution in Sulfuric Acid Solutions. *J. Electroanal. Chem.* 766, 78–86. doi:10.1016/j.jelechem.2016.01.038

Kang, Y. (2021). Interplay between Transition-Metal Dopants and Sulfur Vacancies in MoS2 Electrocatalyst. *Surf. Sci.* 704, 121759. doi:10.1016/j.susc.2020.121759

Kibsgaard, J., Chen, Z., Reinecke, B. N., and Jaramillo, T. F. (2012). Engineering the Surface Structure of MoS2 to Preferentially Expose Active Edge Sites for Electrocatalysis. *Nat. Mater* 11 (11), 963–969. doi:10.1038/nmat3439

Levine, S., and Smith, A. L. (1971). Theory of the Differential Capacity of the Oxide/aqueous Electrolyte Interface. *Discuss. Faraday Soc.* 52 (0), 290–301. doi:10.1039/DF9715200290

Li, C., Liu, Y., Zhuo, Z., Ju, H., Li, D., Guo, Y., et al. (2018). Local Charge Distribution Engineered by Schottky Heterojunctions toward Urea Electrolysis. *Adv. Energy Mat.* 8 (27), 1801775. doi:10.1002/aenm.201801775

Li, H., Tsai, C., Koh, A. L., Cai, L., Contryman, A. W., Fragapane, A. H., et al. (2016a). Activating and Optimizing MoS2 Basal Planes for Hydrogen Evolution through the Formation of Strained Sulphur Vacancies. *Nat. Mater* 15 (1), 48–53. doi:10.1038/nmat4465

Li, H., Tsai, C., Koh, A. L., Cai, L., Contryman, A. W., Fragapane, A. H., et al. (2016b). Erratum: Corrigendum: Activating and Optimizing MoS2 Basal Planes for Hydrogen Evolution through the Formation of Strained Sulphur Vacancies. *Nat. Mater* 15 (3), 364. doi:10.1038/nmat4564

Li, J., Li, Y., Wang, J., Zhang, C., Ma, H., Zhu, C., et al. (2022a). Elucidating the Critical Role of Ruthenium Single Atom Sites in Water Dissociation and Dehydrogenation Behaviors for Robust Hydrazine Oxidation-Boosted Alkaline Hydrogen Evolution. *Adv. Funct. Mater.* 32, 2109439. doi:10.1002/adfm.202109439

Li, J., Zhang, C., Ma, H., Wang, T., Guo, Z., Yang, Y., et al. (2021a). Modulating Interfacial Charge Distribution of Single Atoms Confined in Molybdenum Phosphosulfide Heterostructures for High Efficiency Hydrogen Evolution. *Chem. Eng. J.* 414, 128834. doi:10.1016/j.cej.2021.128834

Li, L., Qin, Z., Ries, L., Hong, S., Michel, T., Yang, J., et al. (2019). Role of Sulfur Vacancies and Undercoordinated Mo Regions in MoS2 Nanosheets toward the Evolution of Hydrogen. *ACS Nano* 13 (6), 6824–6834. doi:10.1021/acsnano.9b01583

Li, S., Sirisomboonchai, S., An, X., Ma, X., Li, P., Ling, L., et al. (2020). Engineering Interfacial Structures to Accelerate Hydrogen Evolution Efficiency of MoS2 over a Wide pH Range. *Nanoscale* 12 (12), 6810–6820. doi:10.1039/D0NR00008F

Li, Y., Wang, H., Xie, L., Liang, Y., Hong, G., and Dai, H. (2011). MoS2 Nanoparticles Grown on Graphene: An Advanced Catalyst for the Hydrogen Evolution Reaction. *J. Am. Chem. Soc.* 133 (19), 7296–7299. doi:10.1021/ja201269b

Li, Y., Zuo, S., Li, Q.-H., Wu, X., Zhang, J., Zhang, H., et al. (2021b). Vertically Aligned MoS2 with In-Plane Selectively Cleaved Mo-S Bond for Hydrogen Production. *Nano Lett.* 21 (4), 1848–1855. doi:10.1021/acs.nanolett.0c04978

Li, Z., Xu, W., Yu, X., Yang, S., Zhou, Y., Zhou, K., et al. (2022b). Synergistic Effect between 1D Co3S4/MoS2 Heterostructures to Boost the Performance for Alkaline Overall Water Splitting. *Inorg. Chem. Front.* 9, 2139–2149. doi:10.1039/D1QI01646F

Lin, H., Li, H., Li, Y., Liu, J., Wang, X., and Wang, L. (2017). Hierarchical CoS/MoS2 and Co3S4/MoS2/Ni2P Nanotubes for Efficient Electrocatalytic Hydrogen Evolution in Alkaline Media. *J. Mat. Chem. A* 5 (48), 25410–25419. doi:10.1039/C7TA08760H

Lin, J., Wang, P., Wang, H., Li, C., Si, X., Qi, J., et al. (2019). Defect-Rich Heterogeneous MoS 2/NiS 2 Nanosheets Electrocatalysts for Efficient Overall Water Splitting. *Adv. Sci.* 6 (14), 1900246. doi:10.1002/advs.201900246

Liu, D., Lv, Z., Dang, J., Ma, W., Jian, K., Wang, M., et al. (2021). Nitrogen-Doped MoS2/Ti3C2TX Heterostructures as Ultra-efficient Alkaline HER Electrocatalysts. *Inorg. Chem.* 60 (13), 9932–9940. doi:10.1021/acs.inorgchem.1c01193

Liu, G., Robertson, A. W., Li, M. M.-J., Kuo, W. C. H., Darby, M. T., Muhieddine, M. H., et al. (2017). MoS2 Monolayer Catalyst Doped with Isolated Co Atoms for the Hydrodeoxygenation Reaction. *Nat. Chem.* 9 (8), 810–816. doi:10.1038/nchem.2740

Liu, L., Wang, Y., Zhao, Y., Wang, Y., Zhang, Z., Wu, T., et al. (2022a). Ultrahigh Pt-Mass-Activity Hydrogen Evolution Catalyst Electrodeposited from Bulk Pt. *Adv. Funct. Mater.* 32 (20), 2112207. doi:10.1002/adfm.202112207

Liu, S., Li, S., Sekar, K., Li, R., Zhu, Y., Xing, R., et al. (2019). Hierarchical ZnS@C@MoS2 Core-Shell Nanostructures as Efficient Hydrogen Evolution Electrocatalyst for Alkaline Water Electrolysis. *Int. J. Hydrogen Energy* 44 (47), 25310–25318. doi:10.1016/j.ijhydene.2019.08.048

Liu, W., Wang, X., Yu, H., and Yu, J. (2018). Direct Photoinduced Synthesis of Amorphous CoMoSx Cocatalyst and Its Improved Photocatalytic H2-Evolution Activity of CdS. *ACS Sustain. Chem. Eng.* 6 (9), 12436–12445. doi:10.1021/acssuschemeng.8b02971

Liu, X., Yin, Z., Cui, M., Gao, L., Liu, A., Su, W.-N., et al. (2022b). Double Shelled Hollow CoS2@MoS2@NiS2 Polyhedron as Advanced Trifunctional Electrocatalyst for Zinc-Air Battery and Self-Powered Overall Water Splitting. *J. Colloid Interface Sci.* 610, 653–662. doi:10.1016/j.jcis.2021.11.115

Luo, Y., Li, X., Cai, X., Zou, X., Kang, F., Cheng, H.-M., et al. (2018). Two-Dimensional MoS2 Confined Co(OH)2 Electrocatalysts for Hydrogen Evolution in Alkaline Electrolytes. *ACS Nano* 12 (5), 4565–4573. doi:10.1021/acsnano.8b00942

Luo, Z., Zhang, H., Yang, Y., Wang, X., Li, Y., Jin, Z., et al. (2020). Reactant Friendly Hydrogen Evolution Interface Based on Di-anionic MoS2 Surface. *Nat. Commun.* 11 (1), 1116. doi:10.1038/s41467-020-14980-z

Ma, Y., Hai, G., Atinafu, D. G., Dong, W., Li, R., Hou, C., et al. (2020). Carbon Inserted Defect-Rich MoS2−X nanosheets@CdSnanospheres for Efficient Photocatalytic Hydrogen Evolution under Visible Light Irradiation. *J. Colloid Interface Sci.* 569, 89–100. doi:10.1016/j.jcis.2020.02.071

Nguyen, D. C., Luyen Doan, T. L., Prabhakaran, S., Tran, D. T., Kim, D. H., Lee, J. H., et al. (2021). Hierarchical Co and Nb Dual-Doped MoS2 Nanosheets Shelled Micro-TiO2 Hollow Spheres as Effective Multifunctional Electrocatalysts for HER, OER, and ORR. *Nano Energy* 82, 105750. doi:10.1016/j.nanoen.2021.105750

Park, S., Park, J., Abroshan, H., Zhang, L., Kim, J. K., Zhang, J., et al. (2018). Enhancing Catalytic Activity of MoS2 Basal Plane S-Vacancy by Co Cluster Addition. *ACS Energy Lett.* 3 (11), 2685–2693. doi:10.1021/acsenergylett.8b01567

Qi, K., Cui, X., Gu, L., Yu, S., Fan, X., Luo, M., et al. (2019). Single-atom Cobalt Array Bound to Distorted 1T MoS2 with Ensemble Effect for Hydrogen Evolution Catalysis. *Nat. Commun.* 10 (1), 5231. doi:10.1038/s41467-019-12997-7

Smyth, D. M. (2000). The Effects of Dopants on the Properties of Metal Oxides. *Solid State Ion.* 129 (1), 5–12. doi:10.1016/S0167-2738(99)00312-4

Tian, J., Liu, Q., Asiri, A. M., and Sun, X. (2014). Self-Supported Nanoporous Cobalt Phosphide Nanowire Arrays: An Efficient 3D Hydrogen-Evolving

Cathode over the Wide Range of pH 0-14. *J. Am. Chem. Soc.* 136 (21), 7587–7590. doi:10.1021/ja503372r

Tsai, C., Li, H., Park, S., Park, J., Han, H. S., Nørskov, J. K., et al. (2017). Electrochemical Generation of Sulfur Vacancies in the Basal Plane of MoS2 for Hydrogen Evolution. *Nat. Commun.* 8 (1), 15113. doi:10.1038/ncomms15113

Venkateshwaran, S., and Senthil Kumar, S. M. (2019). Template-Driven Phase Selective Formation of Metallic 1T-MoS2 Nanoflowers for Hydrogen Evolution Reaction. *ACS Sustain. Chem. Eng.* 7 (2), 2008–2017. doi:10.1021/acssuschemeng.8b04335

Wang, D., Li, Q., Han, C., Xing, Z., and Yang, X. (2019a). Single-atom Ruthenium Based Catalyst for Enhanced Hydrogen Evolution. *Appl. Catal. B Environ.* 249, 91–97. doi:10.1016/j.apcatb.2019.02.059

Wang, F., Yu, H., Feng, T., Zhao, D., Piao, J., and Lei, J. (2020a). Surface Roughed and Pt-Rich Bimetallic Electrocatalysts for Hydrogen Evolution Reaction. *Front. Chem.* 8, 9. doi:10.3389/fchem.2020.00422

Wang, H., Tsai, C., Kong, D., Chan, K., Abild-Pedersen, F., Nørskov, J. K., et al. (2015). Transition-metal Doped Edge Sites in Vertically Aligned MoS2 Catalysts for Enhanced Hydrogen Evolution. *Nano Res.* 8 (2), 566–575. doi:10.1007/s12274-014-0677-7

Wang, J., Bo, T., Shao, B., Zhang, Y., Jia, L., Tan, X., et al. (2021a). Effect of S Vacancy in Cu3SnS4 on High Selectivity and Activity of Photocatalytic CO2 Reduction. *Appl. Catal. B Environ.* 297, 120498. doi:10.1016/j.apcatb.2021.120498

Wang, R., Sun, P., Wang, H., and Wang, X. (2017). Pulsed Laser Deposition of Amorphous Molybdenum Disulfide Films for Efficient Hydrogen Evolution Reaction. *Electrochimica Acta* 258, 876–882. doi:10.1016/j.electacta.2017.11.138

Wang, X., Zhang, Y., Si, H., Zhang, Q., Wu, J., Gao, L., et al. (2020b). Single-Atom Vacancy Defect to Trigger High-Efficiency Hydrogen Evolution of MoS2. *J. Am. Chem. Soc.* 142 (9), 4298–4308. doi:10.1021/jacs.9b12113

Wang, Y.-l., Huang, Q., Sun, G.-q., Li, X.-y., Chen, L.-h., Su, B.-l., et al. (2021b). Synergistic Zinc Doping and Defect Engineering toward MoS2 Nanosheet Arrays for Highly Efficient Electrocatalytic Hydrogen Evolution. *Dalton Trans.* 50 (17), 5770–5775. doi:10.1039/D0DT04207B

Wang, Y.-l., Sun, G.-q., Chen, L.-h., Du, Z.-k., Li, X.-y., Ye, C.-f., et al. (2021c). Engineering Dual Defective Graphenes to Synergistically Improve Electrocatalytic Hydrogen Evolution. *Appl. Surf. Sci.* 566, 150712. doi:10.1016/j.apsusc.2021.150712

Wang, Y., Lu, F., Su, K., Zhang, N., Zhang, Y., Wang, M., et al. (2020c). Engineering Mo-O-C Interface in MoS2@rGO via Charge Transfer Boosts Hydrogen Evolution. *Chem. Eng. J.* 399, 126018. doi:10.1016/j.cej.2020.126018

Wang, Y., Qi, K., Yu, S., Jia, G., Cheng, Z., Zheng, L., et al. (2019b). Revealing the Intrinsic Peroxidase-Like Catalytic Mechanism of Heterogeneous Single-Atom Co-MoS2. *Nano-Micro Lett.* 11 (1), 102. doi:10.1007/s40820-019-0324-7

Xie, J., Zhang, H., Li, S., Wang, R., Sun, X., Zhou, M., et al. (2013a). Defect-Rich MoS2Ultrathin Nanosheets with Additional Active Edge Sites for Enhanced Electrocatalytic Hydrogen Evolution. *Adv. Mat.* 25 (40), 5807–5813. doi:10.1002/adma.201302685

Xie, J., Zhang, J., Li, S., Grote, F., Zhang, X., Zhang, H., et al. (2013b). Controllable Disorder Engineering in Oxygen-Incorporated MoS2 Ultrathin Nanosheets for Efficient Hydrogen Evolution. *J. Am. Chem. Soc.* 135 (47), 17881–17888. doi:10.1021/ja408329q

Xu, X., Shi, W., Li, P., Ye, S., Ye, C., Ye, H., et al. (2017). Facile Fabrication of Three-Dimensional Graphene and Metal-Organic Framework Composites and Their Derivatives for Flexible All-Solid-State Supercapacitors. *Chem. Mat.* 29 (14), 6058–6065. doi:10.1021/acs.chemmater.7b01947

Xu, Y., Wang, L., Liu, X., Zhang, S., Liu, C., Yan, D., et al. (2016). Monolayer MoS2with S Vacancies from Interlayer Spacing Expanded Counterparts for Highly Efficient Electrochemical Hydrogen Production. *J. Mat. Chem. A* 4 (42), 16524–16530. doi:10.1039/C6TA06534A

Yan, Y., Huang, J., Wang, X., Gao, T., Zhang, Y., Yao, T., et al. (2018). Ruthenium Incorporated Cobalt Phosphide Nanocubes Derived from a Prussian Blue Analog for Enhanced Hydrogen Evolution. *Front. Chem.* 6, 8. doi:10.3389/fchem.2018.00521

Yao, N., Li, P., Zhou, Z., Meng, R., Cheng, G., and Luo, W. (2019). Nitrogen Engineering on 3D Dandelion-Flower-Like CoS 2 for High-Performance Overall Water Splitting. *Small* 15 (31), 1901993. doi:10.1002/smll.201901993

Yin, H., Zhao, S., Zhao, K., Muqsit, A., Tang, H., Chang, L., et al. (2015). Ultrathin Platinum Nanowires Grown on Single-Layered Nickel Hydroxide with High Hydrogen Evolution Activity. *Nat. Commun.* 6 (1), 6430. doi:10.1038/ncomms7430

Yu, H., Yu, X., Chen, Y., Zhang, S., Gao, P., and Li, C. (2015). A Strategy to Synergistically Increase the Number of Active Edge Sites and the Conductivity of MoS2 Nanosheets for Hydrogen Evolution. *Nanoscale* 7 (19), 8731–8738. doi:10.1039/C5NR00670H

Yuan, L., Zhang, Y., Chen, J., Li, Y., Ren, X., Zhang, P., et al. (2022). MoS2 Nanosheets Vertically Grown on CoSe2 Hollow Nanotube Arrays as an Efficient Catalyst for the Hydrogen Evolution Reaction. *Nanoscale* 14 (6), 2490–2501. doi:10.1039/D1NR05941F

Zhang, J., Xu, X., Yang, L., Cheng, D., and Cao, D. (2019a). Single-Atom Ru Doping Induced Phase Transition of MoS 2 and S Vacancy for Hydrogen Evolution Reaction. *Small Methods* 3 (12), 1900653. doi:10.1002/smtd.201900653

Zhang, X., Zhou, F., Zhang, S., Liang, Y., and Wang, R. (2019b). Engineering MoS 2 Basal Planes for Hydrogen Evolution via Synergistic Ruthenium Doping and Nanocarbon Hybridization. *Adv. Sci.* 6 (10), 1900090. doi:10.1002/advs.201900090

Zhao, G., Lin, Y., Rui, K., Zhou, Q., Chen, Y., Dou, S. X., et al. (2018). Epitaxial Growth of Ni(OH)2 Nanoclusters on MoS2 Nanosheets for Enhanced Alkaline Hydrogen Evolution Reaction. *Nanoscale* 10 (40), 19074–19081. doi:10.1039/C8NR07045H

Zhou, G., Wu, X., Zhao, M., Pang, H., Xu, L., Yang, J., et al. (2021a). Interfacial Engineering-Triggered Bifunctionality of CoS 2/MoS 2 Nanocubes/Nanosheet Arrays for High-Efficiency Overall Water Splitting. *ChemSusChem* 14 (2), 699–708. doi:10.1002/cssc.202002338

Zhou, W., Dong, L., Tan, L., and Tang, Q. (2021b). First-principles Study of Sulfur Vacancy Concentration Effect on the Electronic Structures and Hydrogen Evolution Reaction of MoS2. *Nanotechnology* 32 (14), 145718. doi:10.1088/1361-6528/abd49f

Zhu, Y., Song, L., Song, N., Li, M., Wang, C., and Lu, X. (2019). Bifunctional and Efficient CoS2-C@MoS2 Core-Shell Nanofiber Electrocatalyst for Water Splitting. *ACS Sustain. Chem. Eng.* 7 (3), 2899–2905. doi:10.1021/acssuschemeng.8b05462

Conflict of Interest: The authors declare that the research was conducted in the absence of any commercial or financial relationships that could be construed as a potential conflict of interest.

Publisher's Note: All claims expressed in this article are solely those of the authors and do not necessarily represent those of their affiliated organizations, or those of the publisher, the editors, and the reviewers. Any product that may be evaluated in this article, or claim that may be made by its manufacturer, is not guaranteed or endorsed by the publisher.

frontiers | Frontiers in Chemistry

TYPE Perspective
PUBLISHED 14 July 2022
DOI 10.3389/fchem.2022.959525

OPEN ACCESS

EDITED BY
Yuefeng Liu,
Dalian Institute of Chemical Physics (CAS), China

REVIEWED BY
Sen Lin,
Fuzhou University, China

*CORRESPONDENCE
Haifeng Xiong,
haifengxiong@xmu.edu.cn

SPECIALTY SECTION
This article was submitted to Catalytic Reactions and Chemistry, a section of the journal Frontiers in Chemistry

RECEIVED 01 June 2022
ACCEPTED 27 June 2022
PUBLISHED 14 July 2022

CITATION
Liu S, Li J and Xiong H (2022), Thermally-stable single-atom catalysts and beyond: A perspective. *Front. Chem.* 10:959525. doi: 10.3389/fchem.2022.959525

Thermally-stable single-atom catalysts and beyond: A perspective

Sixu Liu[1,2], Jiwei Li[1,2] and Haifeng Xiong[1,2]*

[1]State Key Laboratory of Physical Chemistry of Solid Surfaces, College of Chemistry and Chemical Engineering, Xiamen University, Xiamen, China, [2]Innovation Laboratory for Sciences and Technologies of Energy Materials of Fujian Province (IKKEM), Xiamen, China

Single-atom catalysis is a research Frontier and has attracted extensive interests in catalysis. Significant progresses have been carried out in the synthesis and characterization of metal single-atom catalysts (SACs). However, the stability and catalytic reactivity of metal SAC at elevated temperatures are not well documented because single atoms sinter at elevated temperatures. Therefore, the development of stable and reactive SAC at high temperatures remains a formidable challenge. In this perspective, we summarize recent efforts on the preparation of the thermally-stable SACs synthesized at elevated temperature *via* the reverse-Ostwald ripening mechanism, including the approaches of atom trapping and vapor-phase self-assembly. The reducibility of lattice oxygen, the loading upper limit and the location of the metal single atom are discussed, combining experiments with simulations. In addition, we demonstrate that the coordination structure of the metal single atom can be tailored to address the relationship of structure and performances of the metal SAC in reactions. We expect that this perspective can provide some insights to guide the study for the rational design of thermally-stable and active single atom catalysts, which are especially suitable for high-temperature reactions.

KEYWORDS

single-atom catalysts, thermally stable, atom trapping, metal-support interaction, vapor-phase self-assembly

Introduction

Catalysis has been in the era of the precise design and manipulation of catalyst structure in the atomic scale for developing highly efficient catalysts (Guan et al., 2021). Single-atom catalysis has attracted extensive attention since it was proposed by Zhang et al., in 2011 (Qiao et al., 2011) in that it can bridge the gap between homogeneous catalysis and heterogeneous catalysis. Because of the high atom efficiency, single-atom catalysts (SACs) have therefore attracted ever-increasing attention from numerous fields including material science, catalysis and electrochemistry. To date, much progress has been achieved on the studies of metal SACs in catalysis, especially on the synthesis and characterization of metal SACs (Li et al., 2018; Ji et al., 2020). Furthermore, metal SACs have been found to present superior reactivity (selectivity or activity) than nanoparticles in several catalytic reactions, such as hydrogenation (Yan et al., 2015) and oxidation

(Zhang et al., 2022a). However, most of these reactions were carried out at relatively low reaction temperatures (<100°C) and catalytic reactions performed at temperatures of >200°C, such as dehydrogenation and reforming, are rarely reported since metal SACs are thermodynamically unstable and are prone to agglomerate at elevated temperatures due to Ostwald ripening (OR).

Metal SACs must keep stable during chemical reactions under industrial conditions, including at elevated temperatures (Xiong et al., 2021a). Especially, in the transition from the academic curiosity to an industrially relevant technology, the thermal stability of metal SAC became much more important (Datye and Guo, 2021). Previous work has indicated that metal SACs prepared by atom trapping (AT) can withstand the temperature up to 800°C in oxidizing conditions (Jones et al., 2016; Lang et al., 2019). However, many metal SACs are not stable under reaction atmospheres or at elevated temperatures. These SACs have been demonstrated to agglomerate to form nanoclusters due to the high free energy of SACs under reaction conditions (Yang et al., 2013). For example, atomically dispersed metal atoms can rapidly agglomerate to metal clusters or nanoparticles under catalytic reactions (CO oxidation, hydrogenation and dehydrogenation) (Liu et al., 2019). Moreover, the size of Pt particles formed from single atoms on a Pt/Al_2O_3 increases with the reaction temperature from 150 to 325°C, indicating that Pt species undergo dynamic structural transformation during reaction (Liu et al., 2019). Therefore, the development of metal SACs that are stable under reaction conditions is pivotal, which is prerequisite for future commercialization of these catalysts (Datye and Guo, 2021).

In this perspective, we discuss the progress on the preparation and activation of thermally-stable single-atom catalysts (TSSAC) in catalysis. We firstly introduce atom trapping (AT) and vapor-phase self-assembly (VPSA) to prepare thermally stable single atom catalysts, including on the supports of ceria (CeO_2) and $MgAl_2O_4$. The ceria represents the supports with strong metal-support interaction, while the $MgAl_2O_4$ represents the supports with weak metal-support interaction. We also describe two approaches to tailor the coordination structure of the Pt single atoms on the thermally-stable Pt_1/CeO_2 catalyst. Finally, the atom-trapped Pt_1/CeO_2 SAC can be used to load a second metal atoms to generate two-dimensional metal oxides which shows superior catalytic reactivity than three-dimensional metal oxides. For the general and comprehensive understanding of SAC or TSSAC, such as support choices or carbon-supported SAC, the readers are referred to other important review articles (Liu et al., 2019; Xiong et al., 2021a; Singh et al., 2021).

Atom trapping for the preparation of TSSAC

Metal atoms in nanoparticles are mobile at high temperatures, leading to the sintering of the nanoparticles *via* the Ostwald Ripening mechanism. The mobile atom can be trapped by oxide supports such as PdO (Xiong et al., 2016), CeO_2 (Jones et al., 2016; Wan et al., 2018) and Fe_2O_3 (Lang et al., 2019) or carbon materials (Wei et al., 2018) to form single-atom catalysts (Figures 1A,B). The trapping of the mobile metal atom by CeO_2 and Fe_2O_3 is due to the strong metal atom-support interaction. In 2016, we first reported the evaporated migration of Pt species from Pt nanoparticles on alumina to ceria surface *via* a reverse Ostwald ripening mechanism (Jones et al., 2016). The Pt species was then trapped by the ceria and located on the ceria surface to form Pt_1/CeO_2 SAC. Further study found that the $Pt1/CeO_2$ SAC can be formed by directly dispersing Pt salt precursors onto the ceria, followed by annealing the material at elevated temperatures in air. The locations and the maximum loading of the Pt single atom on the polyhedral ceria was further investigated (Kunwar et al., 2019). It is demonstrated that cerium oxide supported Pt single atoms at high metal loading up to 3 wt.% Pt. This Pt loading corresponds to the maximum density of Pt single atom on the ceria surface is ca. 1 Pt atom/nm^2.

The catalytic reactivity of the Pt_1/CeO_2 SAC prepared by the high temperature vapor phase synthesis (atom trapping, AT) was compared with Pt_1/CeO_2 SAC prepared by conventional wetness synthesis (strong electrostatic adsorption-SEA) with calcination at 350°C in air in CO oxidation (Pereira-Hernández et al., 2019). The AT sample led to ionic Pt being trapped on the CeO_2 in a thermally stable form. The as-synthesized, both SACs are inactive for low- temperature (<150°C) CO oxidation. After treatment in CO at 275°C, both catalysts show enhanced reactivity. Despite similar Pt metal particle size, the AT catalyst is significantly more active, with onset of CO oxidation near room temperature. A combination of near-ambient pressure X-ray photoelectron spectroscopy (NAP-XPS) and CO temperature-programmed reduction (CO-TPR) showed that the high reactivity at low temperatures was related to the improved reducibility of lattice oxygen on the CeO_2 support.

Vapor-phase self-assembly for the preparation of TSSAC

For the oxide supports with a weak metal-support interaction such as Al_2O_3 and $MgAl_2O_4$, experiment results showed that these oxide supports could not directly trap the mobile metal atom to form single-atom catalyst at high temperatures. Instead, the mobile metal atoms agglomerated to form large particles due to sintering at elevated temperatures (Xiong et al., 2016). Recently, an approach termed as "vapor-phase self-assembly" was reported to trap the mobile metal single atoms on the support having a weak metal-support interaction (Li et al., 2022). The new design principle, efficiently anchored Pt single atoms on a conventional support $MgAl_2O_4$ with the assistant of K ions at elevated temperature in air. A stable triangular

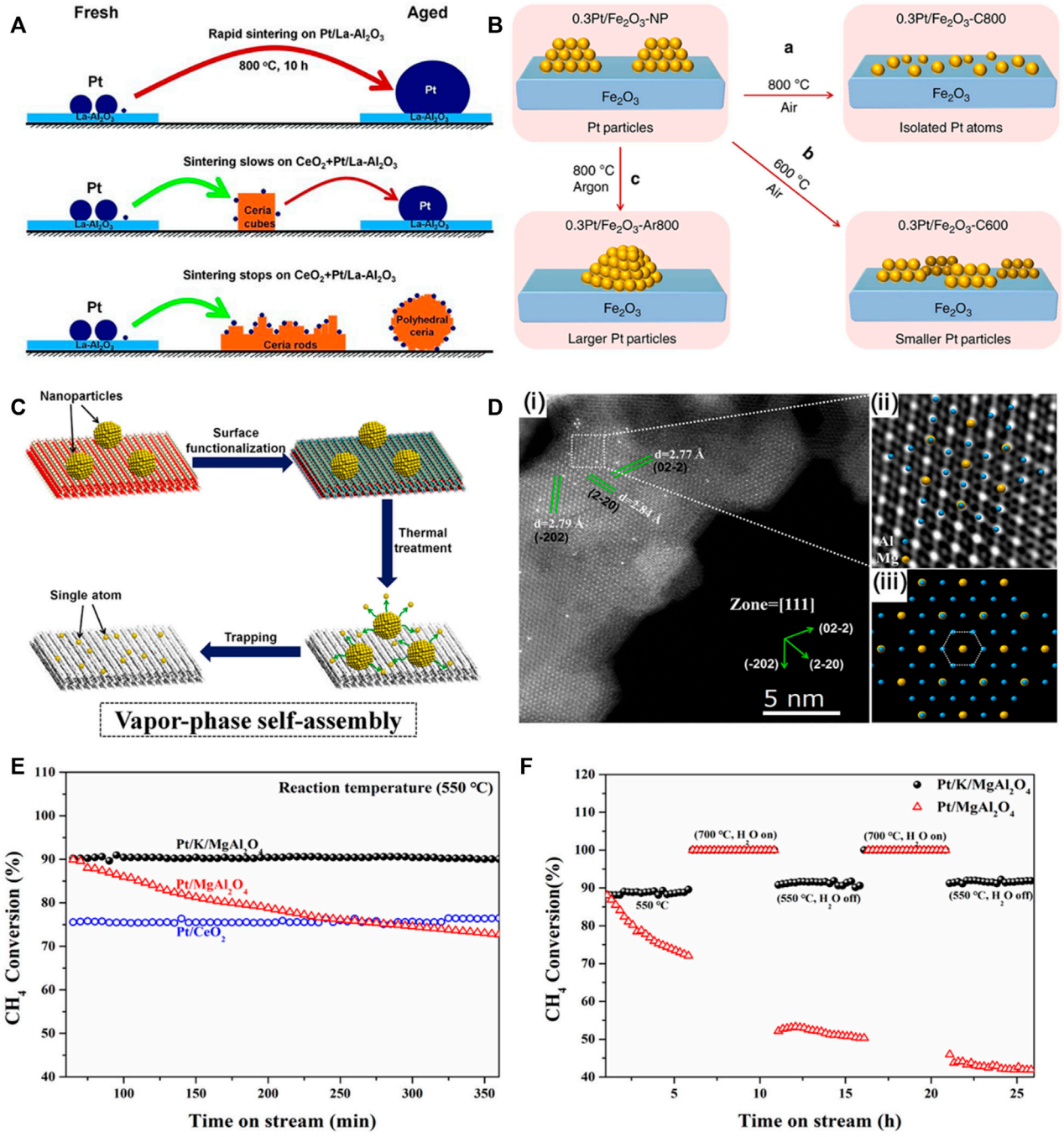

FIGURE 1
Atom trapping for the preparation of thermally-stable Pt single atom catalysts. **(A)** Illustration of Pt nanoparticle sintering and redispersion. Reproduced with permission (Jones et al., 2016). Copyright 2016, American Association for the Advancement of Science. **(B)** Illustration of the redispersion of Pt nanoparticle to Pt single atoms on Fe_2O_3. Reproduced with permission (Lang et al., 2019). Copyright 2019, Springer Nature. **(C)** Schematic illustration of the vapor-phase self-assembly processes. **(D)** AC-STEM image of Pt/K/$MgAl_2O_4$ SAC. **(E)** Catalytic reactivity and stability of Pt catalysts. **(F)** Reactivity and stability of Pt/K/$MgAl_2O_4$ SAC and Pt/$MgAl_2O_4$ nanocatalyst in methane oxidation. Reproduced with permission (Li et al., 2022). Elsevier.

K_3O_3 structure serves as sites for trapping isolated Pt species over $MgAl_2O_4$ (111), leading to a superior stability in methane oxidation. Such Pt single atoms trapped by the triangle motif are capable of withstanding exposure to high temperatures in oxidizing conditions. The Pt/K/$MgAl_2O_4$ SAC presented excellent thermal/hydrothermal stability and reactivity in

methane oxidation in the presence of steam at elevated temperatures (Figures 1C–F), as compared to the Pt/$MgAl_2O_4$ nanocatalyst without K and the Pt_1/CeO_2 SAC.

The generalizability of the vapor-phase self-assembly mechanism on stabilizing metal single atoms was investigated on other alkali metal cations, metal centers and oxide supports. Alkali metal cations of Li^+, Na^+ and Cs^+, metal centers (Ru, Ir and Au) and oxide supports (SiO_2, $NiAl_2O_4$, $CoAl_2O_4$ and $MgCr_2O_4$) as well as density functional theory (DFT) simulations were used to explain the different effects of these structural parameters on stabilizing the metal single atoms during the VPSA process. Results show that alkali Na^+ and Cs^+ can stabilize the Pt single atoms on $MgAl_2O_4$ after the VPSA, whereas Li^+ cannot trap Pt single atoms. DFT simulations revealed that for the Na^+, K^+ and Cs^+, the atoms in the M-O motifs (M = Na, K and Cs) are in the same plane, while the atoms of Li-O motif in the *Z* direction are not in the same plane, leading to a weak interaction between Li and O on $MgAl_2O_4$ (111). As for other metal single atoms (Ru, Ir and Au), the K-modified $MgAl_2O_4$ can stabilize Ru and Ir atoms with VPSA, while it cannot stabilize Au atom. DFT calculations showed that after depositing M_1, a stable triangle M_1O_3 structure is formed for Ru and Ir, similar to the case of Pt_1 single atom. For oxide supports, γ-Al_2O_3 cannot trap Pt single atoms *via* VPSA because of the irregular surface revealed by DFT simulation, which cannot stabilize KO motif. The K/$NiAl_2O_4$ and K/$CoAl_2O_4$ cannot trap the Pt single atoms, whereas K/$MgCr_2O_4$ can partially trap the mobile Pt atoms at elevated temperatures. DFT simulations confirm the above observations.

Modulation of the coordination structure of TSSAC

Pt_1/CeO_2 SAC prepared by AT is thermally stable, while it is not as active as Pt/CeO_2 nanocatalyst in CO oxidation (Gänzler et al., 2017; Pereira-Hernández et al., 2019). This is because the Pt single atom on the AT sample was strongly bound on the ceria. To improve the reactivity of the Pt_1/CeO_2 SAC, the coordination environment of the Pt single atom must be tailored. Two strategies were reported to modulate the coordination structure of the Pt single atom in the Pt_1/CeO_2 SAC. One is the addition of a second metal atom into the Pt_1/CeO_2 SAC (Xiong et al., 2017), such as Sn or Ga. The reactivity and stability of Pt single-atom species was investigated in the industrially important light alkane dehydrogenation reaction. The Pt_1/CeO_2 single-atom catalyst is active during propane dehydrogenation, but not selective for yielding propylene. DFT calculations show strong adsorption of the olefin produced, leading to C-C cleavage to produce CH_4. In contrast, the addition of tin (Sn) into Pt_1/CeO_2 SAC allows the modified SAC to achieve high selectivity towards propylene because of facile desorption of the product. Furthermore, upon oxidation the Pt-Sn species readily revert to the atomically dispersed species on CeO_2, making Pt-Sn/CeO_2 a fully regenerable catalyst. Ga was also used to modify the coordination structure of the Pt_1/CeO_2 SAC in CO oxidation (Feng et al., 2018). Significantly, the stability of Pt single atoms anchored on the Ga site was enhanced compared with those on the bare ceria surface.

The other approach used to modify the coordination structure of Pt_1/CeO_2 SAC is to treat the Pt_1/CeO_2 SAC in a high-temperature steam (750°C) (Nie et al., 2017). The results demonstrated that the Pt_1/CeO_2 was activated *via* steam treatment (at 750°C) to simultaneously achieve the low-temperature CO oxidation activity while keeping Pt atomically dispersed after the high-temperature steam treatment. The treated Pt_1/CeO_2 SAC reached 100% CO conversion at 150°C, as compared to the inactive Pt_1/CeO_2 SAC at the same temperature in CO oxidation. A new type of active site is created on CeO_2 in the vicinity of Pt^{2+}, where Pt cation is coordinated with $O_{lattic}H$ to provide the improved reactivity in the oxidations of CO, NO and propane. These active sites are stable up to 800°C in oxidizing environments.

Engineering catalyst support *via* TSSAC

Metal single atoms in SAC can be used to engineer the properties of the support surface. Relying on the trapping of Pt single atoms on the CeO_2 surface in thermally stable form, the nature of the deposited metal/metal oxide clusters can be modified (Xiong et al., 2021b). In particular, two-dimensional (2D) rafts of PtO_x on the engineered catalyst support are formed by this approach (Figures 2A–C), as opposed to three-dimensional (3D) metal oxide nanoparticles on conventional supports. This 2D rafts of PtO_x showed much higher reactivity than a Pt_1/CeO_2 SAC and the 3D Pt/CeO_2 catalyst in CO oxidation (Xiong et al., 2021b). Adopting this approach for the synthesis of bimetallic catalysts *via* addition of Pd to the atom-trapped catalyst support (Pt@CeO_2), the resulting Pd/Pt@CeO_2 catalyst (Figures 2D–F) provides three times higher reaction rate and improved water tolerance than an impregnated PtPd/CeO_2 catalyst during methane oxidation. The improved performance is attributed to the 2D morphology of the PdO_x phase presented on the atom-trapped Pt@CeO_2 support. The results showed that modifying the support by trapping single atoms provided an important addition to the toolkit of catalyst designers to engineer catalyst supports for controlling the nucleation and growth of metal and metal oxide clusters in heterogeneous catalysts.

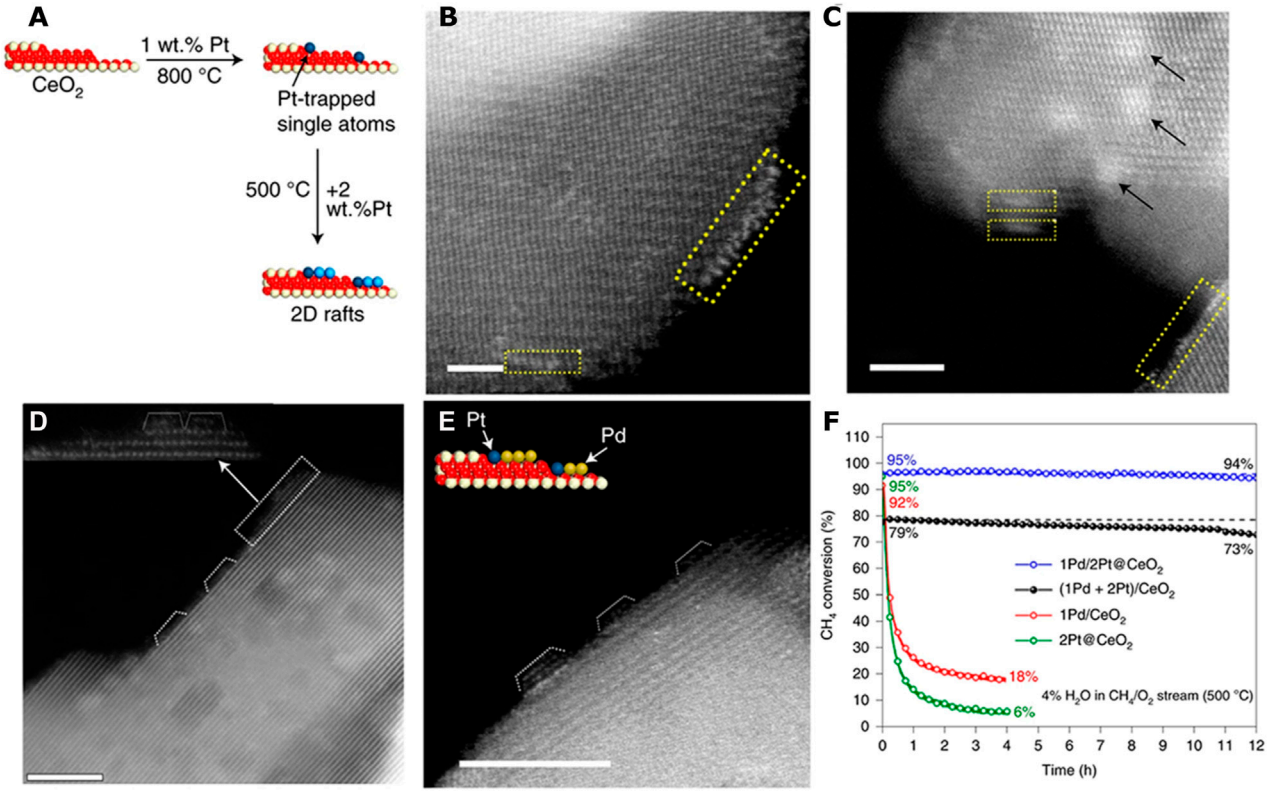

FIGURE 2
Engineering catalyst support *via* thermally-stable single-atom catalyst. **(A)** Schematic illustration showing the morphologies of Pt catalysts supported on ceria prepared by depositing Pt on a Pt-trapped ceria (Pt@CeO_2) **(B,C)** AC-STEM images of the catalyst prepared by depositing 2 wt.% Pt on atom-trapped 1 wt.% Pt@CeO_2. **(D,E)** AC-STEM image of Pd deposited on the catalyst shown in **(E)**. **(F)** Comparison of catalyst stability for the as-synthesized 1Pd/2Pt@CeO_2 and (1Pd + 2Pt)/CeO_2 catalysts, reduced 2Pt@CeO_2 and reduced 1Pd/CeO_2 catalysts in CH_4 oxidation at 500°C in 4% H_2O. Reproduced with permission (Xiong et al., 2021b). Copyright 2021, Springer Nature.

Summary and perspective

To summarize, single-atom catalysts (SACs) are promising because of their maximum atom efficiency and unique property in catalysis. However, recent studies demonstrate that metal SACs tend to sinter to form clusters under reaction conditions, especially at elevated temperatures. Considering many catalytic reactions such as dehydrogenation, syngas chemistry and reforming, are carried out at temperatures of >200°C, it is therefore important to develop approaches to prepare thermally stable and active SACs for their future commercialization. In this perspective, the preparation and catalytic application of thermally-stable metal SACs are summarized, mainly on Pt-based SACs. *Via* the reverse-Ostwald ripening mechanism, approaches including atom trapping and vapor-phase self-assembly were applied to prepare stable and active Pt SACs. The locations of the Pt single atoms on the supports (CeO_2 and $MgAl_2O_4$) were also corroborated using both experiments and simulations, and the properties of the Pt SACs were well demonstrated by advanced techniques such as XAS, LEIS, AC-STEM and CO-DRIFTS. In addition, the coordination environment of the metal SACs was tailored by different approaches such as adding the second metal or treating SAC in high-temperature steam. We also discuss the engineering of the catalyst support by atom-trapped single atoms, which modified the morphology of the deposited metal/metal oxide to achieve unique catalytic performances in catalysis.

Metal SAC used in practical catalytic reactions must be thermally stable under realistic conditions and therefore this area will unambiguously attract continuing attention in future. Focusing on thermally stable and active metal SACs, we would like to provide our insights on the future studies in this field. Firstly, metal SAC that is stable under oxidizing conditions may be not stable under reducing conditions, especially at elevated temperatures. Future work needs to perform to improve the catalyst stability under reducing conditions at elevated temperatures. Secondly, not all stable metal SACs are active or selective in catalysis. Therefore, the coordination structure of the metal single atom needs to be tailored to improve the activity/

selectivity. Although there are a couple of strategies reported to adjust the coordination structure of metal center, a general approach applicable to other metal SACs is lacking. Thirdly, photocatalysis and electrocatalysis have attracted the ever-increasing interests in catalysis because these energies are renewable, and the use of these energies have the potent to go net zero. Since noble metal catalysts are widely used in these processes (Zhang et al., 2022b), photo-/electro- stability of metal single-atom catalysts suitable for both photocatalysis and electrocatalysis is therefore worthy investigating. Finally, current studies on metal SACs are mostly tested in several model reactions, including CO oxidation, semi-alkyne hydrogenation and the preferential oxidation of CO (PROX). The temperatures in these reactions are relatively low. Therefore, the stability of metal SACs must be examined in other conventional reactions such as syngas conversion and reforming, where a couple of recent studies have pioneered in this field recently (Akri et al., 2019; Tang et al., 2019).

Data availability statement

The original contributions presented in the study are included in the article/Supplementary material, further inquiries can be directed to the corresponding author.

Author contributions

SL wrote the first draft of the manuscript. JL participated in literature collection and collation. HX supervised the project, revised the manuscript and provided the financial supports. All authors agree to be accountable for the content of the work.

Funding

The work was financially supported by the National High-Level Talent Fund and the National Natural Science Foundation of China (Grant Nos 22072118 and 22121001).

Conflict of interest

The authors declare that the research was conducted in the absence of any commercial or financial relationships that could be construed as a potential conflict of interest.

The reviewer SL declared a past co-authorship with the author HX to the handling editor.

Publisher's note

All claims expressed in this article are solely those of the authors and do not necessarily represent those of their affiliated organizations, or those of the publisher, the editors and the reviewers. Any product that may be evaluated in this article, or claim that may be made by its manufacturer, is not guaranteed or endorsed by the publisher.

Acknowledgments

We also thank financial support from the State Key Laboratory of Physical Chemistry of Solid Surfaces of Xiamen University. Part fund was supported by Science and Technology Projects of Innovation Laboratory for Sciences and Technologies of Energy Materials of Fujian Province (IKKEM) (HRTP-[2022]-3).

References

Akri, M., Zhao, S., Li, X., Zang, K., Lee, A. F., Isaacs, M. A., et al. (2019). Atomically dispersed nickel as coke-resistant active sites for methane dry reforming. *Nat. Commun.* 10, 5181. doi:10.1038/s41467-019-12843-w

Datye, A. K., and Guo, H. (2021). Single atom catalysis poised to transition from an academic curiosity to an industrially relevant technology. *Nat. Commun.* 12, 895. doi:10.1038/s41467-021-21152-0

Feng, Y., Wan, Q., Xiong, H., Zhou, S., Chen, X., Pereira Hernandez, X. I., et al. (2018). Correlating DFT calculations with CO oxidation reactivity on Ga-doped Pt/CeO2 single-atom catalysts. *J. Phys. Chem. C* 122, 22460–22468. doi:10.1021/acs.jpcc.8b05815

Gänzler, A. M., Casapu, M., Vernoux, P., Loridant, S., Cadete Santos Aires, F. J., Epicier, T., et al. (2017). *Angew. Chem. Int. Ed.* 56, 13078–13082.

Guan, Q., Zhu, C., Lin, Y., Vovk, E. I., Zhou, X., Yang, Y., et al. (2021). Bimetallic monolayer catalyst breaks the activity-selectivity trade-off on metal particle size for efficient chemoselective hydrogenations. *Nat. Catal.* 4, 840–849. doi:10.1038/s41929-021-00679-x

Ji, S., Chen, Y., Wang, X., Zhang, Z., Wang, D., and Li, Y. (2020). Chemical synthesis of single atomic site catalysts. *Chem. Rev.* 120 (21), 11900–11955. doi:10.1021/acs.chemrev.9b00818

Jones, J., Xiong, H., Delariva, A. T., Peterson, E. J., Pham, H., Challa, S. R., et al. (2016). Thermally stable single-atom platinum-on-ceria catalysts via atom trapping. *Science* 353, 150–154. doi:10.1126/science.aaf8800

Kunwar, D., Zhou, S., DeLaRiva, A., Peterson, E. J., Xiong, H., Pereira-Hernández, X. I., et al. (2019). Stabilizing high metal loadings of thermally stable platinum single atoms on an industrial catalyst support. *ACS Catal.* 9, 3978–3990. doi:10.1021/acscatal.8b04885

Lang, R., Xi, W., Liu, J.-C., Cui, Y.-T., Li, T., Lee, A. F., et al. (2019). Non defect-stabilized thermally stable single-atom catalyst. *Nat. Commun.* 10, 234. doi:10.1038/s41467-018-08136-3

Li, H., Wan, Q., Du, C., Liu, Q., Qi, J., Ding, X., et al. (2022). Vapor-phase self-assembly for generating thermally stable single-atom catalysts. *Chem* 8, 731–748. doi:10.1016/j.chempr.2021.11.002

Li, Z., Wang, D., Wu, Y., and Li, Y. (2018). Recent advances in the precise control of isolated single-site catalysts by chemical methods. *Natl. Sci. Rev.* 5, 673–689. doi:10.1093/nsr/nwy056

Liu, L., Meira, D. M., Arenal, R., Concepcion, P., Puga, A. V., and Corma, A. (2019). Determination of the evolution of heterogeneous single metal atoms and nanoclusters under reaction conditions: Which are the working catalytic sites? *ACS Catal.* 9, 10626–10639. doi:10.1021/acscatal.9b04214

Nie, L., Mei, D., Xiong, H., Peng, B., Ren, Z., Hernandez, X. I. P., et al. (2017). Activation of surface lattice oxygen in single-atom Pt/CeO 2 for low-temperature CO oxidation. *Science* 358, 1419–1423. doi:10.1126/science.aao2109

Pereira-Hernández, X. I., DeLaRiva, A., Muravev, V., Kunwar, D., Xiong, H., Sudduth, B., et al. (2019). *Nat. Commu.* 10, 1358.

Qiao, B., Wang, A., Yang, X., Allard, L. F., Jiang, Z., Cui, Y., et al. (2011). Single-atom catalysis of CO oxidation using Pt1/FeOx. *Nat. Chem.* 3, 634–641. doi:10.1038/nchem.1095

Singh, B., Gawande, M. B., Kute, A. D., Varma, R. S., Fornasiero, P., McNeice, P., et al. (2021). Single-atom (Iron-Based) catalysts: Synthesis and applications. *Chem. Rev.* 121, 13620–13697. doi:10.1021/acs.chemrev.1c00158

Tang, Y., Wei, Y., Wang, Z., Zhang, S., Li, Y., Nguyen, L., et al. (2019). Synergy of single-atom Ni1 and Ru1 sites on CeO2 for dry reforming of CH4. *J. Am. Chem. Soc.* 141, 7283–7293. doi:10.1021/jacs.8b10910

Wan, Q., Wei, F., Wang, Y., Wang, F., Zhou, L., Lin, S., et al. (2018). Single atom detachment from Cu clusters, and diffusion and trapping on CeO2(111): Implications in Ostwald ripening and atomic redispersion. *Nanoscale* 10, 17893–17901. doi:10.1039/c8nr06232c

Wei, S., Li, A., Liu, J.-C., Li, Z., Chen, W., Gong, Y., et al. (2018). Direct observation of noble metal nanoparticles transforming to thermally stable single atoms. *Nat. Nanotech* 13, 856–861. doi:10.1038/s41565-018-0197-9

Xiong, H., Datye, A. K., and Wang, Y. (2021a). Thermally stable single-atom heterogeneous catalysts. *Adv. Mat.* 33, 2004319. doi:10.1002/adma.202004319

Xiong, H., Kunwar, D., Jiang, D., García-Vargas, C. E., Li, H., Du, C., et al. (2021b). Engineering catalyst supports to stabilize PdOx two-dimensional rafts for water-tolerant methane oxidation. *Nat. Catal.* 4, 830–839. doi:10.1038/s41929-021-00680-4

Xiong, H., Lin, S., Goetze, J., Pletcher, P., Guo, H., Kovarik, L., et al. (2017). Thermally stable and regenerable platinum-tin clusters for propane dehydrogenation prepared by atom trapping on ceria. *Angew. Chem. Int. Ed.* 56, 8986–8991. doi:10.1002/anie.201701115

Xiong, H., Peterson, E., Qi, G., and Datye, A. K. (2016). Trapping mobile Pt species by PdO in diesel oxidation catalysts: Smaller is better. *Catal. Today* 272, 80–86. doi:10.1016/j.cattod.2016.01.022

Yan, H., Cheng, H., Yi, H., Lin, Y., Yao, T., Wang, C., et al. (2015). Single-atom Pd1/graphene catalyst achieved by atomic layer deposition: Remarkable performance in selective hydrogenation of 1,3-butadiene. *J. Am. Chem. Soc.* 137, 10484–10487. doi:10.1021/jacs.5b06485

Yang, X.-F., Wang, A., Qiao, B., Li, J., Liu, J., and Zhang, T. (2013). Single-atom catalysts: A new frontier in heterogeneous catalysis. *Acc. Chem. Res.* 46, 1740–1748. doi:10.1021/ar300361m

Zhang, L., Xue, L., Lin, B., Zhao, Q., Wan, S., Wang, Y., et al. (2022). Noble metal single-atom catalysts for the catalytic oxidation of volatile organic compounds. *ChemSusChem* 15, e202200357. doi:10.1002/cssc.202200357

Zhang, X., Shi, R., Li, Z., Zhao, J., Huang, H., Zhou, C., et al. (2022). Photothermal-assisted photocatalytic nitrogen oxidation to nitric acid on palladium-decorated titanium oxide. *Adv. Energy Mat.* 12, 2103740. doi:10.1002/aenm.202103740

frontiers | Frontiers in Chemistry

ORIGINAL RESEARCH
published: 14 July 2022
doi: 10.3389/fchem.2022.944552

Synergetic Effect of Mo, Mg-Modified Sn-β Over Moderate-Temperature Conversion of Hexose to Alkyl Lactate

*Yanru Hu, Gengrui Zhang, Lele Liu, ZiXin Chi, Shuai Wang, Jingdong Lin, Haifeng Xiong and Shaolong Wan**

College of Chemistry and Chemical Engineering, Xiamen University, Xiamen, China

The thermocatalytic conversion of hexose into valuable chemicals such as methyl lactate under mild conditions is very appealing. Here, we report that Mo, Mg co-modified Sn-β catalyst can effectively catalyze the transformation of glucose and fructose into alkyl lactate at moderate temperatures. A maximum yield of around 35% of methyl lactate was achieved from the conversion of glucose in methanol at 100°C over Sn-β catalyst modified with 3 wt% Mo and 0.5 wt% Mg. However, up to 82.8% yield of ethyl lactate was obtained in the case of fructose in ethanol upon the same catalytic condition, suggesting a significant solvent effect. The Mo species plays a key role to enable the retro-aldol condensation of fructose, in which the competing side reactions are significantly suppressed with the assistance of neighboring Mg species probably through a synergetic effect of Lewis acid-base.

Keywords: alkaline-earth metal, alkyl lactate, glucose, modified Sn-β, molybdenum, retro-aldol condensation

OPEN ACCESS

Edited by:
Shanhui Zhu,
Institute of Coal Chemistry (CAS), China

Reviewed by:
Lisha Yang,
University of Nevada, Reno, United States
Zheng Shen,
Tongji University, China

****Correspondence:***
Shaolong Wan
swan@xmu.edu.cn

Specialty section:
This article was submitted to Catalytic Reactions and Chemistry, a section of the journal Frontiers in Chemistry

Received: *15 May 2022*
Accepted: *20 June 2022*
Published: *14 July 2022*

Citation:
Hu Y, Zhang G, Liu L, Chi Z, Wang S, Lin J, Xiong H and Wan S (2022) Synergetic Effect of Mo, Mg-Modified Sn-β Over Moderate-Temperature Conversion of Hexose to Alkyl Lactate. Front. Chem. 10:944552. doi: 10.3389/fchem.2022.944552

1 INTRODUCTION

As an abundant, renewable, and nonedible organic carbon resource, lignocellulose biomass is expected to be a promising alternative to fossil resources (Corma et al., 2007; Ong et al., 2019). The carbohydrates, rich in this so-called "second generation" biomass, motivate researchers to devise efficient systems to massively convert them into valuable chemicals, as an appealing way of valorization (Chheda et al., 2007; Hu et al., 2012; Santhanaraj et al., 2014; Gérardy et al., 2020). Among the chemicals, lactic acid/alkyl lactate has been receiving extensive attention, since it can also serve as the feedstock for biodegradable polyester production (Dusselier and Sels, 2014; Mäki-Arvela et al., 2014), other than the applications in food, pharmaceuticals, and cosmetic industries (Datta and Henry, 2006; Eş et al., 2018). As the main approach to current lactic acid production, the fermentation of glucose suffers from some shortcomings, such as low overall productivity, and a complex operation processes (Wasewar et al., 2004; Dong et al., 2016). Alternatively, considerable efforts have been devoted to the development of thermocatalytic processes for lactic acid/alkyl lactate production from carbohydrates over heterogeneous catalysts (Choudhary et al., 2015; Yang et al., 2016; Pang et al., 2017; Wattanapaphawong et al., 2017; Duan et al., 2022).

Amongst the reported heterogeneous catalyst, Sn-containing zeolite is a class of representative solid Lewis acid catalysts (Holm et al., 2010; de Clippel et al., 2012; Holm et al., 2012; Tang et al., 2020). β zeolite with Sn incorporation into the framework as strong Lewis acid sites has been demonstrated to possess good catalytic performance in glucose isomerization to fructose and retro-aldol condensation of C6 carbohydrates at high reaction temperatures (Holm et al., 2010). These two reactions are the key steps involved in the transformation of glucose into alkyl lactate. It is the isolated Sn species in the framework with unsaturated tetracoordinated coordination that exhibit excellent Lewis acidity responsible for the conversion (Li et al., 2011). In addition, our previous work found that the ion exchange with alkaline earth cations (Ca^{2+}, Mg^{2+}) appears to improve the retro-

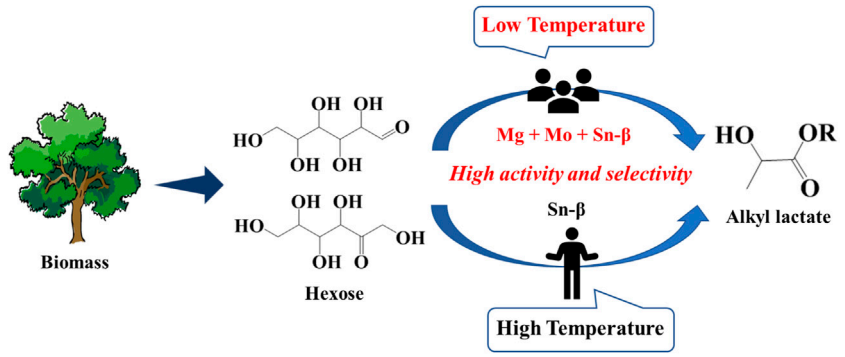

GRAPHICAL ABSTRACT |

aldol condensation capacity of Sn-β. It was speculated that the Ca^{2+} or Mg^{2+} neutralized the Brønsted acid sites, thereby mitigating the formation of byproducts. In the meantime, the Ca^{2+} or Mg^{2+} can stabilize the deprotonated alkoxide formed after the proton of the -OH group attached to the C3 of fructose is abstracted by the basic O^{2-} site of Si-O-M (Ca^{2+} or Mg^{2+}) (Hu et al., 2020).

Notably, the aforementioned conversions proceeded at high temperatures (>160°C), as the retro-aldol condensation of glucose is insufficient over Sn-β catalysts at moderate temperature. Higher reaction temperatures have an adverse effect on the catalyst durability and need higher requirements for production equipment. Hence, the development of active catalysts is highly desired, in order to achieve a good yield of lactic acid/alkyl lactate at moderate temperatures. In this respect, the pioneering work conducted by Orazov and Davis, 2015. revealed that the hexoses can be converted to ethyl lactate over a mixed catalyst consisting of MoO_3 and Sn-doping zeolite at around 100°C, achieving a yield of around 70% thanks to the catalytic ability of MoO_3 toward the retro-aldol reactions. Other oxides like WO_3 as the co-catalyst mixed with Sn-β were also screened in fructose conversion to methyl lactate, only resulting in an 18% yield at 120°C after 5 h of reaction time (Yang et al., 2019). **Supplementary Table S1** presents the catalytic activity of Sn-β and Mo-β-Mg in the present work with the reported literature.

Enlightened by the aforementioned research, herein, we report the Mo, Mg-modified Sn-β catalyst for moderate-temperature conversion of hexose to alkyl lactate. The Mo species loaded on Sn-β zeolite enabled the conversion to proceed at 100°C, thanks to its strong activity for retro-aldol reaction. Moreover, the addition of MgO can tune the Brønsted acid sites and facilitate the rate-determining retro-aldol reaction, the synergetic effects of which with Mo and Sn sites enable the side-reactions limited to a very low extent and thus achieve a superior yield of alkyl lactate.

2 MATERIALS AND METHODS

2.1 Materials

Glucose, fructose, mannose, and 5-hydroxymethyl furfural were obtained from Aladdin Reagent Co., Ltd., (Shanghai, China). Tin (II) acetate (99%), methyl lactate (99%), Pyruvic aldehyde dimethyl acetal, magnesium nitrate (99.0%), commercial H-β zeolite (Si/Al = 12.5), HNO_3 (65%–68%) were supplied by Sinopharm Chemical Reagent Co., Ltd. (Shanghai, China). N_2 (99.999%) was purchased from Linde Industrial Gases.

2.2 Catalyst Preparation

2.2.1 Synthesis of Sn-β

The Sn-β zeolite was prepared by a post-treatment method reported by Hammond et al. (Hammond et al., 2012; Hammond et al., 2015). Specifically, the H-β was treated in concentrated HNO_3 (65%–68%, 20 mLg^{-1} zeolite) at 333 K for 20 h to remove Al, followed by filtration, being washed thoroughly and dried at 120°C overnight. The resulting solid was denoted as DeAl-β. The solid-state ion exchange method was employed to incorporate Sn into DeAl-β. An appropriate amount of tin (II) acetate was mixed with DeAl-β powder and the mixture was ground manually, and subsequently calcinated at 550°C (10°C/min) in a N_2 flow for 6 h and airflow for another 3 h. The obtained sample was denoted as Sn-β.

2.2.2 Synthesis of Mo-Modified Sn-β, Mg-Modified Sn-β and Mo, Mg-Modified Sn-β

Both Mo-modified Sn-β and Mo, Mg-modified Sn-β were prepared by the incipient wetness impregnation method. Briefly, 1 g of Sn-β was added with ammonium molybdate solution under vigorous stirring. Then, the mixture was placed for 6 h, followed by drying overnight at 120°C and calcinated at 550°C for 5 h. The resulted solid was referred to Mo modified Sn-β and denoted as Mo-Sn-β. The same procedure mentioned earlier was employed to prepare the Mg-modified Sn-β catalyst, except replacing the ammonium molybdate with magnesium nitrate. With the Mo-Sn-β as the support, the same procedure above was employed to prepare the Mo, Mg-modified Sn-β catalyst, except replacing the ammonium molybdate with magnesium nitrate.

2.2.3 Synthesis of Mo-β and Mg-Modified Mo-β

Both the Mo-β and Mg-modified Mo-β were prepared by the incipient wetness impregnation method. Briefly, 1 g of DeAl-β was added with ammonium molybdate solution under vigorous

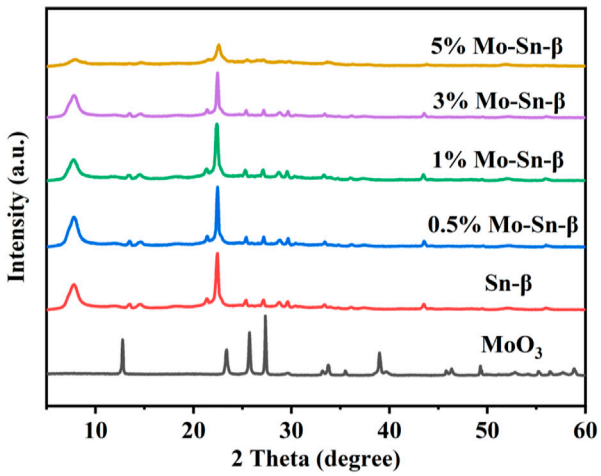

FIGURE 1 | XRD patterns of Mo-modified Sn-β.

stirring. Then, the mixture was placed for 6 h, followed by drying overnight at 120°C and calcinated at 550°C in airflow for 6 h. The resulted solid was referred to as Mo-β and denoted as x% Mo-β. With the Mo-β as the support, the same procedure as before was employed to prepare the Mg-modified Mo-β catalyst, except replacing the ammonium molybdate with magnesium nitrate.

2.3 Catalyst Characterization

X-ray powder diffraction (XRD) patterns were recorded on Rigaku UItima IV X-ray diffractometer with Cu Kα radiation source (40 kV and 30 mA) from 5 o to 60 o and a scan speed of 10°/min. The adsorption-desorption isotherms of N_2 were obtained on a Micromeritics ASAP 2020 M instrument. The surface area was calculated via the Brunauer–Emmett–Teller (BET) equation, and the volume of pores was acquired *via* the single point method. X-ray photoelectron spectra (XPS) were recorded with a Quantum 2,000 Scanning ESCA Microprob instrument (Physical Electronics) using Al Kα radiation. The binding energy was calibrated by using the C1s photoelectron peak at 150 eV as a reference. Quantification of Mo and Mg elements was conducted using a Bruker S8 Tiger X-ray fluorescence (XRF) spectrometer. Fourier transform infrared (FTIR) spectra were collected on a Nicolet 6,700 instrument equipped with an MCT detector at a spectral resolution of 4 cm^{-1}. A self-supporting pellet made of the sample was placed in the flow cell and evacuated under reduced pressure at 623 K for 1 h. After cooling to 373 K, the samples were saturated with pyridine vapor and then evacuated. Subsequently, spectra were recorded at the same temperature in the 4,000–650 cm^{-1} range by using the coaddition of 64 scans.

2.4 Catalytic Evaluation and Product Analysis

The reactions were conducted in a batch-type Teflon-lined stainless steel autoclave reactor with an inner volume of 50 ml. Typically, the glucose and catalyst were added to 20 ml of methanol. Then the autoclave was sealed, purged with N_2, and pressurized with N_2 to 2 MPa. Subsequently, the system was heated up to 373 K. After continuous magnetic stirring (800 rpm) for a given time, the autoclave was cooled to room temperature in cold water, and the liquid was obtained after filtration and analyzed by GC and HPLC. Sample products were first qualitatively analyzed using an Agilent GC-MS equipped with a 1701-ms column. The crude product was dissolved in a silylating agent (bis-(trimethylsilyl) trifluoroacetamide +1% trimethylchlorosilane). This solution was maintained at 65°C for 2 h to ensure the complete silylation which was subsequently injected into the GC-MS. Some peaks in Agilent HPLC were further identified using LC-MS. Quantitative analysis was then performed on an Agilent HPLC system equipped with RI and UV-Vis detectors and a Bio-Rad Aminex HPX-87H ion exclusion column (300 × 7.8 mm), using 0.005 M H_2SO_4 as the mobile phase at a flow rate of 0.6 ml min^{-1}. The column temperature and the detector were both set at 50°C. The number of varied products was determined using calibration curves generated with standard solutions.

TABLE 1 | Physicochemical properties of Mo-modified Sn-β.

Catalyst	S_{BET} (m^2 g^{-1})[a]	V(cm^3 g^{-1})[a]	Mo content (wt%)[b]
0.5% Mo-Sn-β	423	0.41	0.6
1% Mo-Sn-β	411	0.39	0.9
3% Mo-Sn-β	420	0.35	2.8
5% Mo-Sn-β	417	0.29	5.1

[a]S_{BET} = Brunauer-Emmet-Teller surface area, V = pore volume.
[b]Determined by XRF.

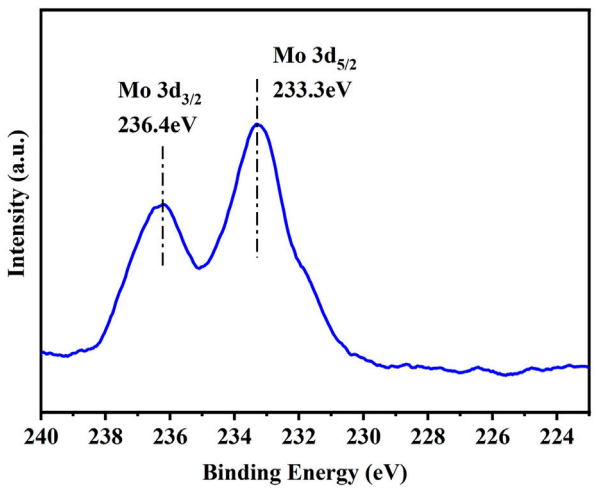

FIGURE 2 | Mo 3 days XPS spectrum of Mo-modified Sn-β catalyst.

3 RESULTS AND DISCUSSION

3.1 Catalyst Characterization

3.1.1 X-ray Powder Diffraction

The XRD diffraction patterns for the prepared Sn-β modified by different contents of Mo are displayed in **Figure 1**. The peaks

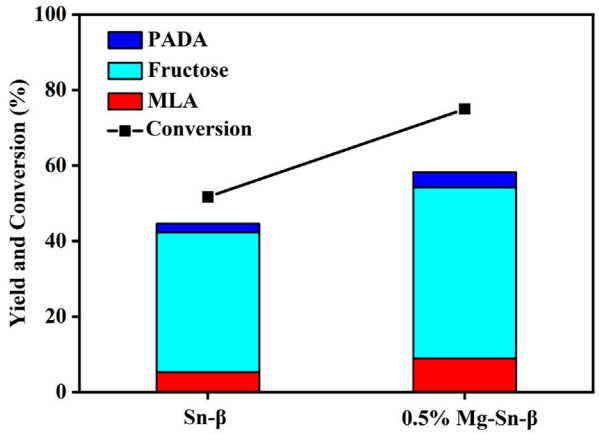

FIGURE 3 | Catalytic performance of Sn-β catalysts and Mg-modified Sn-β catalysts at moderate temperature. Reaction conditions: glucose, 0.055 g; catalyst, 0.4 g; methanol, 20 ml; N_2 2 MPa; 4 h; 100°C.

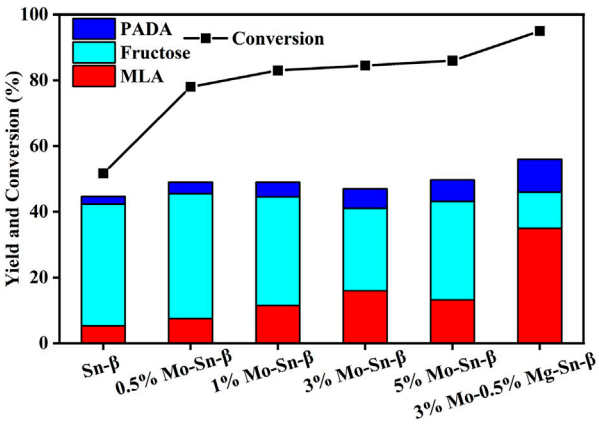

FIGURE 4 | Moderate-temperature catalytic activity of Mo-modified Sn-β catalysts. Reaction conditions: glucose, 0.055 g; catalyst, 0.4 g; methanol, 20 ml; N_2, 2 MPa; 4 h; 100°C.

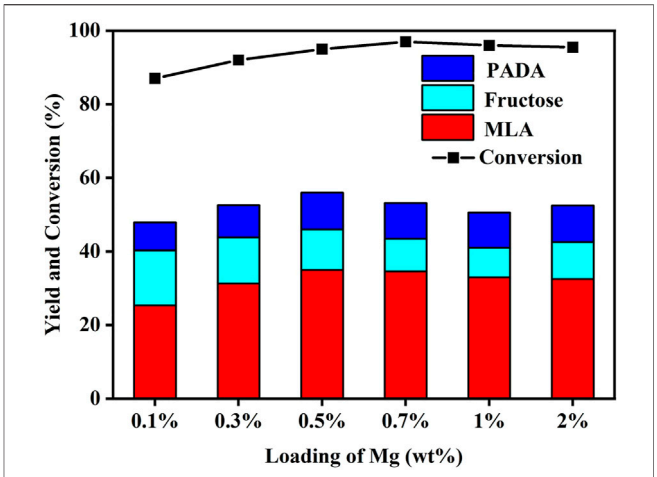

FIGURE 5 | Effect of loading amount of Mg on the moderate-temperature catalytic activity of Mo-modified Sn-β catalysts. Reaction conditions: glucose, 0.055 g; catalyst, 0.4 g; methanol, 20 ml; N_2, 2 MPa; 4 h; 100°C.

appearing at 27° and 34°, corresponding to (021) and (111) of MoO_3 respectively, were observed for 5 wt% loading content of Mo. This is probably caused by the aggregation of excessive Mo on the surface of the catalyst. For the samples in which the loading contents of Mo were below 5 wt%, the peaks attributed to the MoO_3 phase were not observable, indicating the good dispersion of Mo species on the surface.

3.1.2 Brunauer-Emmett-Teller

Brunauer–Emmett–Teller (BET) gas sorptometry measurements were conducted to examine the pore nature of Mo-modified Sn-β catalysts. As listed in **Table 1**, at Mo contents below 5 wt%, the BET surface area of Mo-modified Sn-β catalysts did not vary significantly, with values in the range of 413–425 $m^2 g^{-1}$. In contrast, the pore volume decreased by approximately 25% as the Mo content increased from 0 to 5 wt%, which may result from the blocking of pores by the excessive Mo species.

3.1.3 X-ray Photoelectron Spectra

X-ray photoelectronspectroscopy (XPS) was used to characterize the Mo oxidation state. The Mo 3 days spectrum exhibits two peaks, located at 236.5 and 233.3 eV respectively, which can be assigned to Mo^{6+} species, as shown in **Figure 2**. Previous work has verified that Mo^{6+} species possess better catalytic performance in the retro-aldol reaction of fructose than Mo^{4+} (Orazov and Davis, 2015).

3.2 Catalytic Performances

The initial catalytic tests were performed over Sn-β catalysts and Mg-modified counterparts at moderate temperatures. As present in **Figure 3**, in the absence of Mg modification, fructose was the primary product and accompanied by the production of a small amount of PADA (Pyruvic aldehyde dimethyl acetal), and the yields of methyl lactate were below 10% at 100°C after 4 h over Sn-β catalysts. Comparatively, the Mg-modified Sn-β catalysts promoted the glucose conversion remarkably but still failed to increase the selectivity toward methyl lactate remarkably. The main product was also fructose, implying that the Sn sites alone can catalyze the glucose isomerization to fructose, but exhibited a rather limited catalytic activity for the retro-aldol reaction of fructose at 100°C.

The influence of Mo modification on the catalytic performance of the Sn-β catalyst is shown in **Figure 4**. Without Mo modification, merely a 5% yield of methyl lactate with a glucose conversion of 51.7% was achieved. By contrast, the glucose conversion was increased by above 30% over Sn-β loaded with Mo catalysts, accompanied by promotion in methyl lactate (MLA) yield to a significant extent. The MLA yield first increased and then decreased with the loading content of Mo, reaching a maximum of 16% at 3 wt% of loading content. The 3 wt% Mo

TABLE 2 | Conversion of different substrates catalyzed by modified or unmodified Sn-β catalysts.

Catalyst	Substrate	Conv. (%)	Yield (%)			
			MLA	Fructose	Mannose	PADA
3% Mo-β	Glucose	40	—	7	13	6
Sn-β	Glucose	36	2	25	—	2
3% Mo-Sn-β	Glucose	73	6	30	12	4
			MLA	Glucose	Mannose	PADA
3% Mo-β	Fructose	29	1	—	—	8
Sn-β	Fructose	16	3	2	—	2
3% Mo-Sn-β	Fructose	33	7	1	—	3
			MLA			
3% Mo-β-	DHA	80	2			
Sn-β	DHA	95	65			
3% Mo-Sn-β	DHA	100	47			

Reaction conditions: substrate, 0.055 g; catalyst, 0.4 g; methanol, 20 ml; N_2, 2 MPa; 1 h; 100°C.

enabled the MLA selectivity to increase from 10.3% to 18.9%, revealing that Mo^{6+} species promoted the retro-aldol condensation of fructose to C3 intermediates for the formation of MLA. However, Mo content exceeding 3 wt% resulted in a decrease in both MLA yield and selectivity, which is probably because the excessive Mo species blocked the pores of Sn-β and thus hindered the access of fructose to the Sn sites as reflected in **Table 1**. Surprisingly, 36.8% of selectivity and 35% yield of MLA were achieved over Mg, Mo co-modified Sn-β catalyst, outperforming the sole Mg or Mo modified counterparts. This implied that a synergistic effect exists between Mg and Mo promoters.

Given that the modification of Mg is capable of facilitating the MLA formation, the effect of Mg content on the MLA yield was further investigated. As present in **Figure 5**, with Mo content fixed at 3 wt% and Mg content range of 0.1%–2%, the maximum yield of MLA was attained at 0.5 wt% Mg. The higher content of Mg cannot further contribute to the MLA formation.

The catalytic performances at various reaction temperatures were also studied, and the results are shown in **Supplementary Figure S1.** The MLA yield was increased by elevating the reaction temperature in the range of 100–160°C over all the Sn-β catalysts, regardless of the modification. The highest MLA yield was achieved at 160°C over 3% Mo-0.5% Mg-Sn-β catalyst. This suggests that the kinetic-relevant retro-aldol condensation step is further favored at a higher temperature, against the competing side reactions. However, the structure of zeolite would be undermined after such severe reaction conditions, which limits its practical application (Hu et al., 2020). We did perform the recycling test to evaluate the durability of the catalyst at 100°C. After each run, the spent catalyst was recovered from the reaction mixture, which was subsequently washed with deionized water, dried overnight, and calcinated at 550°C for 5 h in a muffle furnace. Compared to the fresh catalyst, the spent catalyst after four cycles showed a slight loss of activity. This result suggests that the catalyst is relatively stable under moderate temperature conditions (**Supplementary Figure S2**).

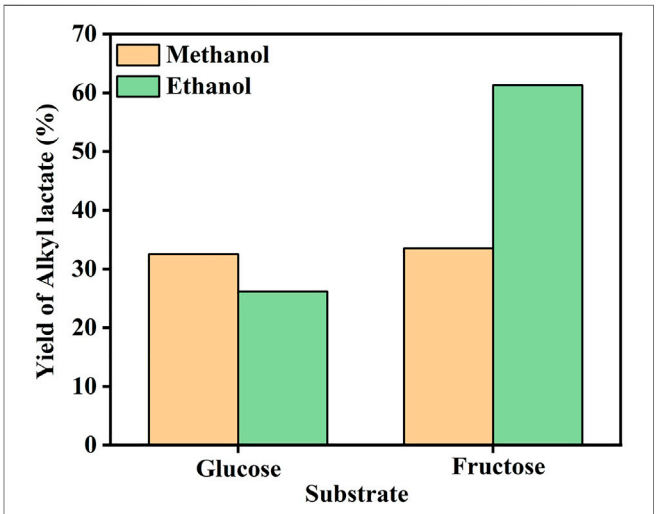

FIGURE 6 | Effect of solvent on the alkyl lactate yield over 3% Mo-0.5% Mg-Sn-β catalyst. Reaction conditions: substrate, 0.15 g; 3% Mo-0.5% Mg-Sn-β, 0.15 g, solvent, 20 ml, 100°C, N_2, 2 MPa, 20 h.

To understand the catalytic function of distinct function sites in-depth, we conducted the conversion of different substrates in the presence of various catalysts within a short reaction time. As depicted in **Table 2**, upon glucose as the substrate, no MLA formed over the 3% Mo-β catalyst, indicating that the Mo species alone is unable to catalyze the glucose conversion to MLA. A 25% yield of fructose, accompanied by a 2% yield of MLA, was obtained over Sn-β suggests that the Sn species is capable of catalyzing the glucose isomerization but less for retro-aldol condensation of fructose. The latter is the kinetic-relevant step in MLA formation. The co-existence of Sn and Mo species enabled an increase in both glucose conversion and MLA yield, indicating that both species are responsible for glucose isomerization. Regarding the fructose substrate, a higher fructose conversion was observed over 3% Mo-Sn-β catalyst, compared to that over Sn-β catalyst. The PADA also formed during the

TABLE 3 | Catalytic performance of a physical mixture of modified β catalysts at moderate temperature.

Entry	Catalyst	Yield of ELA (%)
1	0.5% Mg-β + Sn-β	5
2	0.5% Mg-β + 3% Mo-Sn-β	54
3	Sn-β + 3% Mo-β	52
4	0.5% Mg-Sn-β + 3% Mo-β	60
5	Sn-β + 0.5% Mg-3% Mo-β	70

Reaction conditions: substrate, 0.15 g fructose; catalyst, (0.15 g + 0.15 g); ethanol, 20 ml; N_2, 2 MPa, 100°C; 20 h.

reaction. These results clearly suggest that Mo species can effectively catalyze the retro-aldol condensation. Nevertheless, without the assistance of Sn sites, the MLA can hardly form. This is because the C3 intermediates (1,3-dihydroxyacetone and pyruvaldehyde) generated through the retro-aldol reaction of fructose still need to undergo a 1,2-H shift reaction prior to MLA formation, which has to be catalyzed by the isolated Sn sites featured of strong Lewis acidic property. Unfortunately, the Mo species does not possess the corresponding catalytic capacity, thus the employment of which alone can hardly produce any MLA. This speculation was further confirmed by the results using 1,3-dihydroxyacetone (DHA) as the substrate. A distinct difference exists in MLA yield and selectivity provided by Sn-β catalyst and 3% Mo-β catalyst, respectively. The former catalyst afforded a selectivity of 68.4% toward MLA, while merely 2.5% was obtained over the latter catalyst. The addition of 3% Mo into Sn-β even caused a notable decrease in MLA yield, further confirming the argument made earlier.

It should be noted that the amount of substrate used in the tests above is quite low, which may cause concern over its potential practical application. Hence, we also performed a series of tests with much larger ratios of substrate/catalyst amount. The results in **Supplementary Figure S3** show that comparable MLA yields as earlier were obtained, even with the glucose amount increased to 0.25 g and the catalyst reduced to 0.16 g.

It has been reported that the use of varied solvents, such as methanol and ethanol, can make quite a notable difference over the yield of the desired products (Orazov and Davis, 2015). In our work, the solvents appeared not to affect the formation of alkyl lactate significantly upon glucose as the substrate but did cause a drastic change in the case of fructose, as exhibited in **Figure 6**. The yield of alkyl lactate is only about 25% in methanol solvent, while reached up to 61.3% in ethanol solution. Further experiments of fructose conversion over Sn-β and 3% Mo-β catalyst were conducted, respectively. The results in **Supplementary Figure S5** show that in the presence of Sn species alone, the fructose conversions in methanol and ethanol were quite similar, while Mo species alone provided a much higher conversion of fructose in ethanol than that in methanol. It was then speculated that the Mo sites were more prone to be affected by the solvent, rather than the Sn sites. Mo species exhibited a lower catalytic performance in retro-aldol condensation of fructose in methanol. It may be attributed to the stronger binding of Mo sites with methanol, hindering the absorption and turnover of fructose on Mo sites.

The aforementioned results demonstrate the indispensable role of Mo and Mg over the modified Sn-β catalysts toward the moderate temperature conversion of C6 monosaccharide. Further experiments show that the physical mixture of 0.5% Mg-β and Sn-β only resulted in about 5% ELA, suggesting neither of them can effectively catalyze the retro-aldol condensation at the moderate temperature. Moreover, the combination of 0.5% Mg-β and 3% Mo-Sn-β could achieve an ELA yield of 54%, which is less than that (61.3%) of 0.3% Mo-0.5% Mg-Sn-β. This demonstrated that the MgO species should stay in close proximity to Mo or Sn sites to have a synergy effect and enhance the yield of ELA. A question then arises whether the Mg species have a synergy effect mainly with Mo or Sn sites in the working catalyst. Hence, we prepared Sn-β, 3% Mo-β and their Mg-modified counterparts to shed light on the intrinsic mechanism. Indeed, the physical mixture of Sn-β and 3% Mo-β in ethanol results in a relatively

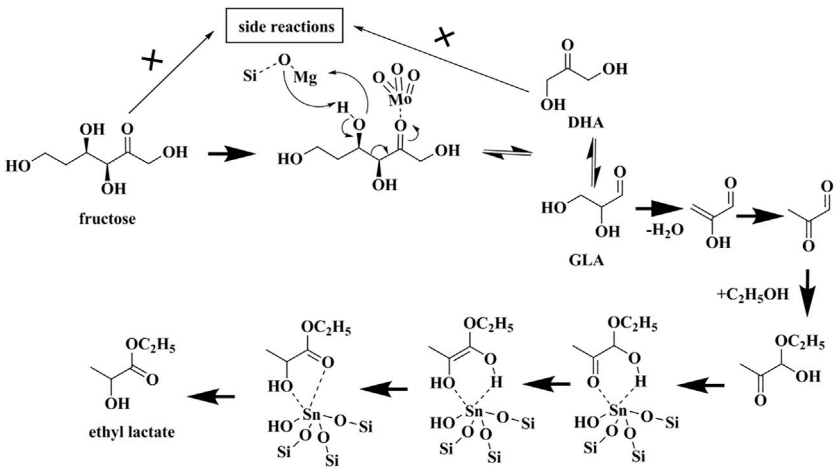

SCHEME 1 | The plausible mechanism of fructose conversion to ethyl lactate over Mo, Mg-co-modified Sn-β catalyst.

lower ELA yield at 52%, thanks to the absence of Mg species. The combination of 0.5% Mg-Sn-β and 3% Mo-β can improve the yield of ELA to 60%, comparable to that of 0.3% Mo-0.5% Mg-Sn-β. Thanks to the lack of catalytic ability for the retro-aldol condensation reaction, the addition of basic MgO in Sn-β could probably tune the Brønsted acid sites near the Sn sites, thus mitigating the side-reactions from fructose and intermediate products such as DHA/GLA during the conversion (Hu et al., 2020). However, the employment of Sn-β and 0.5% Mg-3% Mo-β can achieve the highest yield up to 70%, which can be further improved to nearly 82.8% with the extended reaction time (**Supplementary Figure S4**). This result is superior to most of the prior works reported in the literature, as compared in **Supplementary Table S1**. It appears that MgO species can cooperate more effectively with Mo-site during the rate-determining retro-aldol reaction step, thus significantly mitigating the side reactions. The weakened Brønsted acid sites near the Mo sites should play a role to abate the production of side products, similar to that of Mg-Sn-β. Pyridine-probed FTIR analysis could readily distinguish the Bronsted and Lewis acid sites. As shown in **Supplementary Figure S6**, the strength of Bronsted acid was weakened after adding Mg to the 3% Mo-Sn-β catalyst. Our earlier work shows that MgO species attached to the zeolite framework can have a synergy effect with the Lewis Sn site to directly enhance the retro-aldol condensation at a more severe temperature like 160°C. Through functioning as Lewis acid-base pair, MgO can facilitate the abstract of the proton from the OH groups of fructose and stabilize the deprotonated alkoxide that is subsequently subjected to retro-aldol condensation catalyzed by the strong Lewis Sn sites (Hu et al., 2020). It is speculated that a similar mechanism can take place between MgO and the nearby Mo sites in this work, where fructose can be readily deprotonated and stabilized for the subsequent retro-aldol condensation. Hence, the side reactions were further restricted to a very limited extent, leading to a much higher yield of ELA than the other cases listed in **Table 3**.

Based on the results above, a mechanism is proposed as **Scheme 1** below. The ketonic oxygen of fructose adsorbs onto the Mo sites first, followed by the occurrence of retro-aldol condensation to generate 1,3-dihydroxyacetone (DHA) and glyceraldehyde (GLA). In this process, the framework O atom of Si-O-Mg, as the Lewis base site, assists to abstract the H atom of -OH attached to the C3 of fructose, while Mg^{2+} is the Lewis acidic site can stabilize the deprotonated alkoxide. A keto-enol tautomerization exists between DHA and GLA. The formed GLA undergoes dehydration and addition reaction with ethanol molecule, generating the hemiacetal compound 1. Subsequently, compound 1 is transformed into ethyl lactate *via* 1,2-H shift as catalyzed by Sn sites. The side reactions are significantly suppressed during the whole process, thanks to the addition of MgO species.

4 CONCLUSION

The Mo, Mg co-modified Sn-β catalysts are capable of effectively catalyzing the hexose conversion to alkyl lactate at moderate temperature. Especially, an 82.8% yield of ethyl lactate can be achieved from fructose with a combination of 0.5% Mg-3% Mo-β and Sn-β at 100°C. The framework Sn sites are mainly responsible for the isomerization of glucose and 1,2-H shift of formed trioses, while the Mo species mainly account for the C3-C4 bond cleavage of fructose to generate 1,3-dihydroxyacetone and glyceraldehyde (trioses) via retro-aldol condensation. The presence of MgO in close proximity to Mo sites can tune the nearby Brønsted acid sites and facilitate the retro-aldol condensation, thus limiting the side reactions and greatly enhancing the ELA yield.

DATA AVAILABILITY STATEMENT

The raw data supporting the conclusion of this article will be made available by the authors, without undue reservation.

AUTHOR CONTRIBUTIONS

YH conducted the catalyst preparation and wrote the manuscript. GZ and LL performed the activity test and characterization. JL, SW, HX, and SW analyzed the catalytic results. SW conceived the idea for the project and directed the research. All authors contributed to manuscript revision, read, and approved the submitted version.

FUNDING

The authors are grateful for the financial support from the National Natural Science Foundation of China (NSFC) (No. 22172125).

SUPPLEMENTARY MATERIAL

The Supplementary Material for this article can be found online at: https://www.frontiersin.org/articles/10.3389/fchem.2022.944552/full#supplementary-material

REFERENCES

Chheda, J. N., Huber, G. W., and Dumesic, J. A. (2007). Liquid-Phase Catalytic Processing of Biomass-Derived Oxygenated Hydrocarbons to Fuels and Chemicals. *Angew. Chem. Int. Ed.* 46 (38), 7164–7183. doi:10.1002/anie.200604274

Choudhary, H., Nishimura, S., and Ebitani, K. (2015). Synthesis of High-Value Organic Acids from Sugars Promoted by Hydrothermally Loaded Cu Oxide Species on Magnesia. *Appl. Catal. B Environ.* 162, 1–10. doi:10.1016/j.apcatb.2014.05.012

Corma, A., Iborra, S., and Velty, A. (2007). Chemical Routes for the Transformation of Biomass into Chemicals. *Chem. Rev.* 107 (6), 2411–2502. doi:10.1021/cr050989d

Datta, R., and Henry, M. (2006). Lactic Acid: Recent Advances in Products, Processes and Technologies - a Review. *J. Chem. Technol. Biotechnol.* 81 (7), 1119–1129. doi:10.1002/jctb.1486

de Clippel, F., Dusselier, M., Van Rompaey, R., Vanelderen, P., Dijkmans, J., Makshina, E., et al. (2012). Fast and Selective Sugar Conversion to Alkyl Lactate and Lactic Acid with Bifunctional Carbon-Silica Catalysts. *J. Am. Chem. Soc.* 134 (24), 10089–10101. doi:10.1021/ja301678w

Dong, W., Shen, Z., Peng, B., Gu, M., Zhou, X., Xiang, B., et al. (2016). Selective Chemical Conversion of Sugars in Aqueous Solutions without Alkali to Lactic Acid over a Zn-Sn-Beta Lewis Acid-Base Catalyst. *Sci. Rep.* 6 (1), 26713. doi:10.1038/srep26713

Duan, Y., Luo, Q., Nie, R., Wang, J., Zhang, Y., Lu, T., et al. (2022). Catalytic Conversion of Glycerol to Methyl Lactate over Au-CuO/Sn-Beta: The Roles of Sn-Beta. *Catalysts* 12 (1), 104. doi:10.3390/catal12010104

Dusselier, M., and Sels, B. F. (2014). Selective Catalysis for Cellulose Conversion to Lactic Acid and Other α-Hydroxy Acids. *Sel. Catal. Renew. Feed. Chem.* 35, 85–125. doi:10.1007/128_2014_540

Eş, I., Mousavi Khaneghah, A., Barba, F. J., Saraiva, J. A., Sant'Ana, A. S., and Hashemi, S. M. B. (2018). Recent Advancements in Lactic Acid Production - a Review. *Food Res. Int.* 107, 763–770. doi:10.1016/j.foodres.2018.01.001

Gérardy, R., Debecker, D. P., Estager, J., Luis, P., and Monbaliu, J.-C. M. (2020). Continuous Flow Upgrading of Selected C2-C6 Platform Chemicals Derived from Biomass. *Chem. Rev.* 120 (15), 7219–7347. doi:10.1021/acs.chemrev.9b00846

Hammond, C., Conrad, S., and Hermans, I. (2012). Simple and Scalable Preparation of Highly Active Lewis Acidic Sn-β. *Angew. Chem. Int. Ed.* 51 (47), 11736–11739. doi:10.1002/anie.201206193

Hammond, C., Padovan, D., Al-Nayili, A., Wells, P. P., Gibson, E. K., and Dimitratos, N. (2015). Identification of Active and Spectator Sn Sites in Sn-β Following Solid-State Stannation, and Consequences for Lewis Acid Catalysis. *ChemCatChem* 7 (20), 3322–3331. doi:10.1002/cctc.201500545

Holm, M. S., Pagán-Torres, Y. J., Saravanamurugan, S., Riisager, A., Dumesic, J. A., and Taarning, E. (2012). Sn-Beta Catalysed Conversion of Hemicellulosic Sugars. *Green Chem.* 14 (3), 702–706. doi:10.1039/C2GC16202D

Holm, M. S., Saravanamurugan, S., and Taarning, E. (2010). Conversion of Sugars to Lactic Acid Derivatives Using Heterogeneous Zeotype Catalysts. *Science* 328 (5978), 602–605. doi:10.1126/science.1183990

Hu, W., Chi, Z., Wan, Y., Wang, S., Lin, J., Wan, S., et al. (2020). Synergetic Effect of Lewis Acid and Base in Modified Sn-β on the Direct Conversion of Levoglucosan to Lactic Acid. *Catal. Sci. Technol.* 10 (9), 2986–2993. doi:10.1039/D0CY00089B

Hu, X., Wu, L., Wang, Y., Mourant, D., Lievens, C., Gunawan, R., et al. (2012). Mediating Acid-Catalyzed Conversion of Levoglucosan into Platform Chemicals with Various Solvents. *Green Chem.* 14 (11), 3087–3098. doi:10.1039/C2GC35961H

Li, P., Liu, G., Wu, H., Liu, Y., Jiang, J. G., and Wu, P. (2011). Postsynthesis and Selective Oxidation Properties of Nanosized Sn-Beta Zeolite. *J. Phys. Chem. C* 115 (9), 3663–3670. doi:10.1021/jp1076966

Mäki-Arvela, P., Simakova, I. L., Salmi, T., and Murzin, D. Y. (2014). Production of Lactic Acid/Lactates from Biomass and Their Catalytic Transformations to Commodities. *Chem. Rev.* 114 (3), 1909–1971. doi:10.1021/cr400203v

Ong, H. C., Chen, W.-H., Farooq, A., Gan, Y. Y., Lee, K. T., and Ashokkumar, V. (2019). Catalytic Thermochemical Conversion of Biomass for Biofuel Production: A Comprehensive Review. *Renew. Sustain. Energy Rev.* 113, 109266. doi:10.1016/j.rser.2019.109266

Orazov, M., and Davis, M. E. (2015). Tandem Catalysis for the Production of Alkyl Lactates from Ketohexoses at Moderate Temperatures. *Proc. Natl. Acad. Sci. U.S.A.* 112 (38), 11777–11782. doi:10.1073/pnas.1516466112

Pang, J., Zheng, M., Li, X., Song, L., Sun, R., Sebastian, J., et al. (2017). Catalytic Conversion of Carbohydrates to Methyl Lactate Using Isolated Tin Sites in SBA-15. *ChemistrySelect* 2 (1), 309–314. doi:10.1002/slct.201601752

Santhanaraj, D., Rover, M. R., Resasco, D. E., Brown, R. C., and Crossley, S. (2014). Gluconic Acid from Biomass Fast Pyrolysis Oils: Specialty Chemicals from the Thermochemical Conversion of Biomass. *ChemSusChem* 7 (11), 3132–3137. doi:10.1002/cssc.201402431

Tang, B., Li, S., Song, W.-C., Yang, E.-C., Zhao, X.-J., Guan, N., et al. (2020). Fabrication of Hierarchical Sn-Beta Zeolite as Efficient Catalyst for Conversion of Cellulosic Sugar to Methyl Lactate. *ACS Sustain. Chem. Eng.* 8 (9), 3796–3808. doi:10.1021/acssuschemeng.9b07061

Wasewar, K. L., Yawalkar, A. A., Moulijn, J. A., and Pangarkar, V. G. (2004). Fermentation of Glucose to Lactic Acid Coupled with Reactive Extraction: A Review. *Ind. Eng. Chem. Res.* 43 (19), 5969–5982. doi:10.1021/ie049963n

Wattanapaphawong, P., Reubroycharoen, P., and Yamaguchi, A. (2017). Conversion of Cellulose into Lactic Acid Using Zirconium Oxide Catalysts. *RSC Adv.* 7 (30), 18561–18568. doi:10.1039/C6RA28568F

Yang, X., Yang, L., Fan, W., and Lin, H. (2016). Effect of Redox Properties of LaCoO3 Perovskite Catalyst on Production of Lactic Acid from Cellulosic Biomass. *Catal. Today* 269, 56–64. doi:10.1016/j.cattod.2015.12.003

Yang, X., Zhang, Y., Zhou, L., Gao, B., Lu, T., Su, Y., et al. (2019). Production of Lactic Acid Derivatives from Sugars over Post-synthesized Sn-Beta Zeolite Promoted by WO3. *Food Chem.* 289, 285–291. doi:10.1016/j.foodchem.2019.03.039

Conflict of Interest: The authors declare that the research was conducted in the absence of any commercial or financial relationships that could be construed as a potential conflict of interest.

Publisher's Note: All claims expressed in this article are solely those of the authors and do not necessarily represent those of their affiliated organizations, or those of the publisher, the editors and the reviewers. Any product that may be evaluated in this article, or claim that may be made by its manufacturer, is not guaranteed or endorsed by the publisher.

frontiers | Frontiers in Chemistry

MINI REVIEW
published: 18 July 2022
doi: 10.3389/fchem.2022.956223

CO_2 Hydrogenation on Metal-Organic Frameworks-Based Catalysts: A Mini Review

Qian Zhang[1,2], *Sen Wang*[1]*, *Mei Dong*[1] *and Weibin Fan*[1]*

[1]State Key Laboratory of Coal Conversion, Institute of Coal Chemistry, Chinese Academy of Sciences, Taiyuan, China, [2]University of the Chinese Academy of Sciences, Beijing, China

Conversion of carbon dioxide (CO_2) into value-added fuels and chemicals can not only reduce the emission amount of CO_2 in the atmosphere and alleviate the greenhouse effect but also realize carbon recycling. Through hydrogenation with renewable hydrogen (H_2), CO_2 can be transformed into various hydrocarbons and oxygenates, including methanol, ethanol, methane and light olefins, etc. Recently, metal-organic frameworks (MOFs) have attracted extensive attention in the fields of adsorption, gas separation, and catalysis due to their high surface area, abundant metal sites, and tunable metal-support interface interaction. In CO_2 hydrogenation, MOFs are regarded as important supports or sacrificed precursors for the preparation of high-efficient catalysts, which can uniformly disperse metal nanoparticles (NPs) and enhance the interaction between metal and support to prevent sintering and aggregation of active metal species. This work summarizes the recent process on hydrogenation of CO_2 to methanol, methane and other C_{2+} products over various MOFs-based catalysts, and it will provide some dues for the design of MOFs materials in energy-efficient conversion and utilization.

Keywords: MOFs, CO_2 hydrogenation, methanol, methane, C2+ Products

OPEN ACCESS

Edited by:
Haifeng Xiong,
Xiamen University, China

Reviewed by:
Shunji Xie,
Xiamen University, China
Zupeng Chen,
Nanjing Forestry University, China

***Correspondence:**
Sen Wang
wangsen@sxicc.ac.cn
Weibin Fan
fanwb@sxicc.ac.cn

Specialty section:
This article was submitted to Catalytic Reactions and Chemistry, a section of the journal Frontiers in Chemistry

Received: *30 May 2022*
Accepted: *15 June 2022*
Published: *18 July 2022*

Citation:
Zhang Q, Wang S, Dong M and Fan W (2022) CO_2 Hydrogenation on Metal-Organic Frameworks-Based Catalysts: A Mini Review. Front. Chem. 10:956223. doi: 10.3389/fchem.2022.956223

INTRODUCTION

Due to the rapid consumption of fossil resources, e.g., coal, petroleum, and natural gas, a large number of CO_2 have been released into the atmosphere (Song, 2006). From 2006 to 2021, the global CO_2 concentration in the atmosphere has been elevated from 381 to 415 ppm (NOAA, 2022). The massive emission of CO_2 has brought serious environmental problems, such as global climate change and ocean acidification (Valles-Regino et al., 2015). Hence, reduction of CO_2 amount and mitigation of greenhouse effect are the major challenges faced by the whole human society.

Regardless of this, CO_2 is an important C1 platform molecule. Conversion of CO_2 through sustainable catalytic processes into valuable chemicals and clean fuels is a promising way for CO_2 utilization which could promote a circular carbon economy (Srinivas et al., 2014; Didas et al., 2015; Porosoff et al., 2016; Rafiee et al., 2018). CO_2 conversion can be achieved by electro-catalysis, photo-catalysis, and thermal-catalysis processes. Electro-catalysis or photo-catalysis from clean and renewable electrical or solar energy is regarded as an important route for CO_2 reduction reaction (CO_2 RR). Through the rational design of high efficient catalysts, these reactions can be performed under relatively mild conditions that considerably decrease the energy consumption (Liu et al., 2012; Handoko et al., 2013; Jhong et al., 2013; Wang et al., 2015; Perathoner and Centi, 2019; Wang J.-J. et al., 2021; Zhang et al., 2021; Zhang et al., 2022a). Nevertheless, the electro-catalysis or photo-catalysis for CO_2 conversion is time or geographically dependent, which, thus, decreases their

economic viability. Compared to the former two manners, the thermal catalytic conversion of CO_2 shows higher efficiency and it is more potential for industrial application. Since the CO_2 molecule is thermodynamically stable and kinetically inert, the activation of the C=O bond in CO_2 needs to overcome a high energy barrier. Renewable hydrogen (H_2) generated from photolysis or electrolysis of water has high energy density and it can effectively reduce CO_2. Thus, hydrogenation of CO_2 into high-value hydrocarbons and oxygenates, including methane (CH_4), methanol (CH_3OH), ethanol (C_2H_5OH), and light olefins ($C_2^=$-$C_4^=$), has received increasing research interest (Sha et al., 2020).

The catalytic system for CO_2 hydrogenation mainly consists of metal sites and support, including metal oxide/carbide, zeolite, graphene, and so on. Coperet and co-workers prepared zirconia-supported copper nanoparticles (NPs), which showed methanol selectivity of 75% (Larmier et al., 2017). Encapsulation of Cu NPs in Beta zeolite elevates ethanol selectivity and space-time yield (STY) to ~ 100% and 398 mg g_{cat}^{-1} h^{-1} (Ding et al., 2020). Highly selective conversion of CO_2 into light olefins, aromatics, gasolines, and diesel was also achieved over metal oxides/zeolites bifunctional catalysts (Gao et al., 2017; Wang Y. et al., 2018; Zhou et al., 2019; Wang S. et al., 2020; Wei et al., 2021; Zhang et al., 2022b; Wang et al., 2022). In general, improvement of metal site dispersion and modulation of metal-support interaction can increase CO_2 conversion and product selectivity.

In recent years, metal-organic frameworks (MOFs) have been considered important host materials in adsorption, gas separation and catalysis processes, due to their large surface area, abundant metal sites, and three-dimensional (3D) porous structure (Kumar et al., 2017; Guntern et al., 2021). MOFs are composed of metal-oxygen clusters serving as secondary building units (SBUs) that are connected by the organic ligands (Ranocchiari and Bokhoven, 2011; Chavan et al., 2012). The cages and the missing linker defects in MOFs are ideal places for confining ultra-small metal NPs, thus, inhibiting the sintering and aggregation of active sites (An et al., 2017; Zhao et al., 2018; Abdel-Mageed et al., 2019; Hu et al., 2019; Zhu et al., 2020; Yu et al., 2021). The metal-support interaction can be adjusted by controlling the pyrolysis of nodes and linkers in MOFs (Furukawa et al., 2010; Abdel-Mageed et al., 2019; Wang, 2022). This work gives a short review about the recent progress on the application of MOFs-based catalysts in CO_2 hydrogenation to methanol, methane, and some C_{2+} products. Synthesis and structural regulation of MOFs materials have been reviewed in many other literatures (Eddaoudi et al., 2002; Cavka et al., 2008; Wang C. et al., 2018; Usman et al., 2021).

CO_2 Hydrogenation to Methanol

Methanol is an important platform compound in the chemical industry, and it can be transformed into commodity olefins, aromatics, formaldehyde, and longer-chain alcohols (Liu et al., 2018; Yarulina et al., 2018). Considering the unique features role of methanol in energy conversion, a concept of "methanol economy" was proposed by Olah and co-workers (Goeppert et al., 2014). Hydrogenation of CO_2 to methanol is described as the following **Equation 1**

$$\boldsymbol{CO_2 + 3H_2 = CH_3OH + H_2O\ \Delta H_{298K} = -49.3kJ/mol} \quad (1)$$

Although CO_2 hydrogenation to methanol is exothermic, the activation of O=C=O bond requires to overcome a high energy barrier that makes operating temperature generally as high as 240–300°C (Murthy et al., 2021). An increase in reaction temperature not only accelerates competitive reverse water-gas shift (RWGS) reaction (**Equation 2**) and produces more CO but also induces sintering and aggregation of active metal NPs.

$$\boldsymbol{CO_2 + H_2 = CO + H_2O\ \Delta H_{298K} = 41.1kJ/mol} \quad (2)$$

One efficient method to improve the sintering resistance of active metal species is the enhancement of metal-support interface interaction through confining ultrasmall metal NPs within the pores or cages of MOFs. Yaghi and co-workers prepared the catalyst with the single Cu nanocrystal encapsulated in the cage of UiO-66 (Cu@UiO-66); Cu@UiO-66 shows 100% methanol selectivity, and 8 times higher yield than $Cu/ZnO/Al_2O_3$ in CO_2 hydrogenation (Rungtaweevoranit et al., 2016). It suggests that the strong interaction between Cu nanocrystal and Zr-based SBUs of UiO-66 effectively stabilizes Cu active sites. Anchoring Cu NPs into the missing-linker defects of UiO-66 considerably enhances the interaction of metallic Cu with Zr_6O_8 nodes of UiO-66. It is found that the isolated Cu can only produce CO via RWGS reaction, whereas Cu NPs anchored on the Zr_6O_8 nodes generates larger numbers of Cu-O-Zr interface sites that show higher activity for methanol synthesis (**Figure 1A**) (Zhu et al., 2020). An and co-workers reported that the organic coordinating groups in MOFs play a vital role in stabilizing metal NPs (An et al., 2017). The ultra-small Cu/ZnO_x NPs are *in situ* generated through the reduction of frameworks Cu^{2+} and Zn^{2+} ions in Zr_6 clusters of UiO-bpy (2,2-bipyridine) MOF (**Figure 1B**). The strong interaction between Cu/ZnO_x NPs and bpy moieties in MOFs prevents the phase separation of Cu/ZnO_x. Thus, the prepared Cu/ZnO_x@MOFs catalyst shows methanol selectivity of 100% in CO_2 hydrogenation, with the STY as high as 2.59 g_{MeOH} kg_{Cu}^{-1} h^{-1}. It should be noticed that although these MOF catalysts have been widely used in CO_2 hydrogenation, they usually need to be carried out at a relatively low temperature, because of their low thermal/hydrothermal stability. It is found that the organic ligands in MOF decompose easily at the high reaction temperature, causing the collapse of the pore structure and the decrease of catalytic activity.

Another way to enhance the metal-support interaction is to pyrolyze the metal-loaded MOF precursors in an inert atmosphere. Liu and co-workers fabricated a stable $Cu@ZrO_x$ catalyst via *in situ* treatment of Cu/UiO-66 in H_2 flow at different temperatures (Liu et al., 2019). $Cu@ZrO_x$ possesses abundant Cu-ZrO_x interfaces and a stable 3D ZrO_x framework that leads to the formation of more Cu^+ species on the surface of ZrO_2. As a result, CO_2 hydrogenation to methanol is significantly improved via forming more formate and methoxy intermediates. An inverse ZnO/Cu catalyst with closer proximity to ZnO-Cu interface was prepared by Hu and co-workers through directly calcining Cu@ZIF-8 (Hu et al., 2019). It is shown that the small ZnO NPs on the surface of Cu promote the formation of methanol in CO_2 hydrogenation. HKUST-1 was used as the Cu source to

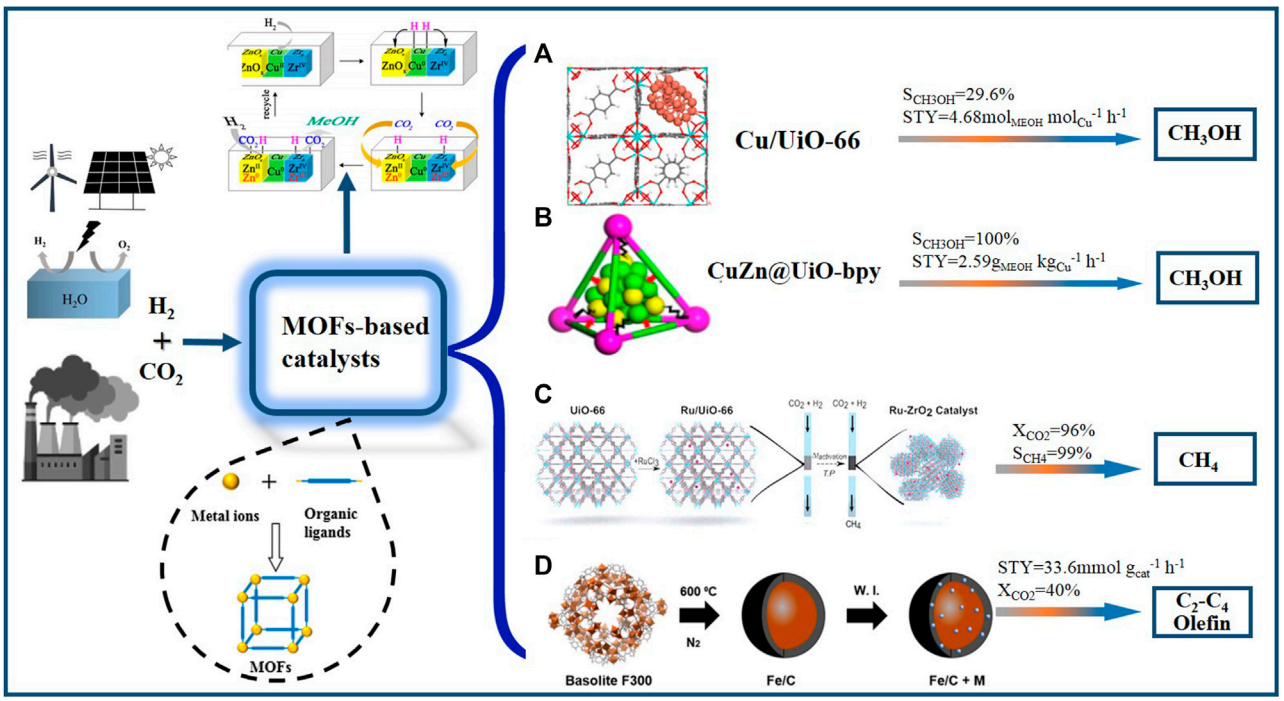

FIGURE 1 | CO_2 hydrogenation over various MOFs-based catalysts. **(A)** Interface bonding of sub-nanometer Cu clusters with Zr_6O_8 nodes over Cu/UiO-66 and its catalytic results in CO_2 hydrogenation to methanol. Reproduced with permission from Zhu et al. (2020). Copyright 2020 Springer Nature. **(B)** The Cu/ZnO_x NPs embedded UiO-bpy and its catalytic results in CO_2 hydrogenation to methanol. Reproduced with permission from An et al. (2017). Copyright 2017 American Chemical Society. **(C)** Structural evolution in the decomposition process of Ru/UiO-66 and its catalytic results obtained material for CO_2 hydrogenation to CH_4. Reproduced with permission from Lippi et al. (2017). Copyright 2017 Royal Society of Chemistry. **(D)** Fe/C-K catalyst fabricated through decomposition of Basolite F300 MOF and its catalytic results obtained material for CO_2 hydrogenation to CH_4. Reproduced with permission from Ramirez et al. (2018). Copyright 2018 American Chemical Society.

prepare the ZrO_2@HKUST-1 core-shell precursor via one-step hydrothermal method. Upon calcination and reduction, the Cu nanoclusters are highly dispersed on ZrO_2, forming strong Cu-ZrO_2 interface interaction. This nano Cu-ZrO_2 catalyst gives a methanol space-time yield (STY) of about 5.2 times higher than that of the sample obtained by the traditional impregnation method (Yu et al., 2021).

Besides Cu-based catalysts, other metals-loaded MOFs have been developed for CO_2 hydrogenation to methanol. Yin and co-workers embedded ultrasmall Pd crystals into ZIF-8 and further pyrolyzed them into PdZn alloy after calcination under airflow (Yin et al., 2018). The strong interface interaction between PdZn and ZnO not only prevents the aggregation of metal sites but also leads to the formation of more oxygen defects, thereby enhancing catalytic activity and stability of PdZn catalyst in CO_2 hydrogenation to methanol. Co_3O_4 coated by amorphous In_2O_3 shell was synthesized through decomposition of In-modified ZIF-67(Co) (Pustovarenko et al., 2020). Co_3O_4/In_2O_3 core-shell catalyst exhibits a maximum methanol STY of 0.65 g_{MeOH} g_{cat}^{-1} h^{-1} over 100 h time on stream. Olsbye and co-workers (Gutterod et al., 2019) encapsulated Pt NPs into the octahedral cavity of UiO-67. The Pt-embedded UiO-67 produces more methanol but less methane in CO_2 hydrogenation than the Pt/C, Pt/SiO_2 and Pt/Al_2O_3 at 170°C and 1–8 bar. It is shown that the interface between Pt NPs and linker-deficient Zr_6O_8 nodes is the main site for methanol formation. A decrease in missing-linker defects lowered the methanol formation rate (Gutterød et al., 2020). Introduction of H_2O is beneficial to increase in methanol selectivity, due to the facilitation of methanol desorption. The catalytic results of some MOFs-based catalysts in CO_2 hydrogenation to methanol are summarized in **Table 1**.

CO_2 Hydrogenation to Methane

Methane (CH_4) is the main component of natural gas and it is also an important building block in the chemical industry, and can be further transformed into downstream products such as ethyne and ammonia (Bai et al., 2008; Sha et al., 2020). Hydrogenation of CO_2 to CH_4 provides an alternative solution to alleviated methane market shortage (Qin et al., 2017). Although CO_2 methanation is a strongly exothermic reaction (**Equation 3**), it is always operated at high temperatures because of the kinetic limitation.

$$\boldsymbol{CO_2 + 4H_2 = CH_4 + 2H_2O\ \Delta H_{298K} = -165.0kJ/mol} \quad (3)$$

Supported ruthenium (Ru), rhodium (Rh), nickel (Ni), and cobalt (Co) catalysts are commonly used, as their high activity in CO_2 hydrogenation. Strong metal-support interaction (SMSI) improves the dispersion of metal species and the stability of catalyst. Using SMSI to mediate the catalytic behavior of supported metal species is of significance in CO_2

TABLE 1 | Summary performance of catalysts for CO_2 hydrogenation reaction.

Catalysts	Main Product	H_2/CO_2 Ratio	T (°C)	P (MPa)	Loading (Wt%)	X_{CO2} (%)	Selectivity (%)	STY (g kg_{cat}^{-1} h^{-1})	TOS (h)	Ref
Cu-UiO-66	Methanol	3:1	175	1	1.0	1	100	—	—	Rungtaweevoranit et al. (2016)
Cu/UiO-66	Methanol	3:1	250	3.2	1.4	-	29.6	679.76	50	Zhu et al. (2020)
Cu@3D-ZrOx	Methanol	3:1	260	4.5	12.4	13.1	78.8	796	105	Liu et al. (2019)
Cu/ZnO_x@UiO-66	Methanol	3:1	250	4	5.9	4.3	87	28.3	100	Yang et al. (2021)
Cu/ZnO_x@UiO-bpy	Methanol	3:1	250	4	6.9	3.3	100	37.5	100	An et al. (2017)
Cu-ZrO_2(ZrO_2@ HKUST-1)	Methanol	3:1	220	3	11	6.8	64.4	287.9	16	Yu et al. (2021)
ZnO/Cu(Cu@ZIF-8)	Methanol	3:1	260	4.5	57.6	—	—	933	76	Hu et al. (2019)
PdZn (Cu@ZIF-8)	Methanol	3:1	270	4.5	—	14	55	650	50	Yin et al. (2018)
In_2O_3/Co_3O_4(In@ ZIF-67)	Methanol	3:1	300	5	—	—	87	650	100	Pustovarenko et al. (2020)
Ni@MIL-101	Methane	8:1	320	0.1	10	56.4	91.6	—	10	Mihet et al. (2019)
Ni@MOF-5	Methane	4:1	320	0.1	10	75.1	100	—	100	Zhen et al. (2015)
Ni@UiO-66	Methane	3:1	300	—	20	57.6	100	—	100	Zhao et al. (2018)
Ru/UiO-66	Methane	4:1	350	0.5	1.0	96	99	—	—	Lippi et al. (2017)
K-CuZnAl + Na-Fe@C	Ethanol	3:1	350	5	—	39.2	35	—	50	Wang Y. et al., 2021
Fe/C-K (Basolite F300)	Olefins	3:1	320	3	—	40	~40	—	50	Ramirez et al. (2018)

hydrogenation. MOFs are believed as promising supports or sacrificed templates, as they can promote active metal species dispersion and enhance the metal-support interaction.

Mihet and co-workers encapsulated Ni into MIL-101 (Ni@MIL-101) using the impregnation method. The high surface area ($2{,}497\ m^2\ g^{-1}$) and pore volume ($1.75\ cm^3\ g^{-1}$) of Ni@MIL-101 make the Ni particles highly dispersed in MIL-101 which enhances the adsorption and activation of CO_2. With such a catalyst, CO_2 conversion reaches 56.4%, with CH_4 selectivity of 91.6% at 320°C and gas hourly space velocity (GHSV) of $4{,}650\ ml\ g^{-1}\ h^{-1}$ (Mihet et al., 2019). Ni@MOF-5 shows higher Ni dispersion due to a larger surface area ($2{,}961\ m^2\ g^{-1}$) and thus resulting in higher CO_2 conversion and CH_4 selectivity of 75.1 and ~100% respectively at 300°C, 1 atm and GHSV of $2000\ ml\ g^{-1}\ h^{-1}$ (Zhen et al., 2015). In addition, the metal-support interaction is also enhanced by anchoring Ni on MOFs. Zhao and co-workers prepared a series of UiO-66-supported Ni-based catalysts using impregnation and reduction methods (Zhao et al., 2018). Encapsulation of ultrasmall Ni particles in UiO-66 can increase the interface interaction of Ni with UiO-66 support, which, hence, inhibits the sintering of Ni species. The prepared 20%Ni@UiO-66 exhibits CO_2 conversion of 57.6% and CH_4 selectivity of 100% in CO_2 hydrogenation. Interestingly, no significant deactivation was observed even after a reaction of 100 h.

Lippi and co-workers investigated the structural evolution in the decomposition process of metal-loaded MOFs (Lippi et al., 2017; Lippi et al., 2021). The 3D framework of Ru-impregnated UiO-66 (Ru/UiO-66) gradually collapsed under CO_2 methanation conditions to form amorphous C and Zr containing phase structure, which is then transformed into tetragonal ZrO_2(t) and finally into more stable monoclinic ZrO_2(m) (**Figure 1C**). The structure and morphology of catalyst can be precisely controlled by altering the treatment conditions during MOFs decomposition. The Ru/ZrO_2(m) is a highly active and stable CO_2 methanation catalyst and it gives the CO_2 conversion of 96% and CH_4 selectivity of 99% at 350°C and 5 bar. The catalytic results of reported MOFs-based catalysts for CO_2 hydrogenation to CH_4 was shown in **Table 1**.

CO_2 Hydrogenation to C_{2+} Products

Conversion of CO_2 to C_{2+} products, such as alcohol, olefins and aromatics, is highly desirable but remains a greater challenge than to C1 compounds due to the high C-C coupling barrier (Guo et al., 2018; Wei et al., 2021). Although CO_2 hydrogenation to ethanol, light olefin, or aromatic is exothermic (**Equations 4–6**), relatively high temperature and pressure are always necessary for the activation of CO_2 molecules.

$$2CO_2 + 6H_2 = C_2H_5OH + 3H_2O\ \Delta H_{298K} = -173.3kJ/mol \quad (4)$$

$$2CO_2 + 6H_2 = C_2H_4 + 4H_2O\ \Delta H_{298K} = -127.9kJ/mol \quad (5)$$

$$6CO_2 + 15H_2 = C_6H_6 + 12H_2O\ \Delta H_{298K} = -457.9kJ/mol \quad (6)$$

Recently, some researchers suggested that direct pyrolysis of metal-loaded MOFs in an inert atmosphere can generate various metal-carbides, in which the metal NPs are closely confined in the carbon porous materials to achieve strong metal-support interaction and avoid aggregation of active sites. Tsubaki and co-workers designed the K-CuZnAl and Na-Fe@C composite catalyst. This catalyst enhances the ethanol selectivity as high as 35.0% and CO_2 conversion of 39.2%, at 350°C and 5.0 MPa in CO_2 hydrogenation (Wang Y. et al., 2021). The K-CuZnAl activates CO_2 to form methanol and CO, and Na-Fe@C promotes the C-C coupling, with Na-Fe@C obtained from the pyrolysis of Fe-based MOFs under N_2 flow. The carbon matrix effectively prevents Fe sintering and achieves the uniform dispersion of Fe active sites.

The hydrogenation of CO_2 to olefins is a potential way of achieving a sustainable carbon cycle. It is generally performed via a two-step process on Fe-based catalysts: CO_2 is firstly converted to CO via RWGS reaction, and then CO is hydrogenated to olefins via Fischer-Tropsch synthesis (FTS) reaction (Yang et al.,

2017; De et al., 2020). Ramirez and co-workers prepared the Fe/C-K catalyst through the decomposition of Basolite F300 MOF under N_2 atmosphere (Ramirez et al., 2018). It shows good catalytic performance for CO_2 hydrogenation to olefins; CO_2 conversion and $C_2^=$-$C_4^=$ STY reach 40% and 33.6 mmol g_{cat}^{-1} h^{-1} at 320°C and 3 MPa (**Figure 1D**). The uniform distribution of Fe active sites is considered effectively promote RWGS and FTS reactions.

Similarly, Li and co-workers fabricated $ZnZrO_x$@C catalyst with three-dimensional (3D) hierarchical structure through carbonization of Zn-modified UiO-66 (Wang Y. et al., 2020). The introduction of Zn into the synthesis gel of UiO-66 induces the formation of more defects due to the substitution of Zn for Zr. Upon coupling with H-ZSM-5 zeolite, it affords the selectivity of aromatics in hydrocarbons as high as 73.1%, CH_4 is decreased to 3.4%. Compared with possesses traditional $ZnZrO_x$ oxides, $ZnZrO_x$@C catalyst formed by the carbonization of defective MOFs owns richer surface vacancies, and hence, shows higher CO/CO_2 conversion due to their strong adsorption. In addition, the 3D hierarchical carbon framework structure facilitates the diffusion of products, thus, avoiding secondary reactions and elevating the proportion of benzene, toluene, and xylene (BTX) in aromatics.

DISCUSSION

Metal-organic frameworks (MOFs) are burgeoning porous materials and they are widely used in adsorption, separation, and catalysis processes due to their unique pore structure, versatile compositions, and large surface area. The cages and the missing-linker defects in MOFs provide ideal places for encapsulating or anchoring metal nanoparticles, thereby preventing the sintering and aggregation of active sites. Nevertheless, MOFs are also important sacrificed templates for the preparation of high-efficient metal oxides or carbides. Some MOFs derived metal@C were designed, and exhibited high catalytic performance in CO_2 hydrogenation to methanol, methane, and other C_{2+} products, due to high dispersion of active sites and strong metal-support interaction.

Despite that MOFs as supports or catalysts have received extensive attention and they show superior catalytic activity and product selectivity in CO_2 hydrogenation, however, the much lower thermal and hydrothermal stability of MOFs than SiO_2, Al_2O_3, and zeolites limits the applications in many industrial processes. This is because the organic ligands are nearly impossible to resist high temperature or their facile pyrolysis character. Nevertheless, there are potential candidates for preparing highly dispersed oxide-supported metal catalysts with strong metal-support interaction.

AUTHOR CONTRIBUTIONS

QZ: conceptualization, writing—original draft; SW: conceptualization, funding acquisition, writing—review and editing; MD: conceptualization, funding acquisition; WF: supervision, conceptualization, funding acquisition, writing—review and editing.

ACKNOWLEDGMENTS

The authors thank the financial support from the National Natural Science Foundation of China (U1910203, U1862101, 21991090, 21991092, 21802157), National Key R&D Program of China (2018YFB0604802, 2020YFA0210900); Natural Science Foundation of Shanxi Province of China (201901D211581), Youth Innovation Promotion Association CAS (2021172), Young Talent Training Program of State Key Laboratory of Coal Conversion, Institute of Coal Chemistry, CAS (2021BWZ003), and Excellent Doctoral Student Award and Subsidy program of Shanxi Province (BK2018001).

REFERENCES

Abdel-Mageed, A. M., Rungtaweevoranit, B., Parlinska-Wojtan, M., Pei, X., Yaghi, O. M., and Behm, R. J. (2019). Highly Active and Stable Single-Atom Cu Catalysts Supported by a Metal-Organic Framework. *J. Am. Chem. Soc.* 141, 5201–5210. doi:10.1021/jacs.8b11386

An, B., Zhang, J., Cheng, K., Ji, P., Wang, C., and Lin, W. (2017). Confinement of Ultrasmall Cu/ZnOx Nanoparticles in Metal-Organic Frameworks for Selective Methanol Synthesis from Catalytic Hydrogenation of CO_2. *J. Am. Chem. Soc.* 139, 3834–3840. doi:10.1021/jacs.7b00058

Bai, M., Zhang, Z., Bai, M., Bai, X., and Gao, H. (2008). Synthesis of Ammonia Using CH4/N2 Plasmas Based on Micro-Gap Discharge under Environmentally Friendly Condition. *Plasma Chem. Plasma Process* 28, 405–414. doi:10.1007/s11090-008-9132-4

Cavka, J. H., Jakobsen, S., Olsbye, U., Guillou, N., Lamberti, C., Bordiga, S., et al. (2008). A New Zirconium Inorganic Building Brick Forming Metal Organic Frameworks with Exceptional Stability. *J. Am. Chem. Soc.* 130, 13850–13851. doi:10.1021/ja8057953

Chavan, S., Vitillo, J. G., Gianolio, D., Zavorotynska, O., Civalleri, B., Jakobsen, S., et al. (2012). H2 Storage in Isostructural UiO-67 and UiO-66 MOFs. *Phys. Chem. Chem. Phys.* 14, 1614–1626. doi:10.1039/c1cp23434j

De, S., Dokania, A., Ramirez, A., and Gascon, J. (2020). Advances in the Design of Heterogeneous Catalysts and Thermocatalytic Processes for CO_2 Utilization. *ACS Catal.* 10, 14147–14185. doi:10.1021/acscatal.0c04273

Didas, S. A., Choi, S., Chaikittisilp, W., and Jones, C. W. (2015). Amine-Oxide Hybrid Materials for CO_2 Capture from Ambient Air. *Acc. Chem. Res.* 48, 2680–2687. doi:10.1021/acs.accounts.5b00284

Ding, L., Shi, T., Gu, J., Cui, Y., Zhang, Z., Yang, C., et al. (2020). CO_2 Hydrogenation to Ethanol over Cu@Na-Beta. *Chem* 6, 2673–2689. doi:10.1016/j.chempr.2020.07.001

Eddaoudi, M., Kim, J., Rosi, N., Vodak, D., Wachter, J., O'Keeffe, M., et al. (2002). Systematic Design of Pore Size and Functionality in Isoreticular MOFs and Their Application in Methane Storage. *Science* 295, 469–472. doi:10.1126/science.1067208

Furukawa, H., Ko, N., Go, Y. B., Aratani, N., Choi, S. B., Choi, E., et al. (2010). Ultrahigh Porosity in Metal-Organic Frameworks. *Science* 329, 424–428. doi:10.1126/science.1192160

Gao, P., Dang, S., Li, S., Bu, X., Liu, Z., Qiu, M., et al. (2017). Direct Production of Lower Olefins from CO_2 Conversion via Bifunctional Catalysis. *ACS Catal.* 8, 571–578. doi:10.1021/acscatal.7b02649

Goeppert, A., Czaun, M., Jones, J.-P., Surya Prakash, G. K., and Olah, G. A. (2014). Recycling of Carbon Dioxide to Methanol and Derived Products - Closing the Loop. *Chem. Soc. Rev.* 43, 7995–8048. doi:10.1039/c4cs00122b

Guntern, Y. T., Vávra, J., Karve, V. V., Varandili, S. B., Segura Lecina, O., Gadiyar, C., et al. (2021). Synthetic Tunability of Colloidal Covalent Organic Framework/nanocrystal Hybrids. *Chem. Mat.* 33, 2646–2654. doi:10.1021/acs.chemmater.1c00501

Guo, L., Sun, J., Ge, Q., and Tsubaki, N. (2018). Recent Advances in Direct Catalytic Hydrogenation of Carbon Dioxide to Valuable C_{2+} Hydrocarbons. *J. Mat. Chem. A* 6, 23244–23262. doi:10.1039/c8ta05377d

Gutterød, E. S., Pulumati, S. H., Kaur, G., Lazzarini, A., Solemsli, B. G., Gunnæs, A. E., et al. (2020). Influence of Defects and H2O on the Hydrogenation of CO_2 to Methanol over Pt Nanoparticles in UiO-67 Metal-Organic Framework. *J. Am. Chem. Soc.* 142, 17105–17118. doi:10.1021/jacs.0c07153

Gutterod, E. S., Lazzarini, A., Fjermestad, T., Kaur, G., Manzoli, M., Bordiga, S., et al. (2019). Hydrogenation of CO_2 to Methanol by Pt Nanoparticles Encapsulated in UiO-67: Deciphering the Role of the Metal–Organic Framework. *J. Am. Chem. Soc.* 142, 999–1009. doi:10.1021/jacs.9b10873

Handoko, A. D., Li, K., and Tang, J. (2013). Recent Progress in Artificial Photosynthesis: CO_2 Photoreduction to Valuable Chemicals in a Heterogeneous System. *Curr. Opin. Chem. Eng.* 2, 200–206. doi:10.1016/j.coche.2012.12.003

Hu, B., Yin, Y., Zhong, Z., Wu, D., Liu, G., and Hong, X. (2019). Cu@ZIF-8 Derived Inverse ZnO/Cu Catalyst with Sub-5 Nm ZnO for Efficient CO_2 Hydrogenation to Methanol. *Catal. Sci. Technol.* 9, 2673–2681. doi:10.1039/c8cy02546k

Jhong, H.-R. M., Ma, S., and Kenis, P. J. (2013). Electrochemical Conversion of CO_2 to Useful Chemicals: Current Status, Remaining Challenges, and Future Opportunities. *Curr. Opin. Chem. Eng.* 2, 191–199. doi:10.1016/j.coche.2013.03.005

Kumar, P., Vellingiri, K., Kim, K.-H., Brown, R. J. C., and Manos, M. J. (2017). Modern Progress in Metal-Organic Frameworks and Their Composites for Diverse Applications. *Microporous Mesoporous Mater.* 253, 251–265. doi:10.1016/j.micromeso.2017.07.003

Larmier, K., Liao, W.-C., Tada, S., Lam, E., Verel, R., Bansode, A., et al. (2017). CO_2-to-Methanol Hydrogenation on Zirconia-Supported Copper Nanoparticles: Reaction Intermediates and the Role of the Metal-Support Interface. *Angew. Chem. Int. Ed.* 56, 2318–2323. doi:10.1002/anie.201610166

Lippi, R., D'Angelo, A. M., Li, C., Howard, S. C., Madsen, I. C., Wilson, K., et al. (2021). Unveiling the Structural Transitions during Activation of a CO_2 Methanation Catalyst Ru0/ZrO2 Synthesised from a MOF Precursor. *Catal. Today* 368, 66–77. doi:10.1016/j.cattod.2020.04.043

Lippi, R., Howard, S. C., Barron, H., Easton, C. D., Madsen, I. C., Waddington, L. J., et al. (2017). Highly Active Catalyst for CO_2 Methanation Derived from a Metal Organic Framework Template. *J. Mat. Chem. A* 5, 12990–12997. doi:10.1039/c7ta00958e

Liu, L., Zhao, H., Andino, J. M., and Li, Y. (2012). Photocatalytic CO_2 Reduction with H_2O on TiO_2 Nanocrystals: Comparison of Anatase, Rutile, and Brookite Polymorphs and Exploration of Surface Chemistry. *ACS Catal.* 2, 1817–1828. doi:10.1021/cs300273q

Liu, T., Hong, X., and Liu, G. (2019). *In Situ* Generation of the Cu@3D-ZrOx Framework Catalyst for Selective Methanol Synthesis from CO_2/H_2. *ACS Catal.* 10, 93–102. doi:10.1021/acscatal.9b03738

Liu, W.-C., Baek, J., and Somorjai, G. A. (2018). The Methanol Economy: Methane and Carbon Dioxide Conversion. *Top. Catal.* 61, 530–541. doi:10.1007/s11244-018-0907-4

Mihet, M., Grad, O., Blanita, G., Radu, T., and Lazar, M. D. (2019). Effective Encapsulation of Ni Nanoparticles in Metal-Organic Frameworks and Their Application for CO_2 Methanation. *Int. J. Hydrogen Energy* 44, 13383–13396. doi:10.1016/j.ijhydene.2019.03.259

Murthy, P. S., Liang, W., Jiang, Y., and Huang, J. (2021). Cu-Based Nanocatalysts for CO_2 Hydrogenation to Methanol. *Energy fuels.* 35, 8558–8584. doi:10.1021/acs.energyfuels.1c00625

NOAA (2022). Trends in Atmospheric Carbon Dioxide: Full Record. ESRL Global Monitoring Division, Global Greenhouse Gas Reference Network. Available at: https://gml.noaa.gov/ccgg/trends/global.html (Accessed Apr 15, 2022).

Perathoner, S., and Centi, G. (2019). Catalysis for Solar-Driven Chemistry: The Role of Electrocatalysis. *Catal. Today* 330, 157–170. doi:10.1016/j.cattod.2018.03.005

Porosoff, M. D., Yan, B., and Chen, J. G. (2016). Catalytic Reduction of CO_2 by H_2 for Synthesis of CO, Methanol and Hydrocarbons: Challenges and Opportunities. *Energy Environ. Sci.* 9, 62–73. doi:10.1039/c5ee02657a

Pustovarenko, A., Dikhtiarenko, A., Bavykina, A., Gevers, L., Ramírez, A., Russkikh, A., et al. (2020). Metal-Organic Framework-Derived Synthesis of Cobalt Indium Catalysts for the Hydrogenation of CO_2 to Methanol. *ACS Catal.* 10, 5064–5076. doi:10.1021/acscatal.0c00449

Qin, Z., Zhou, Y., Jiang, Y., Liu, Z., and Ji, H. (2017). "Recent Advances in Heterogeneous Catalytic Hydrogenation of CO_2 to Methane," in *New Advances in Hydrogenation Processes - Fundamentals and Applications* (Londan: IntechOpen), 57–82.

Rafiee, A., Rajab Khalilpour, K., Milani, D., and Panahi, M. (2018). Trends in CO_2 Conversion and Utilization: A Review from Process Systems Perspective. *J. Environ. Chem. Eng.* 6, 5771–5794. doi:10.1016/j.jece.2018.08.065

Ramirez, A., Gevers, L., Bavykina, A., Ould-Chikh, S., and Gascon, J. (2018). Metal Organic Framework-Derived Iron Catalysts for the Direct Hydrogenation of CO_2 to Short Chain Olefins. *ACS Catal.* 8, 9174–9182. doi:10.1021/acscatal.8b02892

Ranocchiari, M., and Bokhoven, J. A. v. (2011). Catalysis by Metal–Organic Frameworks: Fundamentals and Opportunities. *Phys. Chem. Chem. Phys.* 13, 6388. doi:10.1039/c0cp02394a

Rungtaweevoranit, B., Baek, J., Araujo, J. R., Archanjo, B. S., Choi, K. M., Yaghi, O. M., et al. (2016). Copper Nanocrystals Encapsulated in Zr-Based Metal-Organic Frameworks for Highly Selective CO_2 Hydrogenation to Methanol. *Nano Lett.* 16, 7645–7649. doi:10.1021/acs.nanolett.6b03637

Sha, F., Han, Z., Tang, S., Wang, J., and Li, C. (2020). Hydrogenation of Carbon Dioxide to Methanol over Non-cu-based Heterogeneous Catalysts. *ChemSusChem* 13, 6160–6181. doi:10.1002/cssc.202002054

Song, C. (2006). Global Challenges and Strategies for Control, Conversion and Utilization of CO_2 for Sustainable Development Involving Energy, Catalysis, Adsorption and Chemical Processing. *Catal. Today* 115, 2–32. doi:10.1016/j.cattod.2006.02.029

Srinivas, G., Krungleviciute, V., Guo, Z.-X., and Yildirim, T. (2014). Exceptional CO_2capture in a Hierarchically Porous Carbon with Simultaneous High Surface Area and Pore Volume. *Energy Environ. Sci.* 7, 335–342. doi:10.1039/c3ee42918k

Usman, M., Helal, A., Abdelnaby, M. M., Alloush, A. M., Zeama, M., and Yamani, Z. H. (2021). Trends and Prospects in UiO-66 Metal-Organic Framework for CO 2 Capture, Separation, and Conversion. *Chem. Rec.* 21, 1771–1791. doi:10.1002/tcr.202100030

Valles-Regino, R., Tate, R., Kelaher, B., Savins, D., Dowell, A., and Benkendorff, K. (2015). Ocean Warming and CO_2-Induced Acidification Impact the Lipid Content of a Marine Predatory Gastropod. *Mar. Drugs* 13, 6019–6037. doi:10.3390/md13106019

Wang, C., An, B., and Lin, W. (2018). Metal-Organic Frameworks in Solid-Gas Phase Catalysis. *ACS Catal.* 9, 130–146. doi:10.1021/acscatal.8b04055

Wang, H. (2022). Nanostructure@metal-organic Frameworks (MOFs) for Catalytic Carbon Dioxide (CO_2) Conversion in Photocatalysis, Electrocatalysis, and Thermal Catalysis. *Nano Res.* 15, 2834–2854. doi:10.1007/s12274-021-3984-9

Wang, J.-J., Li, X.-P., Cui, B.-F., Zhang, Z., Hu, X.-F., Ding, J., et al. (2021). A Review of Non-noble Metal-Based Electrocatalysts for CO_2 Electroreduction. *Rare Met.* 40, 3019–3037. doi:10.1007/s12598-021-01736-x

Wang, S., Zhang, L., Wang, P., Liu, X., Chen, Y., Qin, Z., et al. (2022). Highly Effective Conversion of CO_2 into Light Olefins Abundant in Ethene. *Chem* 8, 1376–1394. doi:10.1016/j.chempr.2022.01.004

Wang, S., Zhang, L., Zhang, W., Wang, P., Qin, Z., Yan, W., et al. (2020). Selective Conversion of CO_2 into Propene and Butene. *Chem* 6, 3344–3363. doi:10.1016/j.chempr.2020.09.025

Wang, W.-H., Himeda, Y., Muckerman, J. T., Manbeck, G. F., and Fujita, E. (2015). CO_2 Hydrogenation to Formate and Methanol as an Alternative to Photo- and Electrochemical CO_2 Reduction. *Chem. Rev.* 115, 12936–12973. doi:10.1021/acs.chemrev.5b00197

Wang, Y., Tan, L., Tan, M., Zhang, P., Fang, Y., Yoneyama, Y., et al. (2018). Rationally Designing Bifunctional Catalysts as an Efficient Strategy to Boost CO_2 Hydrogenation Producing Value-Added Aromatics. *ACS Catal.* 9, 895–901. doi:10.1021/acscatal.8b01344

Wang, Y., Wang, K., Zhang, B., Peng, X., Gao, X., Yang, G., et al. (2021). Direct Conversion of CO_2 to Ethanol Boosted by Intimacy-Sensitive Multifunctional Catalysts. *ACS Catal.* 11, 11742–11753. doi:10.1021/acscatal.1c01504

Wang, Y., Zhan, W., Chen, Z., Chen, J., Li, X., and Li, Y. (2020). Advanced 3D Hollow-Out ZnZrO@C Combined with Hierarchical Zeolite for Highly Active and Selective CO Hydrogenation to Aromatics. *ACS Catal.* 10, 7177–7187. doi:10.1021/acscatal.0c01418

Wei, J., Yao, R., Han, Y., Ge, Q., and Sun, J. (2021). Towards the Development of the Emerging Process of CO_2 Heterogenous Hydrogenation into High-Value Unsaturated Heavy Hydrocarbons. *Chem. Soc. Rev.* 50, 10764–10805. doi:10.1039/d1cs00260k

Yang, H., Zhang, C., Gao, P., Wang, H., Li, X., Zhong, L., et al. (2017). A Review of the Catalytic Hydrogenation of Carbon Dioxide into Value-Added Hydrocarbons. *Catal. Sci. Technol.* 7, 4580–4598. doi:10.1039/c7cy01403a

Yang, Y., Xu, Y., Ding, H., Yang, D., Cheng, E., Hao, Y., et al. (2021). Cu/ZnOx@UiO-66 Synthesized from a Double Solvent Method as an Efficient Catalyst for CO_2 Hydrogenation to Methanol. *Catal. Sci. Technol.* 11, 4367–4375. doi:10.1039/d0cy02450c

Yarulina, I., Chowdhury, A. D., Meirer, F., Weckhuysen, B. M., and Gascon, J. (2018). Recent Trends and Fundamental Insights in the Methanol-To-Hydrocarbons Process. *Nat. Catal.* 1, 398–411. doi:10.1038/s41929-018-0078-5

Yin, Y., Hu, B., Li, X., Zhou, X., Hong, X., and Liu, G. (2018). Pd@zeolitic Imidazolate Framework-8 Derived PdZn Alloy Catalysts for Efficient Hydrogenation of CO_2 to Methanol. *Appl. Catal. B Environ.* 234, 143–152. doi:10.1016/j.apcatb.2018.04.024

Yu, J., Liu, S., Mu, X., Yang, G., Luo, X., Lester, E., et al. (2021). Cu-ZrO2 Catalysts with Highly Dispersed Cu Nanoclusters Derived from ZrO2@ HKUST-1 Composites for the Enhanced CO_2 Hydrogenation to Methanol. *Chem. Eng. J.* 419, 129656. doi:10.1016/j.cej.2021.129656

Zhang, W., Jin, Z., and Chen, Z. (2022a). Rational-Designed Principles for Electrochemical and Photoelectrochemical Upgrading of CO_2 to Value-Added Chemicals. *Adv. Sci.* 9, 2105204. doi:10.1002/advs.202105204

Zhang, W., Ma, D., Pérez-Ramírez, J., and Chen, Z. (2021). Recent Progress in Materials Exploration for Thermocatalytic, Photocatalytic, and Integrated Photothermocatalytic CO 2 -to-Fuel Conversion. *Adv Energy Sustain Res* 3, 2100169. doi:10.1002/aesr.202100169

Zhang, W., Wang, S., Guo, S., Qin, Z., Dong, M., Wang, J., et al. (2022b). Effective Conversion of CO_2 into Light Olefins over a Bifunctional Catalyst Consisting of La-Modified ZnZrOx Oxide and Acidic Zeolite. *Catal. Sci. Technol.* 12, 2566–2577. doi:10.1039/d2cy00210h

Zhao, Z.-W., Zhou, X., Liu, Y.-N., Shen, C.-C., Yuan, C.-Z., Jiang, Y.-F., et al. (2018). Ultrasmall Ni Nanoparticles Embedded in Zr-Based MOFs Provide High Selectivity for CO_2 Hydrogenation to Methane at Low Temperatures. *Catal. Sci. Technol.* 8, 3160–3165. doi:10.1039/c8cy00468d

Zhen, W., Li, B., Lu, G., and Ma, J. (2015). Enhancing Catalytic Activity and Stability for CO_2 Methanation on Ni@MOF-5 via Control of Active Species Dispersion. *Chem. Commun.* 51, 1728–1731. doi:10.1039/c4cc08733j

Zhou, C., Shi, J., Zhou, W., Cheng, K., Zhang, Q., Kang, J., et al. (2019). Highly Active ZnO-ZrO2 Aerogels Integrated with H-ZSM-5 for Aromatics Synthesis from Carbon Dioxide. *ACS Catal.* 10, 302–310. doi:10.1021/acscatal.9b04309

Zhu, Y., Zheng, J., Ye, J., Cui, Y., Koh, K., Kovarik, L., et al. (2020). Copper-zirconia Interfaces in UiO-66 Enable Selective Catalytic Hydrogenation of CO_2 to Methanol. *Nat. Commun.* 11, 5849. doi:10.1038/s41467-020-19438-w

Conflict of Interest: The authors declare that the research was conducted in the absence of any commercial or financial relationships that could be construed as a potential conflict of interest.

Publisher's Note: All claims expressed in this article are solely those of the authors and do not necessarily represent those of their affiliated organizations, or those of the publisher, the editors, and the reviewers. Any product that may be evaluated in this article, or claim that may be made by its manufacturer, is not guaranteed or endorsed by the publisher.

frontiers | Frontiers in Chemistry

TYPE Review
PUBLISHED 19 July 2022
DOI 10.3389/fchem.2022.958626

OPEN ACCESS

EDITED BY
Yulian He,
Shanghai Jiao Tong University, China

REVIEWED BY
Meng Zhou,
University of Science and Technology of China, China
Hui Jiang,
Southeast University, China

*CORRESPONDENCE
Ke Hu,
khu@fudan.edu.cn

SPECIALTY SECTION
This article was submitted to Photocatalysis and Photochemistry, a section of the journal Frontiers in Chemistry

RECEIVED 31 May 2022
ACCEPTED 28 June 2022
PUBLISHED 19 July 2022

CITATION
Cheng D, Liu R and Hu K (2022), Gold nanoclusters: Photophysical properties and photocatalytic applications. *Front. Chem.* 10:958626. doi: 10.3389/fchem.2022.958626

Gold nanoclusters: Photophysical properties and photocatalytic applications

Dajiao Cheng, Rong Liu and Ke Hu*

Department of Chemistry, Fudan University, Shanghai, China

Atomically precise gold nanoclusters (Au NCs) have high specific surface area and abundant unsaturated active sites. Traditionally, Au NCs are employed as thermocatalysts for multielectron transfer redox catalysis. Meanwhile, Au NCs also exhibit discrete energy levels, tunable photophysical and electrochemical properties, including visible to near infrared absorption, microsecond long-lived excited-state lifetime, and redox chemistry. In recent years, Au NCs are increasingly employed as visible to near infrared photocatalysts for their high photocatalytic activity and unique selectivity. This review focuses on the photophysical properties of a variety of Au NCs and their employment as photocatalysts in photocatalytic reactions and related applications including solar energy conversion and photodynamic therapies.

KEYWORDS

gold nanoclusters, photophysics, photocatalysis, solar energy conversion, phototherapy

Introduction

Metal nanoclusters (NCs) are a new type of nanomaterials with core-shell structures. The core comprises a few to hundreds of metal atoms and the outer shell consists of ligands protecting the core from aggregation (Figure 1A) (Chen and Li, 2020). In recent decades, noble metal nanoclusters especially gold have attracted extensive attention. The size of gold nanoclusters (Au NCs) is typically less than 2 nm, which is between that of small molecules and metal nanoparticles (NPs). Because the size is close to the de Broglie wavelength of the electron at the Fermi level of Au atoms (about 0.5 nm) (Xu and Suslick, 2010), Au NCs exhibit discrete energy levels and a variety of molecular-like properties (Aikens, 2011), such as the atomically precise molecular formula, multiple visible absorption peaks, tunable luminescence, and molecular-like excited-state dynamics (Figure 1B) (Song et al., 2016; Maity et al., 2019; Zhou et al., 2021).

Unlike small molecules, Au NCs possess high specific surface areas and a large number of unsaturated reaction sites (Du et al., 2020), which lead to high catalytic activities and unique selectivity in catalytic reactions such as oxidation, hydrogenation, and C-C coupling (Li and Jin, 2013; Fang et al., 2016; Jin et al., 2016). It is worth mentioning that monodisperse Au NCs with well-defined structures can be used as model catalysts to reveal the correlation between catalyst performance and structure at the atomic scale (Du et al., 2020). The focus of this review will be on the optical properties

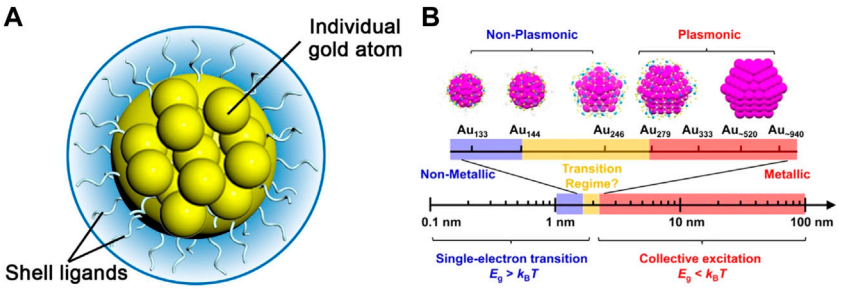

FIGURE 1
(A) Schematic illustration of the core-shell structure of Au NCs **(B)** Changes in the band gap as the number of atoms in a material decreases. Reprinted with permission from (Zhou et al., 2021). Copyright 2021 American Chemical Society.

from Au NC's unique electronic transitions as well as the practical applications of photocatalysis, solar energy conversion, and phototherapies that make use of Au NC's electronically excited states.

Photophysical properties

Basic theories of gold nanocluster structure

The photophysical properties of atomically precise gold nanoclusters are closely related to the number of gold atoms. Researchers found that Au NCs had a specific number of atoms, known as the "magic number" (Negishi et al., 2004; Negishi et al., 2007). The magic-number gold nanoclusters exhibit high stability and similar photophysical properties. The "superatom electronic theory" proposed by Häkkinen et al. explained the stability of magic-number gold nanoclusters (Hakkinen, 2008; Walter et al., 2008). The core of Au NCs has delocalized "superatomic orbitals" including 1S, 1P, 1D, 2S, 1F, 2P, 1G, 2D, 1H, 3S, 1I.... The effective valence electrons of the gold core are filled into superatomic orbitals in turn according to the aufbau rule. Closed electron shells appear for the gold cores similar to the chemically inert noble gases, so Au NCs are chemically stable. For example, $Au_{102}(SR)_{44}$ protected by organic thiolate ligands (-SR), the first Au NCs to be comprehensively characterized by X-ray crystal structure determination, has the exact formula of Au_{79} [Au (*p*-MBA)$_2$]$_{19}$ [Au (*p*-MBA)$_3$]$_2$ (Jadzinsky et al., 2007). The effective valence electron number of the Au_{79} core is 58 (= 79-19-2), which just meets the closed-electron-shell configuration of $1S^21P^61D^{10}2S^21F^{14}2P^61G^{18}$, so the Au_{79} core exhibits high stability (Walter et al., 2008).

The correlation between the photophysical properties and the number of gold atoms is attributed to the discrete energy levels, which are affected by the quantum size effect. The quantum size effect was explained in detail by the Kubo criterion and the Jellium model (Kubo, 1962; Wood and Ashcroft, 1982).

Kubo proposed that the gap between the highest occupied state and the lowest unoccupied state (called the Kubo gap δ) of a particle consisting of N atoms was proportional to E_f/N, where E_f is the Fermi potential of the bulk metal. Comparing d and thermal energy (kT), it is possible to judge whether a material has metallic or non-metallic properties (Kubo, 1962). When d is less than kT, electrons are excited thermally to generate free electron-hole pairs. However, when d is much larger than kT, free electrons are confined to the discrete energy levels (Roduner, 2006). Metal nanoclusters are usually non-metallic with molecular-like photophysical properties.

Later, the Jellium model clarified the quantitative relationship between the electronic structure of the cores in the metal nanoclusters and the number of metal atoms. In the Jellium model, the valence electrons of the metal core are confined in orbitals that have the same symmetry as the atomic orbitals. The valence electrons are also filled according to the aufbau rule. D. M. Wood and N. W. Ashcroft proved that the energy gap of metal nanoclusters was about $E_f/N^{1/3}$ through the Jellium model, where N was the number of metal atoms in the cluster and E_f was the Fermi potential energy of the bulk metal (Wood and Ashcroft, 1982).

UV-vis absorption

Ultrasmall-sized gold nanoclusters with discrete energy levels exhibit unique optical absorption, radiative transitions, and excited-state dynamics (Aikens, 2011). Researchers delved into the origin and influencing factors of these photophysical properties, including the cluster geometry such as size, crystal structure and atomic packing, the charge state of the cluster, and the nature of the ligands.

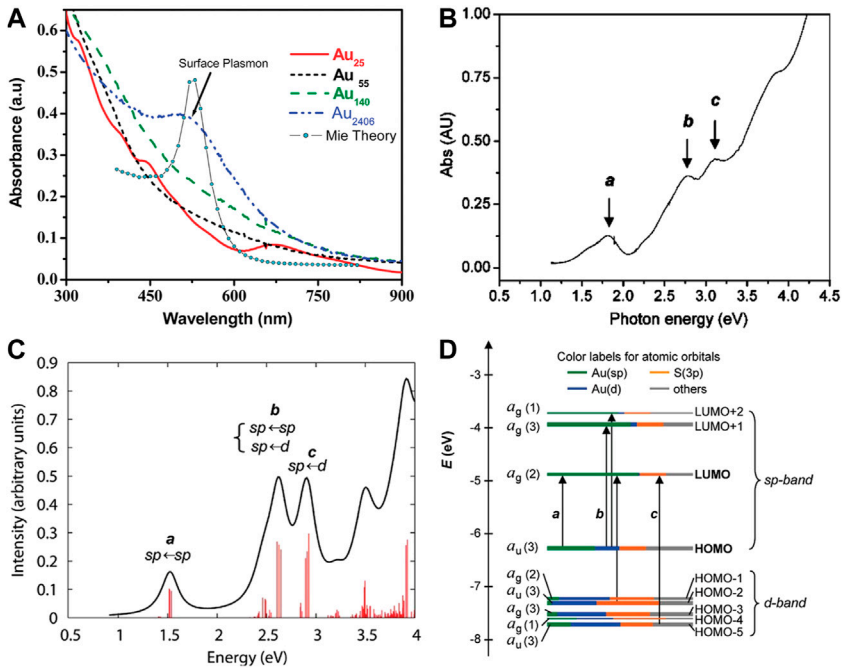

FIGURE 2
(A) UV-vis-NIR absorption spectra of gold nanoparticles and gold nanoclusters. Reprinted with permission from (Yau et al., 2010). Copyright 2010 American Chemical Society **(B)** The experimental absorption spectrum and **(C)** the theoretical absorption spectrum of $Au_{25}(SH)_{18}^-$ **(D)** Kohn–Sham orbital energy level diagram for a model compound $Au_{25}(SH)_{18}^-$. Reprinted with permission from (Zhu et al., 2008a). Copyright 2008 American Chemical Society.

The optical absorption spectra of gold nanoparticles and gold nanoclusters have obvious differences. Gold nanoparticles such as Au_{2406} NPs have the surface plasmonic resonance peak, while Au NCs do not have (Figure 2A) (Yau et al., 2010). The single-electron transitions between discrete energy levels of Au NCs constitute the molecular absorption (Aikens, 2011).

In 2008, Jin and co-workers first reported the crystal structure of $Au_{25}(SR)_{18}$ and studied the correlation between the electronic structure and optical properties by time-dependent density functional theory (TDDFT) calculations (Zhu et al., 2008a). The theoretical absorption spectrum of $Au_{25}(SH)_{18}^-$ is in good agreement with the experimental absorption spectrum (Figures 2B,C). Peak a is attributed to the HOMO-LUMO intraband transition (sp←sp). Peak c corresponds to the interband transition (sp←d) from HOMO-n to LUMO. Peak b belongs to the mixed transition (Figure 2D).

Crystal structure analysis shows that the center of $Au_{25}(SR)_{18}$ is an icosahedral Au_{13} core and the outer layer is composed of twelve Au atoms and eighteen thiolate ligands. Each outer Au-Au pair (six pairs in total) is bridged by one-SR ligand and with two other-SR ligands bridging between the outer Au atoms and the icosahedral Au_{13} core. HOMO, LUMO, LUMO+1, LUMO+2 and other orbitals are almost entirely composed of the atomic orbitals of thirteen Au atoms in the icosahedral core. Therefore, the absorption peak a at 1.52 eV (Figures 2B,C) is regarded as a transition caused by the electronic structure and geometry of the Au_{13} core (Zhu et al., 2008a). Biicosahedral $[Au_{25}(PPh_3)_{10}(SC_nH_{2n+1})_5Cl_2]^{2+}$ clusters have the completely different crystal structure (Shichibu et al., 2007). The optical absorption peak at 1.76 eV originates from the interaction between two icosahedral Au_{13} units sharing vertices rather than the electronic transitions within a single Au_{13} unit. The above two findings indicate that the crystal structure of Au NCs also affects the optical absorption.

Although the $Au_{25}(SR)_{18}$ cluster is divided into two parts including the Au_{13} core and the ligand layer, the optical absorption spectrum of $Au_{25}(SH)_{18}^-$ cluster is not a simple linear combination of the spectra from the metal core and the ligand, which is demonstrated with more detailed TDDFT calculations. The complex absorption spectrum of the $Au_{25}(SR)_{18}$ cluster arises from the geometrical and electronic interactions between the metal core and ligands (Aikens, 2008).

Optical absorption of Au NCs is affected by the quantum size effect. As the size of the Au NCs decreases, the gap of discrete energy levels increases and the optical absorption of the clusters shows blue shifts (Figure 3A). For example, the absorption onsets of $Au_{10\text{-}12}(SG)_{10\text{-}12}$ cluster, $Au_{15}(SG)_{13}$ cluster, $Au_{18}(SG)_{14}$ cluster, and $Au_{25}(SG)_{18}$ cluster are 450, 650, 700, and 900 nm,

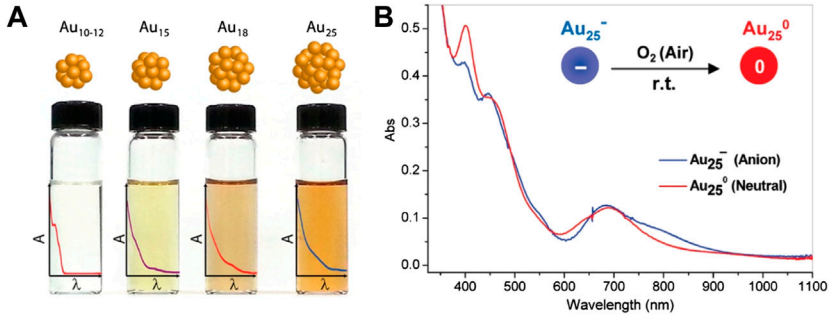

FIGURE 3
(A) The structural diagram and the optical absorption spectra changes of different sizes of Au NCs. Reprinted with permission from (Stamplecoskie and Kamat, 2014). Copyright 2014 American Chemical Society **(B)** Optical absorption spectra of anionic Au_{25}^- cluster (blue) and charge neutral Au_{25} cluster (red) in solution. Reprinted with permission from (Zhu et al., 2008b). Copyright 2008 American Chemical Society.

respectively (Yu Y. et al., 2013; Stamplecoskie and Kamat, 2014). The absorption onset of the $Au_{144}(SR)_{60}$ cluster is located at 700 nm (Qian and Jin, 2011). Meanwhile, when the cluster size is reduced to $Au_{25}(SR)_{18}$, the absorption onset shows the blue shift to 670 nm. Jin summarizes the stable sizes of thiolate-protected gold nanoclusters and the size dependence of the optical absorption in detail (Jin, 2015).

However, there are exceptions to the size dependence of the optical absorption. For example, the size of the $Au_{22}(SR)_{18}$ cluster is larger than that of the $Au_{18}(SR)_{14}$ cluster, but its absorption onset shows a blue shift of 20 nm (Yu et al., 2014; Pyo et al., 2015; Yu et al., 2015). This phenomenon suggests that the optical absorption of Au NCs is not only related to the size but also to the ratio between the number of ligands and the number of metal atoms.

The electron-withdrawing properties of surface-protecting ligands in Au NCs also affect the optical absorption of the Au NCs. For example, the introduction of electron-withdrawing groups (-X) into p-thiophenol (p-SPhX) ligands induces distortion to the $Au_{25}(SPhX)_{18}$ framework and the degree of distortion increases with enhancement of the electron-withdrawing properties. As the distorted degree of the cluster framework increases, the HOMO-LUMO gap becomes smaller and the optical absorption exhibits red shifts (Tlahuice-Flores et al., 2013). A similar phenomenon is also observed in the $Au_{38}(SPhX)_{24}$ cluster, where the optical absorption exhibits a slight red shift with the enhancement of the electron-withdrawing properties of the -X substituent. However, Murray and co-workers believe that the ligand layer affects the electron energy of the gold core in the cluster but does not change the HOMO-LUMO energy gap (Guo and Murray, 2005). The HOMO-LUMO electronic absorption peak of the $Au_{25}(SNap)_{18}^-$ cluster (SNap = 1-naphthalenethiolate) shows a red shift of about 10 nm compared with that of the $Au_{25}(SC_2H_4Ph)_{18}^-$ cluster, which is attributed to the expansion of the Au_{13} core induced by the aromatic thiolate ligands (Li et al., 2016).

Au NC surface charges from surface-protecting ligands also affect the optical absorption of Au NCs. Xie et al. used multiple ligands with different charges, such as $-COO^-$, $-NH_3^+$, and $-OH$, to induce the surface charge anisotropy of the Au_{25} clusters. This results in structural distortion, which in turn leads to the anomalous optical absorptions at about 780 and 980 nm (Yuan et al., 2016).

In addition to the charges of the ligands, the surface charge states of the clusters also have an effect on the optical absorption spectra (Lee et al., 2004; Negishi et al., 2007; Zhu et al., 2008b). For example, anionic Au_{25}^- cluster loses one electron and counterion tetraoctylammonium TOA^+ when it is oxidized to charge neutral Au_{25} cluster in air, resulting in the structural distortion of the gold core which affects the optical absorption of the cluster. The optical absorption spectra of the anionic cluster and the charge neutral cluster are generally similar in shape. However, the absorption around 800 nm in the anionic cluster disappears in the charge neutral cluster, while the weak absorption around 400 nm in the anionic cluster is significantly enhanced in the charge neutral cluster (Figure 3B) (Zhu et al., 2008b). When the $Au_{25}(SC_2H_4Ph)_{18}^q$ cluster is oxidized, the surface charge q gradually changes from negative charge to positive charge, resulting in an enlarged HOMO-LUMO gap and a red shift in the optical absorption (Venzo et al., 2011). Density functional theory (DFT) calculations further verify the correlation between the surface charge states of the cluster and the optical absorption (Antonello et al., 2013).

Photoluminescence

Au NCs exhibit visible to near-infrared (NIR) emission (Bigioni et al., 2000; Huang and Murray, 2001; Link et al., 2002). The origin of Au NCs photoluminescence remains debatable. Ramakrishna et al. employing time-resolved

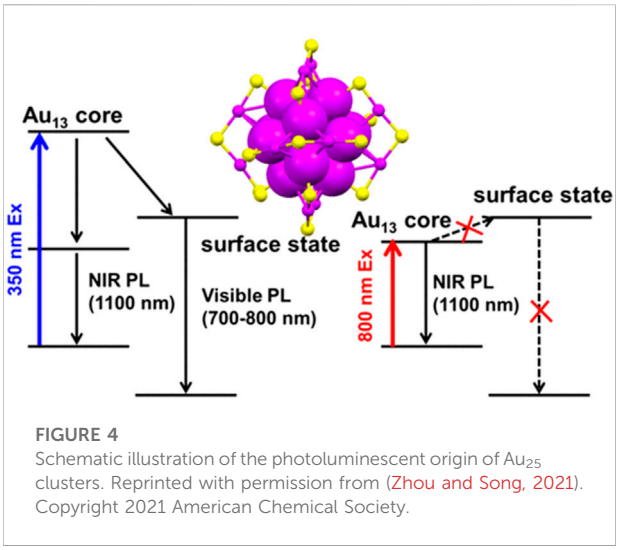

FIGURE 4
Schematic illustration of the photoluminescent origin of Au_{25} clusters. Reprinted with permission from (Zhou and Song, 2021). Copyright 2021 American Chemical Society.

luminescence spectroscopy of monolayer thiolate-protected Au_{25} clusters have revealed that the NIR luminescence originates from the S-Au-S-Au-S semi-ring states and the visible luminescence originates from the Au_{13} core states (Devadas et al., 2010). However, Aikens et al. calculated that photoluminescence of the Au_{25} cluster were all ascribed to core-based orbitals. Variation of the ligand lengths only influenced photoluminescence spectra from molecular orbital energy shifts. (Weerawardene and Aikens, 2016). A more recent study of the Au_{25} clusters photoluminescence asserted that NIR emission around 1,100 nm should be the dominant gap emission of the Au_{13} core state rather than the weak emission around 700 nm of the core-shell charge transfer state because the photoluminescent excitation spectra with emission monitored at ~700 nm showed a different profile in comparison with the absorption spectra of Au_{13} clusters. In addition, the lifetime of the Au_{25} clusters excited state obtained from transient absorption spectroscopy is highly consistent with the lifetime of that obtained from the NIR photoluminescence. (Figure 4) (Zhou and Song, 2021). The detailed photoluminescence origin of the Au NCs is subject to data interpretation possibly due to different charge-donating capability or hydrophilicity of ligands. The changes under different experimental conditions may also vary significantly.

In earlier studies, the quantum yields (QY) of most thiolate-protected gold nanoclusters are less than 1% and the utilization of incident light is low (Link et al., 2002; Negishi et al., 2004; Negishi et al., 2005). A few Au NCs exhibit higher quantum yields including the $Au_{18}(SG)_{14}$ cluster with a QY of 5.3% and the $Au_{22}(SG)_{18}$ cluster with a QY of about 8% (Ghosh et al., 2012; Yu et al., 2014). Researchers find that the size and structure of Au NCs determine the photoluminescence emission wavelength and QY. Meanwhile, both different surface-protecting ligands and aggregation-induced emission (AIE) can enhance QY.

Bulk metals with no band gap and non-radiative decay usually have weak photoluminescent emission. As the size shrinks to the nanometer scale and approaches the Fermi wavelength of electrons, the bulk metal transforms into the cluster. The discrete energy levels of clusters cause strong luminescence in addition to the molecular-like optical absorption. According to the Jellium model (Wood and Ashcroft, 1982), as the atom numbers in the metal core of the cluster increase, there is a red shift in the photoluminescence. For example, pepsin-protected Au_8 cluster, Au_{13} cluster, and Au_{25} cluster synthesized by changing the pH emit blue, green, and red photoluminescent emission, respectively (Kawasaki et al., 2011). Adjusting the molar ratios among the dendrimer ligands, Au^{3+}, and the amount of $NaBH_4$, a series of Au_5 clusters, Au_8 clusters, Au_{13} clusters, Au_{23} clusters, and Au_{31} clusters of the same type were synthesized and their photoluminescent emission bands shift from UV to NIR (Figure 5A) (Zheng et al., 2004).

Optical properties of Au NCs are not only related to the size but also to the crystal structure. Biicosahedral $[Au_{25}(PPh_3)_{10}(SC_nH_{2n+1})_5Cl_2]^{2+}$ clusters and the icosahedral $Au_{25}(SC_2H_4Ph)_{18}$ have completely different crystal structures (Zhu et al., 2008a). Although both clusters have 25 gold atoms, they have different UV-vis absorption and photoluminescent emission.

The photoluminescence of Au NCs is also affected by the surface ligands, which have little effect on the photoluminescence wavelength but significantly affect QY. Ligands with electron-rich atoms (such as N, O) or groups (such as –COOH, NH_2) can interact with the surface of Au NCs and transfer delocalized electrons directly to the Au core to effectively enhance QY. For example, water-soluble thiolate GSH-protected $Au_{25}(SG)_{18}^-$ clusters show stronger photoluminescence emission than hydrophobic organic thiolate-protected $Au_{25}(SR)_{18}^-$ clusters (Wu and Jin, 2010).

Electron donating ligands can enhance ligand-to-metal charge transfer (LMCT) and ligand-to-metal-metal charge transfer (LMMCT) to strengthen the photoluminescent emission intensity. Jin and co-workers find that the photoluminescence intensity of hydrophobic thiolate-protected gold nanoclusters is proportional to the electron-donating properties of the ligands (Figure 5B) (Wu and Jin, 2010). In the follow-up work, Jin et al. verify the conclusion again that the lower electronegativity or the stronger electron-donating property of the ligands have, the stronger the photoluminescence of the $Au_{36}(SR)_{24}$ clusters are (Kim et al., 2017). The decreased electronegativity of the cluster can also strengthen the electron transfer between the ligand and the gold core to enhance photoluminescent emission. The higher valence of the surface charge q the $Au_{25}(SC_2H_4Ph)_{18}^q$ cluster has, the stronger photoluminescence intensity the cluster shows (Wu and Jin, 2010).

Polar ligands can also affect the electron transfer between thiolate ligands and the gold core to change the photoluminescence intensity of the cluster. For example, an

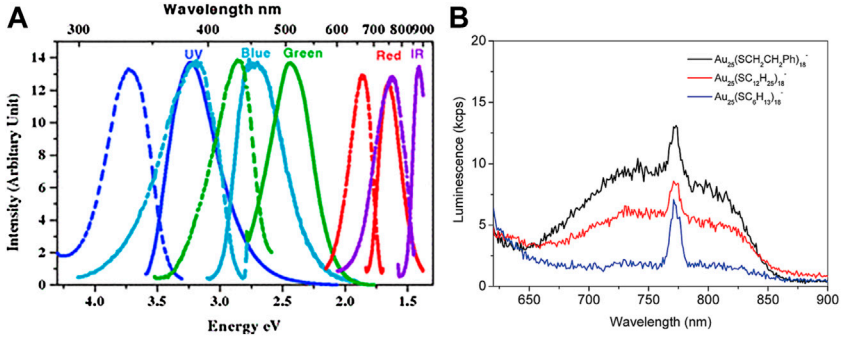

FIGURE 5
(A) Excitation spectra (dashed) and emission spectra (solid) of dendrimer-protected gold nanoclusters different sizes. Reprinted with permission from (Zheng et al., 2004). Copyright 2004 by the American Physical Society **(B)** Photoluminescence spectra of $Au_{25}(SR)_{18}^-$ with different –R groups ($-C_2H_4Ph$, $-C_{12}H_{25}$, $-C_6H_{13}$). Reprinted with permission from (Wu and Jin, 2010). Copyright 2010 American Chemical Society.

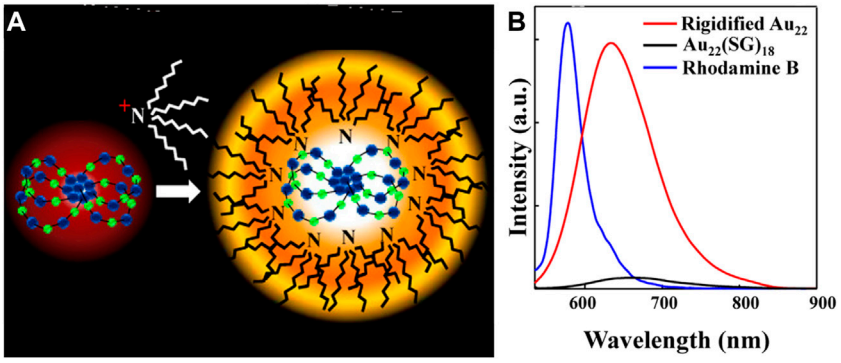

FIGURE 6
(A) Schematic representation of TOA^+ binding to the $Au_{22}(SG)_{18}$ cluster (Au in blue and S in green) **(B)** Photoluminescence spectra of $Au_{22}(SG)_{18}$ clusters in aqueous solution and TOA–Au_{22} clusters in toluene. Reprinted with permission from (Pyo et al., 2015). Copyright 2015 American Chemical Society.

increase in the polarization of the Au-S bond can enhance the photoluminescence intensity. Murray et al. find that when the non-polar ligands on the surface of Au_{38} clusters and Au_{140} clusters are replaced by polar ligands, the NIR photoluminescence intensity of the clusters increases and the intensity is related to the number of polar ligands linearly (Wang et al., 2006).

The photoluminescence intensity of non-photoluminescent polydentate polymer-protected gold nanoclusters is proportional to the electron-donating ability of the ligands and is also affected by the steric hindrance of the polymer (Li et al., 2013). Au NCs protected by sterically hindered polymer PTMP-P*t*BMA have the highest QY of about 20.1%. The rigid Au(I)-thiolate shell can also improve the QY of the clusters (Pyo et al., 2015). The QY of the $Au_{22}(SG)_{18}$ cluster is increased to 60% after the gold shell was rigidified by TOA^+ (Figure 6).

Aggregation-induced emission can significantly enhance the luminescence intensity of Au NCs. Xie and co-workers have synthesized ultrabright Au (0)@Au(I)-thiolate core-shell nanoclusters (Luo et al., 2012). The addition of a weakly polar solvent disrupts the hydration shell and neutralizes the surface charge so that the short Au(I)-thiolate motifs aggregates on the Au (0) core. Conventional Au(I)-thiolate NCs, which originally do not emit light in aqueous solution, emit strong photoluminescence after aggregation with a QY of about 15%.

The excited state dynamics

The excited state dynamics of Au NCs are so unique that they differ significantly from gold nanoparticles. Firstly, the excited-state

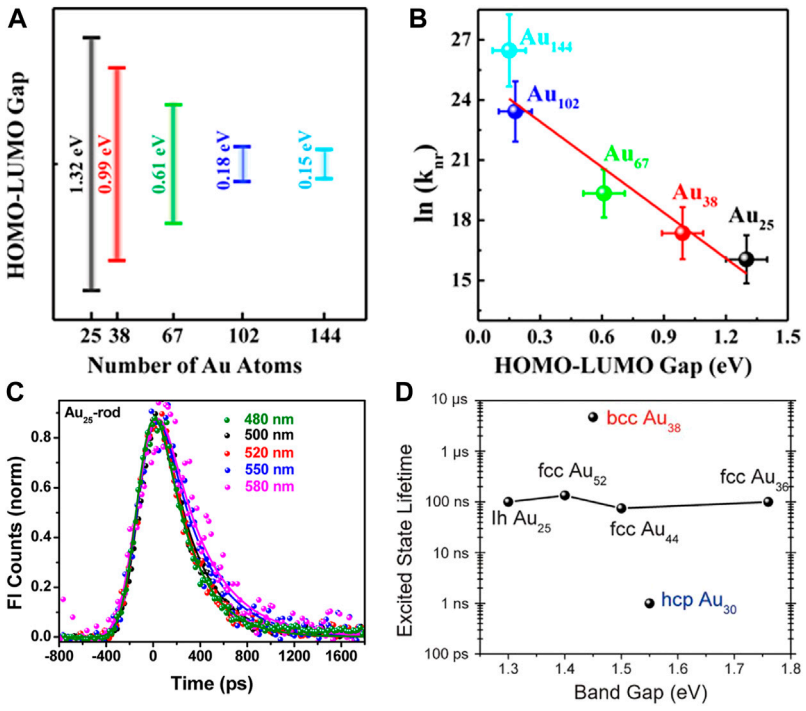

FIGURE 7
(A) Plot of the HOMO-LUMO energy gap versus the number of Au atoms for Au NCs **(B)** Plot of the logarithmic form of the nonradiative decay transition rate (referred to as ln (k_{nr})) versus HOMO-LUMO gap. Reprinted with permission from (Kwak et al., 2017). Copyright 2017 American Chemical Society **(C)** Luminescence kinetic decay traces of Au_{25}-rod at different excitation wavelengths. Reprinted with permission from (Devadas et al., 2013). Copyright 2013 American Chemical Society **(D)** Plot of the Excited state lifetime versus band gap of bcc Au_{38}, hcp Au_{38}, and fcc Au_{36}/Au_{44}/Au_{52}. Reprinted with permission from (Zhou et al., 2019). Copyright 2019 American Association for the Advancement of Science.

lifetime of Au NCs (~ns) is much longer than that of gold nanoparticles (~70 fs) (Varnavski et al., 2001; Zhou et al., 2017b). Typically, Jin et al. reported the excited state lifetime of body-centered cubic Au_{38} cluster is about 5 microseconds (Zhou et al., 2019). Furthermore, high pump power prolongs the electron-phonon coupling time of gold nanoparticles. (Zhou et al., 2016). However, the excited state dynamics of Au NCs is independent on the pump laser intensity, which is similar to the properties of molecules (Yau et al., 2010; Stamplecoskie and Kamat, 2014; Zhou et al., 2016). Au_{55} NCs exhibit a molecular-like single-electron relaxation process. The transient absorption at 640 nm of the Au_{55} clusters decays from the initial state to the intermediate state quickly and then decay back to the ground state slowly (Varnavski et al., 2010; Yau et al., 2010).

At present, it is generally accepted that the core-shell relaxation model is used to analyze the excited state dynamics of Au NCs. When the $Au_{25}(SR)_{18}^-$ cluster is excited, the ultrafast charge relaxation at the Au_{13} core is less than 200 fs and the relaxation from the gold core state to the semi-ring state is about 1 ps (Miller et al., 2009; Devadas et al., 2010). Goodson and Kamat et al. find that the excited state dynamics of Au NCs are mainly affected by the properties of the S-Au-S-Au-S semi-ring state through transient absorption spectroscopy (Devadas et al., 2010; Yau et al., 2010; Stamplecoskie et al., 2014).

As mentioned previously, the photophysical properties of Au NCs are highly dependent on the size. Lee and Ramakrishna et al. observe that the excited state lifetimes of Au NCs also show the distinct size dependence. As the size of Au NCs decreases or the number of Au atoms decreases, the enlarged HOMO-LUMO gap leads to the reduced nonradiative decay transition rate and the increased exciton lifetime (Figures 7A,B) (Kwak et al., 2017). This phenomenon indicates that the excited state dynamics of Au NCs can be explained by the energy gap law, which states that the nonradiative decay dynamics are inversely proportional to the energy gap (Englman and Jortner, 1970). However, Kamat et al. find that $Au_{18}(SR)_{14}$ cluster has the longest excited state lifetime among $Au_{10\text{-}12}(SR)_{10\text{-}12}$ cluster, $Au_{15}(SR)_{13}$ cluster, $Au_{18}(SR)_{14}$ cluster, and $Au_{25}(SR)_{18}$ cluster (Stamplecoskie and Kamat, 2014). This result deviates from the expectation of the energy gap law. The explanation is that $Au_{18}(SG)_{14}$ cluster and $Au_{25}(SG)_{18}$ cluster with the gold core exhibit fast relaxation of less than 1 ps and long-lived LMCT of about 200 ns, while small-sized Au NCs only show long-lived LMCT without fast relaxation processes in the gold core.

The structure of how the gold atoms arrange inside the cluster also affects its excited state dynamics. Ramakrishna et al. compared the femtosecond luminescence dynamics of Au_{25}-rod clusters, Au_{25}-sphere clusters, and Au_{38}-rod clusters. They find that the luminescence kinetic decay traces of Au_{25}-rod are independent of the excitation wavelength (Figure 7C), while the kinetic growth traces and the kinetic decay traces of Au_{25}-spheres and Au_{38}-rods show the specific excitation wavelength dependence, which is attributed to the cascade relaxation from core-gold to shell-gold (Devadas et al., 2013). Jin et al. studied two structural isomers of $Au_{38}(SC_2H_4Ph)_{24}$ in which the Au_{23} core of the Au_{38Q} cluster was the bi-icosahedron and that of the Au_{38T} cluster wass made up of a mono-icosahedral Au_{13} capped by a Au_{12} tri-tetrahedron by sharing two atoms (Zhou et al., 2017a). The Au_{38Q} cluster shows a rapid decay of 1.5 ps followed by nanosecond relaxation back to the ground state. The excited state dynamics of the Au_{38T} cluster is similar to that of the Au_{38Q} cluster except that the rapid decay process is accelerated by about 50%. The picosecond decay originates from the core-shell charge transfer or the electron rearrangement in the gold core, so it is speculated that the accelerated picosecond decay in the Au_{38T} cluster is attributed to its unique core structure.

Jin et al. also find that the atomic packing of Au NCs also greatly affects its excited state dynamics (Zhou et al., 2019). As shown in Figure 7D, the HOMO-LUMO gaps of face-centered cubic (fcc) Au NCs with different sizes vary greatly, but the excited state lifetimes hardly change. The excited state lifetime of hexagonal close-packed (hcp) $Au_{30}(SR)_{18}$ cluster is reduced by about two orders of magnitude and that of body-centered cubic (bcc) $Au_{38}S_2(SR)_{20}$ cluster is increased by nearly two orders of magnitude. This significant excited state lifetime difference is related to the distance and their connection modes between the Au_4 tetrahedral units.

The surface charge state of the cluster also affects its excited state dynamics in addition to the geometry and size. Taking the ultrafast electron relaxation dynamics of $Au_{25}(SR)_{18}^{q}$ ($q = 0, -1$) as an example, the core excitation lifetime of the anionic cluster is about 1,000 times longer than that of the neutral cluster (Qian et al., 2010). The excited state relaxation of $Au_{25}(SC_2H_4Ph)_{18}^{q}$ ($q = 0, -1$) mainly originates from the nonradiative energy transfer from the gold core to the ligands. The energy is transferred from the LUMO orbital to the ligands in the neutral cluster, while the energy is transferred from the LUMO+1 orbital above the LUMO orbital for the anionic cluster and the excited state lifetime is extended by about a hundred times (Green and Knappenberger, 2012).

Besides the excited state lifetime, the electron transfer ability of the excited state is also crucial for the material to become a potential photosensitizer. Methyl viologen [(MV^{2+})] is often used as an electron acceptor to examine the photoinduced electron transfer kinetics in Au NCs and its correlation with photocatalytic activity. Kamat et al. find that only long-lived semi-ring states (or LMCT states) of Au NCs are involved in electron transfer processes (Stamplecoskie et al., 2014). Therefore, the effect of different ligands on the LMCT states can tune the electron transfer efficiency of Au NCs. Meanwhile, Marcus theory suggests that the electron transfer rate decreases rapidly as the distance between the donor and acceptor becomes longer (Silverstein, 2012). Theoretically, the larger the shell ligands are, the smaller the electron transfer rates of Au NCs become (Chen and Li, 2020). Kamat et al. also demonstrate that the electron transfer efficiency is highly correlated with the size of Au NCs. As the size of clusters decreases, the electron transfer efficiency increases (Figure 8) (Stamplecoskie and Kamat, 2014). Au NCs with high electron transfer efficiencies and good visible light absorption have the potential to be excellent photosensitizers (Abbas et al., 2016).

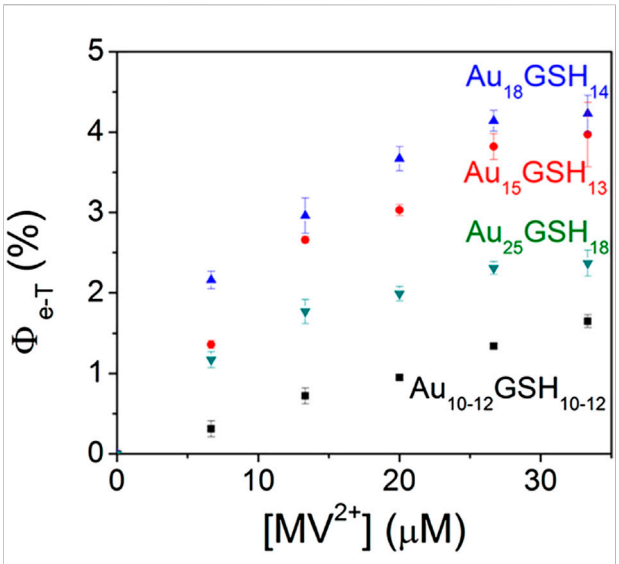

FIGURE 8
Quantum efficiency of electron transfer, $\Phi_{e\text{-}T}$, following the 355 nm laser pulse excitation of aqueous Au_xGSH_y solution containing different concentrations of (MV^{2+}). Reprinted with permission from (Stamplecoskie and Kamat, 2014). Copyright 2014 American Association for the Advancement of Science.

Photocatalytic applications of gold nanoclusters

The current society is facing the dual pressure of economic development and environmental protection. Photocatalysis is an environmentally friendly technology that can realize solar energy conversion and has broad development prospects. Suitable photocatalysts enable efficient and selective photocatalytic reactions and their optical properties have a great influence on the catalytic efficiency and selectivity (Du et al., 2020). Good photocatalysts have the following characteristics: 1) broad visible light absorption to maximize sunlight utilization

and gain selectivity; 2) long-lived photoinduced charge separated states to react with substrate molecules before relaxation to the ground states; 3) high reduction or oxidation potentials to react with a range of substrates; 4) the ability to transfer photogenerated electrons and holes to the reactive interface efficiently (Chai et al., 2019; Witzel et al., 2021).

As mentioned above, Au NCs with the ultra-small size and atomically precise composition exhibit high specific surface area, abundant unsaturated active sites, discrete energy levels, and controllable electronic properties. Therefore, Au NCs have received extensive attention in the fields of thermocatalysis and electrocatalysis (Fang et al., 2016; Chai et al., 2019; Du et al., 2020). Au NCs serving as promising photocatalysts have also raised increasing interest. With the in-depth study of the synthetic methods and optical properties of Au NCs, the energy level gap and the band position of Au NCs can be tuned by adjusting the size, crystal structure, atomic packing, surface charge state or surface ligands. The change of the energy level gap and the band position affect the optical absorption, the separation lifetime of photogenerated electron-hole pairs and the redox ability. At present, Au NCs have been used in photocatalytic conversion (oxidation and reduction) of the organics, photocatalytic degradation of the organic dyes, photocatalytic water splitting, photocatalytic CO_2 reduction and phototherapy.

Photocatalytic conversion of organics to value added products

Reactive oxygen species (ROS) are a class of chemically active molecules containing oxygen including singlet oxygen ($^1O_2$), superoxide, hydrogen peroxide (H_2O_2), and hydroxyl radicals (•OH). Photosensitizers can generate ROS through the photochemical reactions, which are mainly divided into two reaction pathways (Foote, 1991). In the type I reaction pathway, various oxygen radicals, such as superoxide and hydroxyl radicals, are generated by the electron transfer from the excited state photosensitizers to the substrates. In the type II reaction pathway, the photosensitizer is excited to form the singlet excited state (S_1) and then transformed into the triplet excited state (T_1) through the intersystem crossing. The triplet photosensitizer generates $^1O_2$ by the energy transfer with triplet oxygen ($^3O_2$).

The photosensitizers are usually organic dye molecules with strong absorption or nanomaterials such as quantum dots (QDs) (Samia et al., 2003; Ma et al., 2008), silicon nanocrystals (Kovalev and Fujii, 2005), and metal nanoparticles (Vankayala et al., 2011; Long et al., 2013; Vankayala et al., 2013). Au NCs have been demonstrated to act as photosensitizers and generate $^1O_2$ efficiently by tuning the electronic structure of the clusters (Kawasaki et al., 2014; Zhang et al., 2018; Du et al., 2020). Au NCs can undergo thermal catalytic oxidation reaction using the organic oxidant PhIO (Li et al., 2012; Liu et al., 2015) or photocatalytic oxidation reaction using $^1O_2$ generated from energy transfer, the latter being more environmentally friendly.

Jin et al. demonstrate that the ability of $^1O_2$ generation is related to the size of Au NCs (Kawasaki et al., 2014). Regardless of the surface charge state and the solubility, Au_{25} clusters can generate $^1O_2$ under the visible or NIR light irradiation (Figure 9A). Because of the large HOMO-LUMO gap (1.3 eV), Au_{25} clusters have a high T_1 yield. In contrast, the HOMO-LUMO gap of Au_{38} clusters is small (0.9 eV) and the energy of T_1 is lower than that required to excite $^3O_2$ to form $^1O_2$ (0.97 eV). Therefore, Au_{38} clusters cannot generate $^1O_2$. $^1O_2$ produced by photoexciting Au_{25} clusters can catalyze the oxidation of organic sulfide to sulfoxide with selectivity close to 100%. Besides, Zhu et al. also find that the arylthiolated $Au_{25}(F\text{-}Ph)_{18}^-$ nanocluster with NIR emission can photosensitize $^3O_2$ to produce $^1O_2$ for photocatalytic oxidative functionalization of sulfide, β-ketoesters, and 2-aryl-1,2,3,4-tetrahydroisoquinoline (Wang et al., 2022).

Maran et al. further investigate the effect of the surface charge state of $Au_{25}(SC3)_{18}^q$ clusters on the photocatalytic performance of $^1O_2$ generation by time-resolved electron paramagnetic resonance (TR-EPR) (Agrachev et al., 2019). The anion clusters generate $^1O_2$ under photoexcitation through the type II photoreaction pathway and then the EPR signal is observed. Under the same experimental conditions, neutral clusters cannot generate $^1O_2$ and no EPR signal is observed.

The above study by Jin et al. shows that $Au_{38}(SC_2H_4Ph)_{24}$ cannot photo-generate $^1O_2$ due to the small HOMO-LUMO gap (0.9 eV) (Kawasaki et al., 2014). Li et al. have shown that the energy gap of clusters can be adjusted by changing the atomic packing to improve the photocatalytic performance (Li et al., 2017). The $Au_{38}S_2(SAdm)_{20}$ clusters (–SAdm = 1-adamantanethiolate) are body-centered cubic atomic packing, which is different from the face-centered cubic atomic packing of common Au NCs. The $Au_{38}S_2(SAdm)_{20}$ clusters with the HOMO-LUMO gap of 1.57 eV can photo-generate $^1O_2$ and the photocatalytic efficiency is higher than that of $Au_{25}(SR)_{18}^-$ described above. In this work, $^1O_2$ can oxidize not only sulfides to sulfoxides but also benzylamines to imines selectively (Figure 9B).

In summary, Au NCs can be used as photosensitizers to photo-generate $^1O_2$ for the selective oxidation of organics. In addition, Au NCs can also be combined with semiconductor materials to improve the efficiency of photocatalytic organic conversion under visible light excitation by broadening the optical absorption range or separating photogenerated electron-hole pairs effectively.

Wang and Li et al. synthesized the $Au_{25}(PPh_3)_{10}(SC_3H_6SiO_3)_5Cl_2/TiO_2$ composite for the photocatalytic oxidation of amines to imines efficiently and selectively under mild reaction conditions (Chen et al., 2017). $Au_{25}(PPh_3)_{10}(SR)_5Cl_2$ clusters can separate the photogenerated electron-hole pairs effectively leading to the high catalytic

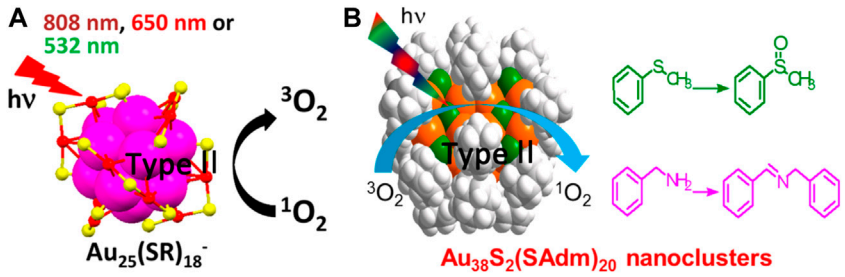

FIGURE 9
(A) Schematic diagram and the characterizations of $^1O_2$ generation from Au_{25} clusters under the visible or NIR light irradiation. Reprinted with permission from (Kawasaki et al., 2014). Copyright 2014 American Chemical Society **(B)** Au_{38} clusters generate $^1O_2$ under light and catalyze the oxidation of sulfides to sulfoxides and that of benzylamines to imines selectively. Reprinted with permission from (Li et al., 2017). Copyright 2017 American Chemical Society.

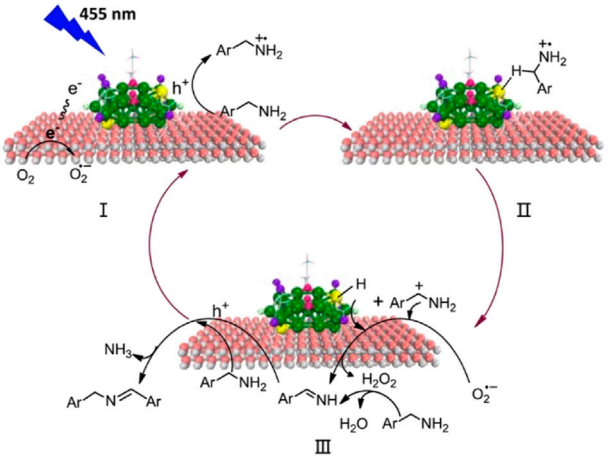

FIGURE 10
(A) The mechanism diagram of the photocatalytic oxidation of benzylamine by Au_{25}/TiO_2. Reprinted with permission from (Chen et al., 2017). Copyright 2017 American Chemical Society.

activity. The photocatalytic reaction involves an Au-H intermediate and a carbocation intermediate derived from benzylamine (Figure 10), and the reactive sites are the bare Au atoms due to the removal of part of the PPh_3 ligands.

Liu and co-workers construct Au_x/NP-TNTA heterostructure by depositing Au_x clusters onto highly ordered nanoporous layer-covered TiO_2 nanotube arrays (NP-TNA) *via* a facile electrostatic self-assembly strategy (Xiao et al., 2015). Au_x/NP-TNTA heterostructures can be used as photocatalysts for the reduction of nitroaromatics. Au_x clusters photo-generate electron-hole pairs under sunlight illumination. Because the potential of LUMO in Au_x NCs is more negative than the conduction band (CB) edge of TiO_2 and the interaction between them is tight, the photogenerated electrons of Au_x clusters are easily injected into the CB of TiO_2 to reduce the nitroaromatics adsorbed on the surface of the materials, while the photogenerated holes oxidize ammonium formate as the electron donor. It should be noted that the above reactions occurred in N_2 to avoid the participation of O_2. The condition ensured that the nitroaromatics were all reduced by the photogenerated electrons. Au_x/NP-TNTA heterostructures enhance the performance of photocatalytic reduction of organics through the efficient separation of photogenerated electron-hole pairs.

Photocatalytic degradation of organic pollutants

The composites composed of semiconductors and Au NCs as photosensitizers can also degrade organic dyes through photocatalysis. Jin et al. investigated the performance and mechanism of $Au_{25}(SC_2H_4Ph)_{18}/TiO_2$ composites to generate ROS for the degradation of methyl orange (MO) under the visible light irradiation (Figure 11A) (Yu C. et al., 2013). $Au_{25}(SR)_{18}$ clusters expand the optical absorption range to NIR region which results in a 1.6-fold increase in the activity of photocatalytic degradation of MO under the visible light irradiation. The photogenerated electrons of $Au_{25}(SR)_{18}$ clusters are injected into the conduction band of TiO_2 to inhibit the recombination of photogenerated electrons and holes effectively, which also contributes to the improvement of the photocatalytic degradation of MO.

Au_x/NP-TNTA heterostructures constructed by Liu and co-workers are also used for the photocatalytic degradation of MO (Xiao et al., 2015). The photogenerated electrons transferred to the conduction band of TiO_2 and the photogenerated holes of Au_x clusters can react with H_2O to generate ROS for the degradation of MO. The efficient separation of the

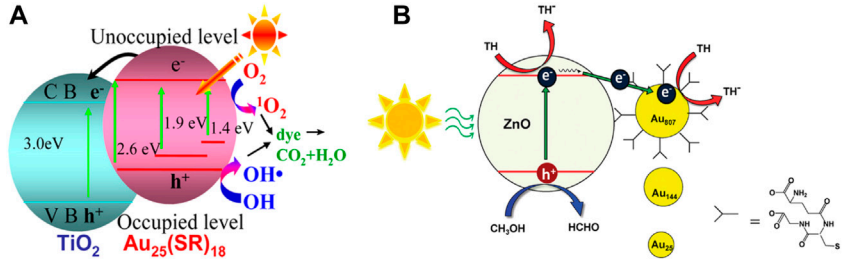

FIGURE 11
(A) Mechanism of the photocatalytic degradation of organic dyes by $Au_{25}(SC_2H_4Ph)_{18}/TiO_2$ composites. Reprinted with permission from (Yu C. et al., 2013). Copyright 2013 American Chemical Society **(B)** The photocatalytic degradation of TH of ZnO-Au composites under visible light irradiation. Reprinted with permission from (Lee et al., 2011). Copyright 2011 American Chemical Society.

photogenerated electron-hole pairs enhances the performance of the photocatalytic degradation of organic dyes.

How to improve the photostability of Au NCs at the interface of composites is a long-standing challenge. Xu and Chen et al. report the SiO_2-Au GSH clusters-BPEI@TiO_2 (SABT) composites assembled by a simple method (Weng et al., 2018). Branched polyethyleneimine (BPEI) is not only the surface modifier but also the stabilizer and the reducing agent, which can prevent the oxidation of the ligands on the surface of the clusters. Therefore, the size and structure of Au GSH clusters can be maintained for more than 10 h under the continuous visible light irradiation. The thickness-controllable TiO_2 coating stabilizes the ultra-small Au GSH clusters supported on the SiO_2 sphere. As a result, the SABT composite has good photostability and its photocatalytic activity for the degradation of rhodamine B has little change in 10 cycles.

In composites composed of the semiconductor and Au NCs as photocatalysts, Au NCs generally act as photosensitizers to capture the visible light. Au NCs can also accept the photogenerated electrons to catalyze reactions. Both the size and surface ligands of Au NCs affect the efficiency of the photocatalytic degradation of organic dyes.

Three different sizes of Au_x $(SG)_y$ clusters synthesized by Lee and Song et al. were deposited on the surface of ZnO through the carboxyl groups in their ligands (Lee et al., 2011). It is speculated that the photogenerated electrons of ZnO under visible light irradiation are injected into the Au NCs to reduce thionine (TH) on the surface of the Au NCs. The absorption spectrum of ZnO hardly changes after the cluster deposition indicating that the light-harvesting ability is not enhanced, so the photocatalytic performance is only related to the efficiency of the charge separation. The increased sizes of Au NCs accelerate the electron transfer rate to improve the efficiency of the charge separation (Figure 11B). Therefore, the ZnO-Au composite composed of Au NCs with the large size has higher photocatalytic performance for the degradation of TH.

Xie et al. synthesized thio-β-cyclodextrin (SH-β-CD) protected gold nanoclusters to decorate TiO_2 (Zhu et al., 2018). TiO_2-Au NCs@β-CD composites can photocatalyze the degradation of MO efficiently. The mechanism indicates that photogenerated electrons from TiO_2 under UV light are injected into the gold core to form the catalytic center, which reduces O_2 to superoxide anion ($O_2^{-\bullet}$) for the degradation of MO. In addition, the photogenerated holes of TiO_2 can also oxidize H_2O to •OH for the degradation of MO. The SH-β-CD ligands on the surface of the clusters can capture MO efficiently through the host-guest interaction. Therefore, the enhanced photocatalytic degradation of MO originates from the synergistic effect of the gold core, SH-β-CD ligands and TiO_2 in the TiO_2-Au NCs@β-CD composite.

Wang et al. synthesized the silane-stabilized Au NCs by a simple photoreduction method. The Au NCs act as stand-alone photocatalysts for the photocatalytic degradation of methylene blue (MB) under visible light irradiation (Zhou S. et al., 2017). The silane-stabilized Au NCs degrade about 96% of MB after exposure to the visible light for 1 h. It has been confirmed that the mechanism of the photocatalytic degradation of organic dyes of the silane-stabilized Au NCs is similar to that of semiconductors.

Photocatalytic water splitting and CO_2 reduction

Au NCs can be used as the cocatalysts in photocatalytic water splitting for the conversion of solar energy to chemical energy. Monodisperse $Au_{25}(SG)_{18}$ clusters with unchanged sizes are supported on the $BaLa_4Ti_4O_{15}$ photocatalysts and the prepared composites can be used for photocatalytic water splitting (Figure 12A) (Negishi et al., 2013). The experimental results show that the catalytic performance of the Au_{25} cluster cocatalyst is 2.6 times higher than that of the gold nanoparticle cocatalyst. This may be due to the fact that ultra-small Au_{25} clusters can introduce the same number of active sites as the gold

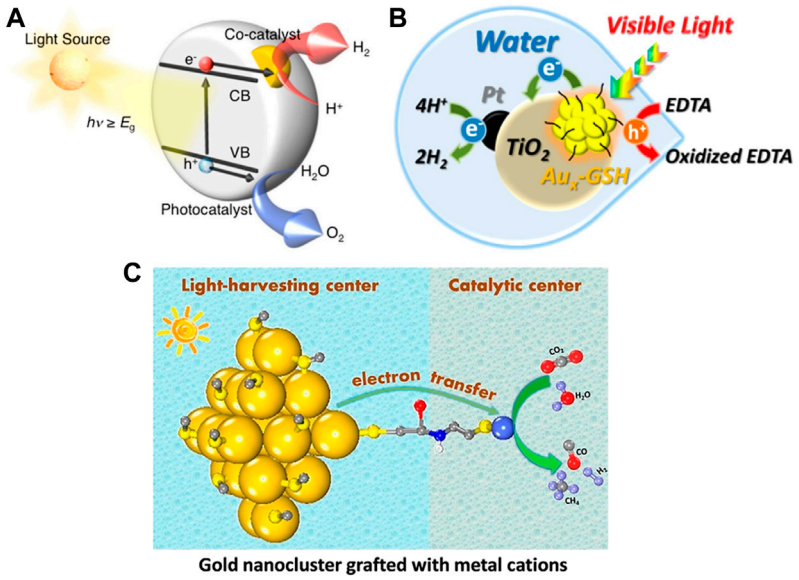

FIGURE 12
(A) Schematic of photocatalytic water splitting by composites *via* a one-step method: conduction band (CB), valence band (VB), band gap (E_g). Reprinted with permission from (Negishi et al., 2015). Copyright 2015 American Chemical Society **(B)** Illustration of Au_x-GSH NCs sensitized Pt/TiO_2 NPs for photocatalytic water splitting reaction. Reprinted with permission from (Chen and Kamat, 2014). Copyright 2014 American Chemical Society **(C)** Schematic of covalently bridged Au-GSH clusters and metal cations for the visible-light-driven CO_2 reduction. Reprinted with permission from (Cui et al., 2018). Copyright 2018 American Chemical Society.

nanoparticles at lower loadings to reduce the interference of cocatalysts on the optical absorption of catalysts. It has also been found that the stability of Au NCs precursors is crucial to achieve the controllable loading. Meanwhile, the photocatalytic activity increases as the size of the cocatalyst decreases (Negishi et al., 2015).

Besides acting as the cocatalysts, Au NCs can also be the photosensitizers for H_2 generation in the photocatalytic water splitting. Kamat and coworkers find that the reversible reduction (E^0 = −0.63 V vs. RHE) and oxidation (E^0 = 0.97 and 1.51 V vs. RHE) potentials of glutathione-capped metal nanoclusters (Au_x-GSH NCs) are suitable for driving water splitting (Chen and Kamat, 2014). Au_x-GSH NCs sensitized Pt/TiO_2 NPs in aqueous slurry system can generate H_2 with sacrificial electron donors, such as EDTA, under the visible light irradiation (Figure 12B). The Au_x-GSH NCs expand the photoresponse range of the large band gap semiconductor to efficiently realize the conversion of light energy to chemical energy. However, the Au_x-GSH NCs aggregate into large NPs upon continuous illumination, which limits the photoconversion efficiency.

Au NCs as photosensitizers can also photocatalyze CO_2 reduction. Xiong and co-workers attach M^{2+} metal cations (Fe^{2+}, Co^{2+}, Ni^{2+}, and Cu^{2+}) to Au-GSH NCs covalently through L-cysteine as a bridging ligand to achieve the stable connection between the light-harvesting center and the catalytic site (Cui et al., 2018). The photogenerated electrons are transferred from the Au-GSH NC to M^{2+} *via* the bridge bond and are used to reduce CO_2 at the catalytic site M^{2+} (Figure 12C). It is noteworthy to overcome the instability of Au-GSH NCs in this reaction system to prevent aggregation.

It has been confirmed that the protection of Au NCs by a metal-organic framework (MOF) can improve the stability of Au NCs in photocatalytic CO_2 reduction effectively. Recently, Fei et al. prepare N-heterocyclic carbene (NHC)-stabilized ultrasmall Au NCs in a MOF by the heterogeneous nucleation method (Jiang et al., 2021). Au-NC@MOF composites exhibit the stable and excellent catalytic activity for photocatalytic CO_2 reduction. It has been demonstrated that the photogenerated electrons are transferred from Au NCs to MOFs *via* the MOF-NHC-Au covalent bond bridge to separate photogenerated electron-hole pairs rapidly, which enables the synergistic catalysis of Au NCs and MOFs.

Phototherapy

Phototherapy is a promising cancer treatment technology with minimal trauma, few side effects and high efficacy (Lin et al., 2021). Photodynamic therapy (PDT) is a clinically licensed non-invasive phototherapy (Dolmans et al., 2003). In the aerobic environment, photosensitizers excited by light with appropriate

wavelengths generate ROS through either type I or type II reaction pathways to oxidize adjacent biological macromolecules such as DNA. The photochemical reactions causes the local oxidative damage to kill cancer cells (Li and Grant, 2016).

It has been demonstrated that Au NCs exhibit excellent biocompatibility, pharmacokinetics, renal clearance and biodegradability (Zhang et al., 2012; Zheng et al., 2021). Therefore, Au NCs can be widely used in biomedical fields such as biosensing, photoluminescence imaging, and cancer therapy (Yang et al., 2019; Zheng et al., 2021). At the same time, ultra-small Au NCs exhibit unique optical properties including high two-photon absorption cross section, long-lived triplet state, and high photoluminescence quantum yields. Combining the above two points, Au NCs can be used as photosensitizers in PDT.

Au NCs with high two-photon absorption cross section can improve the efficacy of PDT significantly. Dihydrolipoic acid coated gold nanoclusters (AuNC@DHLA) as photosensitizers can take full advantage of high two-photon absorption and mediate the single electron transfer to generate $O_2^{-\bullet}$ for the efficient photodynamic therapy (type I) (Han et al., 2020). Meanwhile, two-photon excitation can increase the penetration depth in tissue.

The combination of Au NCs and semiconductors can improve the charge separation efficiency, which also improves the efficacy of PDT significantly. Li and Zhang et al. prepare TiO_2 NPs-Au NC-graphene composites (TAG) for the efficient PDT (Cheng et al., 2017). Au NCs with narrow band gaps have the cut-off absorption wavelength at 617 nm for the efficient utilization of simulated sunlight. Meanwhile, Au NCs, TiO_2 NPs, and graphene have staggered energy levels which can separate photogenerated electron-hole pairs effectively. Based on the above two advantages, TAG composites generate a large amount of •OH and $O_2^{-\bullet}$ *via* the water oxidation and oxygen reduction under simulated sunlight irradiation to induce severe cancer cell death. It demonstrates the significant PDT (type I) efficacy of TAG.

The functional molecules can be bound to the surface of Au NCs covalently through the terminal functional groups, which can also enhance the PDT efficacy of the clusters and expand the applications. A common covalent conjugation scheme is the coupling of carboxyl groups to primary amines *via* 1-ethyl-(3-dimethylaminopropyl)carbodiimide (EDC). For example, a tumor-targeting agent (folic acid) and a photosensitizer (protoporphyrin IX) can be covalently bound to lipoic acid protected Au_{18} clusters to form a multifunctional PFL-AuC nanocomposites, which can be used as a photosensitizer for photoluminescence imaging assisted PDT (type II) with tumor targeting (Nair et al., 2015). PFL-AuC nanocomposite is more efficient for the photo-generation of $^1O_2$ compared with protoporphyrin IX alone. The tumor-targeting agents cause the local aggregation of PFL-AuC nanocomposites. Therefore, the PFL-AuC nanocomposites can induce PDT to cause the cancer cell death with a low-energy laser. In addition, the NIR emission of the PFL-AuC nanocomposite can track the PDT process in real time. This method of constructing nanocomposites through covalent binding also enables organelle-targeting of Au NCs. For example, the multifunctional nuclear-targeting TAT peptide-Au NCs (peptide sequence: N-GRKKRRQRRR-C) can simultaneously perform photoluminescence imaging, gene delivery, and NIR-excited PDT (type II) to kill cancer cells effectively (Vankayala et al., 2015).

The severely hypoxic environment in solid tumors limits the efficacy of traditional PDT (Li et al., 2018; Liu et al., 2018). Nitroaromatic compounds are bioreductive prodrugs that are activated by nitroreductase (NTR) overexpressed in hypoxic tissues to generate DNA-reactive cytotoxic arylamines, which enables hypoxia-targeting tumor therapy (Searle et al., 2004; Wilson and Hay, 2011). However, the activation of nitroaromatic prodrugs by NTR shows slow reaction kinetics and the regulation of the reaction kinetics is complicated (Searle et al., 2004). In addition, native NTR is difficult to obtain in large quantities and loses its activity easily when pH or temperature changes (Yanto et al., 2010). At present, it has been reported that nanomaterials with catalytic activity can mimic natural enzymes to convert prodrugs into bioactive molecules for cancer treatment (Soldevila-Barreda and Metzler-Nolte, 2019; Oliveira et al., 2020; Vong et al., 2020). Visible light that excites nanomaterials to activate prodrugs is spatially and temporally controllable (Alonso-de Castro et al., 2018; Gurruchaga-Pereda et al., 2019; Zhang and Liu, 2020).

Common photosensitizers are difficult to mimic NTR because the reduction of nitroaromatics to arylamines requires a challenging six-electron/six-proton process. Meanwhile, the selective catalytic reduction of nitroaromatics is also a long-standing challenge. Our group used the glutathione protected Au NCs as photosensitizers to mimic NTRs for the selective photocatalytic reduction of nitrobenzene to aniline (AN) in a hypoxic environment (Figure 13A) (Liu et al., 2021). Notably, the catalytic activity of Au NCs can be regulated by the temporally and spatially controllable light (Figure 13B). Finally, Au NCs photocatalyze the activation of nitroaromatic prodrugs in tumor cells to achieve the photochemotherapy against the hypoxic condition of solid tumors, which overcomes the oxygen dependence of the traditional PDT.

However, Au NCs only absorb little blue light and have low utilization of visible light, so the photocatalytic reduction of nitrobenzene is less efficient. In an effort to eliminate this drawback, our group prepared the functionalized gold nanoclusters (Au-PS) as the photocatalyst by covalently linking ruthenium coordination compounds as the photosensitizers to Au NCs (Cheng et al., 2021). In the

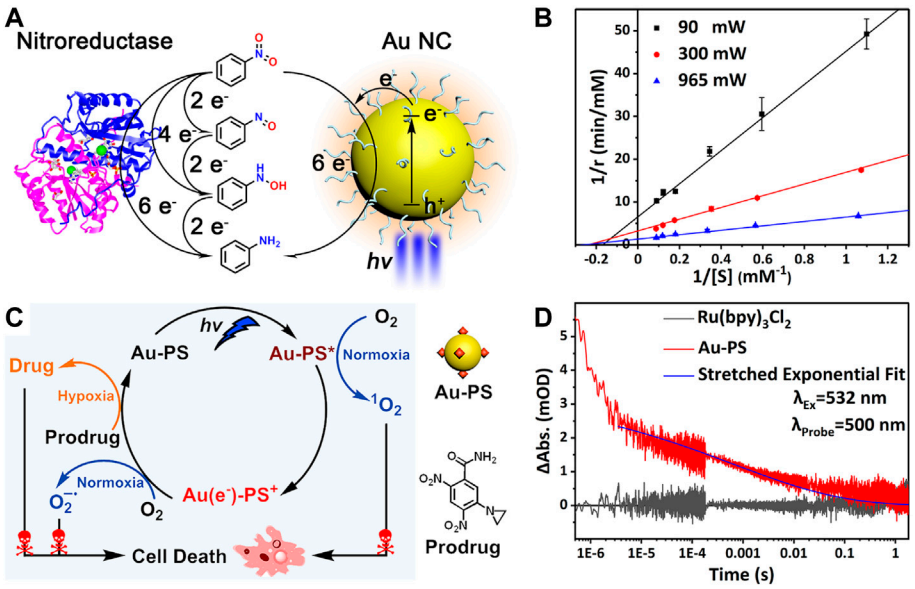

FIGURE 13
(A) Gold nanoclusters perform enzyme-like photocatalysis for nitrobenzene **(B)** Enzyme-like reaction kinetics of gold nanoclusters tuned by the light intensity. Reprinted with permission from (Liu et al., 2021). Copyright 2021 American Chemical Society **(C)** Proposed mechanism of the functionalized gold nanoclusters for photodynamic and photocatalytic double killing of cancer cells **(D)** Time-dependent decay of the transient absorption of charge-separated states in Au-PS. Reprinted with permission from (Cheng et al., 2021). Copyright 2021 American Chemical Society.

hypoxic conditions, Au-PS still exhibits the selective photocatalytic reduction of nitrobenzene to aniline under the visible light excitation. At the same time, this functionalization strategy broadens the optical absorption range of the material and prolongs the separation lifetime of photogenerated electron-hole pairs by utilizing the charge transfer from the excited PS to the Au NC core (Figure 13C), so the photocatalytic efficiency is improved significantly. In the normoxic conditions, ROS are generated after the photoexcitation of Au-PS. Therefore, Au-PS can be used both as the photosensitizer for photodynamic therapy in the normoxic conditions as well as being the photocatalyst to activate the nitroaromatic prodrug CB1954 in the hypoxic conditions (Figure 13D). This constitutes a dual kill mechanism to induce the cancer cell death in both normoxic and hypoxic conditions.

Summary and outlook

The art of synthesizing monodisperse and atomically precise Au NCs makes it possible to finely tune the geometric structure and composition. Au NCs with discrete energy levels exhibit controllable photophysical properties, including optical absorption, redox capacity, and the excited-state lifetime. These tunable photophysical properties give Au NCs great potential for the photocatalytic applications. Although Au NCs can be used for the solar energy conversion, including the degradation of organic pollutants, the conversion of organics, water splitting, and CO_2 reduction, the photocatalytic reactions of Au NCs are less reported than their applications in thermal catalysis.

In future endeavors of expanding photocatalytic potentials of Au NCs particularly in solar energy conversion, we think a good research direction would be making the best use of the versatile surface chemistry of Au NCs while combining the excellent visible light absorption and charge separation properties. Molecular light harvesters typically do not possess the capability of both light harvesting and multi-electron transfer catalysis whereas Au NCs do. Some organic transformations such as benzylamine oxidation or nitroaromatics reduction discussed in this review have proven Au NCs their potential. With targeted design of the gold core as well as smart choice of Au NC surface-protecting ligands, Au NCs have a bright future as the photocatalysts to utilize solar energy for value added chemical reactions.

In addition to solar energy conversion, Au NCs with good biocompatibility also have great potential as photocatalysts for biomedical application. They can be delivered into mammalian cells for the photocatalytic generation of bioactive molecules. The functionalization of surface ligands can transform Au NCs into targeted multifunctional nanocomposites and enhance the photocatalytic performance in living organisms. So far, reports

on Au NC *in vivo* photocatalysis are still very rare. More research is waiting ahead.

Author contributions

KH designed the content of the review. DC drafted the review. DC, RL, and KH are all involved in revising the manuscript.

Funding

This work was sponsored by the National Natural Science Foundation of China (21872037) and Natural Science Foundation of Shanghai (21ZR1404400).

Conflict of interest

The authors declare that the research was conducted in the absence of any commercial or financial relationships that could be construed as a potential conflict of interest.

Publisher's note

All claims expressed in this article are solely those of the authors and do not necessarily represent those of their affiliated organizations, or those of the publisher, the editors and the reviewers. Any product that may be evaluated in this article, or claim that may be made by its manufacturer, is not guaranteed or endorsed by the publisher.

References

Abbas, M. A., Kim, T.-Y., Lee, S. U., Kang, Y. S., and Bang, J. H. (2016). Exploring interfacial events in gold-nanocluster-sensitized solar cells: Insights into the effects of the cluster size and electrolyte on solar cell performance. *J. Am. Chem. Soc.* 138 (1), 390–401. doi:10.1021/jacs.5b11174

Agrachev, M., Ruzzi, M., Venzo, A., and Maran, F. (2019). Nuclear and electron magnetic resonance spectroscopies of atomically precise gold nanoclusters. *Acc. Chem. Res.* 52 (1), 44–52. doi:10.1021/acs.accounts.8b00495

Aikens, C. M. (2011). Electronic structure of ligand-passivated gold and silver nanoclusters. *J. Phys. Chem. Lett.* 2 (2), 99–104. doi:10.1021/jz101499g

Aikens, C. M. (2008). Origin of discrete optical absorption spectra of M25(SH) 18− nanoparticles (M = Au, Ag). *J. Phys. Chem. C* 112 (50), 19797–19800. doi:10.1021/jp8090914

Alonso-de Castro, S., Cortajarena, A. L., Lopez-Gallego, F., and Salassa, L. (2018). Bioorthogonal catalytic activation of platinum and ruthenium anticancer complexes by FAD and flavoproteins. *Angew. Chem. Int. Ed.* 57 (12), 3143–3147. doi:10.1002/anie.201800288

Antonello, S., Perera, N. V., Ruzzi, M., Gascón, J. A., and Maran, F. (2013). Interplay of charge state, lability, and magnetism in the molecule-like Au25(SR) 18 cluster. *J. Am. Chem. Soc.* 135 (41), 15585–15594. doi:10.1021/ja407887d

Bigioni, T. P., Whetten, R. L., and Dag, Ö. (2000). Near-infrared luminescence from small gold nanocrystals. *J. Phys. Chem. B* 104 (30), 6983–6986. doi:10.1021/jp993867w

Chai, O. J. H., Liu, Z., Chen, T., and Xie, J. (2019). Engineering ultrasmall metal nanoclusters for photocatalytic and electrocatalytic applications. *Nanoscale* 11 (43), 20437–20448. doi:10.1039/c9nr07272a

Chen, D., and Li, J. (2020). Ultrasmall Au nanoclusters for bioanalytical and biomedical applications: The undisclosed and neglected roles of ligands in determining the nanoclusters' catalytic activities. *Nanoscale Horiz.* 5 (10), 1355–1367. doi:10.1039/d0nh00207k

Chen, H., Liu, C., Wang, M., Zhang, C., Luo, N., Wang, Y., et al. (2017). Visible light gold nanocluster photocatalyst: Selective aerobic oxidation of amines to imines. *ACS Catal.* 7 (5), 3632–3638. doi:10.1021/acscatal.6b03509

Chen, Y. S., and Kamat, P. V. (2014). Glutathione-capped gold nanoclusters as photosensitizers. Visible light-induced hydrogen generation in neutral water. *J. Am. Chem. Soc.* 136 (16), 6075–6082. doi:10.1021/ja5017365

Cheng, D., Liu, R., Tian, L., Zhou, Q., Niu, F., Yue, Y., et al. (2021). Photocatalytic nitroaromatic prodrug activation by functionalized gold nanoclusters. *ACS Appl. Nano Mat.* 4 (12), 13413–13424. doi:10.1021/acsanm.1c02926

Cheng, Y., Chang, Y., Feng, Y., Liu, N., Sun, X., Feng, Y., et al. (2017). Simulated sunlight-mediated photodynamic therapy for melanoma skin cancer by titanium-dioxide-nanoparticle-gold-nanocluster-graphene heterogeneous nanocomposites. *Small* 13 (20), 1603935–1603946. doi:10.1002/smll.201603935

Cui, X., Wang, J., Liu, B., Ling, S., Long, R., Xiong, Y., et al. (2018). Turning Au nanoclusters catalytically active for visible-light-driven CO2 reduction through bridging ligands. *J. Am. Chem. Soc.* 140 (48), 16514–16520. doi:10.1021/jacs.8b06723

Devadas, M. S., Kim, J., Sinn, E., Lee, D., Goodson, T., Ramakrishna, G., et al. (2010). Unique ultrafast visible luminescence in monolayer-protected Au25 clusters. *J. Phys. Chem. C* 114 (51), 22417–22423. doi:10.1021/jp107033n

Devadas, M. S., Thanthirige, V. D., Bairu, S., Sinn, E., and Ramakrishna, G. (2013). Temperature-dependent absorption and ultrafast luminescence dynamics of bi-icosahedral Au25 clusters. *J. Phys. Chem. C* 117 (44), 23155–23161. doi:10.1021/jp408333h

Dolmans, D. E. J. G. J., Fukumura, D., and Jain, R. K. (2003). Photodynamic therapy for cancer. *Nat. Rev. Cancer* 3 (5), 380–387. doi:10.1038/nrc1071

Du, Y., Sheng, H., Astruc, D., and Zhu, M. (2020). Atomically precise noble metal nanoclusters as efficient catalysts: A bridge between structure and properties. *Chem. Rev.* 120 (2), 526–622. doi:10.1021/acs.chemrev.8b00726

Englman, R., and Jortner, J. (1970). The energy gap law for radiationless transitions in large molecules. *Mol. Phys.* 18 (2), 145–164. doi:10.1080/00268977000100171

Fang, J., Zhang, B., Yao, Q., Yang, Y., Xie, J., Yan, N., et al. (2016). Recent advances in the synthesis and catalytic applications of ligand-protected, atomically precise metal nanoclusters. *Coord. Chem. Rev.* 322, 1–29. doi:10.1016/j.ccr.2016.05.003

Foote, C. S. (1991). Definition of type I and type II photosensitized oxidation. *Photochem. Photobiol.* 54 (5), 659. doi:10.1111/j.1751-1097.1991.tb02071.x

Ghosh, A., Udayabhaskararao, T., and Pradeep, T. (2012). One-step route to luminescent Au18SG14 in the condensed phase and its closed shell molecular ions in the gas phase. *J. Phys. Chem. Lett.* 3 (15), 1997–2002. doi:10.1021/jz3007436

Green, T. D., and Knappenberger, K. L., Jr. (2012). Relaxation dynamics of Au25L18 nanoclusters studied by femtosecond time-resolved near infrared transient absorption spectroscopy. *Nanoscale* 4 (14), 4111–4118. doi:10.1039/c2nr31080e

Guo, R., and Murray, R. W. (2005). Substituent effects on redox potentials and optical gap energies of molecule-like Au38(SPhX)24 nanoparticles. *J. Am. Chem. Soc.* 127 (34), 12140–12143. doi:10.1021/ja053119m

Gurruchaga-Pereda, J., Martínez-Martínez, V., Rezabal, E., Lopez, X., Garino, C., Mancin, F., et al. (2019). Flavin bioorthogonal photocatalysis toward platinum substrates. *ACS Catal.* 10 (1), 187–196. doi:10.1021/acscatal.9b02863

Hakkinen, H. (2008). Atomic and electronic structure of gold clusters: Understanding flakes, cages and superatoms from simple concepts. *Chem. Soc. Rev.* 37 (9), 1847–1859. doi:10.1039/b717686b

Han, R., Zhao, M., Wang, Z., Liu, H., Zhu, S., Huang, L., et al. (2020). Super-efficient *in vivo* two-photon photodynamic therapy with a gold nanocluster as a type I photosensitizer. *ACS Nano* 14 (8), 9532–9544. doi:10.1021/acsnano.9b05169

Huang, T., and Murray, R. W. (2001). Visible luminescence of water-soluble monolayer-protected gold clusters. *J. Phys. Chem. B* 105 (50), 12498–12502. doi:10.1021/jp0041151

Jadzinsky, P. D., Calero, G., Ackerson, C. J., Bushnell, D. A., and Kornberg, R. D. (2007). Structure of a thiol monolayer-protected gold nanoparticle at 1.1 Å resolution. *Science* 318 (5849), 430–433. doi:10.1126/science.1148624

Jiang, Y., Yu, Y., Zhang, X., Weinert, M., Song, X., Ai, J., et al. (2021). N-heterocyclic carbene-stabilized ultrasmall gold nanoclusters in a metal-organic framework for photocatalytic CO_2 reduction. *Angew. Chem. Int. Ed.* 60 (32), 17388–17393. doi:10.1002/anie.202105420

Jin, R. (2015). Atomically precise metal nanoclusters: Stable sizes and optical properties. *Nanoscale* 7 (5), 1549–1565. doi:10.1039/c4nr05794e

Jin, R., Zeng, C., Zhou, M., and Chen, Y. (2016). Atomically precise colloidal metal nanoclusters and nanoparticles: Fundamentals and opportunities. *Chem. Rev.* 116 (18), 10346–10413. doi:10.1021/acs.chemrev.5b00703

Kawasaki, H., Hamaguchi, K., Osaka, I., and Arakawa, R. (2011). ph-Dependent synthesis of pepsin-mediated gold nanoclusters with blue green and red fluorescent emission. *Adv. Funct. Mat.* 21 (18), 3508–3515. doi:10.1002/adfm.201100886

Kawasaki, H., Kumar, S., Li, G., Zeng, C., Kauffman, D. R., Yoshimoto, J., et al. (2014). Generation of singlet oxygen by photoexcited Au25(SR)18 clusters. *Chem. Mat.* 26 (9), 2777–2788. doi:10.1021/cm500260z

Kim, A., Zeng, C., Zhou, M., and Jin, R. (2017). Surface engineering of Au36(SR) 24 nanoclusters for photoluminescence enhancement. *Part. Part. Syst. Charact.* 34 (8), 1600388–1600393. doi:10.1002/ppsc.201600388

Kovalev, D., and Fujii, M. (2005). Silicon nanocrystals: Photosensitizers for oxygen molecules. *Adv. Mat.* 17 (21), 2531–2544. doi:10.1002/adma.200500328

Kubo, R. (1962). Electronic properties of metallic fine particles. I. *J. Phys. Soc. Jpn.* 17 (6), 975–986. doi:10.1143/JPSJ.17.975

Kwak, K., Thanthirige, V. D., Pyo, K., Lee, D., and Ramakrishna, G. (2017). Energy gap law for exciton dynamics in gold cluster molecules. *J. Phys. Chem. Lett.* 8 (19), 4898–4905. doi:10.1021/acs.jpclett.7b01892

Lee, D., Donkers, R. L., Wang, G., Harper, A. S., and Murray, R. W. (2004). Electrochemistry and optical absorbance and luminescence of molecule-like Au38 nanoparticles. *J. Am. Chem. Soc.* 126 (19), 6193–6199. doi:10.1021/ja049605b

Lee, J., Shim, H. S., Lee, M., Song, J. K., and Lee, D. (2011). Size-controlled electron transfer and photocatalytic activity of ZnO–Au nanoparticle composites. *J. Phys. Chem. Lett.* 2 (22), 2840–2845. doi:10.1021/jz2013352

Li, G., Abroshan, H., Liu, C., Zhuo, S., Li, Z., Xie, Y., et al. (2016). Tailoring the electronic and catalytic properties of Au25 nanoclusters via ligand engineering. *ACS Nano* 10 (8), 7998–8005. doi:10.1021/acsnano.6b03964

Li, G., and Jin, R. (2013). Atomically precise gold nanoclusters as new model catalysts. *Acc. Chem. Res.* 46 (8), 1749–1758. doi:10.1021/ar300213z

Li, G., Qian, H., and Jin, R. (2012). Gold nanocluster-catalyzed selective oxidation of sulfide to sulfoxide. *Nanoscale* 4 (21), 6714–6717. doi:10.1039/c2nr32171h

Li, L., Li, Z., Zhang, H., Zhang, S., Majeed, I., Tan, B., et al. (2013). Effect of polymer ligand structures on fluorescence of gold clusters prepared by photoreduction. *Nanoscale* 5 (5), 1986–1992. doi:10.1039/c2nr33693f

Li, X., Kwon, N., Guo, T., Liu, Z., and Yoon, J. (2018). Innovative strategies for hypoxic-tumor photodynamic therapy. *Angew. Chem. Int. Ed.* 57 (36), 11522–11531. doi:10.1002/anie.201805138

Li, Z., and Grant, K. B. (2016). DNA photo-cleaving agents in the far-red to near-infrared range – A review. *RSC Adv.* 6 (29), 24617–24634. doi:10.1039/c5ra28102d

Li, Z., Liu, C., Abroshan, H., Kauffman, D. R., and Li, G. (2017). Au38S2(SAdm) 20 photocatalyst for one-step selective aerobic oxidations. *ACS Catal.* 7 (5), 3368–3374. doi:10.1021/acscatal.7b00239

Lin, Z., Goswami, N., Xue, T., Chai, O. J. H., Xu, H., Liu, Y., et al. (2021). Engineering metal nanoclusters for targeted therapeutics: From targeting strategies to therapeutic applications. *Adv. Funct. Mat.* 31 (51), 2105662–2105680. doi:10.1002/adfm.202105662

Link, S., Beeby, A., FitzGerald, S., El-Sayed, M. A., Schaaff, T. G., Whetten, R. L., et al. (2002). Visible to infrared luminescence from a 28-atom gold cluster. *J. Phys. Chem. B* 106 (13), 3410–3415. doi:10.1021/jp014259v

Liu, C., Yan, C., Lin, J., Yu, C., Huang, J., Li, G., et al. (2015). One-pot synthesis of Au144(SCH2Ph)60 nanoclusters and their catalytic application. *J. Mat. Chem. A Mat.* 3 (40), 20167–20173. doi:10.1039/c5ta05747g

Liu, R., Cheng, D., Zhou, Q., Niu, F., and Hu, K. (2021). Gold nanoclusters perform enzyme-like photocatalysis for prodrug activation. *ACS Appl. Nano Mat.* 4 (2), 990–994. doi:10.1021/acsanm.1c00014

Liu, Y., Jiang, Y., Zhang, M., Tang, Z., He, M., Bu, W., et al. (2018). Modulating hypoxia via nanomaterials chemistry for efficient treatment of solid tumors. *Acc. Chem. Res.* 51 (10), 2502–2511. doi:10.1021/acs.accounts.8b00214

Long, R., Mao, K., Ye, X., Yan, W., Huang, Y., Wang, J., et al. (2013). Surface facet of palladium nanocrystals: A key parameter to the activation of molecular oxygen for organic catalysis and cancer treatment. *J. Am. Chem. Soc.* 135 (8), 3200–3207. doi:10.1021/ja311739v

Luo, Z., Yuan, X., Yu, Y., Zhang, Q., Leong, D. T., Lee, J. Y., et al. (2012). From aggregation-induced emission of Au(I)-thiolate complexes to ultrabright Au(0) @Au(I)-thiolate core-shell nanoclusters. *J. Am. Chem. Soc.* 134 (40), 16662–16670. doi:10.1021/ja306199p

Ma, J., Chen, J.-Y., Idowu, M., and Nyokong, T. (2008). Generation of singlet oxygen via the composites of water-soluble thiol-capped CdTe quantum dots-sulfonated aluminum phthalocyanines. *J. Phys. Chem. B* 112 (15), 4465–4469. doi:10.1021/jp711537j

Maity, S., Bain, D., and Patra, A. (2019). An overview on the current understanding of the photophysical properties of metal nanoclusters and their potential applications. *Nanoscale* 11 (47), 22685–22723. doi:10.1039/c9nr07963g

Miller, S. A., Womick, J. M., Parker, J. F., Murray, R. W., and Moran, A. M. (2009). Femtosecond relaxation dynamics of Au25L18− monolayer-protected clusters. *J. Phys. Chem. C* 113 (22), 9440–9444. doi:10.1021/jp9025046

Nair, L. V., Nazeer, S. S., Jayasree, R. S., and Ajayaghosh, A. (2015). Fluorescence imaging assisted photodynamic therapy using photosensitizer-linked gold quantum clusters. *ACS Nano* 9 (6), 5825–5832. doi:10.1021/acsnano.5b00406

Negishi, Y., Chaki, N. K., Shichibu, Y., Whetten, R. L., and Tsukuda, T. (2007). Origin of magic stability of thiolated gold clusters: A case study on Au25(SC6H13) 18. *J. Am. Chem. Soc.* 129 (37), 11322–11323. doi:10.1021/ja073580+

Negishi, Y., Matsuura, Y., Tomizawa, R., Kurashige, W., Niihori, Y., Takayama, T., et al. (2015). Controlled loading of small au_n clusters (n = 10–39) onto $BaLa_4Ti_4O_{15}$ photocatalysts: Toward an understanding of size effect of cocatalyst on water-splitting photocatalytic activity. *J. Phys. Chem. C* 119 (20), 11224–11232. doi:10.1021/jp5122432

Negishi, Y., Mizuno, M., Hirayama, M., Omatoi, M., Takayama, T., Iwase, A., et al. (2013). Enhanced photocatalytic water splitting by BaLa4Ti4O15 loaded with ~1 nm gold nanoclusters using glutathione-protected Au25 clusters. *Nanoscale* 5 (16), 7188–7192. doi:10.1039/c3nr01888a

Negishi, Y., Nobusada, K., and Tsukuda, T. (2005). Glutathione-protected gold clusters revisited: Bridging the gap between gold(I)−thiolate complexes and thiolate-protected gold nanocrystals. *J. Am. Chem. Soc.* 127 (14), 5261–5270. doi:10.1021/ja042218h

Negishi, Y., Takasugi, Y., Sato, S., Yao, H., Kimura, K., Tsukuda, T., et al. (2004). Magic-numbered au_n clusters protected by glutathione monolayers (n = 18, 21, 25, 28, 32, 39): isolation and spectroscopic characterization. *J. Am. Chem. Soc.* 126 (21), 6518–6519. doi:10.1021/ja0483589

Oliveira, B. L., Stenton, B. J., Unnikrishnan, V. B., de Almeida, C. R., Conde, J., Negrao, M., et al. (2020). Platinum-triggered bond-cleavage of pentynoyl amide and N-propargyl handles for drug-activation. *J. Am. Chem. Soc.* 142 (24), 10869–10880. doi:10.1021/jacs.0c01622

Pyo, K., Thanthirige, V. D., Kwak, K., Pandurangan, P., Ramakrishna, G., Lee, D., et al. (2015). Ultrabright luminescence from gold nanoclusters: Rigidifying the Au(I)-thiolate shell. *J. Am. Chem. Soc.* 137 (25), 8244–8250. doi:10.1021/jacs.5b04210

Qian, H., and Jin, R. (2011). Ambient synthesis of Au144(SR)60 nanoclusters in methanol. *Chem. Mat.* 23 (8), 2209–2217. doi:10.1021/cm200143s

Qian, H., Sfeir, M. Y., and Jin, R. (2010). Ultrafast relaxation dynamics of $[Au_{25}(SR)_{18}]^q$ nanoclusters: Effects of charge state. *J. Phys. Chem. C* 114 (47), 19935–19940. doi:10.1021/jp107915x

Roduner, E. (2006). Size matters: Why nanomaterials are different. *Chem. Soc. Rev.* 35 (7), 583–592. doi:10.1039/b502142c

Samia, A. C. S., Chen, X., and Burda, C. (2003). Semiconductor quantum dots for photodynamic therapy. *J. Am. Chem. Soc.* 125 (51), 15736–15737. doi:10.1021/ja0386905

Searle, P. F., Chen, M.-J., Hu, L., Race, P. R., Lovering, A. L., Grove, J. I., et al. (2004). Nitroreductase: A prodrug-activating enzyme for cancer gene therapy. *Clin. Exp. Pharmacol. Physiol.* 31 (11), 811–816. doi:10.1111/j.1440-1681.2004.04085.x

Shichibu, Y., Negishi, Y., Watanabe, T., Chaki, N. K., Kawaguchi, H., Tsukuda, T., et al. (2007). Biicosahedral gold clusters $[Au_{25}(PPh_3)_{10}(SC_nH_{2n+1})_5Cl_2]^{2+}$ (n = 2–18): A stepping stone to cluster-assembled materials. *J. Phys. Chem. C* 111 (22), 7845–7847. doi:10.1021/jp073101t

Silverstein, T. P. (2012). Marcus theory: Thermodynamics can control the kinetics of electron transfer reactions. *J. Chem. Educ.* 89 (9), 1159–1167. doi:10.1021/ed1007712

Soldevila-Barreda, J. J., and Metzler-Nolte, N. (2019). Intracellular catalysis with selected metal complexes and metallic nanoparticles: Advances toward the development of catalytic metallodrugs. *Chem. Rev.* 119 (2), 829–869. doi:10.1021/acs.chemrev.8b00493

Song, X. R., Goswami, N., Yang, H. H., and Xie, J. (2016). Functionalization of metal nanoclusters for biomedical applications. *Analyst* 141 (11), 3126–3140. doi:10.1039/c6an00773b

Stamplecoskie, K. G., Chen, Y.-S., and Kamat, P. V. (2014). Excited-state behavior of luminescent glutathione-protected gold clusters. *J. Phys. Chem. C* 118 (2), 1370–1376. doi:10.1021/jp410856h

Stamplecoskie, K. G., and Kamat, P. V. (2014). Size-dependent excited state behavior of glutathione-capped gold clusters and their light-harvesting capacity. *J. Am. Chem. Soc.* 136 (31), 11093–11099. doi:10.1021/ja505361n

Tlahuice-Flores, A., Whetten, R. L., and Jose-Yacaman, M. (2013). Ligand effects on the structure and the electronic optical properties of anionic Au25(SR) 18 clusters. *J. Phys. Chem. C* 117 (40), 20867–20875. doi:10.1021/jp407150t

Vankayala, R., Kuo, C.-L., Nuthalapati, K., Chiang, C.-S., and Hwang, K. C. (2015). Nucleus-targeting gold nanoclusters for simultaneous *in vivo* fluorescence imaging, gene delivery, and NIR-light activated photodynamic therapy. *Adv. Funct. Mat.* 25 (37), 5934–5945. doi:10.1002/adfm.201502650

Vankayala, R., Kuo, C. L., Sagadevan, A., Chen, P. H., Chiang, C. S., Hwang, K. C., et al. (2013). Morphology dependent photosensitization and formation of singlet oxygen (1Δg) by gold and silver nanoparticles and its application in cancer treatment. *J. Mat. Chem. B* 1 (35), 4379–4387. doi:10.1039/c3tb20806k

Vankayala, R., Sagadevan, A., Vijayaraghavan, P., Kuo, C. L., and Hwang, K. C. (2011). Metal nanoparticles sensitize the formation of singlet oxygen. *Angew. Chem. Int. Ed.* 50 (45), 10640–10644. doi:10.1002/anie.201105236

Varnavski, O., Ispasoiu, R. G., Balogh, L., Tomalia, D., and Goodson, T. (2001). Ultrafast time-resolved photoluminescence from novel metal–dendrimer nanocomposites. *J. Chem. Phys.* 114 (5), 1962–1965. doi:10.1063/1.1344231

Varnavski, O., Ramakrishna, G., Kim, J., Lee, D., and Goodson, T. (2010). Optically excited acoustic vibrations in quantum-sized monolayer-protected gold clusters. *ACS Nano* 4 (6), 3406–3412. doi:10.1021/nn1003524

Venzo, A., Antonello, S., Gascón, J. A., Guryanov, I., Leapman, R. D., Perera, N. V., et al. (2011). Effect of the charge state (z = −1, 0, +1) on the nuclear magnetic resonance of monodisperse Au25[S(CH2)2Ph]18z clusters. *Anal. Chem.* 83 (16), 6355–6362. doi:10.1021/ac2012653

Vong, K., Yamamoto, T., Chang, T. C., and Tanaka, K. (2020). Bioorthogonal release of anticancer drugs via gold-triggered 2-alkynylbenzamide cyclization. *Chem. Sci.* 11 (40), 10928–10933. doi:10.1039/d0sc04329j

Walter, M., Akola, J., Lopez-Acevedo, O., Jadzinsky, P. D., Calero, G., Ackerson, C. J., et al. (2008). A unified view of ligand-protected gold clusters as superatom complexes. *Proc. Natl. Acad. Sci. U. S. A.* 105 (27), 9157–9162. doi:10.1073/pnas.0801001105

Wang, G., Guo, R., Kalyuzhny, G., Choi, J.-P., and Murray, R. W. (2006). NIR luminescence intensities increase linearly with proportion of polar thiolate ligands in protecting monolayers of Au38 and Au140 quantum dots. *J. Phys. Chem. B* 110 (41), 20282–20289. doi:10.1021/jp0640528

Wang, S., Tang, L., Cai, B., Yin, Z., Li, Y., Xiong, L., et al. (2022). Ligand modification of Au25 nanoclusters for near-infrared photocatalytic oxidative functionalization. *J. Am. Chem. Soc.* 144 (9), 3787–3792. doi:10.1021/jacs.2c01570

Weerawardene, K. L. D. M., and Aikens, C. M. (2016). Theoretical insights into the origin of photoluminescence of Au25(SR)18− nanoparticles. *J. Am. Chem. Soc.* 138 (35), 11202–11210. doi:10.1021/jacs.6b05293

Weng, B., Lu, K. Q., Tang, Z., Chen, H. M., and Xu, Y. J. (2018). Stabilizing ultrasmall Au clusters for enhanced photoredox catalysis. *Nat. Commun.* 9, 1543–1553. doi:10.1038/s41467-018-04020-2

Wilson, W. R., and Hay, M. P. (2011). Targeting hypoxia in cancer therapy. *Nat. Rev. Cancer* 11 (6), 393–410. doi:10.1038/nrc3064

Witzel, S., Hashmi, A. S. K., and Xie, J. (2021). Light in gold catalysis. *Chem. Rev.* 121 (14), 8868–8925. doi:10.1021/acs.chemrev.0c00841

Wood, D. M., and Ashcroft, N. W. (1982). Quantum size effects in the optical properties of small metallic particles. *Phys. Rev. B* 25 (10), 6255–6274. doi:10.1103/PhysRevB.25.6255

Wu, Z., and Jin, R. (2010). On the ligand's role in the fluorescence of gold nanoclusters. *Nano Lett.* 10 (7), 2568–2573. doi:10.1021/nl101225f

Xiao, F. X., Hung, S. F., Miao, J., Wang, H. Y., Yang, H., Liu, B., et al. (2015). Metal-cluster-decorated TiO2 nanotube arrays: A composite heterostructure toward versatile photocatalytic and photoelectrochemical applications. *Small* 11 (5), 554–567. doi:10.1002/smll.201401919

Xu, H., and Suslick, K. S. (2010). Water-soluble fluorescent silver nanoclusters. *Adv. Mat.* 22 (10), 1078–1082. doi:10.1002/adma.200904199

Yang, J., Wang, F., Yuan, H., Zhang, L., Jiang, Y., Zhang, X., et al. (2019). Recent advances in ultra-small fluorescent Au nanoclusters toward oncological research. *Nanoscale* 11 (39), 17967–17980. doi:10.1039/c9nr04301b

Yanto, Y., Hall, M., and Bommarius, A. S. (2010). Nitroreductase from *Salmonella typhimurium*: Characterization and catalytic activity. *Org. Biomol. Chem.* 8 (8), 1826. doi:10.1039/B926274A

Yau, S. H., Varnavski, O., Gilbertson, J. D., Chandler, B., Ramakrishna, G., Goodson, T., et al. (2010). Ultrafast optical study of small gold monolayer protected clusters: A closer look at emission. *J. Phys. Chem. C* 114 (38), 15979–15985. doi:10.1021/jp101420g

Yu, C., Li, G., Kumar, S., Kawasaki, H., and Jin, R. (2013). Stable Au25(SR)18/TiO2 composite nanostructure with enhanced visible light photocatalytic activity. *J. Phys. Chem. Lett.* 4 (17), 2847–2852. doi:10.1021/jz401447w

Yu, Y., Chen, X., Yao, Q., Yu, Y., Yan, N., Xie, J., et al. (2013). Scalable and precise synthesis of thiolated Au10–12, Au15, Au18, and Au25 nanoclusters via pH controlled CO reduction. *Chem. Mat.* 25 (6), 946–952. doi:10.1021/cm304098x

Yu, Y., Li, J., Chen, T., Tan, Y. N., and Xie, J. (2015). Decoupling the CO-reduction protocol to generate luminescent Au22(SR)18 nanocluster. *J. Phys. Chem. C* 119 (20), 10910–10918. doi:10.1021/jp510829d

Yu, Y., Luo, Z., Chevrier, D. M., Leong, D. T., Zhang, P., Jiang, D.-e., et al. (2014). Identification of a highly luminescent Au22(SG)18 nanocluster. *J. Am. Chem. Soc.* 136 (4), 1246–1249. doi:10.1021/ja411643u

Yuan, X., Goswami, N., Chen, W., Yao, Q., and Xie, J. (2016). Insights into the effect of surface ligands on the optical properties of thiolated Au25 nanoclusters. *Chem. Commun.* 52 (30), 5234–5237. doi:10.1039/c6cc00857g

Zhang, J., and Liu, J. (2020). Light-activated nanozymes: Catalytic mechanisms and applications. *Nanoscale* 12 (5), 2914–2923. doi:10.1039/c9nr10822j

Zhang, J., Zhou, Y., Zheng, K., Abroshan, H., Kauffman, D. R., Sun, J., et al. (2018). Diphosphine-induced chiral propeller arrangement of gold nanoclusters for singlet oxygen photogeneration. *Nano Res.* 11 (11), 5787–5798. doi:10.1007/s12274-017-1935-2

Zhang, X.-D., Wu, D., Shen, X., Liu, P.-X., Fan, F.-Y., Fan, S.-J., et al. (2012). *In vivo* renal clearance, biodistribution, toxicity of gold nanoclusters. *Biomaterials* 33 (18), 4628–4638. doi:10.1016/j.biomaterials.2012.03.020

Zheng, J., Zhang, C., and Dickson, R. M. (2004). Highly fluorescent, water-soluble, size-tunable gold quantum dots. *Phys. Rev. Lett.* 93 (7), 077402–077405. doi:10.1103/PhysRevLett.93.077402

Zheng, Y., Wu, J., Jiang, H., and Wang, X. (2021). Gold nanoclusters for theranostic applications. *Coord. Chem. Rev.* 431, 213689–213715. doi:10.1016/j.ccr.2020.213689

Zhou, M., Du, X., Wang, H., and Jin, R. (2021). The critical number of gold atoms for a metallic state nanocluster: Resolving a decades-long question. *ACS Nano* 15 (9), 13980–13992. doi:10.1021/acsnano.1c04705

Zhou, M., Higaki, T., Hu, G., Sfeir Matthew, Y., Chen, Y., Jiang, D.-e., et al. (2019). Three-orders-of-magnitude variation of carrier lifetimes with crystal phase of gold nanoclusters. *Science* 364 (6437), 279–282. doi:10.1126/science.aaw8007

Zhou, M., and Song, Y. (2021). Origins of visible and near-infrared emissions in [Au25(SR)18]− nanoclusters. *J. Phys. Chem. Lett.* 12 (5), 1514–1519. doi:10.1021/acs.jpclett.1c00120

Zhou, M., Tian, S., Zeng, C., Sfeir, M. Y., Wu, Z., Jin, R., et al. (2017a). Ultrafast relaxation dynamics of Au38(SC2H4Ph)24 nanoclusters and effects of structural isomerism. *J. Phys. Chem. C* 121 (20), 10686–10693. doi:10.1021/acs.jpcc.6b10360

Zhou, M., Zeng, C., Chen, Y., Zhao, S., Sfeir, M. Y., Zhu, M., et al. (2016). Evolution from the plasmon to exciton state in ligand-protected atomically precise gold nanoparticles. *Nat. Commun.* 7, 13240–13246. doi:10.1038/ncomms13240

Zhou, M., Zeng, C., Sfeir, M. Y., Cotlet, M., Iida, K., Nobusada, K., et al. (2017b). Evolution of excited-state dynamics in periodic Au28, Au36, Au44, and Au52 nanoclusters. *J. Phys. Chem. Lett.* 8 (17), 4023–4030. doi:10.1021/acs.jpclett.7b01597

Zhou, S., Duan, Y., Wang, F., and Wang, C. (2017). Fluorescent Au nanoclusters stabilized by silane: Facile synthesis, color-tunability and photocatalytic properties. *Nanoscale* 9 (15), 4981–4988. doi:10.1039/c7nr01052d

Zhu, H., Goswami, N., Yao, Q., Chen, T., Liu, Y., Xu, Q., et al. (2018). Cyclodextrin–gold nanocluster decorated TiO2 enhances photocatalytic decomposition of organic pollutants. *J. Mat. Chem. A Mat.* 6 (3), 1102–1108. doi:10.1039/c7ta09443d

Zhu, M., Aikens, C. M., Hollander, F. J., Schatz, G. C., and Jin, R. (2008a). Correlating the crystal structure of a thiol-protected Au25 cluster and optical properties. *J. Am. Chem. Soc.* 130 (18), 5883–5885. doi:10.1021/ja801173r

Zhu, M., Eckenhoff, W. T., Pintauer, T., and Jin, R. (2008b). Conversion of anionic [Au25(SCH2CH2Ph)18]− cluster to charge neutral cluster via air oxidation. *J. Phys. Chem. C* 112 (37), 14221–14224. doi:10.1021/jp805786p

frontiers | Frontiers in Chemistry

ORIGINAL RESEARCH
published: 19 July 2022
doi: 10.3389/fchem.2022.957412

Rational Design of Synergistic Structure Between Single-Atoms and Nanoparticles for CO_2 Hydrogenation to Formate Under Ambient Conditions

Shengliang Zhai†, Ling Zhang†, Jikai Sun†, Lei Sun, Shuchao Jiang, Tie Yu, Dong Zhai, Chengcheng Liu, Zhen Li and Guoqing Ren**

Institute of Molecular Sciences and Engineering, Institute of Frontier and Interdisciplinary Science, Shandong University, Qingdao, China

Single-atom catalysts (SACs) as the new frontier in heterogeneous catalysis have attracted increasing attention. However, the rational design of SACs with high catalytic activities for specified reactions still remains challenging. Herein, we report the rational design of a Pd_1-Pd_{NPs} synergistic structure on *2,6*-pyridinedicarbonitrile-derived covalent triazine framework (*CTF*) as an efficient active site for CO_2 hydrogenation to formate under ambient conditions. Compared with the catalysts mainly comprising Pd_1 and Pd_{NPs}, this hybrid catalyst presented significantly improved catalytic activity. By regulating the ratio of Pd_1 to Pd_{NPs}, we obtained the optimal catalytic activity with a formate formation rate of 3.66 $mol_{HCOOM}{\cdot}mol_{Pd}^{-1}{\cdot}h^{-1}$ under ambient conditions (30°C, 0.1 MPa). Moreover, as a heterogeneous catalyst, this hybrid catalyst is easily recovered and exhibits about a 20% decrease in the catalytic activity after five cycles. These findings are significant in elucidating new rational design principles for CO_2 hydrogenation catalysts with superior activity and may open up the possibilities of converting CO_2 under ambient conditions.

Keywords: synergistic effect, single-atom catalysts (SACs), CO_2 hydrogenation, formic acid, ambient conditions

OPEN ACCESS

Edited by:
Haifeng Xiong, Xiamen University, China

Reviewed by:
Yali Yao, University of South Africa, South Africa
Haibo Zhu, Fuzhou University, China

****Correspondence:***
Tie Yu
yutie@sdu.edu.cn
Guoqing Ren
renguoqing@sdu.edu.cn

†These authors have contributed equally to this work

Specialty section:
This article was submitted to Catalytic Reactions and Chemistry, a section of the journal Frontiers in Chemistry

Received: *31 May 2022*
Accepted: *24 June 2022*
Published: *19 July 2022*

Citation:
Zhai S, Zhang L, Sun J, Sun L, Jiang S, Yu T, Zhai D, Liu C, Li Z and Ren G (2022) Rational Design of Synergistic Structure Between Single-Atoms and Nanoparticles for CO_2 Hydrogenation to Formate Under Ambient Conditions. Front. Chem. 10:957412. doi: 10.3389/fchem.2022.957412

INTRODUCTION

In recent years, single-atom catalysts (SACs) have attracted significant interest in heterogeneous catalysis for their advantages of 100% metal atom use, single active site structure, and unexpected high activity and selectivity for various reactions (Yang et al., 2013; Wang et al., 2018). Since the concept of SACs was proposed in 2011 (Qiao et al., 2011), it has solved the problems of low metal loadings (Liu et al., 2016; Li et al., 2018), poor thermal stability (Jones et al., 2016; Liu et al., 2020a; Liu et al., 2020b), and difficulties in large-scale production (Liu et al., 2020b; He et al., 2020) after nearly 10 years of vigorous development. However, although SACs are presented as homogeneous active centers, their catalytic activity is often difficult to compare with that of homogeneous catalysts and enzyme catalysts, and even lower than that of the corresponding nanocatalyst system in some cases (Ding et al., 2015). One of the reasons is that it is often difficult for a single metal atom center to activate multiple reactants with different properties or a single polyatomic molecule. The catalytic activity of monatomic catalysts does not depend on their single active center, but also on their surrounding chemical environment. The design and controllable construction of the synergistic structure between the single-atom

center and its surrounding active sites is the key to achieving the high-efficiency catalytic performance of SACs.

Synergistic catalysis has been widely studied in the field of nanocatalyst and has shown obvious advantages in improving the activity and product selectivity of catalysts. For example, Liu et al. (2017) designed a Schiff-base-mediated gold catalyst for hydrogenation to formate reaction. The Schiff-base functional group grafted on a SiO_2 support helps CO_2 activation by the formation of a weak carbamate zwitterionic intermediate, and Au is for H_2 dissociation. We previously introduced a CeO_2 promoter with excellent dissociation ability to water molecules and oxygen molecules into an $Au/MgGa_2O_4$ catalyst to establish the synergistic catalytic effect between nano Au and the CeO_2 promoter, which significantly improved the catalytic activity for the water gas shift and catalytic combustion reaction (Ren et al., 2019). As for SACs, although the concept of an atomic scaled synergistic effect has not been clearly proposed and systematically studied, there are some research examples of synergistic effects. For example, we recently reported a highly active dual single-Pd-atom catalyst, which could catalyze the hydrogenation of CO_2 to formate under ambient conditions (Ren et al., 2022). It was found that the pore enrichment effect of microporous structures and the ternary synergetic effect among two neighboring Pd atoms and a rich nitrogen environment were the main reasons for this extraordinary catalytic activity. Liu et al. (2018) prepared a Ni-N-C SAC with metal loading up to 7.5 wt% by using N-doped C as the support, which exhibited excellent catalytic activity and cyclic stability for the hydrogenolysis of cellulose to ethylene glycol. The theoretical calculation results showed that the H_2 molecule was activated by assistance of the nearest uncoordinated pyridine N atom of Ni. Therefore, the design of the synergistic catalytic structure based on the properties of reactants provides a good idea for the rational design of highly effective SACs.

In this work, we focused on the synergistic effect between single atoms and nanoparticles for CO_2 hydrogenation to formate, an attractive reaction to achieve CO_2 emission reduction and safe hydrogen storage (Alvarez et al., 2017; Eppinger and Huang, 2017; Su et al., 2019). Through theoretical calculations, we found that Pd_1 and Pd_{NPs} were the preferred active sites for CO_2 activation and hydrogen dissociation, respectively. Experimentally, we synthesized a Pd_1-Pd_{NPs} synergistic structure on 2,6-pyridinedicarbonitrile-derived covalent triazine framework (*CTF*) by modulating the Pd loadings and reduction time, which exhibited high efficiency for the ambient hydrogenation of CO_2 to formate. The optimal catalytic performance of the catalyst was obtained by regulating the ratio of Pd_1 to Pd_{NPs}. Furthermore, the recycling stability was also investigated. This work provides a new strategy for the rational design of highly active SACs and is very advantageous with regard to putting forward the conversion CO_2 into practical applications.

EXPERIMENT

Chemicals

All the chemicals used in this study were of analytical grade and were used without further purification unless otherwise noted. Anhydrous zinc chloride ($ZnCl_2$, ≥99%), 2,6-pyridinedicarbonitrile (2,6-DCP, ≥ 97%), and palladium trifluoroacetate ($Pd(O_2CCF_3)_2$, ≥98%) were purchased from Shanghai Macklin Biochemical Co., Ltd. Hydrochloric acid (HCl, 36.0–38.0%) and sodium bicarbonate ($NaHCO_3$, ≥99.5%) were purchased from Sinopharm Chemical Reagent Co., Ltd. High purity compressed N_2, 10% H_2/N_2, and 50% CO_2/50% H_2 gases were obtained from the Deyi Gas Products Co., Ltd. (Qingdao, China).

Sample Preparation

The *CTF-400:* 2,6-DCP-derived *CTF* was synthesized as described elsewhere (Kuhn et al., 2008). In detail, 2,6-pyridinedicarbonitrile and anhydrous $ZnCl_2$ were mixed at the ratio of 1:5 (w/w) and ground under the glove box. The mixed powder was transferred into a quartz ampoule tube, and then evacuated, sealed, and heated to 400°C for 40 h. After the reaction, the mixture was subsequently ground and washed with large amounts of water and diluted HCl (2 M) to remove the residual $ZnCl_2$. After that, the resulting black powder was dried in a vacuum at 150°C for 12 h, and the resulting product was denoted to be "*CTF*-400."

Pd/[CTF-400]: Pd/[*CTF-400*] catalysts were prepared by soaking the *CTF-400* support powder in the aqueous solution of palladium trifluoroacetate with a Pd nominal weight loading of 10 wt% and 0.5 wt% for 12 h with magnetic stirring in a N_2 atmosphere. The suspensions were then filtrated and washed with deionized water. The resulting filter cake was dried at 80°C for 12 h under a vacuum. The samples were denoted as *10*Pd/[*CTF-400*] and *0.5*Pd/[*CTF-400*], respectively, and the Pd actual weight loadings were detected to be 6.48 wt% and 0.28 wt% from ICP-AES analysis, respectively. *10*Pd/[*CTF-400*]-R-*t* samples were achieved by hydrogen reduction at 300°C for a different time. Specifically, the sample was heated to 300°C with the programming of 5°C/min under a constant flow of nitrogen. Then, the sample was kept at 300°C for 5, 10, 15, 30, 60, and 180 min under a constant flow of 10% H_2/90% N_2 at 10 ml/min, respectively. Subsequently, the furnace was cooled down to room temperature under the protection of nitrogen.

Characterization

Fourier-transform infrared spectra (FT-IR) were performed in transmission mode on a Bruker VERTEX 70v spectrometer equipped with a DLATGS detector. The sample was diluted with KBr powder.

Surface areas and pore size distribution analyses were measured on Quantachrome Autosorb-iQ. N_2 was used as the adsorbate and surface areas were calculated using the BET analysis method. All of the samples were degassed under a vacuum at 260°C for 8 h before measurement.

Elemental analyses were performed on a Vario El elemental analyzer.

X-ray photoelectron spectroscopy (XPS) data were analyzed on a Thermofisher ESCALAB 250Xi spectrometer using a monochromatized Al Kα X-ray source (1,486.6 eV). All the XPS data were calibrated by using C 1s binding energy at 284.8 eV.

Transmission electron microscopy (TEM) analysis was performed on FEI Tecnai G2 F20 at 200 keV. Aberration-

corrected scanning transmission electron microscopy (AC-STEM) and EDX mapping analysis were performed on a JEOL JEM-ARM200F.

Catalytic Reactions

CO_2 hydrogenation to formate reaction was carried out in a base solution under ambient conditions (30°C and 1 bar). In general, 20 mg catalysts were added into 5 ml $NaHCO_3$ (1 mol/L) in a three-necked bottle connected to a balloon. Then, the feed gas comprising CO_2 (50% vol%) and H_2 (50% vol%) was introduced after purging the residual air. After stirring for 12 h under ambient conditions, formate in the reaction mixture was determined by high-performance liquid chromatography (HPLC). In recycling experiments, the catalyst was recovered by filtration, washed with water, and dried under a vacuum. The reaction rate was calculated according to the following equation:

$$\text{Rate} = \frac{\text{Concentration of formate}\left(\frac{\text{mol}}{\text{L}}\right) \times \text{volume}\,(\text{L})}{Pd\ amount\ (mol) \times time\,(h)}.$$

Computational Methods

The calculation was performed by using the M06l/6-31G* method for nonmetal elements whereas the M06l/LANL2DZ method was used for metal atoms (Hehre et al., 1972; Hay and Wadt, 1985; Zhao and Truhlar, 2006). The metals were augmented with the corresponding LANL2DZ pseudo-potential, which was both acceptable in precision and time-consuming. Vibrational frequencies of the optimized configurations were analyzed to validate that these configurations correspond to the local minima or transition state (TS). The TS with one imaginary frequency was found and verified by the intrinsic reaction coordinate (IRC) method (Fukui, 1981).

The DFT calculations were performed on the Vienna ab initio simulation package (VASP) (Kresse and Furthmuller, 1996b; Kresse and Furthmuller, 1996a) to investigate the CO_2 hydrogenation process on a Pd bulk surface and Pd_1/CTF. The optB88-vdW was used to describe the exchange-correlation functional, which described the van der Waals forces appropriately (Dion et al., 2004; Lee et al., 2010). The projector augmented wave (PAW) potentials (Blochl, 1994) were used for electron–ion interactions, with a plane-wave kinetic energy cutoff of 400 eV. The geometry structures were relaxed until the forces on all atoms were less than 0.05 eV/Å. The transition states were searched using the Climbing Image Nudged Elastic Band (CI-NEB) method (Henkelman et al., 2000). Each transition state was relaxed until the forces on all atoms were less than 0.05 eV/Å.

The Pd (1 1 1) surface was modeled by a three-layer slab with a (4 × 4) surface unit cell and a vacuum thickness of 20 Å. The bottom two atomic layers of Pd (1 1 1) were fixed while the remaining layer, together with the adsorbates, were fully relaxed during relaxation. The lattice constant for Pd_1/CTF is the same as for Pd, with a size of 13.79 Å × 13.79 Å × 24.51 Å. The Brillouin zone was sampled using a (2 × 2×1) k-point grid based on the Monkhorst-Pack (1976) scheme.

RESULTS AND DISCUSSION

Theoretical Predictions

To achieve the most active catalyst structure, two different Pd species, Pd_1 and Pd_{NPs}, were investigated to carry out the CO_2 activation and H_2 dissociation process. We found that *2,6*-pyridinedicarbonitrile-derived *CTF*-coordinated Pd_1 exhibited much higher adsorption energy for the CO_2 molecule than that of the Pd (111) surface (−1.15 vs. −0.28 eV), indicating that Pd_1 could be served as the active site for CO_2 activation (**Figures 1A,B**). However, further calculation showed that the dissociation of the hydrogen molecule on Pd_1 was difficult in thermodynamics. In contrast, the dissociation of the hydrogen molecule on the Pd surface is thermodynamically feasible (**Supplementary Table S1**). Moreover, metallic Pd has also been proved to have high activity in H_2 dissociation with a nearly zero activation barrier (Ni and Zeng, 2009; Lozano et al., 2010). Therefore, we infer that Pd_1 and Pd_{NPs} catalyze CO_2 hydrogenation in collaboration through the hydrogen molecule dissociation on Pd_{NPs} and CO_2 hydrogenation on Pd_1. The potential energy surface (PES) of CO_2 hydrogenation to formic acid on this hybrid catalyst is shown in **Figure 1C**. The first hydrogenation step is the rate-determining step with a barrier energy of 1.37 eV. The second step of hydrogenation is exothermic, with an energy of 2.90 eV. The energy barrier of this step is only 0.12 eV. The theoretical calculations confirm that the hydrogenation of CO_2 catalyzed by the Pd_1-Pd_{NPs} synergistic structure has a low barrier and can occur under ambient conditions.

Catalyst Synthesis and Characterization

The 2,6-pyridinedicarbonitrile-derived covalent triazine framework is formed by the trimerization of 2,6-pyridinedicarbonitrile in molten $ZnCl_2$ at 400°C for 40 h, and is labeled *CTF-400* (**Figure 2A**). FT-IR, shown in **Supplementary Figure S1**, confirmed the formation of the corresponding covalent triazine rings. In addition, the prepared *CTF-400* possessed a surface area of 418 $m^2\,g^{-1}$, a pore size of 0.53 nm, and a total pore volume of 0.21 $m^3\,g^{-1}$ (**Supplementary Table S2**). The nitrogen content was estimated to be 19.51 wt% (**Supplementary Table S3**), which is high enough to load and stabilize the supported Pd species. The Pd/[*CTF-400*] catalyst was prepared by soaking the support powders in aqueous palladium trifluoroacetate followed by filtrating and washing after stirring for 12 h under a N_2 atmosphere. By varying the initial Pd loading percent to be 0.5 wt% and 10 wt%, the single-atomic dispersed sample and the coexistence of Pd_1 and Pd_{NPs} samples were prepared. The samples were denoted to be *0.5*Pd/[*CTF-400*] and *10*Pd/[*CTF-400*], respectively. After further reduction of *10*Pd/[*CTF-400*] at 300°C for 3 h, the Pd_{NPs}-dominated sample was also achieved as the reference, which was denoted to be *10*Pd/[*CTF-400*]-R-*3h*.

Figures 2B–D display the TEM images at low magnification for *0.5*Pd/[*CTF-400*], *10*Pd/[*CTF-400*], and *10*Pd/[*CTF-400*]-R-*3h*, respectively. It is obvious that *0.5*Pd/[*CTF-400*] presents the notable character of *CTF-400* without any Pd nanoparticles, which indicates that Pd is atomically dispersed on *CTF-400*

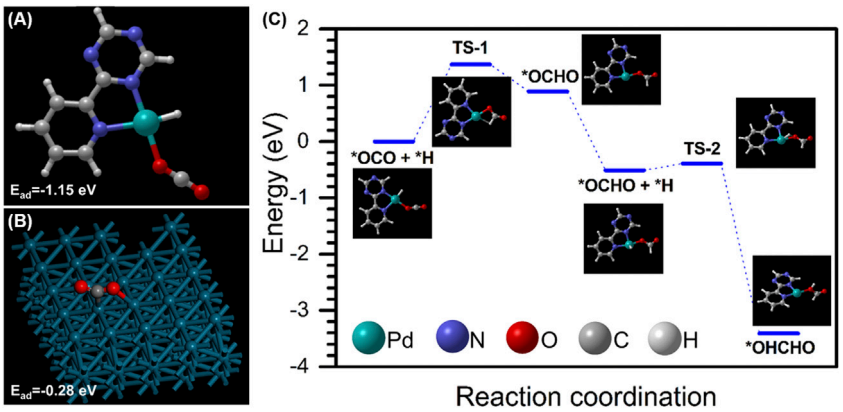

FIGURE 1 | (A,B) CO_2 adsorption energy on Pd_1/*CTF* and the Pd surface; **(C)** the potential energy surface (PES) of CO_2 hydrogenation on Pd_1/*CTF*.

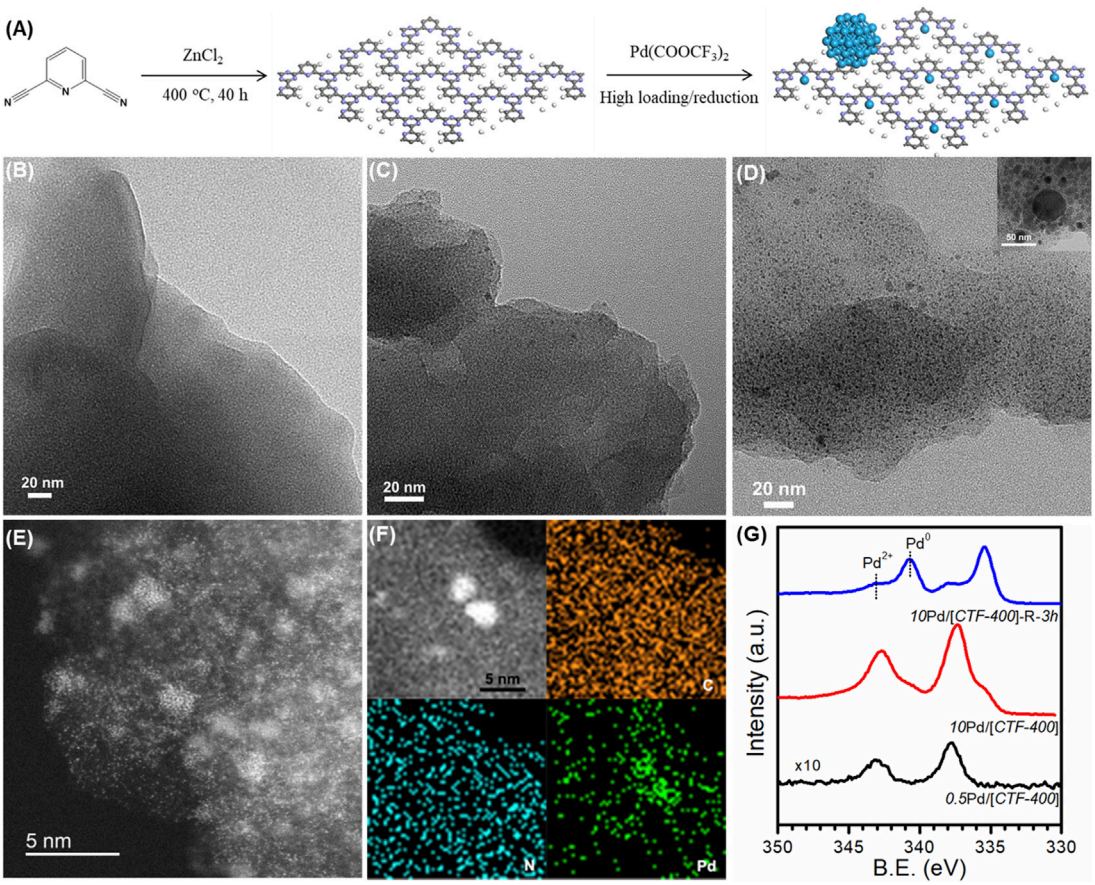

FIGURE2 | Structural characterizations of Pd/[*CTF-400*]. **(A)** Schematic illustration of the fabrication procedures of Pd/[*CTF-400*]. **(B–D)** HRTEM images of the characterization of *0.5*Pd/[*CTF-400*], *10*Pd/[*CTF-400*], and *10*Pd/[*CTF-400*]-R-*3h*. **(E,F)** Aberration-corrected STEM and EDS mapping of *10*Pd/[*CTF-400*]. **(G)** XPS profiles for *0.5*Pd/[*CTF-400*], *10*Pd/[*CTF-400*], and *10*Pd/[*CTF-400*]-R-*3h* samples.

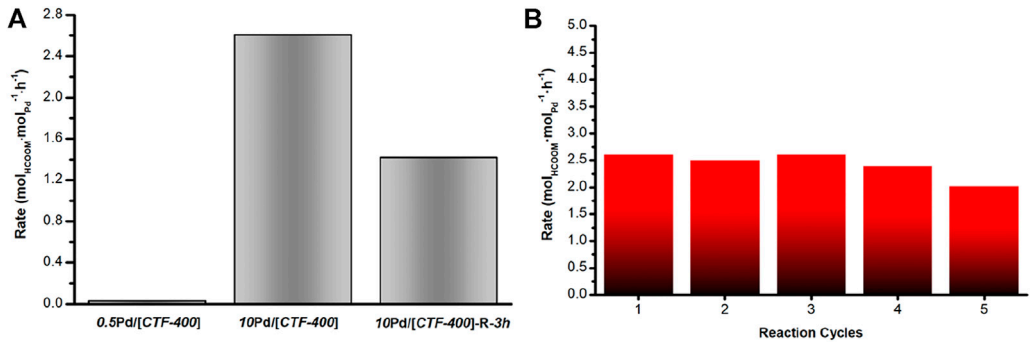

FIGURE 3 | Catalytic performance of Pd/[*CTF-400*] for the hydrogenation of carbon dioxide to formate. **(A)** Formate formation rate of *0.5*Pd/[*CTF-400*], *10*Pd/[*CTF-400*], and *10*Pd/[*CTF-400*]-R-*3h*. **(B)** Reuse test of *10*Pd/[*CTF-400*]. Reaction conditions: 20 mg catalyst, 30°C, 1bar (CO_2/H_2 = 1:1), and 5 ml $NaHCO_3$ (1 M), 12 h.

TABLE 1 | Performance of Pd/[*CTF-400*] for CO_2 hydrogenation to formate.

Entry	Catalyst	HCOOH/mM	Rate ($mol_{HCOOM}·mol_{Pd}^{-1}·h^{-1}$)
1	0.5Pd/[CTF-400]	0.033	0.026
2	10Pd/[CTF-400]	76.4	2.60
3	10Pd/[CTF-400]-R-5 min	86.3	2.86
4	10Pd/[CTF-400]-R-10 min	110.3	3.66
5	10Pd/[CTF-400]-R-15 min	102.2	3.39
6	10Pd/[CTF-400]-R-30 min	88.9	2.94
7	10Pd/[CTF-400]-R-1 h	58.7	1.95
8	10Pd/[CTF-400]-R-3 h	42.8	1.42

Reaction condition: 20 mg catalyst, 5 ml 1M $NaHCO_3$ solvent, 30°C, 0.1 MPa, 12 h.

(**Figure 2B**). Scattered Pd nanoparticles appear on the *10*Pd/[*CTF-400*] sample, which illustrates that Pd atoms on *CTF-400* have partially aggregated to nanoparticles (**Figure 2C**). Further observation of this sample using AC-STEM confirms that Pd single atoms and nanoparticles coexist with good contact (**Figures 2E,F**). However, for the *10*Pd/[*CTF-400*]-R-*3h* sample, a large amount of Pd nanoparticles with a major size of ~3 nm was presented. The formation of Pd_{NPs} was due to the aggregation of highly dispersed Pd atoms. For the as-prepared catalyst, most of the Pd species are well dispersed as single-atoms and sub-nanoparticles (as shown in **Figures 2E,F**), which have high surface energy and are unstable at high temperatures and reductive atmospheres. Therefore, the percentage of Pd_{NPs} in the *10*Pd/[*CTF-400*]-R-*3h* sample increased after reduction for 3 h. In addition, electronic properties for both samples were also estimated by XPS. As shown in **Figure 2G**, the binding energy of Pd $3d_{5/2}$ in *0.5*Pd/[*CTF-400*] is 337.3 eV, which can be attributed to that for Pd^{2+} presented as Pd_1 in geometry. In addition to Pd^{2+}, *10*Pd/[*CTF-400*] also shows the characteristic of metallic Pd corresponding to Pd_{NPs} in geometry with a binding energy of Pd $3d_{5/2}$ at 335.2 eV, and the ratio of Pd^{2+} to Pd^0 is estimated to be about 90%. Different from that of *10*Pd/[*CTF-400*], Pd^0 is dominant in the *10*Pd/[*CTF-400*]-R-*3h* sample with the ratio of Pd^0 to Pd^{2+} being more than 70%. On the whole, the Pd_1, Pd_1-Pd_{NPs} hybrid, and Pd_{NPs}-dominated catalysts were successfully prepared, which can be used as good model catalysts to study the synergistic effect between different Pd active sites.

Catalytic Hydrogenation of CO_2 to Formic Acid Under Ambient Conditions

The catalytic performances of the as-prepared Pd catalysts for CO_2 hydrogenation were studied at 30°C in a H_2/CO_2 mixture (0.1 MPa) with $NaHCO_3$ (1 mol/L) as an additive in the liquid phase. After a reaction of 12 h, the formate was detected by using HPLC. As shown in **Figure 3A** and **Table 1**, compared with the Pd_1 and Pd_{NPs} nanoparticle-dominated catalysts, the CO_2 hydrogenation activity of the *10*Pd/[*CTF-400*] catalyst was significantly enhanced (entries 1, 2 and 8 in **Table 1**). In detail, *10*Pd/[*CTF-400*] exhibited a formate formation rate of 2.60 $mol_{HCOOM}·mol_{Pd}^{-1}·h^{-1}$, which was obviously higher than that of *0.5*Pd/[*CTF-400*] (0.026 $mol_{HCOOM}·mol_{Pd}^{-1}·h^{-1}$) and *10*Pd/[*CTF-400*]-R-*3h* (1.42 $mol_{HCOOM}·mol_{Pd}^{-1}·h^{-1}$). Moreover, the heterogeneous nature of this catalyst allows it to be easily recovered by centrifugation, and the recycling tests indicated that there was around a 20% decrease in the catalytic activity after five uses (**Figure 3B**). This result demonstrates that the catalyst can be reused after a simple separation process, which is very advantageous with regard to practical applications.

The aforementioned result confirms the theoretical predictions that the coexistence of Pd_1 and Pd_{NPs} is necessary for the activation of H_2 and CO_2 at the same time. To obtain the optimized catalytic activity, the ratio of Pd_1 to Pd_{NPs} was optimized. We attempted to get the sample with optimal Pd_1/Pd_{NPs} by lowering the *10*Pd/[*CTF-400*]

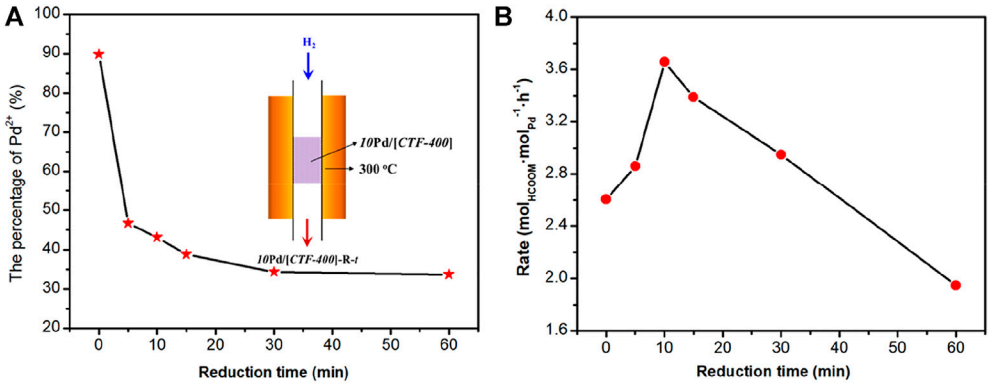

FIGURE 4 | Optimization of the ratio of Pd single-atoms to nanoparticles for the hydrogenation of carbon dioxide to formate. **(A)** Percentage of Pd_1 in *10*Pd/[*CTF-400*]-R-*t* samples. **(B)** Formate formation rate of *10*Pd/[*CTF-400*]-R-*t* samples (*t* = 0, 5, 10, 15, 30, and 60 min).

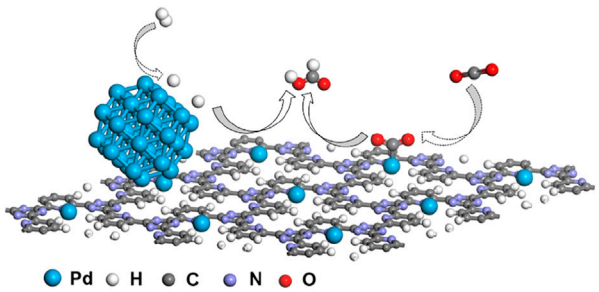

FIGURE 5 | Proposed synergistic effect mechanism of Pd/[*CTF-400*] for the hydrogenation of carbon dioxide to formate.

sample into a tubular furnace at 300°C and reducing it in 10 vol% H_2 for 5, 10, 15, 30, and 60 min, respectively. The corresponding samples are denoted as *10*Pd/[*CTF-400*]-R-*t*, where "*t*" represents the reduction time. X-ray photoelectron spectroscopy (XPS) was performed to get the ratios between Pd single atoms and nanoparticles (**Figure 4A** and **Supplementary Figures S3–S7**). With careful deconvolution from the overlapped peaks of Pd^{2+} 3d and Pd^0 3d, the ratios of Pd_1 ion to the total palladium were estimated to be 89.9, 46.7, 43.1, 38.7, 34.3, and 33.7% with the continuous extension of hydrogen reduction time from 0 to 60 min (**Figure 4A**). **Figure 4B** shows the catalytic performances of *10*Pd/[*CTF-400*]-R-*t* under ambient conditions (30°C, 0.1 MPa). It can be seen that the catalytic activities exhibit a volcano-type curve with a decrease in the Pd_1 ratio. *10*Pd/[*CTF-400*]-R-*10* min with a Pd_1 ratio of 43.1% performs the best catalytic activity, and the formate formation rate reaches 3.66 $mol_{HCOOM}{\cdot}mol_{Pd}{}^{-1}{\cdot}h^{-1}$. The existence of the optimal Pd_1 ratio is due to the rate equilibrium of hydrogen dissociation on Pd^0 nanoparticles and carbon dioxide activation on Pd_1.

Based on the aforementioned analysis, the synergistic effect mechanism of *10*Pd/[*CTF-400*] for the hydrogenation of CO_2 to formate is shown in **Figure 5**. The *10*Pd/[*CTF-400*] catalyst integrates both Pd_{NPs} and Pd_1 into one catalyst system, where the Pd_{NPs} boosts the dissociation of H_2 whereas Pd_1 ions undertake the activation task of CO_2. Through the atom diffusion process, H atoms generated at Pd_{NPs} move to the adsorbed CO_2 on Pd_1 for high-efficiency hydrogenation. Theoretical calculations shown in **Figure 1** confirmed the rationality of the tasks over each active site, that is, hydrogen dissociation occurs more easily on Pd_{NP}, and carbon dioxide hydrogenation activation prefers to occur on Pd_1. Experiments further verified the synergistic effect between Pd_1 and Pd_{NPs}, and the 10Pd/[*CTF-400*] catalyst performed nearly two orders of magnitude higher activity than *0.5*Pd/[*CTF-400*] and twice the reactivity of 10Pd/[*CTF-400*]-R-3 h.

CONCLUSION

In summary, we have rationally designed a highly efficient catalytic system for the hydrogenation of carbon dioxide to formate under ambient conditions based on theoretical predictions. Through modeling the CO_2 adsorption and hydrogen dissociation process on both Pd_1 and Pd_{NPs}, it was found that Pd_1 performed the higher adsorption energy for CO_2 and could be a potential candidate for CO_2 activation. Compared with Pd_1, hydrogen dissociation occurred more easily on Pd nanoparticles. Based on this prediction, the Pd/[*CTF-400*] catalyst integrating both Pd_1 and Pd_{NPs} on one catalyst system was synthesized and realized the hydrogenation of CO_2 to formate with a formate formation rate of 3.66 $mol_{HCOOM}{\cdot}mol_{Pd}{}^{-1}{\cdot}h^{-1}$ under ambient conditions (30°C, 1 bar). This hybrid catalyst presented nearly two orders of magnitude higher than the catalyst containing bare Pd_1 and twice the reactivity of that containing bare Pd^0 nanoparticles. These discoveries may pave the way for the construction of active SACs

with synergistic effects and open up the possibilities of converting CO_2 under ambient conditions.

DATA AVAILABILITY STATEMENT

The original contributions presented in the study are included in the article/**Supplementary Material**; further inquiries can be directed to the corresponding author.

AUTHOR CONTRIBUTIONS

GR conceived the concept and design research. SZ, LZ, and GR designed and carried out the catalyst synthesis, characterization, and catalytic test. LS and JS executed the theoretical calculations. TY carried out the TEM characterization. All authors were involved in the writing of the manuscript. The authors declare no competing interests.

FUNDING

This work was supported by the National Key Research and Development Program of China (No. 2017YFA0204800), the National Natural Science Foundation of China (No. 21525315), the Natural Science Foundation of Shandong Province (ZR2020QB056), and the Fundamental Research Funds of Shandong University (2019GN021 to G. R, 2019GN111 to T. Y., and 2019HW016 to L.S.), Shandong University Future Program for Young Scholars (Nos. 62460082164128 and 62460082064083).

SUPPLEMENTARY MATERIAL

The Supplementary Material for this article can be found online at: https://www.frontiersin.org/articles/10.3389/fchem.2022.957412/full#supplementary-material

REFERENCES

Álvarez, A., Bansode, A., Urakawa, A., Bavykina, A. V., Wezendonk, T. A., Makkee, M., et al. (2017). Challenges in the Greener Production of Formates/Formic Acid, Methanol, and DME by Heterogeneously Catalyzed CO_2 Hydrogenation Processes. *Chem. Rev.* 117 (14), 9804–9838. doi:10.1021/acs.chemrev.6b00816

Blöchl, P. E. (1994). Projector Augmented-Wave Method. *Phys. Rev. B* 50 (24), 17953–17979. doi:10.1103/PhysRevB.50.17953

Ding, K., Gulec, A., Johnson, A. M., Schweitzer, N. M., Stucky, G. D., Marks, L. D., et al. (2015). Identification of Active Sites in CO Oxidation and Water-Gas Shift over Supported Pt Catalysts. *Science* 350 (6257), 189–192. doi:10.1126/science.aac6368

Dion, M., Rydberg, H., Schröder, E., Langreth, D. C., and Lundqvist, B. I. (2004). Van Der Waals Density Functional for General Geometries. *Phys. Rev. Lett.* 92 (24), 246401. doi:10.1103/Physrevlett.92.246401

Eppinger, J., and Huang, K.-W. (2017). Formic Acid as a Hydrogen Energy Carrier. *ACS Energy Lett.* 2 (1), 188–195. doi:10.1021/acsenergylett.6b00574

Fukui, K. (1981). The Path of Chemical Reactions - the IRC Approach. *Acc. Chem. Res.* 14 (12), 363–368. doi:10.1021/Ar00072a001

Hay, P. J., and Wadt, W. R. (1985). Ab Initio effective Core Potentials for Molecular Calculations. Potentials for K to Au Including the Outermost Core Orbitals. *J. Chem. Phys.* 82 (1), 299–310. doi:10.1063/1.448975

He, X., Deng, Y., Zhang, Y., He, Q., Xiao, D., Peng, M., et al. (2020). Mechanochemical Kilogram-Scale Synthesis of Noble Metal Single-Atom Catalysts. *Cell. Rep. Phys. Sci.* 1 (1), 100004. doi:10.1016/j.xcrp.2019.100004

Hehre, W. J., Ditchfield, R., and Pople, J. A. (1972). Self-Consistent Molecular Orbital Methods. XII. Further Extensions of Gaussian-type Basis Sets for Use in Molecular Orbital Studies of Organic Molecules. *J. Chem. Phys.* 56(5), 2257, 2261. doi:10.1063/1.1677527

Henkelman, G., Uberuaga, B. P., and Jónsson, H. (2000). A Climbing Image Nudged Elastic Band Method for Finding Saddle Points and Minimum Energy Paths. *J. Chem. Phys.* 113 (22), 9901–9904. doi:10.1063/1.1329672

Jones, J., Xiong, H., Delariva, A. T., Peterson, E. J., Pham, H., Challa, S. R., et al. (2016). Thermally Stable Single-Atom Platinum-On-Ceria Catalysts via Atom Trapping. *Science* 353 (6295), 150–154. doi:10.1126/science.aaf8800

Kresse, G., and Furthmüller, J. (1996a). Efficiency of Ab-Initio Total Energy Calculations for Metals and Semiconductors Using a Plane-Wave Basis Set. *Comput. Mater. Sci.* 6 (1), 15–50. doi:10.1016/0927-0256(96)00008-0

Kresse, G., and Furthmüller, J. (1996b). Efficient Iterative Schemes Forab Initiototal-Energy Calculations Using a Plane-Wave Basis Set. *Phys. Rev. B* 54 (16), 11169–11186. doi:10.1103/PhysRevB.54.11169

Kuhn, P., Antonietti, M., and Thomas, A. (2008). Porous, Covalent Triazine-Based Frameworks Prepared by Ionothermal Synthesis. *Angew. Chem. Int. Ed.* 47 (18), 3450–3453. doi:10.1002/anie.200705710

Lee, K., Murray, É. D., Kong, L., Lundqvist, B. I., and Langreth, D. C. (2010). Higher-accuracy van der Waals density functional. *Phys. Rev. B* 82 (8), 081101. doi:10.1103/Physrevb.82.081101

Li, H., Wang, L., Dai, Y., Pu, Z., Lao, Z., Chen, Y., et al. (2018). Synergetic Interaction between Neighbouring Platinum Monomers in CO_2 Hydrogenation. *Nat. Nanotech* 13 (5), 411–417. doi:10.1038/s41565-018-0089-z

Liu, K., Tang, Y., Yu, Z., Ge, B., Ren, G., Ren, Y., et al. (2020a). High-loading and Thermally Stable $Pt1/MgA_{l11}.2Fe_{0.8}O_4$ Single-Atom Catalysts for High-Temperature Applications. *Sci. China Mat.* 63 (6), 949–958. doi:10.1007/s40843-020-1267-2

Liu, K., Zhao, X., Ren, G., Yang, T., Ren, Y., Lee, A. F., et al. (2020b). Strong Metal-Support Interaction Promoted Scalable Production of Thermally Stable Single-Atom Catalysts. *Nat. Commun.* 11 (1), 1263. doi:10.1038/S41467-020-14984-9

Liu, P., Zhao, Y., Qin, R., Mo, S., Chen, G., Gu, L., et al. (2016). Photochemical Route for Synthesizing Atomically Dispersed Palladium Catalysts. *Science* 352 (6287), 797–800. doi:10.1126/science.aaf5251

Liu, Q., Yang, X., Li, L., Miao, S., Li, Y., Li, Y., et al. (2017). Direct Catalytic Hydrogenation of CO_2 to Formate over a Schiff-Base-Mediated Gold Nanocatalyst. *Nat. Commun.* 8 (1), 1407. doi:10.1038/s41467-017-01673-3

Liu, W., Chen, Y., Qi, H., Zhang, L., Yan, W., Liu, X., et al. (2018). A Durable Nickel Single-Atom Catalyst for Hydrogenation Reactions and Cellulose Valorization under Harsh Conditions. *Angew. Chem. Int. Ed.* 57 (24), 7071–7075. doi:10.1002/anie.201802231

Lozano, A., Gross, A., and Busnengo, H. F. (2010). Molecular Dynamics Study of H_2 Dissociation on H-Covered Pd(100). *Phys. Rev. B* 81 (12), 121402. doi:10.1103/Physrevb.81.121402

Monkhorst, H. J., and Pack, J. D. (1976). Special Points for Brillouin-Zone Integrations. *Phys. Rev. B* 13 (12), 5188–5192. doi:10.1103/PhysRevB.13.5188

Ni, M., and Zeng, Z. (2009). Density Functional Study of Hydrogen Adsorption and Dissociation on Small Pd_n (N=1-7) Clusters. *J. Mol. Struct. THEOCHEM* 910 (1-3), 14–19. doi:10.1016/j.theochem.2009.06.008

Qiao, B., Wang, A., Yang, X., Allard, L. F., Jiang, Z., Cui, Y., et al. (2011). Single-atom Catalysis of CO Oxidation Using Pt1/FeOx. *Nat. Chem.* 3 (8), 634–641. doi:10.1038/Nchem.1095

Ren, G.-Q., Pei, G.-X., Zhang, J.-C., and Li, W.-Z. (2019). Activity Promotion of Anti-sintering Au $MgGa_2O_4$ Using Ceria in the Water Gas Shift Reaction and Catalytic Combustion Reactions. *Chin. J. Catal.* 40 (4), 600–608. doi:10.1016/S1872-2067(19)63295-X

Ren, G., Sun, J., Zhai, S., Yang, L., Yu, T., Sun, L., et al. (2022). Ambient Hydrogenation of Carbon Dioxide into Liquid Fuel by a Heterogeneous Synergetic Dual Single-Atom Catalyst. *Cell. Rep. Phys. Sci.* 3 (1), 100705. doi:10.1016/j.xcrp.2021.100705

Su, X., Yang, X.-F., Huang, Y., Liu, B., and Zhang, T. (2019). Single-Atom Catalysis toward Efficient CO_2 Conversion to CO and Formate Products. *Acc. Chem. Res.* 52 (3), 656–664. doi:10.1021/acs.accounts.8b00478

Wang, A., Li, J., and Zhang, T. (2018). Heterogeneous Single-Atom Catalysis. *Nat. Rev. Chem.* 2 (6), 65–81. doi:10.1038/s41570-018-0010-1

Yang, X.-F., Wang, A., Qiao, B., Li, J., Liu, J., and Zhang, T. (2013). Single-Atom Catalysts: A New Frontier in Heterogeneous Catalysis. *Acc. Chem. Res.* 46 (8), 1740–1748. doi:10.1021/ar300361m

Zhao, Y., and Truhlar, D. G. (2006). A New Local Density Functional for Main-Group Thermochemistry, Transition Metal Bonding, Thermochemical Kinetics, and Noncovalent Interactions. *J. Chem. Phys.* 125 (19), 194101. doi:10.1063/1.2370993

Conflict of Interest: The authors declare that the research was conducted in the absence of any commercial or financial relationships that could be construed as a potential conflict of interest.

Publisher's Note: All claims expressed in this article are solely those of the authors and do not necessarily represent those of their affiliated organizations, or those of the publisher, the editors, and the reviewers. Any product that may be evaluated in this article, or claim that may be made by its manufacturer, is not guaranteed or endorsed by the publisher.

frontiers | Frontiers in Chemistry

TYPE Review
PUBLISHED 08 August 2022
DOI 10.3389/fchem.2022.959422

OPEN ACCESS

EDITED BY
Shanhui Zhu,
Institute of Coal Chemistry (CAS), China

REVIEWED BY
Maria A. Goula,
University of Western Macedonia, Greece
Miriam Navlani-García,
University of Alicante, Spain

*CORRESPONDENCE
Yulian He,
yulian.he@sjtu.edu.cn

†These authors share first authorship

SPECIALTY SECTION
This article was submitted to Catalytic Reactions and Chemistry, a section of the journal Frontiers in Chemistry

RECEIVED 01 June 2022
ACCEPTED 28 June 2022
PUBLISHED 08 August 2022

CITATION
Gao Y, Jiang M, Yang L, Li Z, Tian F-X and He Y (2022), Recent progress of catalytic methane combustion over transition metal oxide catalysts.
Front. Chem. 10:959422.
doi: 10.3389/fchem.2022.959422

Recent progress of catalytic methane combustion over transition metal oxide catalysts

Yuan Gao[1†], Mingxin Jiang[1†], Liuqingqing Yang[1], Zhuo Li[1], Fei-Xiang Tian[2] and Yulian He[1,3*]

[1]UM-SJTU Joint Institute, Shanghai Jiaotong University, Shanghai, China, [2]State Key Laboratory of Chemical Engineering, East China University of Science and Technology, Shanghai, China, [3]Department of Chemical Engineering, Shanghai Jiao Tong University, Shanghai, China

Methane (CH_4) is one of the cleanest fossil fuel resources and is playing an increasingly indispensable role in our way to carbon neutrality, by providing less carbon-intensive heat and electricity worldwide. On the other hand, the atmospheric concentration of CH_4 has raced past 1,900 ppb in 2021, almost triple its pre-industrial levels. As a greenhouse gas at least 86 times as potent as carbon dioxide (CO_2) over 20 years, CH_4 is becoming a major threat to the global goal of deviating Earth temperature from the +2°C scenario. Consequently, all CH_4-powered facilities must be strictly coupled with remediation plans for unburned CH_4 in the exhaust to avoid further exacerbating the environmental stress, among which catalytic CH_4 combustion (CMC) is one of the most effective strategies to solve this issue. Most current CMC catalysts are noble-metal-based owing to their outstanding C−H bond activation capability, while their high cost and poor thermal stability have driven the search for alternative options, among which transition metal oxide (TMO) catalysts have attracted extensive attention due to their Earth abundance, high thermal stability, variable oxidation states, rich acidic and basic sites, etc. To date, many TMO catalysts have shown comparable catalytic performance with that of noble metals, while their fundamental reaction mechanisms are explored to a much less extent and remain to be controversial, which hinders the further optimization of the TMO catalytic systems. Therefore, in this review, we provide a systematic compilation of the recent research advances in TMO-based CMC reactions, together with their detailed reaction mechanisms. We start with introducing the scientific fundamentals of the CMC reaction itself as well as the unique and desirable features of TMOs applied in CMC, followed by a detailed introduction of four different kinetic reaction models proposed for the reactions. Next, we categorize the TMOs of interests into single and hybrid systems, summarizing their specific morphology characterization, catalytic performance, kinetic properties, with special emphasis on the reaction mechanisms and interfacial properties. Finally, we conclude the review with a summary and outlook on the TMOs for practical CMC applications. In addition, we also further prospect the enormous potentials of TMOs in producing value-added chemicals beyond combustion, such as direct partial oxidation to methanol.

KEYWORDS

methane, catalytic combustion, heterogeneous catalysis, transition metal oxide, reaction mechanism

1 Introduction

CH_4 is the cleanest fossil fuel with the highest energy content (50–55 MJ/kg) among all sources. It emits 50–60% less CO_2, ~ 80% less nitrogen oxides (NO_x), and almost negligible amount of toxic air pollutants including SO_x, Hg, and PM 2.5 compared to that of coals (He L. et al., 2020; Zhang et al., 2021). Today, it has been well recognized that CH_4 will play an indispensable role in the paradigm shift to a more sustainable planet. However, as the main component of natural gas, CH_4 is the second-largest greenhouse gas after CO_2 with a global warming potential almost 86 times that of CO_2 over 20 years (He Y. L. et al., 2020).

Since the beginning of the industrial revolution, CH_4 emissions have raced past 1,900 ppb in 2021, almost triple its pre-industrial levels, and contributed about 20% to the global greenhouse effect so far (Pratt and Tate, 2018; Palella et al., 2021). Specifically in China, circumstances like the incomplete combustion of fossil fuels, natural gas extraction, animal enteric fermentation, crop cultivation, agricultural residue incineration, and solid waste landfills, etc., have resulted in an annual atmospheric CH_4 emission taking up about 60% of the total non-CO_2 greenhouse gas emissions (Teng et al., 2019; Gong and Zeng, 2021). In this sense, the environmental benefits of CH_4 resource itself will be largely balanced by the unburned emission, if no strict remediation plan in the exhaust stream is considered.

Catalytic combustion is one of the most effective means for CH_4 utilization for both clean power generation and emission control (Setiawan et al., 2015; Seeburg et al., 2018). Compared to the traditional flame combustion, where high operational cost and toxic substances such as carbon monoxide (CO) and NO_x caused by the high combustion temperatures (>1,400°C) are almost inevitable (Stoian et al., 2021), flameless combustion of CH_4 under the aid of a solid catalyst allows for not only a much lower operation temperature and much reduced NO_x emission but also a wider range of air-to-fuel ratio with a more stable and efficient combustion process outside the combustion limits (He L. et al., 2020).

At the heart of the CMC reaction lies the development of combustion catalysts, of which the catalytic performance and the cost should be properly balanced for practical implementations. To date, the most extensively explored CMC catalysts are precious metals like palladium, platinum, and rhodium, as is the case in the three-way catalytic converter for emission control in automobiles (Choya et al., 2021).

Noble metal catalysts are typically good at activating the C–H and O–O bonds to form free radicals and triggering the chain reactions, thus driving CMC to a low-temperature regime, while their high cost has never stopped the community searches for promising alternatives of cheaper price (Liu et al., 2015). Over the past decades, TMOs have received tremendous attention as one of the most promising candidates for catalyzing CMC owing to their great Earth abundance, low toxicity, and many outstanding physiochemical properties. Comparable, if not superior, performance to noble-metal-based systems has been reached in some cases such as Fe_2O_3, Co_3O_4, etc., (Li J. A. et al., 2019; He Y. L. et al., 2020; Zheng Y. F. et al., 2020; Yang et al., 2022), while with that being said, their practical uses are still limited by the low-temperature activity, resistivity against water, and sulfur tolerance in the combustion environment. Further improvement of the catalytic performance of TMO catalysts would require a well understanding of the active site structures and the corresponding reaction mechanisms, which unfortunately still remain largely controversial at the current stage, primarily due to 1) the high structural complexity of oxides themselves, involving a variety of surface acidic and basic sites; 2) the competitions between lattice oxygen and the molecular oxygen as the oxidizing sources; 3) oxygen exchange behaviors at the solid–gas interface; and 4) various adsorbed oxygen species (Toscani et al., 2019).

This review presents a systematic compilation of TMO-catalyzed CMC with special focus on the reaction mechanisms. We start with a brief introduction of the scientific fundamentals of the CMC reaction. Then, we move on to discuss the unique and desirable features of TMOs for the CMC reaction and different CH_4 activation pathways, followed by a detailed introduction of four different kinetic reaction models. Next, we categorize the TMOs of interests into single and mixed systems, summarizing their specific morphology characterization, catalytic performance, kinetic properties, with special emphasis on the reaction mechanisms and interfacial properties. Finally, we conclude the review with a summary and outlook on the TMOs for practical CMC applications. Last but not least, we also further prospect the enormous potentials of TMOs beyond CMC, such as partial oxidation to value-added chemicals.

2 Reaction fundamentals

2.1 Catalytic CH_4 combustion reaction

CH_4 is an extremely stable and highly symmetrical tetrahedral structure formed by four identical C–H bonds. In CH_4, the sp^3-hybridized carbon atom locates in the center of the regular tetrahedron, and four hydrogen atoms are distributed on the respective four vertices. CH_4 possesses a high ionization potential (12.5 eV), a low electron affinity (4.4 eV), and a high C–H bond energy (434 kJ/mol), rendering both the nucleophilic and electrophilic attacks on CH_4 extremely challenging under

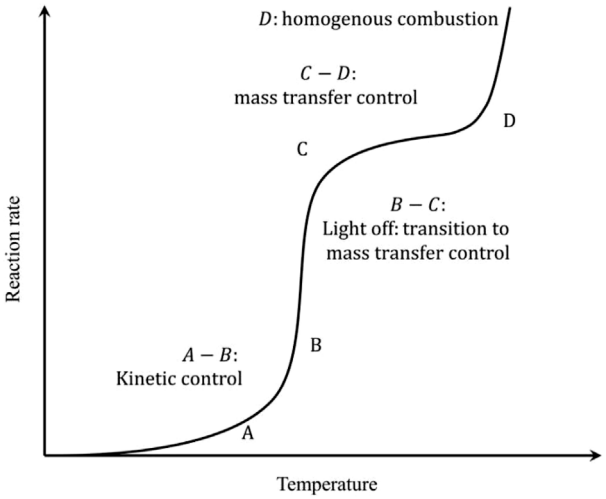

FIGURE 1
The reaction rate of CMC as a function of temperature. Reprinted with permission from He L. et al. (2020). Copyright (2020) Elsevier.

mild conditions (Vickers et al., 2015). The complete oxidation of CH_4 proceeds through the following reaction (1):

$$CH_4 + 2O_2 = CO_2 + 2H_2O\ \Delta H_{(298K)} = -803\ kJ/mol \quad (1)$$

As the combustion reaction is highly exothermic, side reactions such as CH_4–CO_2 reforming (Eq. 2), CH_4-steam reforming (Eq. 3), reverse water gas shift reaction (Eq. 4), partial oxidation (Eq. 5), and water gas shift reaction (Eq. 6) are almost inevitable at high temperature, as shown in the following reactions (Horn and Schlögl, 2014):

$$CH_4 + CO_2 = 2CO + 2H_2\ \Delta H_{(298K)} = 247\ kJ/mol \quad (2)$$

$$CH_4 + H_2O = 3H_2 + CO\ \Delta H_{(298K)} = 205.7\ kJ/mol \quad (3)$$

$$CO_2 + H_2 = CO + H_2O\ \Delta H_{(298K)} = 41.1\ kJ/mol \quad (4)$$

$$CH_4 + 1/2O_2 = CO + 2H_2\ \Delta H_{(298K)} = -36\ kJ/mol \quad (5)$$

$$CO + H_2O = H_2 + CO_2\ \Delta H_{(298K)} = -41.9\ kJ/mol \quad (6)$$

In the 1970s, Pfefferle *et al.* proposed the process of "heterogeneous catalytic combustion" (Pfefferle and Pfefferle, 1987), where a solid catalyst can be used to combust CH_4 in a flameless manner at a much lower reaction temperature (<500°C). Compared with traditional homogeneous flame combustion, the catalytic process owns advantages such as low light-off temperatures, reduced pollutant emission, wide operation ranges, and lower reactor requirement.

The CMC involves heterogeneous reactions, where complex processes such as mass transfer and heat transfer occur between the catalyst surface and the gas phase. Figure 1 shows the schematic relation between the reaction rate and temperature of CMC (He L. et al., 2020).

First part of the curve (A–B) is the kinetic-control zone, in which the reaction rate increases slowly with reaction temperature. At low temperatures, the reaction is limited by the intrinsic kinetics such as the dissociation rate of reactants over the catalytic surfaces. The second part of the curve (B–C) is known as the light-off regime where the reaction rate increases almost exponentially with the increase of the temperature. This is due to the drastic increase of the intrinsic reaction kinetics so that the overall reaction rates gradually transition to be controlled by the mass transfer rates. Upon further increase of the temperature (C–D), the mass transfer finally becomes the rate-limiting step, and there appears the rate plateau. The final part of the curve (D) falls under the regime of homogeneous combustion, where high temperature triggers the free radical formation and the chain reaction directly in the gas phase. The latter two high-temperature regimes impose strict requirements on the reactor design to maintain the catalyst structural stability as well as the sufficient mass and heat transfer rates. A more desirable operation window should fall nearby the light-off regime for milder reaction temperatures and sufficiently high reaction rates.

In CMC, other substances like water and sulfur are easy to get adsorbed onto catalyst surfaces under actual operation conditions; thus, the desirable catalysts for CMC should also possess a good anti-water and anti-sulfur poisoning ability beyond high low-temperature activity and thermal stability. In addition, the economic aspects should also be taken into considerations when it comes to large-scale applications.

2.2 Transition metal oxides

TMOs are one of the most important classes of solid catalysts that have been extensively used in a variety of important industrial processes, such as the water gas shift reaction, CO oxidation, methanol synthesis, etc., owing to their excellent thermal stability, variable valence states, and Earth abundance (Tepamatr et al., 2016; Arena et al., 2017; Huang et al., 2021). In water-containing feed, the surface of TMOs undergo acid–base reaction to form surface hydroxyl groups, which react with other reactants *via* proton or electron transfer (Yang et al., 2022). Transition metal elements could easily alternate between the low oxidation state and the high oxidation state, thus allowing for a facile release and restoration of the lattice oxygen *via* a redox cycle (Chen et al., 2015). Such redox and acid–base properties have rendered TMOs to be one of the most promising candidates for CMC reactions.

TMOs like Co_3O_4, Fe_2O_3, MnO_2, etc., have shown catalytic activities comparable to that of noble metal-based systems in CMC (Pu et al., 2017; He Y. L. et al., 2020; Yang et al., 2021), while the performance can be largely affected by preparation method, carrier, doping, and experimental conditions (such as the presence of water vapor and sulfur). The most common preparation methods of TMOs include thermal decomposition,

precipitation, combustion synthesis, hydrothermal method, dipping, and sol–gel method (Tang et al., 2008). The different preparation methods can lead to diverse structural properties such as particle size, dispersion, surface area, morphology, crystal plane, metal valence states, defects, and reactive oxygen species. Such variances in the TMO crystal structures may result in drastic differences in the expression of catalytic activity, as was found in Co_3O_4, Fe_2O_3, IrO_2, etc., where only certain crystal facets are reactive for CMC reactions (Liang et al., 2017; He L. et al., 2020).

The main exposed crystal planes of TMOs with different morphologies have a significant effect on the catalytic activity of CMC. For example, the (111) and (112) crystal planes of Co_3O_4 and the (110) crystal planes of Fe_2O_3 are considered to be the best catalytic activity for CMC (Hu et al., 2008; He L. et al., 2020). In addition, the structure dimensionality also induces different catalytic properties due to quantum confinement and geometric effect, as was seen in Co_3O_4 where the 2D nanosheets and 3D nanoflowers possess drastically different catalytic performances (Jia Y. C. et al., 2016).

TMO-based catalysts are generally supported in CMC for improved particle dispersion, increased specific surface area, and enhanced catalytic performance. Both inactive and active supports are used to disperse TMOs in CMC. For example, Al_2O_3, as an inactive support, is an acidic oxide capable of adsorbing CH_4 through acid–base pairing (Wang and Lin, 2004; Choya et al., 2018a). Active supports, such as CeO_2, can directly participate in the CMC reaction through its excellent oxygen storage capacity (Pecchi et al., 2005; Li Y. X. et al., 2009).

Doping TMOs with an impurity element is also an effective strategy to improve their catalytic performance in CMC by inducing a great deal of lattice defects, acidic and basic sites, oxygen vacancies, synergistic effect, etc., (Li J. H. et al., 2009). The increased amount of oxygen vacancies can not only improve the mobility of bulk oxygen in the lattice but also creates additional adsorption sites to promote the molecular adsorption from the gas phase, reducing the activation barrier (Wang H. W. et al., 2019). The dopants in TMOs include metal and non-metal elements. Elements like Ca and Mg are often used as promoters, while Ce and Mn are doped to obtain oxygen vacancies (Pecchi et al., 2011; Chen Y. L. et al., 2021). N is a commonly used dopant in non-metal doping, which can create more lattice distortions and further increase active oxygen species (Buchneva et al., 2012; Li et al., 2018).

One of the most serious issues for TMO catalysts in CMC is their resistance to water poisoning. Most polar facets of TMOs are prone to dissociatively adsorb moisture through an acid–base reaction and form rich surface hydroxyl groups, while this process is highly reversible and self-dehydration can occur at elevated temperatures (He Y. L. et al., 2020). Water vapor on the surface of TMOs reacts with chemisorbed oxygen, which hinder the delivery of reactive oxygen species to active sites. Moreover, the formation of hydroxyl groups hinders the desorption of H_2O and CO_2 from the surface of TMOs (He L. et al., 2020). Water vapor poisoning is generally reversible owing to the competitive adsorption of water molecules with reactants. Some TMOs possess inherent water tolerant stability, such as NiO, owing to the modification of water for NiO. Tuning the structure and surface topography of the TMO catalysts is effective in obtaining resistance to water vapor (Liu et al., 2017; Xu et al., 2017). Hydrophobic modification of TMOs or their supports may also be an effective means to improve the water resistance and catalytic activity of catalysts (Kuo et al., 2014).

Sulfur poisoning is another serious issue for TMO catalysts in CMC. Natural gas contains a substantial amount of sulfur element, which can be oxidized into sulfur dioxide (SO_2) and get adsorbed onto the catalyst surface of the catalyst; subsequent oxidation to sulfate could also occur and thus cause serious sulfur poisoning. Some TMOs, such as Cr_2O_3, inherently have excellent sulfur resistance due to its low affinity to acid gases (Ordóñez et al., 2008). Sacrificial component such as Mn-based oxide can be used to guarantee the sulfur resistance of the CMC catalyst (Zhong et al., 2019). Similarly, supports such as Al_2O_3 can react with SO_2 to form sulfates, which protects active sites. But it is unfavorable for the recovery of TMO catalysts. In fuel-rich conditions, an elevated temperature (>500°C) is an effective means of recovery for sulfur-poisoned TMO catalysts (Gremminger et al., 2017).

In addition, carbon deposition can also cause serious catalyst deactivation in CMC, as commonly seen in carbonaceous reactions. Note that the effect can be remediated through carefully controlled reaction conditions, such as adjusting the air-to-fuel ratio, the space velocity, and the reaction temperature. In lean combustion scenario where the oxygen content is in excessive amount, the CH_n species formed from CH_4 dissociation can be rapidly oxidized by dioxygen to form CO_2, thus avoiding coke formation. While if a rich fuel mixture is used, the insufficient oxygen content can result in the formation of coke-like carbon (Tao et al., 2015). Under the circumstance of oxygen source coming from lattice oxygen rather than the molecular oxygen in the gas phase, the CH_4 to TMO catalyst feed ratio should be instead taken in consideration correspondingly. When the lattice oxygen in the TMO catalysts is insufficient to react with CH_4, CH_4 will decompose and then form carbon deposition (Wu and Ku, 2018). Another factor that can induce the catalyst deactivation is the space velocity, a small space velocity of the feed can lead to serious carbon deposition due to the long residence time between CH_n species and the catalysts (He Y. L. et al., 2020). Furthermore, carbon deposition may also result from the decomposition of CH_4 at high temperatures. Promoting coke oxidation can prolong the lifetime of TMO catalysts. TMOs with high

oxygen storage capacity such as CeO_2 can remove coke deposition through the release of lattice oxygen (Wang Y. N. et al., 2022). Therefore, sufficient oxygen content, reasonably short residence time, and low reaction temperature are necessary to reduce carbon deposition in CMC. For TMOs, in particular, a high oxygen storage capacity will be helpful to prevent coke formation.

2.3 Reaction mechanisms

The reaction mechanisms proposed for CMC over many TMOs remain to be controversial, primarily due to the high structural complexity, different oxygen sources, oxygen-exchange behaviors, etc. Such knowledge gaps hinder us from understanding the precise active site structures and the reaction pathways from a molecular level and consequently the optimization of TMO catalysts for CMC. To this end, the existing mechanistic studies of CMC over TMOs are summarized in this section.

2.3.1 C–H and O–O activation

Dissociation of the first C–H bond is the most critical step of CH_4 activation and the following CMC reactions (Feyel et al., 2006). Fu *et al.* studied different C–H activation mechanisms over various TMOs using cluster model calculations. It was found that H abstraction is the primary working mechanism for the activation of CH_4 on most TMOs such as Cr_3O_9 and Mo_3O_9, following the hydrogen atom transfer (HAT) route. H abstraction is a single-electron transfer process forming free radicals *via* the homolytic cleavage of the C–H bond, in which the H atom attacks the terminal oxygen atom from both *trans* and *cis* directions. In terms of activation energy, the H abstraction process in *trans* on the terminal oxygen is more favorable than that from the *cis* directions (Fu et al., 2006). Li *et al.* believed that there is also a proton-coupled electron transfer (PCET) process for the activation of C–H bonds on TMOs, that is, transition metal oxide ions and O^{2-} as a Lewis acid–base pair are served as catalytic active sites. In the process, a proton is abstracted from CH_4 by the Lewis basic O^{2-}, while the methyl anion is transferred to the Lewis-acidic metal center (Li et al., 2016). Thus, the activation of CH_4 on TMOs is usually closely related to the acidity and alkalinity of the surface.

In addition to CH_4 activation, the molecular oxygen also plays a significant role in governing the catalytic performance in CMC. The composition and concentration of reactive oxygen species significantly affect the CMC reaction over TMOs. In CMC, there are primarily two types of oxygen species involved in the TMOs, including surface-adsorbed oxygen and lattice oxygen. According to Eq. 7, the dissociative adsorption of molecular oxygen will result in the formation of a series of different adsorbed oxygen species with electrophilic characters, in the sequence of superoxide O_2^-, peroxide O_2^{2-}, and charged atomic species O^-. The reaction ultimately leads to the incorporation of nucleophilic O^{2-} into the lattice to form lattice oxygen (Wang Y. Q. et al., 2022). It is precisely because of the different activation forms of C–H bonds and oxygen molecules that the mechanism of CMC is such diverse

$$O_2(g) \leftrightarrows O_2(s) \overset{e^-}{\leftrightarrows} O_2^-(s) \overset{e^-}{\leftrightarrows} O_2^{2-}(s) \leftrightarrows 2O_2^-(s) \overset{2e^-}{\leftrightarrows} + 2V_0 2O^{2-} \quad (1)$$

∗ – a free adsorption site;
g – gas surface; l – lattice

(7)

2.3.2 Kinetic models

The various forms of C–H and O–O activation mechanisms undoubtedly result in a complex reaction network for TMO-catalyzed CMC systems. According to the participation forms of different oxygen species, the proposed reaction mechanisms of the CMC currently include the following four mechanisms (Figure 2). Langmuir–Hinshelwood (L–H) mechanism and the Eley–Rideal (E–R) mechanism are dominated by surface-adsorbed oxygen, while the Mars van Krevelen (MvK) mechanism is dominated by lattice oxygen, and the two-term (T-T) mechanism is cooperatively controlled by the L–H mechanism and the MvK mechanism. The rate equations consistent with these mechanisms are as follows:

$$r_{LH} = k_C \frac{K_C P_C \cdot K_O P_O}{(1 + K_C P_C)(1 + K_O P_O)} \quad (8)$$

$$r_{ER} = k_O \frac{K_O P_O \cdot P_C}{(1 + K_O P_O)} \quad (9)$$

$$r_{MvK} = \frac{k_C P_C \cdot k_O P_O}{v k_C P_C + k_O P_O} \quad (10)$$

L–H mechanism. It is believed that the adsorption activation energy of O_2 on the catalyst surface is much smaller than that of CH_4, and O_2 is preferentially adsorbed on the catalyst surface to form adsorbed oxygen. Meanwhile, adsorbed oxygen species are easier to combine with adsorbed CH_4 than O_2 due to their electrophilic attack on CH_4, so that the hydrogen in CH_4 is dissociated, destroying the stable structure of CH_4 and generating active methyl radicals to promote the oxidation of CH_4. The L–H mechanism is mainly found on noble metals and their supported oxide systems (Becker et al., 2011). Trimm *et al.* studied methane oxidation over the Pt/Al_2O_3 porous catalyst and found that the rate equation derived by experimental results was best fit with the L–H mechanism (Trimm and Lam, 1980).

E–R mechanism. In the E–R mechanism, the gaseous O_2 is first adsorbed on the metal atoms of TMOs and then further activated to form surface-adsorbed oxygen, which reacts with

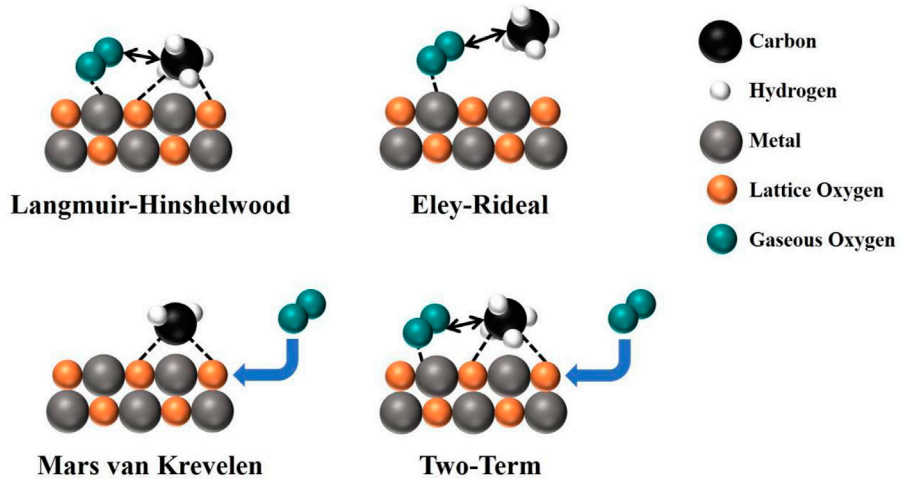

FIGURE 2
The reaction mechanism diagram of CMC.

gaseous CH_4 to form active methyl species, finally oxidized to CO_2 (Belessi et al., 2001). Veldsink *et al.* investigated the reaction rate of CMC over a commercially available CuO-γ-$A1_2O_3$ catalyst and derived a kinetic rate equation from all experimental data. The rate equation is in good accordance with the E–R mechanism, in which catalyst with adsorption of O_2, CO_2, and H_2O, but does not adsorb CH_4 (Veldsink et al., 1995).

MvK mechanism. MvK is a redox mechanism where the catalyst will be reduced by CH_4 at first, and then the active centers will be reoxidized by molecular oxygen uptakes. It includes surface oxygen reaction and lattice oxygen migration, in which the reaction pathway can be divided into the following steps: the surface dissociative adsorption of gaseous CH_4 onto the active site of the catalyst to form adsorbed alkyl and hydroxyl groups, and the reaction spills over to form CO_2 and H_2O products taking the lattice oxygen as the oxidizing source. After product desorption, the active centers will be reduced with a lot of formation of lattice oxygen vacancies, which can be replenished by either lattice oxygen diffusion from the bulk phase or molecular oxygen adsorption from the gas phase. This reaction mechanism is found for several TMOs like Fe_2O_3 and Co_3O_4 (Zasada et al., 2017; He L. et al., 2020).

T-T mechanism. Due to the complex nature of CMC, there are some cases where describing the reaction process on the catalyst by a single mechanism is rather challenging, and then the T-T mechanism is proposed, that is, both surface adsorption oxygen and lattice oxygen participate in the reaction simultaneously (Han et al., 2008). Gaseous oxygen adsorbs on metal active sites and then dissociates to form surface-active oxygen species. It oxidizes CH_4 together with lattice oxygen species that migrate from the bulk to the surface, and the lattice oxygen vacancies will be replenished by gaseous oxygen, resulting in some more suitable explanation of reaction mechanisms in CMC over TMOs (Wang et al., 2018).

Although in some cases that an explicit reaction model can be interpreted to well describe the reaction kinetics of TMO-catalyzed CMC reactions, such as Fe_2O_3, Co_3O_4, etc., the reaction mechanism may vary based on the structure of TMOs or the reaction conditions. For example, Zasada *et al.* systematically examined CMC over Co_3O_4 nanocubes, revealing that the content of oxygen vacancies significantly affects the reaction mechanism. In the low-temperature range (300–450°C), CH_4 is primarily activated by monatomic oxygen species on the catalyst, in which facile decarboxylation and dehydroxylation leave the catalyst surface stoichiometric, thus following the L–H mechanism. From 450 to 650°C, the intrafacial dehydroxylation and decarboxylation of the catalyst accelerated the formation of oxygen vacancies, making the catalyst surface slightly reduced. Then, oxygen vacancies are virtually refilled by O_2, which is in accordance with the coexistence of L–H and MvK mechanisms. Above 650°C, oxygen vacancies formed from the bulk Co_3O_4, so causing the active involvement of the lattice oxygen following the MvK mechanism. In this case, the varying reaction conditions change the catalyst redox states, in which the number of oxygen vacancies leads to a variety of reaction mechanisms (Zasada et al., 2017).

The mechanism of CMC may also be significantly altered by doping or substitution of other transition metal ions with different contents into transition metal oxides. Wang *et al.* demonstrated that the catalytic behavior can be regulated through the substitution of Co by Ni in spinel $ZnNi_xCo_{2-x}O_4$ oxides (Figure 3). In addition, the difference of catalytic behavior can be explained by the interaction between the O *p*-band center and metal *d*-band center. When the metal

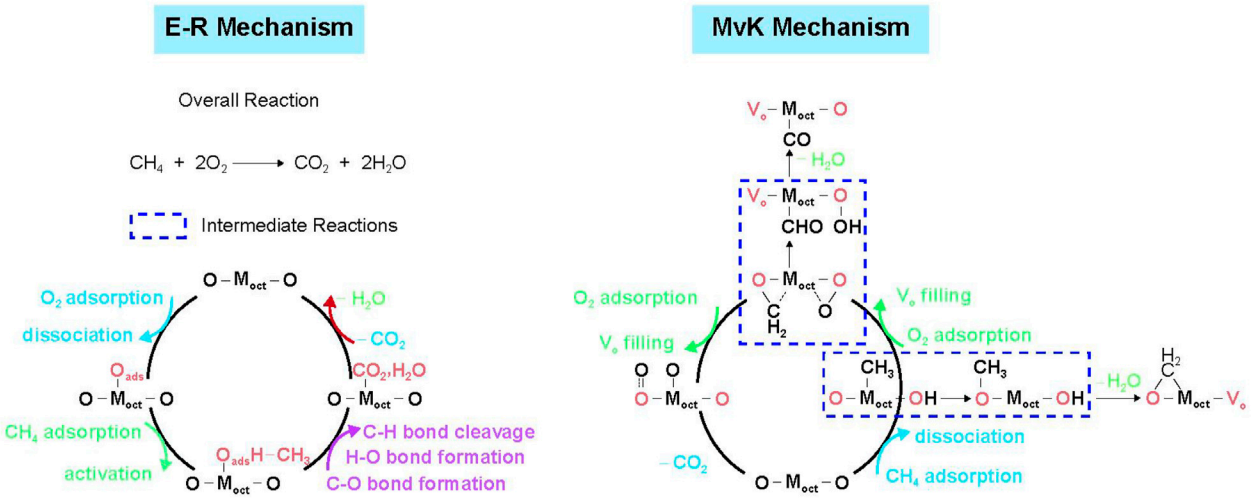

FIGURE 3
The proposed reaction pathways based on the E–R mechanism for Ni-poor spinel oxides and MvK mechanism for Ni-rich spinel oxides. Cited from Wang H. W. et al. (2019).

d-band center exhibits a higher position relative to the O *p*-band center in Ni-poor $ZnNi_xCo_{2-x}O_4$ spinel oxides, the catalyst shows a greater metal character, following the E–R mechanism, among which the first C–H bond cleavage and the H_2O desorption are considered to be the rate-determining steps. On the contrary, Ni-rich spinel oxides with the higher O *p*-band center compared with the metal *d*-band center show greater oxygen character, in accordance with the MvK mechanism, in which the multiple lattice oxygen involved steps are crucial for the entire methane oxidation (Wang T. et al., 2019).

The mechanism of CMC may also be greatly affected by the reaction temperature. He *et al.* investigated CMC over α-Fe_2O_3 *via* a combined experimental and theoretical study and found that $C^{16}O_2$ formed first, followed by $H_2{}^{16}O$, $C^{16,18}O_2$, $H_2{}^{18}O$, and finally $C^{18}O_2$, where $^{18}O_2$ was only used in the gaseous molecular oxygen. The numerical analysis of the mass balance revealed that the ratio $^{16}O/^{18}O > 1$ at $T < 385^{\circ}C$, then $^{16}O/^{18}O \approx 1$ at $T \approx 385^{\circ}C$, and finally $^{16}O/^{18}O < 1$ at $T > 385^{\circ}C$. These indicate that, below 385°C, the lattice oxygen plays a predominant active role in CMC reaction, in accordance with the MvK mechanism. However, above 385°C, the mechanism becomes more complex and difficult to analyze (He Y. L. et al., 2020).

3 Transition metal oxides for catalytic CH_4 combustion

In the application of the CMC, the TMOs such as Co_3O_4, NiO, MnO_2, Cr_2O_3, Fe_2O_3, CeO_2, CuO, and their binary complex oxides have been widely studied. Therefore, the characteristics of these TMOs and the mechanisms of the CMC over these catalysts are comprehensively reviewed in the following sections in order to provide a general guideline about the construction of well-performed catalytic systems for the CMC. The catalytic performances of different TMOs for CMC are shown in Table 1.

3.1 Co_3O_4-based catalysts

3.1.1 Single Co_3O_4

Co_3O_4 is a p-type semiconducting metal oxide with a typical spinel structure, and it has an array based on a cubic close-packed oxide ion whose lattice parameter is a = 0.811 nm with the space group of Fd3m. In the crystal structure of Co_3O_4, Co^{2+} occupies the tetrahedral coordination and Co^{3+} occupies the octahedral coordination, respectively, with a mean cobalt oxidation state of +2.67. Co_3O_4 is considered to be one of the most effective co-oxidation catalysts due to the unfilled 3*d* orbital of Co, the weak Co–O bond strength, a high cycle frequency of redox, and a low barrier of oxygen vacancy. Owing to its unique physical and chemical properties, it has a wide range of applications in sensors, magnetic materials, lithium-ion batteries, and solar cells (Sanchis et al., 2021). In CMC, Co_3O_4 has attracted the attention of many researchers due to its high stability, variable valence, and excellent catalytic performance. Paredes *et al.* found the activity of different bulk TMOs catalysts in methane combustion in the following order: $Co_3O_4 > Mn_2O_3 > Cr_2O_3 > CuO > NiO$ (Paredes et al., 2009). Therefore, Co_3O_4 is considered to be one of the best candidates for CH_4 combustion catalysts

TABLE 1 The catalytic performances of different TMOs for CMC.

TMOs	Preparation method	Surface area (m^2 g^{-1})	Light-off temperature (°C)	E_a (kJ mol^{-1})	Feed composition and GHSV/WHSV (gas/weight hourly space velocity)	Stability	Reaction mechanism	References
Co_3O_4	basic precipitation	14	T_{50} = 330	74 ± 2	1% CH_4, 10% O_2 and 89% N_2 GHSV: 60,000 h^{-1}	anti-H_2O: good (reversible deactivation) anti-SO_2: none	MvK	Choya et al. (2022)
Co-In-0.2 oxide	a designed precipitation	57.3	T_{10} = 265 T_{99} = 395	82.2	1% CH_4, 10% O_2, N_2 (balance); GHSV = 48,000 ml g^{-1} h^{-1}	anti-H_2O: excellent (fully restored) anti-SO_2:: none	none	Zheng Y. et al. (2020)
N-Co_3O_4-110	a facial N_2 plasma engraving	52.3	T_{50} = 342 T_{90} = 412	73.0	2 vol. % CH_4, 20 vol. % O_2, 5 vol. % H_2O, Ar gas; WHSV = 46,800 ml g^{-1} h^{-1}	anti-H_2O: good (reduced by about 3%) anti-SO_2:: none	May be MvK	Yu et al. (2020)
$Co_3O_4/Ce_{0.75}Zr_{0.25}$	solution combustion synthesis	none	T_{50} = 217 (with electric field)	35.8 (with electric field)	[CH_4] = 0.2%, [O_2] = 10%, N_2 (balance gas); GHSV = 30,000 h^{-1}	none	MvK	Li K. et al. (2019)
Mesoporous Co_3O_4	Calcining	136.2	T_{10} = 220 T_{50} = 270	none	1% CH_4, 20% O_2; space velocity = 18,000 ml g^{-1} h^{-1}	none	E-R	Han et al. (2016)
Zr-Doped NiO	homogeneous co-precipitation strategy	142	T_{90} = 380	55.27	1 vol% CH_4, 10 vol% O_2, balanced N_2 GHSV: 30,000 ml g^{-1} h^{-1}	anti-H_2O: good anti-SO_2: none	MvK	Wang et al. (2021)
Ni-Cu mixed oxides	co-precipitation method	147	T_{50} = 370 T_{90} = 410	89	1 vol% CH_4, 5 vol% O_2 and N_2 GHSV: 50 000 ml g^{-1} h^{-1}	anti-H_2O: good anti-SO_2: none	MvK	Fan et al. (2022)
Mn-Ce-RP	redox-precipitation method	none	T_{50} = 446°C	none	CH_4(1%)/O_2(10%)/N_2 WSHV = 30,000 ml/(g*h)	anti-SO_2: excellent anti-H_2O: none	MvK	Zhong et al. (2019)
nanocubic MnO_2	a hydrothermal process	78	T_{50} = 293 T_{90} = 350	none	none	none	L- H	Zhang et al. (2019)
α-MnO_2	a hydrothermal	92.9	T_{50} = 356 T_{90} = 463	none	0.1% CH_4 in air WHSV = 90 L g^{-1} h^{-1}	none	MvK	Jia et al. (2019)
MnO_2/ZrO_2	one-pot hydrothermal	none	T_{50} = 340	none	1,000 ppm CH_4, 10% O_2, and N_2 (balance) WHSV = 45 L g^{-1} h^{-1}	anti-H_2O: good anti-SO_2: good	none	Jia et al. (2018)
Nano-$ZnCr_2O_4$ spinel oxides	a ethylene glycol-mediated solvothermal	96.2	T_{10} = 300 T_{90} = 400	144.8	2 vol% CH_4, 20 vol% O_2, 78 vol% N_2 GHSV = 78,000 h^{-1}	none	L-H	Huang et al. (2019)
Sn-Cr binary oxide	a co-current co-precipitation	133	T_{10} = 320 T_{50} = 400 T_{90} = 490	none	1.0% CH_4 in air; space velocity = 20,000 h^{-1}	none	MvK	Zhu et al. (2003)
Fe and Cr-based oxides $Fe_{60}Cr_{40}$	the citrate sol–gel	82	T_{450}°C = 79% T_{550}°C = 97%	none	347 ppm CH_4+5.1 ppm SO_2	anti-H_2O: good anti-SO_2: excellent	none	García-Vázquez et al. (2020)
Bulk α-Fe_2O_3	precipitation	none	T_{50} = 461	99.9	2000 ppm V CH_4 in air	none	MvK (100–500°C)	Paredes et al. (2004)
Nano sheetα-Fe_2O_3	hard-templating	none	T_{10} = 230 T_{50} = 394	17.60	5% CH_4 and 20% O_2 balanced with 75% Ar; WHSV = 10 000 ml g^{-1} h^{-1}	none	MvK (below 400°C)	He Y. L. et al. (2020)

(Continued on following page)

TABLE 1 (*Continued*) The catalytic performances of different TMOs for CMC.

TMOs	Preparation method	Surface area (m^2 g^{-1})	Light-off temperature (°C)	E_a (kJ mol^{-1})	Feed composition and GHSV/WHSV (gas/weight hourly space velocity)	Stability	Reaction mechanism	References
NiO/CeO_2	Deposition precipitation	none	T_{50} = 465	69.4 ± 4.0	20 ml/min 10% CH_4/Ar and 10 ml/min pure O_2 WHSV = 18 000 ml g^{-1} h^{-1}	anti-H_2O: good anti-SO_2: none	MvK	Zhang et al. (2018)
$MnCeO_x$ (Mn-to-Ce ratio of 1:3)	redox	none	T_{50} = 475 T_{100} = 700	113	CH_4/O_2/He mixture (concentration: 1/4/95); Space velocity = 30,000 h^{-1}	none	MvK	Palella et al. (2021)
$Ce_{0.9}Zr_{0.06}Sc_{0.04}O_{1.98}$	citrate complexation	none	T_{50} = 700	124.3	1 vol% CH_4, 8 vol% O_2 and 91 vol% N_2	none	MvK	Toscani et al. (2019)

among all TMOs and a promising alternative for noble metal combustion catalysts.

According to the previous literature, the common methods for preparing Co_3O_4 include precipitation, sol–gel method, hydrothermal synthesis, impregnation, thermal decomposition, and solid phase reaction. Choya *et al.* prepared several bulk Co_3O_4 catalysts by various synthesis methodologies, among which the solution combustion synthesis route, the basic grinding route, the calcination of the cobalt hydroxycarbonate route, and the precipitation with the sodium carbonate route showed better textural properties than the commercial catalyst due to the higher presence of Co^{3+} on their surface and further resulted in abundant lattice oxygen species. The catalysts exhibited higher catalytic activities due to their favored mobility of lattice oxygen species (Choya et al., 2022). Wang *et al.* prepared a series of Co_3O_4/γ-Al_2O_3 catalysts by a combination of incipient wetness impregnation (IWI) and subsequent combustion synthesis (CS) method. Results revealed that the CS method exhibited higher catalytic activity than the catalysts prepared by the IWI method, attributing to the higher surface area, lower Co_3O_4 crystallization, better dispersion, more surface Co^{3+}, as well as easier and faster redox cycle between Co^{2+} and Co^{3+} (Wang et al., 2015).

Studies have shown that the catalytic behavior of Co_3O_4 catalysts strongly depends on its morphology, structure, and crystal planes, which endow them with different electron transfer abilities and different amounts of active sites, promoting catalytic activity and selectivity. The morphological characteristics can be regulated by the preparation method, such as spheres, nanorods, nanowires, nanobelts, and nanosheets.

Wang *et al.* prepared Co_3O_4 with the shape of nanosheets and nanospheres by the hydrothermal method in media of ethylene glycol and water, respectively. The concentration of ethylene glycol and the hydrothermal temperature significantly influenced the size and shape of the Co_3O_4, which showed that the Co_3O_4 nanosheets exhibited slightly higher catalytic performance than the Co_3O_4 nanoparticle, as more active oxygen species were found in the former (Wang et al., 2017). Chen *et al.* controllably synthesized Co_3O_4 nanocrystals with different morphologies (flower, hexagonal plate, hexagonal sheet, and cube), which showed that the properties of Co_3O_4 were closely related to the morphology. Compared to cubical Co_3O_4 with the (100) plane, the flower-like, hexagonal plate-like, and hexagonal sheet-like Co_3O_4 catalysts were more active, which may be due to more exposed (111) planes (Chen et al., 2016).

In addition, the spatial structures of TMOs also play an important role in the catalytic activity. Sun *et al.* prepared Co_3O_4 catalysts with different spatial structures, such as 0D (nanoparticles), 1D (nanorods), 2D (nanoplates), and 3D (mesoporous and microporous) structures. Among them, 2D structures (nanoplates) have the best catalytic activity, which is contributed to the high refractive index of the exposed (112) crystal planes and the role of surface-active species (such as surface-adsorbed oxygen and Co^{2+}) in the catalytic reaction (Sun et al., 2016).

The use of supports can effectively improve the dispersion and prevent the particle agglomeration caused by the sintering of the Co_3O_4 catalyst, thereby improving the catalytic activity of the catalyst. Feng *et al.* deposited Co_3O_4 on the $SmMn_2O_5$ (SMO) support to prepare Co/SMO composite catalysts and evaluated the performance of Co/SMO catalysts in oxygen-enriched environments. The results showed that the Co/SMO-50% catalyst had high catalytic activity and strong durability. The strong interaction between Co_3O_4 and $SmMn_2O_5$ played a key

role in dispersing and stabilizing Co_3O_4 by preventing catalyst sintering. Highly dispersed Co_3O_4 formed more surface lattice oxygen-oxidized CH_4, leading to the transformation from Co^{3+} to Co^{2+}, along with the formation of an oxygen vacancy, which could be compensated by the gaseous oxygen, so following the MvK mechanism (Feng et al., 2018). Dou *et al.* obtained Co_3O_4/CeO_2 catalysts by supporting Co_3O_4 nanoparticles on CeO_2 nanorods by the deposition precipitation method. The results showed that complete oxidation of CH_4 on Co_3O_4/CeO_2 (43.9 kJ/mol) was obviously lower than pure CeO_2 (95.1 kJ/mol) and pure Co_3O_4 (89.7 kJ/mol). Co_3O_4/CeO_2 showed synergistic effect, in which oxygen vacancies on the surface of CeO_2 were active centers for activating molecular oxygen in the oxidation reaction, thus promoting the improvement of catalytic activity (Dou et al., 2018).

3.1.2 Doped Co_3O_4

The element doping has been considered as an effective way to adjust the surface and electronic structures of nanomaterials. Some studies show that introducing oxygen vacancies will have a huge effect on the oxidation reaction. In the element-doped catalyst, Co_3O_4, as the reactive site, actively participates in CMC, while the doping of other elements often creates more oxygen vacancies to promote the rapid migration of lattice oxygen (Rodríguez-Fernández et al., 2019). Zheng *et al.* believed that Co^{2+} was active species in Co_3O_4. Thus, they prepared Co-In-x oxide *via* a designed precipitation method by taking N-butylamine as the precipitant. The Co–In–O solid solution phase exhibited a superior activity by doping an appropriate amount of In^{3+} to replace the Co^{3+} site of octahedral position, increasing the proportion of active species Co^{2+}, giving rise to abundant active oxygen species, improving reducibility, and optimizing surface acidity. Moreover, Co–In-x oxide also demonstrated excellent stability and water resistance, indicating that the doping of In^{3+} was beneficial to maintain a certain grain size and crystal phase (Zheng Y. F. et al., 2020). Yu *et al.* prepared the defective N-doped Co_3O_4 by efficient N_2 plasma treatment for methane oxidation reaction. N-doped Co_3O_4 could synergistically boost the catalytic performance by increasing active surface oxygen, enhancing redox property, and promoting the C–H bond activation ability. This result may provide a valuable guidance for the defects engineering of Co_3O_4 for the application of CMC (Yu et al., 2020).

However, doping is not always favorable for the catalytic activity of Co_3O_4. Choya *et al.* prepared two bulk Co_3O_4 catalysts with and without residual sodium by precipitation method. It was found that the presence of Na^+ had a negative impact on the properties of the Co_3O_4 catalyst due to diffusion and migration into the spinel lattice. The insertion of Na^+ led to lattice distortion and induced a reduction of the Co^{3+} into Co^{2+} owing to high Lewis acidic properties, along with high electron density within the oxygen ions of the lattice, weakened Co–O bonds, and reduced lattice oxygen species, which pointed out that the doping may be detrimental to catalytic performance. In this sense, appropriate precipitants or preparation methods are important for achieving high-performance CMC catalysts (Choya et al., 2018b).

3.1.3 Binary Co_3O_4-catalysts

Li *et al.* reported the introduction of an electric field on the Co_3O_4/$Ce_{0.75}Zr_{0.25}$ catalyst and found that the presence of the electric field significantly promoted the catalytic oxidation activity of methane. Co_3O_4 provided active sites and oxygen species for methane oxidation, while CeO_2 released lattice O species for the oxidation of CoO and Co to Co_3O_4. The electric field promoted the reduction of Ce^{4+} to Ce^{3+} and promoted the release of oxygen from the lattice. The chemisorption of methane mainly located in the newly formed tetrahedral Co^{3+} in the electric field rather than the active sites formed by octahedral Co^{3+} with gaseous oxygen. The adsorbed CH_4 was oxidized to carbonates species immediately, followed by the formation of CO_2 and refreshment of consumed O species by gaseous oxygen, which is similar to the typical MvK mechanism (Li L. et al., 2019).

3.1.4 Deactivation

Although Co_3O_4 shows a high catalytic activity for the CMC, it still cannot defeat noble metals owing to its low water and sulfur resistance. Generally, the inhibition of water vapor on the catalytic activity is probably due to its competition with the reactant for the active sites. The inhibition of SO_2 is attributed to the formation of sulfate or sulfide on the surface of catalysts, which may cause the loss of active sites, or agglomeration and the loss of surface area. From the existing literature, this problem can be effectively solved when the TMOs are supported on the carriers or some additives are added to the TMOs (Li J. A. et al., 2019).

Li *et al.* prepared a series of CoO_x embedded in the porous SiO_2 matrix by a spontaneous deposition method, which showed enhanced catalytic activity as compared with the simply supported CoO_x/SiO_2 catalyst due to a higher ratio of O_{ads}/O_{latt} and more active sites obtained by embedded CoO_x/SiO_2. Due to the competitive adsorption of water and reaction molecules on the active sites, water vapor inhibits the catalytic efficiency. While when H_2O was removed, the CH_4 conversion nearly fully recovered. Under moisture conditions, the embedded CoO_x@SiO_2 exhibited a high thermal stability and efficient moisture resistance due to the silica encapsulation (Li K. et al., 2019).

3.1.5 Mechanisms

According to the available mechanism study on CMC over TMOs, CMC over Co_3O_4 usually follows the MvK mechanism, which means that CH_4 is actually oxidized by the oxygen species present in the Co_3O_4 lattice, followed by the generation of oxygen vacancies. Then, the O_2 from the gas phase refills the oxygen

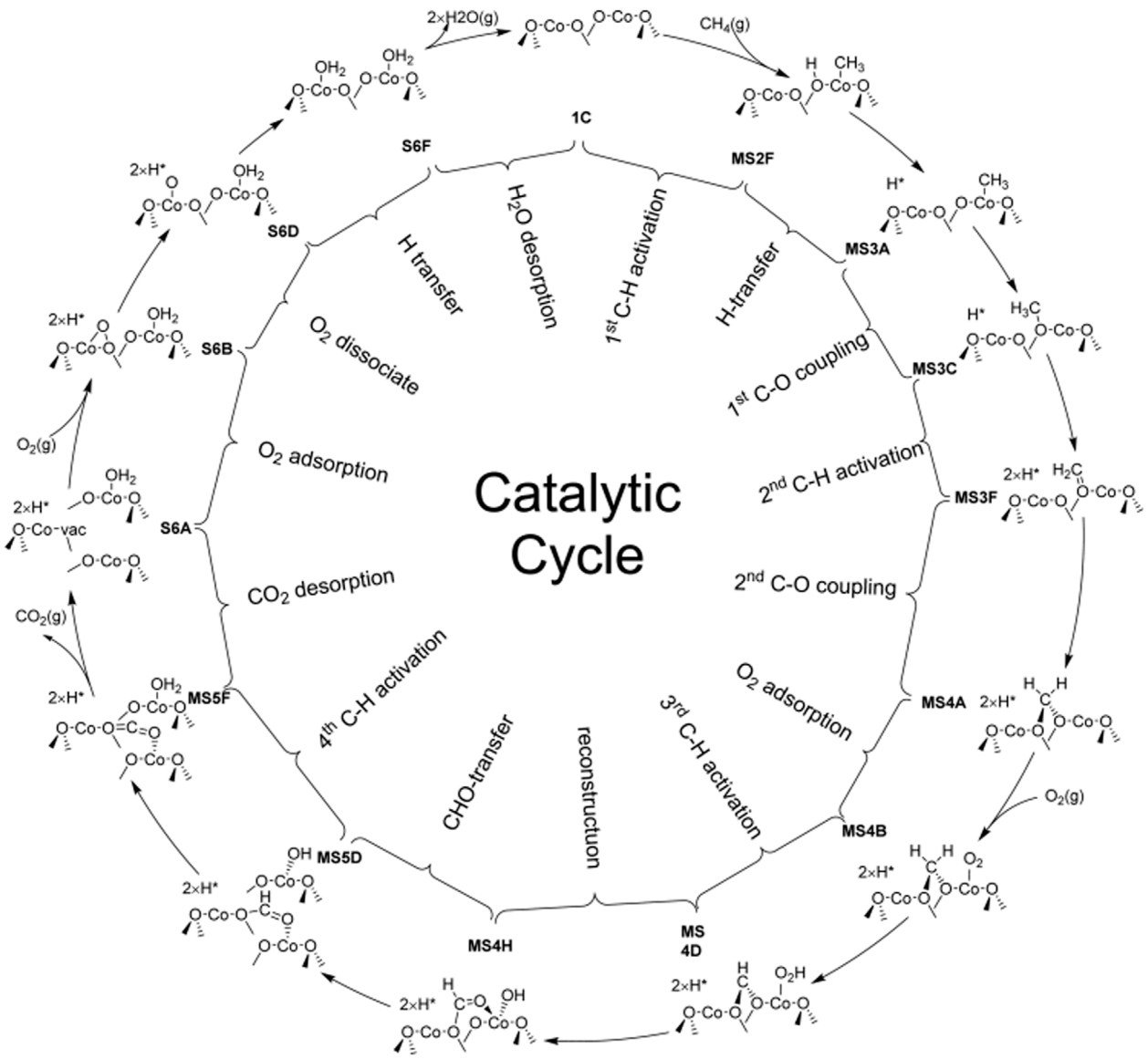

FIGURE 4
Schematic diagram of the whole catalytic cycle of CMC over Co_3O_4 (110) following the optimal reaction mechanism. Reprinted with permission from Hu et al. (2016). Copyright (2016) American Chemical Society.

vacancies, provoking the subsequent reoxidation of the Co_3O_4-basedcatalyst. Wu *et al.* prepared Co_3O_4–CeO_2 mixed oxides using $(NH_4)_2CO_3$, Na_2CO_3, and $CO(NH_2)_2$ as precipitation agents by a precipitation method. The Co_3O_4–CeO_2 with the homogeneous precipitation of $CO(NH_2)_2$ showed excellent catalytic activity owing to the small crystallite size, easy reducibility of Co^{3+}, and high surface Co^{3+} content at the Co_3O_4–CeO_2 interface. The peculiar structure and morphology of CeO_2 played a fundamental role in stabilizing the Co_3O_4 active phase against sintering and promoting its activity. The authors believed that the pathway of CMC over the Co_3O_4–CeO_2 was in accordance with the MvK mechanism, in which the Ce^{4+}/Ce^{3+} couple efficiently released oxygen (Wu et al., 2015).

Hu *et al.* investigated CMC on the Co_3O_4(110) surface with excellent catalytic performance by first-principles calculations as compared with that on the Co_3O_4(100) surface. It is found that the optimal reaction pathway of CMC over Co_3O_4(110) would be $CH_4 \rightarrow CH_3^* \rightarrow CH_3O_{2c} \rightarrow CH_2O_{2c} \rightarrow O_{2c}CH_2O_{2c} \rightarrow O_{2c}CHO_{2c} \rightarrow O_{2c}CHO^* \rightarrow CO_2$, in which the 2-fold coordinated lattice oxygen (O_{2c}) was the key to the first two C–H bond activations and the C–O bond coupling (Figure 4).

According to the figure, H is able to readily transfer swiftly among different surface oxygen species to form adsorbed H_2O^* for the rapid regeneration of active O_{2c}. The cooperation of multiple active sites not only facilitates the H swift transfer in order to maximally prevent the passivation of the active low-coordinated O_{2c} but also stabilizes surface intermediates during the CMC. Due to the synergistic effect of surface-adsorbed oxygen and lattice oxygen, the reaction pathway belongs to the T-T mechanism, in which the first C–H bond activation step would be the rate-determining step for the CMC on the Co_3O_4 (110) surface (Hu et al., 2016).

However, some researchers have proposed different mechanisms for the CMC over Co_3O_4. Han *et al.* prepared a series of Co_3O_4 nanocrystals with different morphologies *via* calcining the $Co(OH)_2$ precursor at different temperatures, among which the mesoporous Co_3O_4 possessed excellent catalytic activity due to the vacancy, antisite, dislocation, and grain boundary defects in the narrow junction regions and the structure of the pore wall. The authors believed that the reaction pathway followed the E–R mechanism, however, without detailed verification (Han et al., 2016).

3.2 NiO-based catalysts

3.2.1 Single NiO

NiO, NaCl-type cubic spar structure, is a typical P-type semiconductor with the intrinsic defects at the Ni^{2+} metal sites, which give rise to positive holes (p^+) to generate Ni^{3+} ($Ni^{2+} + p^+ \rightarrow Ni^{3+}$) or O^- species ($O^{2-} + p^+ \rightarrow O^-$). NiO is extensively used in the field of catalysis, chemical sensors, battery electrodes, and magnetic and electronic devices due to excellent properties such as catalytic activity, thermo-sensitivity, and super-paramagnetic property (Wang et al., 2021). Especially, in the field of catalysis, NiO-based catalysts attract a lot of attention due to the surface electrophilic O^{2-} species being effective for the activation of C–H bonds. NiO have been successfully prepared *via* a variety of methods, including chemical precipitation, electrode deposition, sol–gel technique, surfactant-template, hydrothermal technique, template-free strategy, microwave-assisted gas/liquid interfacial method, and solvothermal method.

Ye *et al.* prepared polymorphous NiO with different morphologies, including nanoparticle-based sheets, octahedra, nanosheet-built agglomerates, and nanoparticle-based microsphere, *via* a simple one-pot thermal decomposition approach. The morphology and crystal properties of NiO can conveniently be achieved by selecting various decomposition temperatures and precursors. The nanoparticle-based sheets and nanosheet-built agglomerates showed a high catalytic performance owing to the small crystal size and large specific surface area by using $NiC_2O_4{\cdot}2H_2O$ and $NiCO_3{\cdot}2Ni(OH)_2{\cdot}4H_2O$ as precursors (Ye et al., 2016).

Chen *et al.* prepared NiO-NSL nanomaterials with a characteristic nanorod structure through the solid–liquid $NH_3{\cdot}H_2O$ precipitation method. The content of Ni^{2+} on the surface of NiO-NSL was higher than traditional NiO-based catalysts, consistent with DFT calculations in which the energy barrier for the C–H bond activation on Ni^{2+} was lower than that on Ni^{3+}. However, the authors did not clearly explain the mechanism of the CMC on the NiO-NSL catalyst, but only highlighted the significant impact of Ni^{2+} on the catalytic performance of the NiO-based catalysts (Chen K. et al., 2021).

3.2.2 Doped NiO

Generally, the synergistic effect induced by the doping can significantly improve catalytic activity. Zhang *et al.* prepared a series of MnO_x–NiO composite oxide catalysts by the co-precipitation method, which exhibits higher catalytic performance compared with the single NiO and MnO_x. The characterization results demonstrate that the Ni–Mn–O solid solution formed by the doping of appropriate amount of Mn, showing abundant highly dispersed Mn^{4+} and higher coordination number as well as certain nickel vacancies, due to the synergy interaction of Ni and Mn (Zhang et al., 2013).

3.2.3 Binary NiO-catalysts

Fan *et al.* introduced Cu into the NiO lattice to generate the Cu–Ni solid solution with the mesoporous structure by the co-precipitation method. Ni–Cu oxide catalysts manifested superior catalytic activity, moisture tolerance, and durability, owing to more unsaturated Ni atoms and lattice defects. Ni–O–Cu bonds could weaken Ni–O and Cu–O bonds, making the lattice oxygen converted into adsorbed oxygen efficiently and creating more oxygen vacancies to promote the activation and adsorption capacity of Ni–Cu oxide for O_2, creating more surface electrophilic species (O_2^{2-}, O_2^- and O^-). Thus, the reaction pathway was in agreement with the MvK mechanism (Figure 5). The electron densities were redistributed because of the interaction between NiO and CuO, where the surface acid–base properties were adjusted. The higher basicity over Cu–Ni oxide could contribute to the adsorption of CH_4 with weak acidity and inhibit the accumulation of surface hydroxyl groups effectively. Meanwhile, the stronger surface acid sites could facilitate the activation of CH_4 *via* heterolytic C–H bond breaking (Fan et al., 2022).

3.2.4 Deactivation

Through the regulation of preparation method and structure, Ni-based catalysts can obtain excellent resistance to water vapor. Liu *et al.* prepared the simple metal oxides (Fe_2O_3, Co_3O_4, NiO, and CuO) by the thermal decomposition of the corresponding metal nitrates. The NiO possessed larger capability for oxygen adsorption, thus exhibiting the best catalytic activity for CMC as compared to other metal oxides, even superior to the perovskite catalyst $LaCoO_3$. Water vapor promoted CH_4 conversion over the

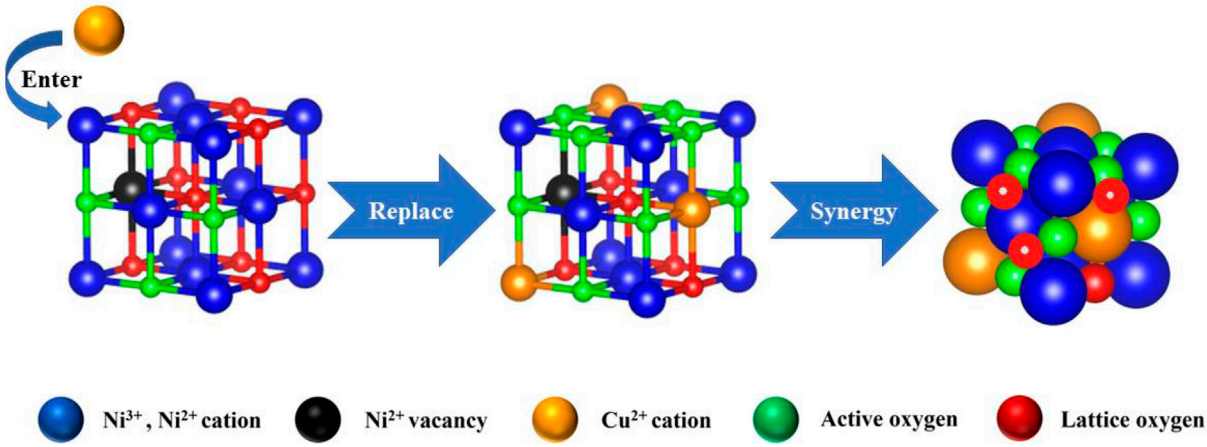

FIGURE 5
Reaction pathway of CMC over Cu–Ni oxide. Cited from Fan et al. (2022).

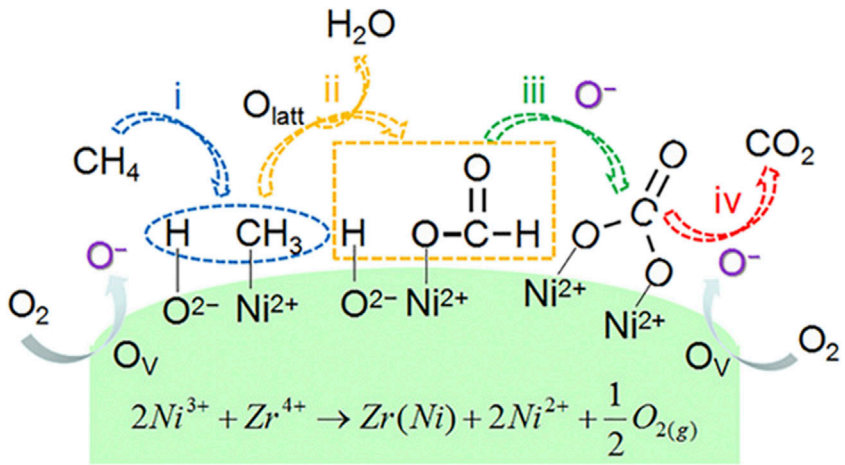

FIGURE 6
Reaction pathway for methane combustion over $Ni_{1-x}Zr_xO_{2-\delta}$ catalysts. Reprinted with permission from Wang et al. (2021). Copyright (2021) American Chemical Society.

NiO catalyst, which could be attributed to H_2O could modify NiO surface and promote the activation of O_2 and CH_4 on the surface (Liu et al., 2017). Xu *et al.* synthesized NiO catalysts with the mesoporous structure by hydrothermal method with polyethylene glycol (NiO-PEG) and polyvinyl pyrrolidone (NiO-PVP) as soft templates. NiO-PEG and NiO-PVP possessed more mobile-active oxygen species, which was beneficial to the activating of the CH_4, due to the mesoporous structure and high surface area. NiO-PEG displayed excellent reaction stability in the presence or absence of water vapor for the reason that its bulk structure possessed certain physical stability (Xu et al., 2017).

3.2.5 Mechanisms

It is generally believed that the pathway of the CMC over nickel-based catalysts is consistent with the MvK mechanism. Shu *et al.* prepared mesoporous NiO with abundant oxygen defects by a NaCl crystalline scaffold-based method. In kinetic measurements, r_{CH4} exhibited a near zero-order dependence on O_2 partial pressure, indicating that CH_4 oxidation was not sensitive to the P_{O2} partial pressure. Due to the depletion of lattice oxygen, the concentrations of $C^{16}O^{16}O$ and $C^{18}O^{16}O$ were reduced, and the concentration of $C^{18}O^{18}O$ was increased, which further demonstrated that the reaction mechanism was accorded

with the MvK mechanism. In this case, the highly abundant lattice oxygen species had great contribution to the excellent performance of NiO (Shu et al., 2022). Wang *et al.* prepared Zr-promoted NiO nanocatalysts by a designed co-precipitation process. $Ni_{0.89}Zr_{0.11}O_{2-\delta}$ solid solution phase exhibited abundant active Ni^{2+} sites and oxygen vacancies, bringing about the increase in surface acidic–basic sites. The mechanism for CMC could be described, as shown in Figure 6. CH_4 was adsorbed on the Ni^{2+}–O^{2-} active site at first and then dissociated to -CH_3 and -OH, followed by the formation of formate and carbonate intermediates. Then, the carbonate species converted to CO_2. The authors did not mention which mechanism the CMC on $Ni_{0.89}Zr_{0.11}O_{2-\delta}$ conforms to, but according to the lattice oxygen and oxygen vacancies involved in the reaction, it is judged that the reaction conforms to the MvK mechanism. Meanwhile, in the stream tests, the steady conversion of CH_4 could be well maintained regardless of the presence of H_2O due on the doping of Zr (Wang et al., 2021).

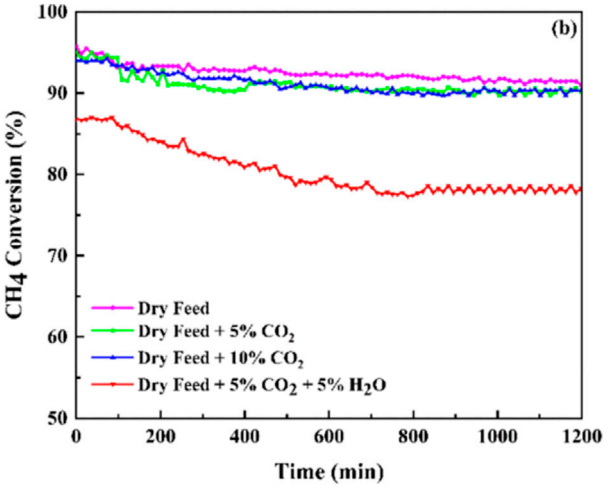

FIGURE 7
Catalytic stability for methane catalytic combustion of the MnO_2 catalyst under different feed compositions. Reprinted with permission from Akbari et al. (2021). Copyright (2021) American Chemical Society.

3.3 MnO_2-based catalysts

3.3.1 Single MnO_2

Mn oxides, such as α- and β-MnO_x, possess the different polymorphic structures, which exhibit mixed valence state of Mn (Mn^{2+}, Mn^{3+}, and Mn^{4+}), and different ways to link together the basic octahedral [MnO_6] units, thereby showing strikingly different and efficient catalytic activities for the CMC (Jia J. B. et al., 2016; Yang et al., 2021). The catalytic activity of the Mn oxides is typically determined by their prepare method, morphology, crystal structure, and degree of oxidation.

Yu *et al.* prepared γ-MnO_2 with abundant surface and lattice defects by a combined ball-milling and selective atom removal method, which showed a high catalytic activity for the CMC owing to the enhanced specific surface area, high Mn^{4+}/Mn^{3+} ratio, more active oxygen species, and enhanced reducibility (Yu et al., 2019). Wasalathanthri *et al.* prepared mesoporous amorphous Meso-Mn-A, Meso-Mn_2O_3, Meso-ε-MnO_2 (epsilon phase), and octahedral molecular sieves MnO_2 (Meso-OMS-2) *via* an inverse surfactant micelle method. Meso-OMS-2 showed the highest catalytic activity, attributing to the narrow and monomodal pore size distribution, higher surface area, the oxidation states, and surface oxygen vacancies, promoting the lattice oxygen mobility, following the MvK mechanism (Wasalathanthri et al., 2015).

3.3.2Doped MnO_2

In addition, compared to pure MnO_x, the doping of other transition metals will also significantly enhance the catalytic performance of Mn-based oxides. Neatu *et al.* studied CeO_2–MnO_x catalysts by three methods, illustrating that the CeO_2–MnO_x catalyst impregnated on the support surface showed superior catalytic activity as compared with the catalyst doped into the bulk. The authors believed that the CMC over the CeO_2–MnO_x catalyst was in accordance with the MvK mechanism, in which the oxidation of CH_4 took place using the lattice oxygen, consecutively with the reduction of Ce^{4+} and Mn^{4+} to Ce^{3+} and Mn^{3+}, respectively. The gaseous O_2 was used to reoxidize the surface to assure another catalytic cycle (Neatu et al., 2019).

3.3.3 Deactivation

However, water vapor will affect the catalytic activity of Mn-based catalysts for the CMC to some extent. Akbari *et al.* prepared nanostructured MnO_2 catalysts with various morphologies by the simple hydrothermal method and the solution method, among which the α-MnO_2 catalyst with a wire-like morphology exhibited the best performance for CMC. However, the stability of the optimal MnO_2 sample reduced to some extent with the water vapor in the reactant feed stream (Figure 7). On one hand, the coverage of the active sites by water vapor inhibited the adsorption of CH_4 and O_2 on the MnO_2 catalyst surface. On the other hand, the -OH group as an inert compound over lattice oxygen could also cause a decline in the catalytic stability (Akbari et al., 2021).

If in an oxidizing atmosphere, SO_2 will be oxidized to form sulfate, which will be deposited on the surface of MnO_2, hindering the multiple adsorption, activation, and oxidation of CH_4 over MnO_2, then causing the deterioration of catalytic activity. Zhong *et al.* synthesized MnCe-RP and MnCe-CP by the redox-precipitation (RP) and co-precipitation (CP) methods,

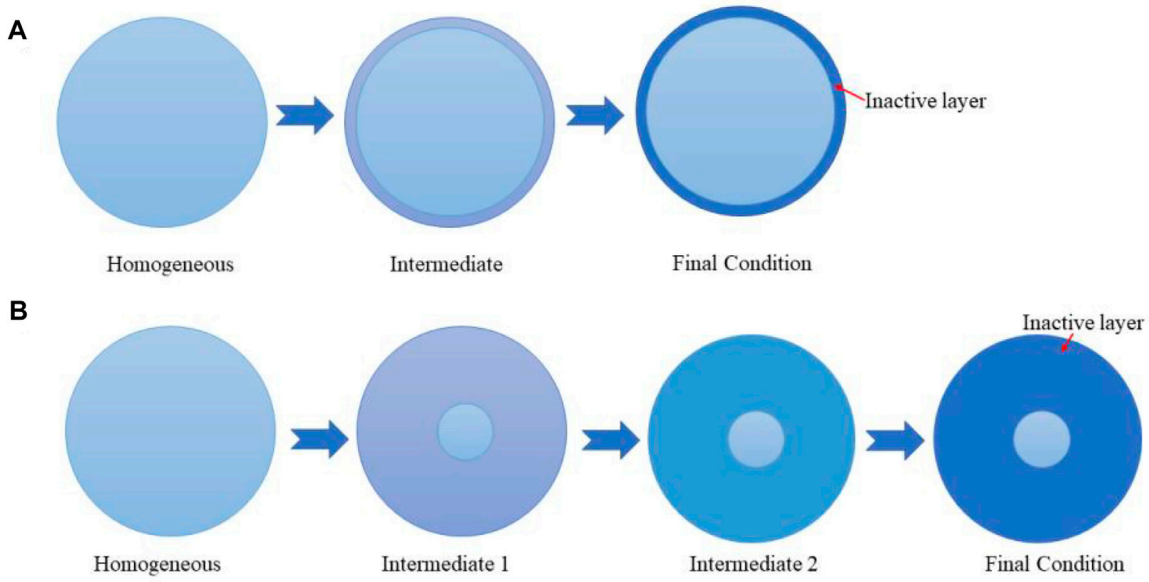

FIGURE 8
SO_2-poisoning mechanism over MnCe-CP **(A)** and MnCe-RP **(B)**. Cited from Zhong et al. (2019).

respectively, and studied SO_2 resistance of the catalysts (Figure 8). The SO_2 would decrease the content of lattice oxygen and Mn^{4+}, so the CH_4 conversion of MnCe-CP reduced by 62.45%. On the contrary, the CH_4 conversion of MnCe-RP only reduced by 1.08% owing to the excellent morphology and the redox potential of $K_xMn_8O_{16}$, absorbing and oxidizing SO_2 to sulfides, freeing from the poison of the downstream catalyst (Zhong et al., 2019).

3.3.4 Mechanisms

There are reported contradictory claims on the CMC over Mn oxides, such as that based on the L–H mechanism involving adsorbed oxygen and that based on the MvK mechanism concerning lattice oxygen.

Zhang *et al.* synthesized nanocubic MnO_2 (MnO_2-C) with planes (101) and nanorod-shaped MnO_2 (MnO_2-R) with planes (110) by a hydrothermal process, illustrating that the morphologies of MnO_2 had significant influence on the catalytic performances of CMC. Due to higher BET surface area, smaller crystalline size, more surface oxygen vacancies, and better low-temperature reducibility, MnO_2-C displayed higher catalytic performances and good thermal stability compared with MnO_2-R. The authors believed that the surface oxygen of MnO_2-C could react with the adsorbed C–H to generate the carboxylate species for the reason of more surface oxygen vacancies, followed by the oxidation of carboxylate species to CO_2, through the L–H mechanism (Zhang et al., 2019). Jia *et al.* synthesized two types of single-phase manganese oxides MnO_2 with different levels of nonstoichiometric defects, α-MnO_2 (Mn1) and γ-MnO_2 (Mn2), compared with a stoichiometric Mn_2O_3 (Mn3) as a reference. Results revealed that both Mn3 and Mn1 exhibited enhanced activities due to more structural defects. It was found that CH_4 was directly oxidized to carbonates on the surface of the pre-oxidized Mn1 and subsequently transformed to CO_2 in the absence of gaseous O_2 by the *in situ* DRIFTS and CH_4-TPD test, which showed that the active oxygen involved in the CH_4 oxidation was largely derived from the surface lattice oxygen of the Mn1, in accordance with the MvK mechanism. The O_2 on–off profiles further demonstrate reaction mechanism, in which the desorbed CO_2 was generated by the reaction between CH_4 and lattice oxygen from Mn1 without O_2, while the increase in CO_2 resulted from the reaction between CH_4 and the constantly refilled oxygen at the vacancies in the presence of O_2 (Jia et al., 2019).

Wang *et al.* studied the roles of the crystallographic structure of Mn-based oxides, among which α-MnO_2 exhibited the superior catalytic performances, attributing to higher surface Mn concentration and more active oxygen species, more mono-μ-oxo bridged (corner-shared) MnO_6 sites, and better reducibility. CMC over the MnO_2 catalyst proceeds *via* both MvK and L–H mechanisms, while the latter was predominant, in which the dehydrogenation of CH* to H* was considered as the rate-determining step and intermediate species -COO and -CH_3O were oxidized by active oxygen species to CO_2 and H_2O (Wang et al., 2018).

3.4 Cr_2O_3-based catalysts

3.4.1 Single Cr_2O_3

The Cr_2O_3, trigonal crystal system belongs to the α-Al_2O_3 structure, which is composed of oxygen ions as the closest hexagonal packing and Cr^{3+} filling the octahedral gap formed by these close packings. The coordination number of Cr^{3+} is 6, and only 2/3 of the octahedral gap is occupied by chromium ions. The activity and selectivity of Cr_2O_3 are closely related to the change of the valence state of chromium ions. Various techniques have been developed to prepare Cr_2O_3 nanoparticles such as co-precipitation, incipient wetness impregnation, sol–gel, solvothermal, solid thermal decomposition, and sonication (El-Sheikh et al., 2009).

Jodłowski *et al.* applied the sonication method to prepare transitional metal oxide catalysts (Co, Cu, Cr), among which the chromium oxide catalyst showed greater catalytic activity as compared to cobalt oxide, copper oxide, and commercial palladium catalysts, attributing to the presence of a high concentration of formate on the surface of chromium oxide (Jodłowski et al., 2016).

3.4.2 Doped Cr_2O_3

The doping of Cr_2O_3 enables the catalyst to exhibit excellent catalytic activity due to the synergistic effect between TMOs. Yuan *et al.* prepared Cr-based catalysts modified by Ce *via* incipient wetness impregnation method and investigated the effects of the Ce loading amount. It was found that the Cr-based catalysts with 3 wt% Ce showed higher catalytic performance due to an increasing amount of reaction site [CrO_4] species, improving the high-temperature-resistant performance and obtaining the synergistic effect between Ce and Cr (Yuan et al., 2013). Dupont *et al.* synthesized Cu/Cr oxides with high specific surface area by the sol–gel route using propionic acid. The results suggested that Cu/Cr oxides prepared by the special sol–gel process showed better catalytic performances compared with Cu/Cr oxide commercial catalysts, attributing to well-dispersed Cu species and the surface enrichment with Cr^{6+}. In addition, though DFT coupled with periodic slab models, the authors believed that O_2 molecules dissociatively adsorbed over the Cu/Cr oxide surface at the first step, along with generating the active oxygen species mainly at the Cr sites (Dupont et al., 2010).

3.4.3 Deactivation

Due to its poor affinity for acid gases, Cr_2O_3 exhibits excellent resistance to sulfur poisoning. Ordo´ñez *et al.* prepared different bulk metal oxides (Cr_2O_3, Co_3O_4, Mn_2O_3, NiO, and CuO) and investigated their catalytic stability for CMC in the presence of SO_2. It was found that Cr_2O_3 exhibited highly sulfur-tolerant, whereas the other materials were deactivated rapidly, even if Co_3O_4 and Mn_2O_3 were more active than Cr_2O_3 for CMC in the absence of sulfur species. Characterization results illustrated that the excellent stability was caused by the low affinity of Cr_2O_3 to acid gases (as SO_2); thus, sulfates would not form on the surface of the catalyst to occupy the active sites (Ordóñez et al., 2008).

3.4.4 Mechanisms

There is still controversy about the mechanism of CMC on Cr_2O_3. Huang *et al.* synthesized a homogeneous $ZnCr_2O_4$ oxides by the ethylene glycol-mediated solvothermal method. Cr^{3+} and Cr^{6+} coexisted in $ZnCr_2O_4$, in which Cr^{6+} probably caused the presence of interstitial oxygen species in the structure. The authors believed that the reaction pathway of CMC over the $ZnCr_2O_4$ catalyst was consistent with the L–H mechanism under low temperature, in which the interstitial oxygen was involved to the methane combustion. However, the mechanism has not been experimentally verified (Huang et al., 2019).

On the contrary, Zhu *et al.* applied the co-current co-precipitation method to prepare a series of Sn–Cr binary oxide catalysts among which the oxide with a Cr/Sn atomic ratio of 3 : 7 showed excellent catalytic activity due to higher surface areas and high oxidation states of chromium ions. Temperature-programmed ^{18}O isotope-exchange measurements confirmed that CMC over Sn–Cr binary oxide catalysts occurred *via* a redox cycle with the chromium ion as the active center, following the MvK mechanism (Zhu et al., 2003).

3.5 Fe_2O_3-based catalysts

3.5.1 Single Fe_2O_3

Fe_2O_3 is an earth-abundant and non-toxic material that has been extensively used to catalyze a wide range of reactions including water gas shift reaction, photocatalytic water splitting, looping combustion, etc. There are four polymorphs of Fe_2O_3, which are Hematite (α-Fe_2O_3), Maghemite (γ-Fe_2O_3), β-Fe_2O_3, and ε-Fe_2O_3. Among which α-Fe_2O_3 is thermodynamically stable and has the corundum(α-Al_2O_3) structure, which is based on a hcp anion packing. γ-Fe_2O_3 is an inverse spinel structure with cation-deficient sites and can be transformed from α-Fe_2O_3 at high temperature. β-Fe_2O_3 andε-Fe_2O_3 have been synthesized only in the laboratory. The former has been obtained by the de-hydroxylation of β-FOOH under high vacuum at 170°C. The structure of ε-Fe_2O_3 is intermediate between those of α-Fe_2O_3 and γ-Fe_2O_3. It can be prepared in various ways and transforms to α-Fe_2O_3 at between 500 and 750°C, apparently according to the method of preparation (Cornell and Schwertmann, 2003).

Among the few researches dealing with the use of Fe_2O_3 in CMC, α-Fe_2O_3 was the dominant catalytic active phase, and preparation method affects its catalytic performance greatly. Barbosa *et al.* synthesized bulk α-Fe_2O_3 by precipitation (α-Fe_2O_3-p) and the citrate method (α-Fe_2O_3-c), finding that the

preparation method strongly influences both the initial activity of the catalyst and its stability under reaction conditions (Barbosa et al., 2001). The α-Fe_2O_3-p catalyst presented higher surface areas, in correlation with greater initial activity and lower light-off temperatures than that of the α-Fe_2O_3-c catalyst. Although all catalysts undergo sintering at the high operation temperature with the loss of active sites, the α-Fe_2O_3-p catalyst exhibited less sintering and better stability. On this basis, Paredes *et al.* prepared α-Fe_2O_3 base catalysts *via* the acid dissolution-alkaline precipitation method using red mud as a raw material, an aluminum industrial waste formed by α-Fe_2O_3, Ti, Al, Ca, and Na, and compared the CMC performance and reaction mechanism with unprocessed red mud, and massive α-Fe_2O_3 synthesized by the precipitation method (α-Fe_2O_3-c mentioned above) (Paredes et al., 2004). For the combustion of 2000 ppm V CH_4 in air, the α-Fe_2O_3-c exhibits the best activity (T_{50} = 461°C), and the activity of processed red mud (T_{50} = 530°C) is much higher than that of unprocessed red mud (T_{50}>650°C) because after treatment the component of Na and Ca, which can hinder the catalyst activity decreases. Moreover, when conversion per Fe content in the catalyst is considered, the difference between α-Fe_2O_3-c and processed red mud catalysts is much smaller at low conversions. This would indicate that the other constituents of red mud have little or no effect on the catalyst activity. As for the mechanism, the CH_4-TPD experiments (100–600°C) suggested that very little CH_4 is adsorbed, the reticular oxygen of the catalyst being enough for its complete oxidation.

In addition, researchers have achieved the catalytic conversion of CH_4 over α-Fe_2O_3 catalysts with different morphologies. Dong *et al.* fabricated 3D urchin-like mesoporous α-Fe_2O_3 nanoarchitectures with the combination of nonhomogeneous ionic liquid/diphenyl ether solvothermal method and solid-state thermal annealing. They found that CH_4 was converted into products containing C–O bonds (CO_2) at 230°C, which is 190°C lower than over bulk α-Fe_2O_3. As for the reason, with the measurement and comparison of adsorbed oxygen on the two material, they inferred that the urchin-like α-Fe_2O_3 nanoarchitectures have a higher density of surface oxygen vacancies than bulk α-Fe_2O_3, which can accelerate the dissociation of oxygen molecules at the surface and increase the mobility of lattice oxygen (Dong et al., 2014). It should be noted that this structure does not exhibit good CH_4 conversion at high temperatures (700°C, conversion = 16%). He *et al.* invented a hard-templating synthetic strategy to guide the anisotropic growth of ultrathin α-Fe_2O_3 nanosheets with a large (110) facet exposure ratio, the catalytic performance of which in low-temperature CH_4 combustion is comparable to that of noble metal-based catalysts (He L. et al., 2020). The antiferromagnetic coupled diiron core on the (110) crystallographic plane of α-Fe_2O_3 is a structurally favorable condition, which resembles the diiron active site in soluble CH_4 monooxygenase, an enzyme that converts CH_4 to methanol in nature (Ross and Rosenzweig, 2017). Meanwhile, they utilized oxygen isotopic tracing experiments and DFT calculations to confirm that CH_4 is primarily activated by lattice oxygen below 400°C, in accordance with the MvK mechanism. They further speculated that at higher temperatures, CH_4 would be activated predominantly by molecular oxygen instead, as the accumulation of lattice oxygen vacancy favoring the adsorption of molecular oxygen from the gas phase (Cheng et al., 2016).

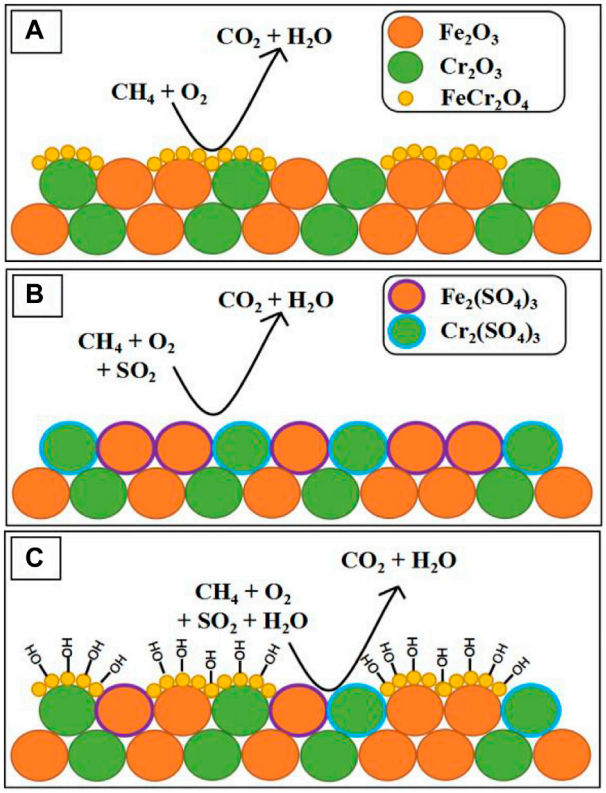

FIGURE 9
Proposed poisoning mechanisms at 450°C under **(A)** sulfur-free conditions, **(B)** dry conditions, and **(C)** wet conditions. Cited from García-Vázquez et al. (2020).

3.5.2 Deactivation

CH_4 emissions are often accompanied by large quantities of steam and traces of sulfur-containing gases, which are the two most performance hindering species present in typical CH_4 after-treatment operating conditions (Raj, 2016). Setiawan *et al.* confirm that α-Fe_2O_3 catalysts are significantly lower activity under the mixture conditions of water vapor and CH_4 due to the strongly bound between water (hydroxyl) species and Fe_2O_3, which destruct the active sites irreversibly (Setiawan et al., 2015). Recently, García-Vázquez *et al.* synthesized iron- and chromium-based oxides by using

the citrate sol–gel method and investigated their catalyst performance of CMC in the presence of SO_2 and steam. They found that catalyst $Fe_{60}Cr_{40}$ (molar ration) exhibited the remarkable performance (366 ppm CH_4 balanced in air, T = 450°C, conversion = 79%) due to the formation of the $FeCr_2O_4$ spinel phase, which is the most active sites in these catalyst for CMC. And because the $FeCr_2O_4$ spinel phase can still exits after being aged under wet conditions, the $Fe_{60}Cr_{40}$ showed the better catalyst conversion of CH_4 than α-Fe_2O_3 catalyst, which can also be found by comparing Figures 9A,B (312 ppm CH_4 + 4.6 ppm SO_2 10% vol H_2O balanced in air, T = 450°C, conversion = 47% vs. 26%). In addition, as has been represented in Figure 9C, the competitive adsorption of hydroxide groups on $FeCr_2O_4$ even slows down the rate at which sulfur dioxide poisons the catalyst's active sites (García-Vázquez et al., 2020).

3.5.3 Mechanisms

In conclusion, the reaction of α-Fe_2O_3 catalyst in CMC involves the MvK mechanism. Recently, Tang *et al.* adopted the generalized gradient approximation (GGA) + U approach to investigate the reaction pathways of complete and partial oxidations of CH_4 on the dominant Fe–O_3–Fe termination of thermodynamically stable hematite (α-Fe_2O_3) (0001) facets. The energy barrier for the first C–H bond activation is 1.04 eV. In the transition state, the dissociating H is in contact with the lattice O and with the dissociating CH_3 is in contact with the Fe site. Subsequent decomposition and oxidation of the CH_x species (x = 1, 2, 3) exploit the lattice O species according to the MvK mechanism, forming CH_xO in more thermodynamically and kinetically favorable pathways. For the two pathways, the overall rate-limiting steps are both the first C–H bond activation. Adsorption of O_2 on the VO site is exothermic (-1.42 eV), with one O atom binding at the VO site and the other O binding on the Fe site. In particular, after the dissociation of O_2 *via* the O–O bond cleavage, one O fills the oxygen vacancy, and the other O became the ferryl O (Fe=O). Although the ferryl O is highly active and capable of lowering the energy barrier of the C–H bond activation, the availability of extremely active ferryl O is expected to be too low on the Fe–O_3–Fe-terminated surface to critically impact the overall catalyst performance (Tang and Liu, 2016).

3.6CeO_2-based catalysts

3.6.1 Single CeO_2

CeO_2 is the most stable form of cerium oxide, which has a face-centered cubic structure and space group of Fm-3m (Trovarell, 2002). The coordination of cerium is 8 and that of oxygen is 4, which means that there are large vacant octahedral holes in the structure. Because of its structure, CeO_2 has an excellent storage-release capacity in a reversible manner. Specifically, Ce^{4+} can be reduced to Ce^{3+} under anoxic conditions, accompanied by a rapid release of lattice oxygen from the solid to the gas phase, leaving oxygen vacancy defects. On the other hand, Ce^{3+} can be re-oxidized into Ce^{4+} by adsorbing oxygen under oxygen-rich conditions and therefore refills the vacancies. Such unique redox properties render CeO_2 a wonderful support for noble metal catalysts in the catalytic oxidation of hydrocarbons, following mostly the MvK mechanism (Aneggi et al., 2016).

3.6.2 Doped CeO_2

CeO_2 has been actively studied in the past few decades as an alternative to noble metal catalysts for CMC (Mukherjee et al., 2016). While pure CeO_2 phase exhibits a poor catalytic activity at low temperatures and a poor thermal stability at high temperatures, which significantly hampers its industrial uses (Kašpar et al., 1999). Efforts have been made to improve the catalytic CH_4 combustion performance of CeO_2-based catalysts such as compositing with other metal oxides, heteroatom doping, etc. For instance, more oxygen vacancies can be introduced into the CeO_2 structure by doping cations with oxidation states below or equivalent to 4^+ such as Ca^{2+}, Mn^{2+}, Ni^{2+}, Cu^{2+}, Fe^{3+}, Co^{3+}, La^{3+}, and Y^{3+} (Palmqvist et al., 1998; Huang et al., 2012; Wu et al., 2015; Zedan and AlJaber, 2019). The presence of abundant oxygen vacancies promotes the mobility of lattice oxygen and subsequently boosts the catalytic activity of CeO_2. Meanwhile, there may also exist a synergistic effect between the doped metals and Ce. Palella *et al.* recently prepared $MnCeO_x$ composites *via* a redox route and demonstrated that Mn^{2+} ions are the active sites for the formation of active oxygen species arising from the oxygen vacancies in low-temperature oxidation of CH_4, while Ce elements can improve the availability of reactant molecules at the active site by introducing oxygen vacancies (Palella et al., 2021). There is a strong synergistic effect between Mn–Ce elements, which stabilizes Mn^{2+} species and facilitates the dispersion of Mn^{2+} ions. The dissociation of CH_4 into CH_n* and H* species was found to be the rate-determining step for the Mn-doped CeO_2 composite system. Apart from Mn, other monometallic elements such as Cu (T_{50} = 350°C), Fe (T_{50} = 378°C), Ni (T_{50} = 415°C), and Co (T_{50} = 380°C) catalysts have also improved catalytic activities and stabilities due to the established synergistic effects that increase the dispersion of active metal oxides, which allow more $M^{n+}/M^{(n-1)+}$ redox couples to participate in the redox cycle; more discussions on the doped CeO_2 catalysts can be found in a recent review by Stoian *et al.* in details (Stoian et al., 2021). Due to the absence of active site, which triggered by grain growth, CeO_2 is sintering at high temperature. Larrondo *et al.* tried to increase the thermal stability of CeO_2 by the addition of ZrO_2 to the structure of CeO_2 and found that ZrO_2 can also slightly facilitate the reducibility of the solids associated with both surface and bulk Ce sites with the evidence of H_2 TPR. And the catalysts with 10% of Zr have higher values of CH_4 conversion than the other

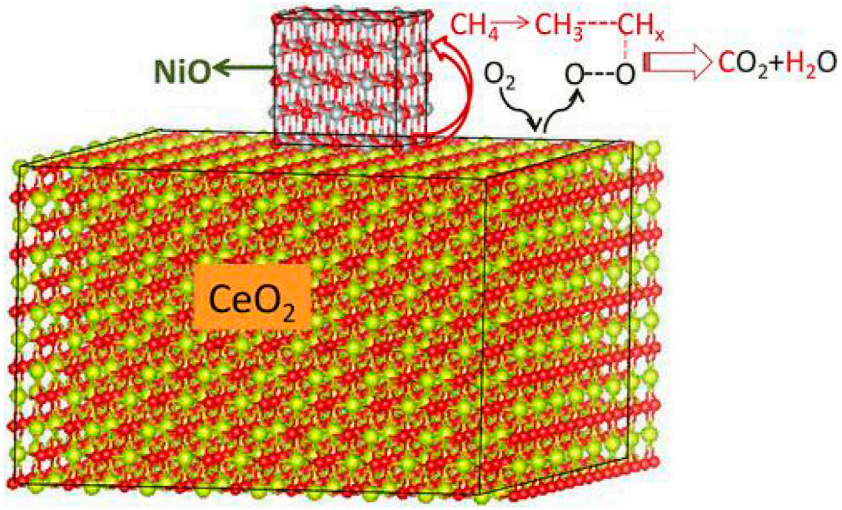

FIGURE 10
Schematic briefly showing activations of C–H of CH_4 and O–O of O_2 and coupling between CH_x species and atomic oxygen at the interface of NiO/CeO_2. Reprinted with permission from Zhang et al. (2018). Copyright (2018) American Chemical Society.

samples with 30% Zr and 50% Zr (Larrondo et al., 2005). Recently, Toscania *et al.* used the citrate complexation route to future prepared $Ce_{0.9}Sc_xZr_{0.1-x}O_{2-\delta}$ (x = 0, 0.02, 0.04, and 0.06) by citrate complexation route, with the aim of combining the improved thermal stability provided by the ZrO_2 with an increase in vacancy concentration upon Sc doping (Toscani et al., 2019). The doped samples exhibited superior redox behavior because the CeO_2 reduction values from TPR experiments and vacancy concentration from Raman tests both increase with increasing Sc content. And in contrast to the binary CeO_2–ZrO_2 sample, the CeO_2–ZrO_2–Sc_2O_3 showed the higher reaction rates and lower apparent activation energies for CMC. In addition, *in situ* XANES experiments confirm the participation of the lattice in the redox mechanism. Huang *et al.* prepared a series of NiO/CeO_2 by a facile impregnation method, which exhibited high catalytic performance and stability due to synergistic interaction between CeO_2 and NiO. The incorporation of Ni^{2+} into the CeO_2 lattice obviously enhanced the concentration of oxygen vacancies and amount of surface oxygen, making the mobility of bulk oxygen in CeO_2 increased, along with the reduction of the activation energy of the CMC. On the other hand, CeO_2 prevented the aggregation of NiO, further improving the reduction properties of NiO (Huang et al., 2020). Apart from this, CeO_2-modified catalytic materials can also be used in the reaction of oxidative coupling of methane (OCM) because of its above redox properties and increased surface basicity (Siakavelas et al., 2021). OCM is an exothermic reaction between CH_4 and O_2 in the range of 700–900°C, forming C_2 hydrocarbons (e.g., C_2H_4 or C_2H_6), *via* CH_4–CH_3–C_2H_6–C_2H_4 progress. Moreover, for OCM, the incorporation of *f*-block elements such as Pr^{3+}, Sm^{3+}, and La^{3+} (redox-active basic ions) into the CeO_2 could modify the acid–base properties, enhance its thermal stability, and generate additional oxygen vacancy sites (Xu et al., 2019; Zhang et al., 2020; Siakavelas et al., 2022a). Furthermore, Siakavelas et al. (2022b) recently added lithium ions into CeO_2- and CeO_2-modified materials (Sm-Ce and La-Sm-Ce metal oxides), using the wet impregnation technique. They argued that the addition of lithium species changed the reaction pathway and drastically enhanced the production of ethylene and ethane, mainly for the promoted catalysts (Li/Sm-Ce and Li/La-Sm-Ce).

3.6.3 Binary CeO_2 catalysts

The CMC involves both the activation of C–H of CH_4 and O–O of O_2. CeO_2 can activate molecular oxygen *via* Ce^{4+} and Ce^{3+} redox couples; however, it is incapable of activating the C–H of CH_4. On the contrary, NiO exhibits high activity in activating C–H, but, does not activate molecular oxygen. Thus, Zhang *et al.* synthesized NiO/CeO_2 through a two-step method, in which nanocomposite consists of CeO_2 nanorods with supported NiO nanoclusters, exhibiting notably higher activity due to the lowest apparent activation energy (69.4 ± 4 kJ/mol). The schematic diagram of the reaction mechanism at the interface is shown in Figure 10. The C–H of CH_4 was activated on the Ni-O species, forming a H_3C–Ni- intermediate on the interface. The formed CH_3 could be further activated to form CH_2 or even CH species, which could couple with surface lattice oxygen atoms to form CO_2 and H_2. The process follows the MvK mechanism, in which NiO nanoclusters and CeO_2 nanorods show a synergistic effect for CMC (Zhang et al., 2018).

3.6.4 Mechanisms

In conclusion, the mechanism of CeO_2 in CMC has been reported to follow the MvK mechanism (Knapp and Ziegler, 2008). Results reported in the literature indicate that the first step is hydrogen abstraction from the CH_4 molecule over the Ce surface. As the (111) surface of CeO_2 is the most stable and predominant, therefore, the exposed oxygen atoms with low coordination on the (111) surface are assumed as the active sites over CeO_2-based catalysts in CMC. CH_4 dissociation is followed by the formation of a CH_3 radical and an adsorbed H* atom. These two species bind to two surface oxygen atoms, leading to the formation of a methyl radical (CH_3^-) and a hydroxyl radical (HO·). Hydrogen adsorption leads to the reduction of one of the neighboring Ce atoms. Afterward, a series of intermediate steps take place, in which the H atoms are abstracted from CH_3* to form CH_2* and CH* until CO is formed by further reducing the Ce with the formation of an oxygen vacancy. Finally, the adsorbed CO reduces Ce by binding with another oxygen allowing the formation of CO_2. Water is formed by the binding of adjacent OH groups. The breaking of the C–H bond is generally the rate-limiting step in all methane activation processes (Tang et al., 2010).

3.7 CuO-based catalysts

3.7.1 Single CuO

CuO is an important p-type semiconducting material with a cubic rock salt structure (c-CuO) and lower-symmetry monoclinic structure (m-CuO). Analysis of the calculated band structures revealed that c-CuO is an indirect gap semiconductor, while m-CuO has metallic behavior (Cao et al., 2018). CuO has been considered as one of the most effective alternatives to noble metal-based catalysts in CMC because of its Earth abundance, non-toxicity, and good catalytic performance (Liu et al., 2010).

Researchers exhibited that Cu loading and the nature of the carrier exert influence on the Cu species present on the catalyst surface. Park and Ledford tested the catalytic activity of Cu/Al_2O_3 catalysts with different Cu loadings for CH_4 combustion reactions and they found that, with increasing Cu content, both the activity per unit mass of Cu and per mole of Cu on the surface decreased (Park and Ledford, 1998). The active phase for CH_4 oxidation is a superficial phase formed by isolated or highly dispersed Cu; as the Cu content increases, the dispersion becomes worse and therefore reduces the total number of active sites. Aguila *et al.* investigated CuO-loaded catalysts with porous media such as Al_2O_3, ZrO_2, and SiO_2 prepared by the impregnation method (Aguila et al., 2008). This work showed that CuO catalysts supported on ZrO_2 have higher activity (per unit mass of Cu) for CH_4 oxidation than when CuO is supported on alumina or silica, which is related to the ability of ZrO_2, stabilizing the highly dispersed Cu species to prevent the formation of bulk CuO. This ability is available when Cu concentrations between 0.25% and 6% for the catalysts are supported on ZrO_2. In addition, they also tested the influence of water for the CuO catalysts supported on ZrO_2. The addition of water produces a decrease of the CH_4 conversion, but, as soon as the water flow is stopped, the catalyst recovers its initial activity, which means that inhibition with water is reversible, at least for the 300 min considered in this experiment.

In addition to dispersion, the acid–base properties of the supports also affect the catalytic performance of Cu-based catalysts. Theoretically, the adsorption and activation of hydrocarbons on oxide-based catalysts and the desorption of reaction products are related not only to the strength and distribution of the Lewis acidic metal cation sites but also to the concentration of lattice oxygen anions as the Lewis base sites (Vedrine et al., 1996). Specifically, the interaction of CH_4 with acid–base pairs on the catalyst surface leads to the heterolytic breakage of the C–H bond and the formation of CH_3^- and H^+ species chemisorbed on the acid and base sites, respectively. Stronger acidic sites enhance the interaction with the carbon anion and therefore facilitate surface catalytic combustion (Choudhary and Rane, 1991). By co-precipitation and calcination methods, Popescu *et al.* synthesized the CuO nanoparticles supported on mixed oxides of Al_2O_3, MgO, and Mg(Al)O and investigated their catalytic properties in the total oxidation of CH_4 (Popescu et al., 2017). Because, on the one hand, CH_4 activation involving the heterolytic C–H bond breaking needs acid–base pairs, on the other hand, the total oxidation reaction is favored in the presence of acid sites of high strengths, which strongly adsorb carbanions, thus undergoing surface reaction with oxygen. The CuMgAl(1)O (Mg/Al atomic ratios is 1) showed the highest activity as it not only contained strong acid sites (ca.50%), which was similar with the CuAlO (strong acid species), but also had strong basic sites (ca. 30%).

3.7.2 Doped CuO

Lu *et al.* prepared CuO–CeO_2 hybrid nanoparticle and created substantial amounts of Cu–Ce–O interfaces by gas-phase evaporation-induced self-assembly. CuO–CeO_2 exhibited excellent catalytic performances with a low light-off temperature, high activity, selectivity, and operation stability. The two possible mechanisms of CMC over CuO and CuO–CeO_2 are shown in Figure 11. The authors conjectured that two routes follow the MvK mechanism. However, the Cu–Ce–O interfacial metal–support interaction promotes the redox cycle of interface, in which CH_4 binds to the surface of CuO, while O_2 is simultaneously adsorbed on the oxygen vacancy of CeO_2, then dissociating to a surface-bound methyl group and oxygen atoms, respectively; after the release of H_2O, an oxygen vacancy

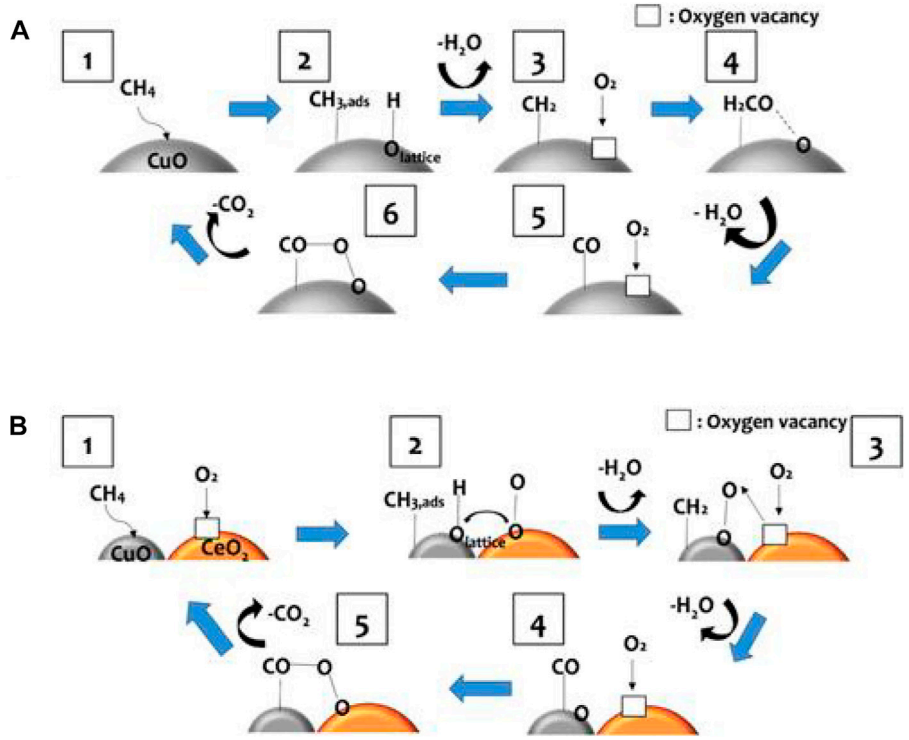

FIGURE 11
Cartoon depiction of methane combustion catalyzed by CuO **(A)** and Cu/CeO_2 **(B)**. Reprinted with permission from Lu et al. (2016). Copyright (2016) American Chemical Society.

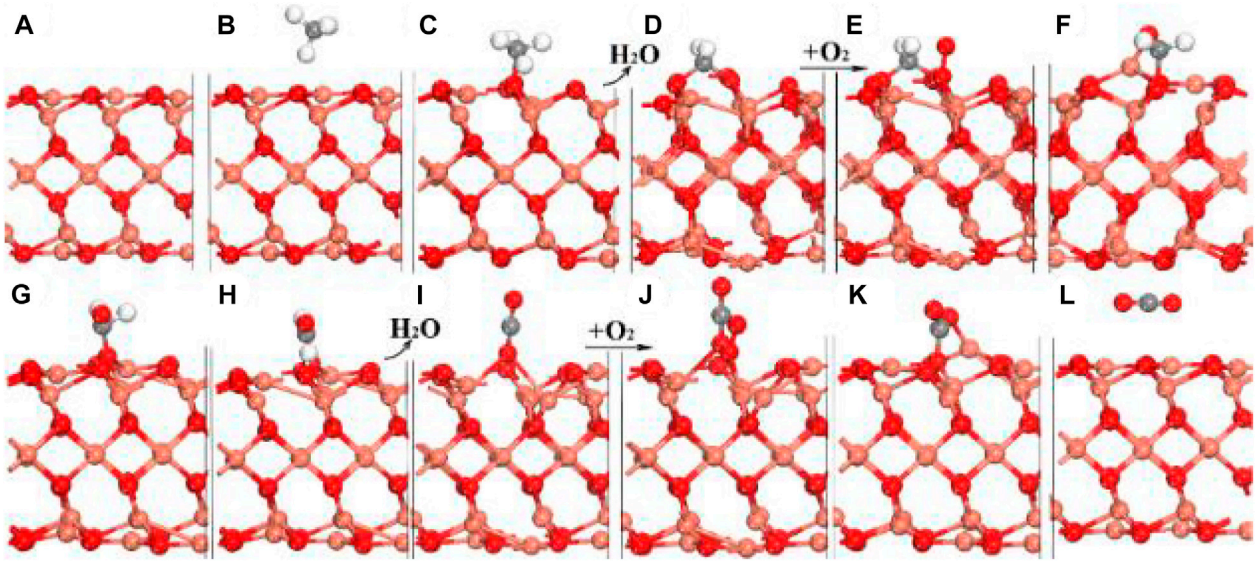

FIGURE 12
(A) Clean (001); **(B)** CH_4 physical adsorption; **(C)** CH_4 dissociative adsorption; **(D)** CH_2* with oxygen vacancy (OV) presented; **(E)** CH_2* with O_2 adsorbed; **(F)** CH_2* rotating and interacting with O_2*; **(G)** transition state (TS) state COH_2*; **(H)** CHO* + H*; **(I)** CO* with OV presented after releasing one H_2O; **(J)** CO* with O_2 adsorbed; **(K)** TS for O transfer to CO*; **(L)** CO_2 physical adsorbed. Cu, O, C, and H are shown as rose-carmine, red, grey and white spheres, respectively. Reprinted with permission from Kong et al. (2018). Copyright (2018) Beilstein-Institut.

regenerates, subsequently combining with the oxygen atoms; the dissociated methyl group is further oxidized by the adsorbed oxygen atoms, and then CO_2 is released from the surface of CuO. The synergistic effect between CuO and CeO_2 increases the rate of CMC, which has shown promise in enhancing the removal rate of hydrocarbon from the catalyst surface (Lu et al., 2016).

3.7.3 Mechanisms

Kong *et al.* identified CuO (001) as an active surface for CMC over CuO among other surfaces, including (110), (111), (101), (010), and (011) *via* DFT calculations (Figure 12). It is not surprising because (001) is strongly polarized and shows high reactivity due to the high ratio of lowly coordinated oxygen. In DFT calculations, CH_4 is firstly adsorbed with AE = -0.86 eV, followed by a spontaneous dissociation with CH_3 and H adsorbed on surface oxygen, as depicted in Figures 12A–C. Surface oxygen is often actively involved and may cleave H from CH_x to form -OH and H_2O, generating an oxygen vacancy (OV), which can be filled with reactant O_2, leading to its dissociation and further oxidizing CH_x intermediates, as shown in Figures 12D–F. With oxygen transferring to bond with carbon, the hydrogen in CH_x can shift to surface oxygen again with an energy release of 3.66 and 1.46 eV, indicating that such a shift is highly favorable, as shown in Figures 12G–I. Again, an OV is generated and refilled by O_2 when H_2O is released, and similarly O_2 is dissociated to release atomic oxygen after exceeding a small barrier of 0.47 eV, which can oxidize adsorbed CO to form CO_2, as outlined in Figures 12I–L. Although the authors did not specify which mechanism the mechanism of CMC over CuO (001) conforms to, given their theoretical calculations, we believe that it is consistent with the MvK mechanism (Kong et al., 2018).

4 Perspectives

It has been well acknowledged that TMOs are one of the most promising candidates as alternatives to noble metal catalysts in CMC. Although promises have seen in some TMOs, problems still exist such as the controversial reaction mechanism, low water vapor, and sulfur resistance. Therefore, it is necessary to explore appropriate preparation methods, suitable modified ions, and the optimal ratios to synthesize novel TMOs with excellent resistance to water vapor and sulfur poisoning, guided by the reaction mechanism (Lin et al., 2017; Chen et al., 2022).

Some TMOs with significant water resistance, such as NiO, should be further studied to enhance sulfur resistance. Cr_2O_3 with excellent sulfur resistance can be selected to prepare binary complexes to enhance its catalytic stability (Ordóñez et al., 2008). Although α-Fe_2O_3 catalysts, especially with two-dimensional nanostructure, have been proven to have excellent catalytic performance in CMC, their performance is significantly reduced in the presence of steam and SO_2. Herein, we can further investigate Fe–Cr mixed catalysts with the emphasis on the creation of spinel structures to increase the sulfur and water resistance of iron-based catalysts (García-Vázquez et al., 2020).

In addition, beyond complete oxidation, TMOs also find great uses in CH_4 partial oxidation reactions, such as direct oxidation to methanol, which is known as the "holy grail" in catalysis community to convert CH_4 into value-added chemicals with a much reduced cost in reaction steps and separation as compared to the conventional industrial route. (Sushkevich et al., 2017). The TMOs reveal the enormous potentials in the direct oxidation of CH_4 to CH_3OH owing to the relatively strong ability to activate the C–H bond and avoid CH_4 overoxidation.

In nature, CH_4 monooxygenase can directly convert CH_4 to CH_3OH using H_2O, O_2, and CO_2 as reactants at an ambient temperature (Sun et al., 2021). However, such biomimetic strategies are often limited by industrial-scale reactions. Some TMOs can dissociate CH_4 at room temperature, which offers the possibility for the direct conversion of CH_4 (Huang et al., 2021). Zuo *et al.* found that an inverse $CeO_2/Cu_2O/Cu$ (111) catalyst is able to bind and dissociate CH_4 at room temperature by mimicking the function of the CH_4 monooxygenase. The catalytic system produced only adsorbed CH_x fragments in the presence of H_2O, along with a high transformation from CH_4 to CH_3OH. The dissociation of H_2O formed OH groups, which occupied the catalyst surface. OH groups removed sites decomposing CH_x fragments, generating centers with special electronic properties. On the special active centers, CH_4 could directly interact to yield CH_3OH (Zuo et al., 2016). Liu *et al.* carefully studied key roles of H_2O for the conversion of CH_4 directly into CH_3OH on $CeO_2/Cu_2O/Cu$ (111). H_2O preferentially dissociated over the active Ce sites at the $CeO_2/Cu_2O/Cu$ (111) interface, hindering O_2 activation and the overoxidation of CH_4. H_2O produced active *OH to promote the direct conversion of CH_4. O_2 dominantly reoxidized the reduced CeO_x, and water adsorption also displaced the produced methanol into the gas phase (Liu et al., 2020).

Some researchers have explored bimetallic oxides with dual roles, in which one oxide activates CH_4 and the other ensures high selectivity to methanol. Yang *et al.* synthesized highly mixed hybrid IrO_2/CuO *via* a bottom-up tactic, which exhibited excellent catalytic performance with a methanol yield of 1937 μmol $gcat^{-1}$ and a methanol selectivity of about 95% through the synergistic effect of IrO_2 for CH_4 activation and CuO for selective oxidation. In the oxidation process of methane, due to the strong electrophilic property of Ir^{4+}, IrO_2 could facilitate the C–H bond cleavage by forming Ir-C σ bond. Then, -CH_3 attached by Ir bound to the neighboring Cu-attached O to form -OCH_3, subsequently extracted by H_2O to accelerate the formation of methanol.

At last, the formed O vacancy is replenished by O_2 (Yang et al., 2019).

It deserves to explore novel metal oxides with low metal-O bond strength and satisfactory methanol selectivity for facilitating the surface methoxy group formation. The metal oxides can also be employed as a cocatalyst being strong electrophilic metal oxides with extraordinary capacity to promote the C–H bond cleavage of CH_4 (Fuller et al., 2016). The synergistic effect of bimetallic oxides offers an alternative route for the design and synthesis of novel catalysts for the direct conversion of CH_4 into methanol (Lyu et al., 2021). In addition, the mechanism by which H_2O promotes the high selectivity of direct CH_4 conversion also needs to be continuously explored.

5 Conclusion

As an important greenhouse gas, the lean emission of CH_4 causes a huge environmental crisis. In this article, all the described results certify that both single and binary TMOs show the great potential of being promising alternatives to the expensive noble metal catalysts. Reviewed novel TMO catalysts exhibit appreciable catalytic reactivity associated with preparation methods, structures, morphologies, exposed crystal planes, crystal defects, oxygen vacancies, doping, and supporting. It can be seen that the structure, morphology, and exposed crystal planes determined by the preparation method significantly influence their catalytic activity for the CMC through the variation in morphology, surface area, and surface or lattice defects. In addition, mixed TMO catalysts prepared by doping and supporting exhibit excellent catalytic performance compared with the corresponding single TMOs due to synergistic interactions between the different TMO species. In general, the deactivation of TMO catalysts due to water vapor poisoning is reversible, while the deactivation due to sulfur poisoning is irreversible. The doping and supporting will improve the stability of TMO catalysts. The reaction mechanism of CMC over TMO catalysts is still controversial. Among the discussed possibilities, the MvK mechanism involves the oxidation of methane only by lattice oxygen with molecular oxygen replenishing the lattice oxygen after its consumption, while the L–H and E–R mechanisms only involve surface-adsorbed oxygen from molecular oxygen in the gas phase as the oxidizing power for methane activation. In addition, the T-T mechanism is also proposed for reactions involving both surface-adsorbed oxygen and lattice oxygen. The dominance of surface-adsorbed oxygen and lattice oxygen may change with the catalyst structure and temperature. As the characteristic techniques are under progressive development, it is expected to reveal the precise reaction mechanism of CMC over different TMO catalytic systems and therefore the identification of the true active site structures.

Author contributions

YG and MJ drafted the article, conceived the concept of the review, conducted literature survey, and arranged the figures. LY, ZL, FT, and YH revised the article and provided comments. All authors contributed to the article and approved the submitted version.

Funding

This project was financially supported by the Shanghai Post-Doctoral Excellence Program, 2021232, and the UM-SJTU Joint Institute and Shanghai Science and Technology Development Funds of “Rising Star” Sailing Program (22YF1419400).

Conflict of interest

The authors declare that the research was conducted in the absence of any commercial or financial relationships that could be construed as a potential conflict of interest.

Publisher’s note

All claims expressed in this article are solely those of the authors and do not necessarily represent those of their affiliated organizations, or those of the publisher, the editors, and the reviewers. Any product that may be evaluated in this article, or claim that may be made by its manufacturer, is not guaranteed or endorsed by the publisher.

References

Aguila, G., Gracia, F., Cortés, J., and Araya, P. (2008). Effect of copper species and the presence of reaction products on the activity of methane oxidation on supported CuO catalysts. *Appl. Catal. B Environ.* 77 (3-4), 325–338. doi:10.1016/j.apcatb.2007.08.002

Akbari, E., Alavi, S. M., Rezaei, M., and Larimi, A. (2021). Catalytic methane combustion on the hydrothermally synthesized MnO_2 nanowire catalysts. *Ind. Eng. Chem. Res.* 60, 7572–7587. doi:10.1021/acs.iecr.1c00881

Aneggi, E., Boaro, M., Colussi, S., de Leitenburg, C., and Trovarelli, A. (2016). Ceria-based materials in catalysis: Historical perspective and future trends. *Handb. Phys. Chem. Rare Earths* 50, 209–242. doi:10.1016/bs.hpcre.2016.05.002

Arena, F., Di Chio, R., Fazio, B., Espro, C., Spiccia, L., Palella, A., et al. (2017). Probing the functionality of nanostructured $MnCeO_x$ catalysts in the carbon monoxide oxidation. *Appl. Catal. B Environ.* 210, 14–22. doi:10.1016/j.apcatb.2017.03.049

Barbosa, A. L., Herguido, J., and Santamaria, J. (2001). Methane combustion over unsupported iron oxide catalysts. *Catal. Today* 64 (1-2), 43–50. doi:10.1016/S0920-5861(00)00507-1

Becker, E., Carlsson, P. A., Kylhammar, L., Newton, M. A., and Skoglundh, M. (2011). *In situ* spectroscopic investigation of low-temperature oxidation of methane over alumina-supported platinum during periodic operation. *J. Phys. Chem. C* 115, 944–951. doi:10.1021/jp103609n

Belessi, V. C., Ladavos, A. K., Armatas, G. S., and Pomonis, P. J. (2001). Kinetics of methane oxidation over La-Sr-Ce-Fe-O mixed oxide solids. *Phys. Chem. Chem. Phys.* 3 (17), 3856–3862. doi:10.1039/b103426j

Buchneva, O., Gallo, A., and Rossetti, I. (2012). Effect of nitrogen-containing impurities on the activity of perovskitic catalysts for the catalytic combustion of methane. *Inorg. Chem.* 51 (21), 11680–11687. doi:10.1021/ic3015892

Cao, H., Zhou, Z., Yu, J., and Zhou, X. (2018). DFT study on structural, electronic, and optical properties of cubic and monoclinic CuO. *J. Comput. Electron.* 17 (1), 21–28. doi:10.1007/s10825-017-1057-9

Chen, J. H., Arandiyan, H., Gao, X., and Li, J. H. (2015). Recent advances in catalysts for methane combustion. *Catal. Surv. Asia* 19 (3), 140–171. doi:10.1007/s10563-015-9191-5

Chen, K., Li, W. Z., Li, X. Z., Ogunbiyi, A. T., and Yuan, L. (2021). Irregularly shaped NiO nanostructures for catalytic lean methane combustion. *ACS Appl. Nano Mat.* 4 (5), 5404–5412. doi:10.1021/acsanm.1c00732

Chen, Y. L., Lin, J., Chen, X. H., Fan, S. Q., and Zheng, Y. (2021). Engineering multicomponent metal-oxide units for efficient methane combustion over palladium-based catalysts. *Catal. Sci. Technol.* 11 (1), 152–161. doi:10.1039/d0cy01742f

Chen, Y., Yao, K., Zhang, X., Shen, B., Smith, R. L., Jr, Guo, H., et al. (2022). Siloxane-modified MnO_x catalyst for oxidation of coal-related o-xylene in presence of water vapor. *J. Hazard. Mat.* 436, 129109. doi:10.1016/j.jhazmat.2022.129109

Chen, Z. P., Wang, S., Liu, W. G., Gao, X. H., Gao, D. N., Wang, M. Z., et al. (2016). Morphology-dependent performance of Co_3O_4 *via* facile and controllable synthesis for methane combustion. *Appl. Catal. A General* 525, 94–102. doi:10.1016/j.apcata.2016.07.009

Cheng, Z., Qin, L., Guo, M., Xu, M., Fan, J. A., Fan, L. S., et al. (2016). Oxygen vacancy promoted methane partial oxidation over iron oxide oxygen carriers in the chemical looping process. *Phys. Chem. Chem. Phys.* 18 (47), 32418–32428. doi:10.1039/C6CP06264D

Choudhary, V., and Rane, V. H. (1991). Acidity/basicity of rare-earth oxides and their catalytic activity in oxidative coupling of methane to C_2-hydrocarbons. *J. Catal.* 130 (2), 411–422. doi:10.1016/0021-9517(91)90124-M

Choya, A., de Rivas, B., González-Velasco, J. R., Gutiérrez-Ortiz, J. I., and López-Fonseca, R. (2018a). Oxidation of residual methane from VNG vehicles over Co_3O_4-based catalysts: Comparison among bulk, Al_2O_3-supported and Ce-doped catalysts. *Appl. Catal. B Environ.* 237, 844–854. doi:10.1016/j.apcatb.2018.06.050

Choya, A., de Rivas, B., Gutiérrez-Ortiz, J. I., and López-Fonseca, R. (2018b). Effect of residual Na^+ on the combustion of methane over Co_3O_4 bulk catalysts prepared by precipitation. *Catalysts* 8 (10), 427. doi:10.3390/catal8100427

Choya, A., Gudyka, S., de Rivas, B., Gutiérrez-Ortiz, J. I., Kotarba, A., López-Fonseca, R., et al. (2021). Design, characterization and evaluation of Ce-modified cobalt catalysts supported on alpha alumina in the abatement of methane emissions from natural gas engines. *Appl. Catal. A General* 617, 118105. doi:10.1016/j.apcata.2021.118105

Choya, A., Rivas, B. D., Gutiérrez-Ortiz, J. I., and López-Fonseca, R. (2022). Bulk Co_3O_4 for methane oxidation: Effect of the synthesis route on physico-chemical properties and catalytic performance. *Catalysts* 12, 87. doi:10.3390/catal12010087

Cornell, R. M., and Schwertmann, U. (2003). *The iron oxides: Structure, properties, reactions, occurrences, and uses*, 2. Weinheim: Wiley VCH, 71. doi:10.1515/CORRREV.1997.15.3-4.533

Dong, B., Zhang, H., Kong, A., Kong, Y., Yang, F., Shan, Y., et al. (2014). Synthesis of urchin-Like FeF_2 nanoarchitectures and their conversion into three-dimensional urchin-like mesoporous α-Fe_2O_3 nanoarchitectures for methane activation. *Eur. J. Inorg. Chem.* 28, 4779–4787. doi:10.1002/ejic.201402152

Dou, J., Tang, Y., Nie, L., Andolina, C. M., Zhang, X., House, S., et al. (2018). Complete oxidation of methane on Co_3O_4/CeO_2 nanocomposite: A synergic effect. *Catal. Today* 311, 48–55. doi:10.1016/j.cattod.2017.12.027

Dupont, N., Kaddouri, A., and Gélin, P. (2010). Physicochemical and catalytic properties of sol gel-prepared copper-chromium oxides. *J. Solgel. Sci. Technol.* 58 (1), 302–306. doi:10.1007/s10971-010-2391-6

El-Sheikh, S. M., Mohamed, R. M., and Fouad, O. A. (2009). Synthesis and structure screening of nanostructured chromium oxide powders. *J. Alloys Compd.* 482 (1-2), 302–307. doi:10.1016/j.jallcom.2009.04.011

Fan, S. Q., Zhang, W., Xu, H., Cai, G. H., Zhan, Y. Y., Chen, X. H., et al. (2022). Tuning lattice defects to facilitate the catalytic performance of Ni-Cu-O hybrid nanoparticles towards methane oxidation. *Int. J. Hydrogen Energy* 47, 4536–4545. doi:10.1016/j.ijhydene.2021.11.060

Feng, Z. J., Du, C., Chen, Y. J., Lang, Y., Zhao, Y. K., Cho, K., et al. (2018). Improved durability of Co_3O_4 particles supported on $SmMn_2O_5$ for methane combustion. *Catal. Sci. Technol.* 8 (15), 3785–3794. doi:10.1039/c8cy00897c

Feyel, S., Döbler, J., Schröder, D., Sauer, J., and Schwarz, H. (2006). Thermal activation of methane by tetranuclear $[V_4O_{10}]^+$. *Angew. Chem. Int. Ed.* 45 (28), 4681–4685. doi:10.1002/anie.200600188

Fu, G., Xu, X., and Wan, H. L. (2006). Mechanism of methane oxidation by transition metal oxides: A cluster model study. *Catal. Today* 117 (1-3), 133–137. doi:10.1016/j.cattod.2006.05.048

Fuller, J. T., Butler, S., Devarajan, D., Jacobs, A., Hashiguchi, B. G., Konnick, M. M., et al. (2016). Catalytic mechanism and efficiency of methane oxidation by Hg (II) in sulfuric acid and comparison to radical initiated conditions. *ACS Catal.* 6 (7), 4312–4322. doi:10.1021/acscatal.6b00226

García-Vázquez, M., Wang, K., González-Carballo, J. M., Brown, D., Landon, P., Tooze, R., et al. (2020). Iron and chromium-based oxides for residual methane abatement under realistic conditions: A study on sulfur dioxide poisoning and steam-induced inhibition. *Appl. Catal. B Environ.* 277, 119139. doi:10.1016/j.apcatb.2020.119139

Gong, D., and Zeng, G. F. (2021). Low-temperature combustion of methane over graphene templated Co_3O_4 defective-nanoplates. *Sci. Rep.* 11, 12604. doi:10.1038/s41598-021-92165-4

Gremminger, A., Lott, P., Merts, M., Casapu, M., Grunwaldt, J. D., Deutschmann, O., et al. (2017). Sulfur poisoning and regeneration of bimetallic Pd-Pt methane oxidation catalysts. *Appl. Catal. B Environ.* 218, 833–843. doi:10.1016/j.apcatb.2017.06.048

Han, Y. F., Chen, L. W., Ramesh, K., Widjaja, E., Chilukoti, S., Surjami, I. K., et al. (2008). Kinetic and spectroscopic study of methane combustion over α-Mn_2O_3 nanocrystal catalysts. *J. Catal.* 253 (2), 261–268. doi:10.1016/j.jcat.2007.11.010

Han, Z., Zhang, H. Q., Dong, B., Ni, Y. Y., Kong, A. G., Shan, Y. K., et al. (2016). High efficient mesoporous Co_3O_4 nanocatalysts for methane combustion at low temperature. *ChemistrySelect* 5, 979–983. doi:10.1002/slct.201600211

He, L., Fan, Y. L., Bellettre, J., Yue, J., and Luo, L. G. (2020). A review on catalytic methane combustion at low temperatures: Catalysts, mechanisms, reaction conditions and reactor designs. *Renew. Sustain. Energy Rev.* 119, 109589. doi:10.1016/j.rser.2019.109589

He, Y. L., Y. L., Guo, F. C., Yang, K. R., Heinlein, J. A., Bamonte, S. M., Fee, J. J., et al. (2020). *In situ* identification of reaction intermediates and mechanistic understandings of methane oxidation over hematite: A combined experimental and theoretical study. *J. Am. Chem. Soc.* 142 (40), 17119–17130. doi:10.1021/jacs.0c07179

Horn, R., and Schlögl, R. (2014). Methane activation by heterogeneous catalysis. *Catal. Lett.* 145 (1), 23–39. doi:10.1007/s10562-014-1417-z

Hu, L. H., Peng, Q., and Li, Y. D. (2008). Selective synthesis of Co_3O_4 nanocrystal with different shape and crystal plane effect on catalytic property for methane combustion. *J. Am. Chem. Soc.* 130 (48), 16136–16137. doi:10.1021/ja806400e

Hu, W. D., Lan, J. G., Guo, Y., Cao, X. M., and Hu, P. (2016). Origin of efficient catalytic combustion of methane over Co_3O_4(110): Active low-coordination lattice oxygen and cooperation of multiple active sites. *ACS Catal.* 6 (8), 5508–5519. doi:10.1021/acscatal.6b01080

Huang, E., Orozco, I., Ramírez, P. J., Liu, Z. Y., Zhang, F., Mahapatra, M., et al. (2021). Selective methane oxidation to methanol on ZnO/Cu_2O/Cu (111) catalysts: Multiple site-dependent behaviors. *J. Am. Chem. Soc.* 143, 19018–19032. doi:10.1021/jacs.1c08063

Huang, L., Zhang, X., Lin, C. H. E. N., and Lecheng, L. (2012). Promotional effect of CeO_2 and Y_2O_3 on CuO/ZrO_2 catalysts for methane combustion. *J. Rare Earths* 30 (2), 123–127. doi:10.1016/S1002-0721(12)60007-6

Huang, W., Zha, W. W., Zhao, D. L., and Feng, S. J. (2019). The effect of active oxygen species in nano-$ZnCr_2O_4$ spinel oxides for methane catalytic combustion. *Solid State Sci.* 87, 49–52. doi:10.1016/j.solidstatesciences.2018.11.006

Huang, X., Li, J., Wang, J., Li, Z., and Xu, J. (2020). Catalytic combustion of methane over a highly active and stable NiO/CeO_2 catalyst. *Front. Chem. Sci. Eng.* 14 (4), 534–545. doi:10.1007/s11705-019-1821-4

Jia, J. B., Ran, R., Guo, R. Q., Wu, X. D., and Weng, D. (2018). ZrO_2-supported α-MnO_2: Improving low-temperature activity and stability for catalytic oxidation of methane. *Prog. Nat. Sci. Mater. Int.* 28, 296–300. doi:10.1016/j.pnsc.2018.04.005

Jia, J. B., Ran, R., Wu, X. D., Chen, W., Si, Z. C., Weng, D., et al. (2019). Tuning nonstoichiometric defects in single-phase MnO_x for methane complete oxidation. *Mol. Catal.* 467, 120–127. doi:10.1016/j.mcat.2019.01.032

Jia, J. B., Zhang, P. Y., and Chen, L. (2016). Catalytic decomposition of gaseous ozone over manganese dioxides with different crystal structures. *Appl. Catal. B Environ.* 189, 210–218. doi:10.1016/j.apcatb.2016.02.055

Jia, Y. C., Wang, S. Y., Lu, J. Q., and Luo, M. F. (2016). Effect of structural properties of mesoporous Co_3O_4 catalysts on methane combustion. *Chem. Res. Chin. Univ.* 32 (5), 808–811. doi:10.1007/s40242-016-6141-3

Jodłowski, P. J., Chlebda, D., Piwowarczyk, E., Chrzan, M., Jędrzejczyk, R. J., Sitarz, M., et al. (2016). *In situ* and operando spectroscopic studies of sonically aided catalysts for biogas exhaust abatement. *J. Mol. Struct.* 1126, 132–140. doi:10.1016/j.molstruc.2016.02.039

Kašpar, J., Fornasiero, P., and Graziani, M. (1999). Use of CeO_2-based oxides in the three-way catalysis. *Catal. Today* 50 (2), 285–298. doi:10.1016/S0920-5861(98)00510-0

Knapp, D., and Ziegler, T. (2008). Methane dissociation on the ceria (111) surface. *J. Phys. Chem. C* 112 (44), 17311–17318. doi:10.1021/jp8039862

Kong, Q., Yin, Y., Xue, B., Jin, Y., Feng, W., Chen, Z. G., et al. (2018). Improved catalytic combustion of methane using CuO nanobelts with predominantly (001) surfaces. *Beilstein J. Nanotechnol.* 9 (1), 2526–2532. doi:10.3762/bjnano.9.235

Kuo, C. H., Li, W. K., Song, W. Q., Luo, Z., Poyraz, A. S., Guo, Y., et al. (2014). Facile synthesis of Co_3O_4@CNT with high catalytic activity for CO oxidation under moisture-rich conditions. *ACS Appl. Mat. Interfaces* 6, 11311–11317. doi:10.1021/am501815d

Larrondo, S., Vidal, M. A., Irigoyen, B., Craievich, A. F., Lamas, D. G., and Fábregas, I. O. (2005). Preparation and characterization of Ce/Zr mixed oxides and their use as catalysts for the direct oxidation of dry CH_4. *Catal. Today* 53–59. doi:10.1016/j.cattod.2005.07.110

Li, J. A., Li, M. M., Gui, P., Zheng, L. N., Liang, J. S., Xue, G., et al. (2019). Hydrothermal synthesis of sandwich interspersed $LaCO_3OH/Co_3O_4$/graphene oxide composite and the enhanced catalytic performance for methane combustion. *Catal. Today* 327, 134–142. doi:10.1016/j.cattod.2018.05.027

Li, J. H., Liang, X., Xu, S. C., and Hao, J. M. (2009). Catalytic performance of manganese cobalt oxides on methane combustion at low temperature. *Appl. Catal. B Environ.* 90 (1-2), 307–312. doi:10.1016/j.apcatb.2009.03.027

Li, J. L., Zhou, S. D., Zhang, J., Schlangen, M., Usharani, D., Shaik, S., et al. (2016). Mechanistic variants in gas-phase metal-oxide mediated activation of methane at ambient conditions. *J. Am. Chem. Soc.* 138 (35), 11368–11377. doi:10.1021/jacs.6b07246

Li, K., Liu, K., Xu, D. J., Ni, H., Shen, F. X., Chen, T., et al. (2019). Lean methane oxidation over $Co_3O_4/Ce_{0.75}Zr_{0.25}$ catalysts at low-temperature: Synergetic effect of catalysis and electric field. *Chem. Eng. J.* 369, 660–671. doi:10.1016/j.cej.2019.03.059

Li, L., Chen, H. W., Zhang, C. Y., and Fei, Z. Y. (2019). Ultrafine cobalt oxide nanoparticles embedded in porous SiO_2 matrix as efficient and stable catalysts for methane combustion. *Mol. Catal.* 469, 155–160. doi:10.1016/j.mcat.2018.12.028

Li, M. M., Gui, P., Zheng, L. N., Li, J. A., Xue, G., Liang, J. S., et al. (2018). Active component migration and catalytic properties of nitrogen modified composite catalytic materials. *Catalysts* 8 (4), 125. doi:10.3390/catal8040125

Li, Y. X., Guo, Y. H., and Xue, B. (2009). Catalytic combustion of methane over M (Ni, Co, Cu) supported on ceria-magnesia. *Fuel Process. Technol.* 90 (5), 652–656. doi:10.1016/j.fuproc.2008.12.002

Liang, Z., Li, T., Kim, M., Asthagiri, A., and Weaver, J. F. (2017). Low-temperature activation of methane on the IrO_2(110) surface. *Science* 356, 299–303. doi:10.1126/science.aam9147

Lin, F. W., Wang, Z. H., Shao, J. M., Yuan, D. K., He, Y., Zhu, Y. Q., et al. (2017). Catalyst tolerance to SO_2 and water vapor of Mn based bimetallic oxides for NO deep oxidation by ozone. *RSC Adv.* 7 (40), 25132–25143. doi:10.1039/c7ra04010e

Liu, C., Xian, H., Jiang, Z., Wang, L. H., Zhang, J., Zheng, L. R., et al. (2015). Insight into the improvement effect of the Ce doping into the SnO_2 catalyst for the catalytic combustion of methane. *Appl. Catal. B Environ.* 176-177, 542–552. doi:10.1016/j.apcatb.2015.04.042

Liu, F. X., Sang, Y. Y., Ma, H. W., Li, Z. P., and Gao, Z. M. (2017). Nickel oxide as an effective catalyst for catalytic combustion of methane. *J. Nat. Gas. Sci. Eng.* 41, 1–6. doi:10.1016/j.jngse.2017.02.025

Liu, L., Yao, Z., Liu, B., and Dong, L. (2010). Correlation of structural characteristics with catalytic performance of $CuO/Ce_xZr_{1-x}O_2$ catalysts for NO reduction by CO. *J. Catal.* 275 (1), 45–60. doi:10.1016/j.jcat.2010.07.024

Liu, Z., Huang, E., Orozco, I., Liao, W. J., Palomino, R. M., Rui, N., et al. (2020). Water-promoted interfacial pathways in methane oxidation to methanol on a CeO_2-Cu_2O catalyst. *Science* 368, 513–517. doi:10.1126/science.aba5005

Lu, Y. F., Chou, F. C., Lee, F. C., Lin, C. Y., and Tsai, D. H. (2016). Synergistic catalysis of methane combustion using Cu-Ce-O hybrid nanoparticles with high activity and operation stability. *J. Phys. Chem. C* 120 (48), 27389–27398. doi:10.1021/acs.jpcc.6b09441

Lyu, Y. M., Jocz, J. N., Xu, R., Williams, O. C., and Sievers, C. (2021). Selective oxidation of methane to methanol over ceria-zirconia supported mono and bimetallic transition metal oxide catalysts. *ChemCatChem* 13 (12), 2832–2842. doi:10.1002/cctc.202100268

Mukherjee, D., Rao, B. G., and Reddy, B. M. (2016). CO and soot oxidation activity of doped ceria: Influence of dopants. *Appl. Catal. B Environ.* 197, 105–115. doi:10.1016/j.apcatb.2016.03.042

Neatu, S., Trandafir, M. M., Stănoiu, A., Florea, O. G., Simion, C. E., Leonat, L. N., et al. (2019). Bulk versus surface modification of alumina with Mn and Ce based oxides for CH_4 catalytic combustion. *Materials* 12 (11), 1771. doi:10.3390/ma12111771

Ordóñez, S., Paredes, J. R., and Díez, F. V. (2008). Sulphur poisoning of transition metal oxides used as catalysts for methane combustion. *Appl. Catal. A General* 341 (1-2), 174–180. doi:10.1016/j.apcata.2008.02.042

Palella, A., Spadaro, L., Di Chio, R., and Arena, F. (2021). Effective low-temperature catalytic methane oxidation over $MnCeO_x$ catalytic compositions. *Catal. Today* 379, 240–249. doi:10.1016/j.cattod.2020.11.010

Palmqvist, A. E. C., Johansson, E. M., Järås, S. G., and Muhammed, M. (1998). Total oxidation of methane over doped nanophase cerium oxides. *Catal. Lett.* 56 (1), 69–75. doi:10.1023/A:1019032306894

Paredes, J. R., Dı´az, E., Dı´ez, F. V., and Ordo´ñez, S. (2009). Combustion of methane in lean mixtures over bulk transition-metal oxides: Evaluation of the activity and self-deactivation. *Energy fuels.* 23 (1), 86–93. doi:10.1021/ef800704e

Paredes, J. R., Ordóñez, S., Vega, A., and Dıez, F. V. (2004). Catalytic combustion of methane over red mud-based catalysts. *Appl. Catal. B Environ.* 47 (1), 37–45. doi:10.1016/S0926-3373(03)00325-4

Park, P. W., and Ledford, J. S. (1998). The influence of surface structure on the catalytic activity of alumina supported copper oxide catalysts. Oxidation of carbon monoxide and methane. *Appl. Catal. B Environ.* 15 (3-4), 221–231. doi:10.1016/S0926-3373(98)80008-8

Pecchi, G., Jiliberto, M. G., Buljan, A., and Delgado, E. J. (2011). Relation between defects and catalytic activity of calcium doped $LaFeO_3$ perovskite. *Solid State Ionics* 187 (1), 27–32. doi:10.1016/j.ssi.2011.02.014

Pecchi, G., Reyes, P., Zamora, R., López, T., and Gómez, R. (2005). Effect of the promoter and support on the catalytic activity of Pd-CeO_2-supported catalysts for CH_4 combustion. *J. Chem. Technol. Biotechnol.* 80 (3), 268–272. doi:10.1002/jctb.1120

Pfefferle, L. D., and Pfefferle, W. C. (1987). Catalysis in combustion. *Catal. Rev.* 29 (2-3), 219–267. doi:10.1080/01614948708078071

Popescu, I., Tanchoux, N., Tichit, D., and Marcu, I. C. (2017). Total oxidation of methane over supported CuO: Influence of the Mg_xAl_yO support. *Appl. Catal. A General* 538, 81–90. doi:10.1016/j.apcata.2017.03.012

Pratt, C., and Tate, K. (2018). Mitigating methane: Emerging technologies to combat climate change's second leading contributor. *Environ. Sci. Technol.* 52, 6084–6097. doi:10.1021/acs.est.7b04711

Pu, Z. Y., Liu, Y., Zhou, H., Huang, W. Z., Zheng, Y. F., Li, X. N., et al. (2017). Catalytic combustion of lean methane at low temperature over ZrO_2-modified Co_3O_4 catalysts. *Appl. Surf. Sci.* 422, 85–93. doi:10.1016/j.apsusc.2017.05.231

Raj, B. A. (2016). Methane emission control. *Johns. Matthey Technol. Rev.* 60 (4), 228–235. doi:10.1595/205651316X692554

Rodríguez-Fernández, J., Sun, Z. Z., Zhang, L., Tan, T., Curto, A., Fester, J., et al. (2019). Structural and electronic properties of Fe dopants in cobalt oxide nanoislands on Au(111). *J. Chem. Phys.* 150, 041731. doi:10.1063/1.5052336

Ross, M. O., and Rosenzweig, A. C. (2017). A tale of two methane monooxygenases. *J. Biol. Inorg. Chem.* 22, 307–319. doi:10.1007/s00775-016-1419-y

Sanchis, R., García, A., Ivars-Barceló, F., Taylor, S. H., García, T., Dejoz, A., et al. (2021). Highly active Co_3O_4-based catalysts for total oxidation of light C_1-C_3 alkanes prepared by a simple soft chemistry method: Effect of the heat-treatment temperature and mixture of alkanes. *Materials* 14, 7120. doi:10.3390/ma14237120

Seeburg, D., Liu, D. J., Radnik, J., Atia, H., Pohl, M. M., Schneider, M., et al. (2018). Structural changes of highly active Pd/MeO_x (Me = Fe, Co, Ni) during catalytic methane combustion. *Catalysts* 8 (2), 42. doi:10.3390/catal8020042

Setiawan, A., Kennedy, E. M., Dlugogorski, B. Z., Adesina, A. A., and Stockenhuber, M. (2015). The stability of Co_3O_4, Fe_2O_3, Au/Co_3O_4 and Au/Fe_2O_3 catalysts in the catalytic combustion of lean methane mixtures in the presence of water. *Catal. Today* 258, 276–283. doi:10.1016/j.cattod.2014.11.031

Shu, Y., Wang, M. Y., Duan, X. L., Liu, D. D., Yang, S. Z., Zhang, P. F., et al. (2022). Low-temperature total oxidation of methane by pore- and vacancy-engineered NiO catalysts. *AIChE J.* 68 (6), e17664. doi:10.1002/aic.17664

Siakavelas, G. I., Charisiou, N. D., AlKhoori, A., Gaber, S., Sebastian, V., and Hinder, S. J. (2022b). Oxidative coupling of methane on Li/CeO_2 based catalysts: Investigation of the effect of Mg- and La-doping of the CeO_2 support. *Mol. Catal.* 520, 112157. doi:10.1016/j.mcat.2022.112157

Siakavelas, G. I., Charisiou, N. D., AlKhoori, A., Sebastian, V., Hinder, S. J., and Baker, M. (2022a). Cerium oxide catalysts for oxidative coupling of methane reaction: Effect of lithium, samarium and lanthanum dopants. *J. Environ. Chem. Eng.* 10 (2), 107259. doi:10.1016/j.jece.2022.107259

Siakavelas, G. I., Charisiou, N. D., AlKhoori, S., AlKhoori, A. A., Sebastian, V., and Hinder, S. J. (2021). Highly selective and stable nickel catalysts supported on ceria promoted with Sm_2O_3, Pr_2O_3 and MgO for the CO_2 methanation reaction. *Appl. Catal. B Environ.* 282, 119562. doi:10.1016/j.apcatb.2020.119562

Stoian, M., Rogé, V., Lazar, L., Maurer, T., Védrine, J. C., Marcu, I. C., et al. (2021). Total oxidation of methane on oxide and mixed oxide ceria-containing catalysts. *Catalysts* 11 (4), 427. doi:10.3390/catal11040427

Sun, L. L., Wang, Y., Wang, C. M., Xie, Z. K., Guan, N. J., Li, L. D., et al. (2021). Water-involved methane-selective catalytic oxidation by dioxygen over copper zeolites. *Chem* 7 (6), 1557–1568. doi:10.1016/j.chempr.2021.02.026

Sun, Y. N., Liu, J. W., Song, J. J., Huang, S. S., Yang, N. T., Zhang, J., et al. (2016). Exploring the effect of Co_3O_4 nanocatalysts with different dimensional architectures on methane combustion. *ChemCatChem* 8 (3), 540–545. doi:10.1002/cctc.201501056

Sushkevich, V. L., Palagin, D., Ranocchiari, M., and van Bokhoven, J. A. (2017). Selective anaerobic oxidation of methane enables direct synthesis of methanol. *Science* 356, 523–527. doi:10.1126/science.aam9035

Tang, J. J., and Liu, B. (2016). Reactivity of the Fe_2O_3 (0001) surface for methane oxidation: A GGA+ U study. *J. Phys. Chem. C* 120 (12), 6642–6650. doi:10.1021/acs.jpcc.6b00374

Tang, W., Hu, Z., Wang, M., Stucky, G. D., Metiu, H., McFarland, E. W., et al. (2010). Methane complete and partial oxidation catalyzed by Pt-doped CeO_2. *J. Catal.* 273 (2), 125–137. doi:10.1016/j.jcat.2010.05.005

Tang, X. F., Li, J. H., and Hao, J. M. (2008). Synthesis and characterization of spinel Co_3O_4 octahedra enclosed by the {111} facets. *Mat. Res. Bull.* 43 (11), 2912–2918. doi:10.1016/j.materresbull.2007.12.009

Tao, F. F., Shan, J. J., Nguyen, L., Wang, Z. Y., Zhang, S. R., Zhang, L., et al. (2015). Understanding complete oxidation of methane on spinel oxides at a molecular level. *Nat. Commun.* 6, 7798. doi:10.1038/ncomms8798

Teng, F., Su, X., and Wang, X. (2019). Can China peak its non-CO_2 GHG emissions before 2030 by implementing its nationally determined contribution? *Environ. Sci. Technol.* 53, 12168–12176. doi:10.1021/acs.est.9b04162

Tepamatr, P., Laosiripojana, N., and Charojrochkul, S. (2016). Water gas shift reaction over monometallic and bimetallic catalysts supported by mixed oxide materials. *Appl. Catal. A General* 523, 255–262. doi:10.1016/j.apcata.2016.06.023

Toscani, L. M., Curyk, P. A., Zimicz, M. G., Halac, E. B., Saleta, M. E., Lamas, D. G., et al. (2019). Methane catalytic combustion over CeO_2-ZrO_2-Sc_2O_3 mixed oxides. *Appl. Catal. A General* 587, 117235. doi:10.1016/j.apcata.2019.117235

Trimm, D. L., and Lam, C. W. (1980). The combustion of methane on platinum-alumina fibre catalysts-I: Kinetics and mechanism. *Chem. Eng. Sci.* 35 (6), 1405–1413. doi:10.1016/0009-2509(80)85134-7

Trovarell, A. (2002). *Catalysis by ceria and related materials*. London: Imperial College Press.

Vedrine, J. C., Millet, J. M. M., and Volta, J. C. (1996). Molecular description of active sites in oxidation reactions: Acid-base and redox properties, and role of water. *Catal. Today* 32 (1-4), 115–123. doi:10.1016/S0920-5861(96)00185-X

Veldsink, J. W., Versteeg, G. F., and van Swaaij, W. P. M. (1995). Intrinsic kinetics of the oxidation of methane over an industrial copper(II) oxide catalyst on a γ-alumina support. *Chem. Eng. J. Biochem. Eng. J.* 57, 273–283. doi:10.1016/0923-0467(94)02872-8

Vickers, S. M., Gholami, R., Smith, K. J., and MacLachlan, M. J. (2015). Mesoporous Mn- and La-doped cerium oxide/cobalt oxide mixed metal catalysts for methane oxidation. *ACS Appl. Mat. Interfaces* 7 (21), 11460–11466. doi:10.1021/acsami.5b02367

Wang, C. H., and Lin, S. S. (2004). Study on catalytic incineration of methane using Cr_2O_3/γ-Al_2O_3 as the catalyst. *J. Environ. Sci. Health Part A* 39 (6), 1631–1641. doi:10.1081/ese-120037859

Wang, F. G., Zhang, L. J., Xu, L. L., Deng, Z. Y., and Shi, W. D. (2017). Low temperature CO oxidation and CH_4 combustion over Co_3O_4 nanosheets. *Fuel* 203, 419–429. doi:10.1016/j.fuel.2017.04.140

Wang, H. W., Li, J. L., Liu, W. G., Xu, X., Wei, X. F., Chao, L., et al. (2019). Enhancing catalytic CH_4 oxidation over Co_3O_4/SiO_2 core-shell catalyst by substituting Co^{2+} with Mn^{2+}. *J. Dispers. Sci. Technol.* 42 (1), 82–92. doi:10.1080/01932691.2019.1661257

Wang, Q., Peng, Y., Fu, J., Kyzas, G. Z., Billah, S. M. R., An, S. Q., et al. (2015). Synthesis, characterization, and catalytic evaluation of Co_3O_4/γ-Al_2O_3 as methane combustion catalysts: Significance of Co species and the redox cycle. *Appl. Catal. B Environ.* 168-169, 42–50. doi:10.1016/j.apcatb.2014.12.016

Wang, T., Wang, J. Y., Sun, Y. M., Duan, Y., Sun, S. N., Hu, X., et al. (2019). Origin of electronic structure dependent activity of spinel $ZnNi_xCo_{2-x}O_4$ oxides for complete methane oxidation. *Appl. Catal. B Environ.* 256, 117844. doi:10.1016/j.apcatb.2019.117844

Wang, X. Y., Liu, Y., Zhang, Y. Y., Zhang, T. H., Chang, H. Z., Zhang, Y. F., et al. (2018). Structural requirements of manganese oxides for methane oxidation: XAS spectroscopy and transition-state studies. *Appl. Catal. B Environ.* 229, 52–62. doi:10.1016/j.apcatb.2018.02.007

Wang, Y. N., Zhang, R. J., and Yan, B. H. (2022). Ni/$Ce_{0.9}Eu_{0.1}O_{1.95}$ with enhanced coke resistance for dry reforming of methane. *J. Catal.* 407, 77–89. doi:10.1016/j.jcat.2022.01.020

Wang, Y. Q., Rosowski, F., Schlögl, R., and Trunschke, A. (2022). Oxygen exchange on vanadium pentoxide. *J. Phys. Chem. C* 126, 3443–3456. doi:10.1021/acs.jpcc.2c00174

Wang, Z. X., Lin, J., Xu, H., Zheng, Y., Xiao, Y. H., Zheng, Y., et al. (2021). Zr-doped NiO nanoparticles for low-temperature methane combustion. *ACS Appl. Nano Mat.* 4, 11920–11930. doi:10.1021/acsanm.1c02487

Wasalathanthri, N. D., Poyraz, A. S., Biswas, S., Meng, Y., Kuo, C.-H., Kriz, D. A., et al. (2015). High-performance catalytic CH_4 oxidation at low temperatures: Inverse micelle synthesis of amorphous mesoporous manganese oxides and mild transformation to K_2-xMn_8O_{16} and ϵ-MnO_2. *J. Phys. Chem. C* 119 (3), 1473–1482. doi:10.1021/jp5108558

Wu, H. C., and Ku, Y. (2018). Enhanced performance of chemical looping combustion of methane with Fe_2O_3/Al_2O_3/TiO_2 oxygen carrier. *RSC Adv.* 8, 39902–39912. doi:10.1039/c8ra07863g

Wu, H., Pantaleo, G., Di Carlo, G., Guo, S., Marcì, G., Concepción, P., et al. (2015). Co_3O_4 particles grown over nanocrystalline CeO_2: Influence of precipitation agents and calcination temperature on the catalytic activity for methane oxidation. *Catal. Sci. Technol.* 5 (3), 1888–1901. doi:10.1039/c4cy01158a

Xu, J., Zhang, Y., Liu, Y., Fang, X., Xu, X., and Liu, W. (2019). Optimizing the reaction performance of $La_2Ce_2O_7$-based catalysts for oxidative coupling of methane (OCM) at lower temperature by lattice doping with Ca cations. *Eur. J. Inorg. Chem.* 2, 183–194. doi:10.1002/ejic.201801250

Xu, X. L., Li, L., Yu, F., Peng, H. G., Fang, X. Z., Wang, X., et al. (2017). Mesoporous high surface area NiO synthesized with soft templates: Remarkable for catalytic CH_4 deep oxidation. *Mol. Catal.* 441, 81–91. doi:10.1016/j.mcat.2017.08.005

Yang, L., Huang, J. X., Ma, R., You, R., Zeng, H., Rui, Z. B., et al. (2019). Metal-organic framework-derived IrO_2/CuO catalyst for selective oxidation of methane to methanol. *ACS Energy Lett.* 4 (12), 2945–2951. doi:10.1021/acsenergylett.9b01992

Yang, L. Q. Q., Heinlein, J., Hua, C., Gao, R. X., Hu, S., Pfefferle, L. D., et al. (2022). Emerging dual-functional 2D transition metal oxides for carbon capture and utilization: A review. *Fuel* 324, 124706. doi:10.1016/j.fuel.2022.124706

Yang, R. J., Guo, Z. J., Cai, L. X., Zhu, R. S., Fan, Y. Y., Zhang, Y. F., et al. (2021). Investigation into the phase-activity relationship of MnO_2 nanomaterials toward ozone-assisted catalytic oxidation of toluene. *Small* 17 (50), 2103052. doi:10.1002/smll.202103052

Ye, Y. C., Zhao, Y. T., Ni, L. L., Jiang, K. D., Tong, G. X., Zhao, Y. L., et al. (2016). Facile synthesis of unique NiO nanostructures for efficiently catalytic conversion of CH_4 at low temperature. *Appl. Surf. Sci.* 362, 20–27. doi:10.1016/j.apsusc.2015.11.213

Yu, Q., Liu, C. X., Li, X. Y., Wang, C., Wang, X. X., Cao, H. J., et al. (2020). N-doping activated defective Co_3O_4 as an efficient catalyst for low-temperature methane oxidation. *Appl. Catal. B Environ.* 269, 118757. doi:10.1016/j.apcatb.2020.118757

Yu, Q., Wang, C., Li, X. Y., Li, Z., Wang, L., Zhang, Q., et al. (2019). Engineering an effective MnO_2 catalyst from $LaMnO_3$ for catalytic methane combustion. *Fuel* 239, 1240–1245. doi:10.1016/j.fuel.2018.11.094

Yuan, X. Z., Chen, S. Y., Chen, H., and Zhang, Y. C. (2013). Effect of Ce addition on Cr/γ-Al_2O_3 catalysts for methane catalytic combustion. *Catal. Commun.* 35, 36–39. doi:10.1016/j.catcom.2013.02.005

Zasada, F., Janas, J., Piskorz, W., Gorczyńska, M., and Sojka, Z. (2017). Total oxidation of lean methane over cobalt spinel nanocubes controlled by the self-adjusted redox state of the catalyst: Experimental and theoretical account for

interplay between the Langmuir-hinshelwood and mars-van krevelen mechanisms. *ACS Catal.* 7 (4), 2853–2867. doi:10.1021/acscatal.6b03139

Zedan, A. F., and AlJaber, A. S. (2019). Combustion synthesis of non-precious CuO-CeO_2 nanocrystalline catalysts with enhanced catalytic activity for methane oxidation. *Materials* 12 (6), 878. doi:10.3390/ma12060878

Zhang, K., Peng, X. B., Cao, Y. N., Yang, H. G., Wang, X. Y., Zhang, Y. Y., et al. (2019). Effect of MnO_2 morphology on its catalytic performance in lean methane combustion. *Mat. Res. Bull.* 111, 338–341. doi:10.1016/j.materresbull.2018.11.023

Zhang, X., Jin, X., Bao, L. R., Zhang, M. C., Song, R. M., Yu, W., et al. (2021). Construction of defective cobalt oxide for methane combustion by oxygen vacancy engineering. *New J. Chem.* 45 (28), 12655–12660. doi:10.1039/d1nj01296g

Zhang, X. Y., House, S. D., Tang, Y., Nguyen, L., Li, Y. T., Opalade, A. A., et al. (2018). Complete oxidation of methane on NiO nanoclusters supported on CeO_2 nanorods through synergistic effect. *ACS Sustain. Chem. Eng.* 6, 6467–6477. doi:10.1021/acssuschemeng.8b00234

Zhang, Y. G., Qin, Z. F., Wang, G. F., Zhu, H. Q., Dong, M., Li, S. N., et al. (2013). Catalytic performance of MnO_x-NiO composite oxide in lean methane combustion at low temperature. *Appl. Catal. B Environ.* 129, 172–181. doi:10.1016/j.apcatb.2012.09.021

Zhang, Y., Xu, J., Xu, X., Xi, R., Liu, Y., and Fang, X. (2020). Tailoring $La_2Ce_2O_7$ catalysts for low temperature oxidative coupling of methane by optimizing the preparation methods. *Catal. Today* 355, 518–528. doi:10.1016/j.cattod.2019.06.060

Zheng, Y. F., Yu, Y. Q., Zhou, H., Huang, W. Z., and Pu, Z. Y. (2020). Combustion of lean methane over Co_3O_4 catalysts prepared with different cobalt precursors. *RSC Adv.* 10 (8), 4490–4498. doi:10.1039/c9ra09544f

Zheng, Y., Wang, C., Li, J. J., Zhong, F. L., Xiao, Y. H., Jiang, L. L., et al. (2020). Enhanced methane oxidation over Co_3O_4-In_2O_3-x composite oxide nanoparticles via controllable substitution of Co^{3+}/Co^{2+} by In^{3+} Ions. *ACS Appl. Nano Mat.* 3, 9470–9479. doi:10.1021/acsanm.0c02075

Zhong, L., Fang, Q. Y., Li, X., Li, Q., Zhang, C., Chen, G., et al. (2019). SO_2 resistance of Mn-Ce catalysts for lean methane combustion: Effect of the preparation method. *Catal. Lett.* 149 (12), 3268–3278. doi:10.1007/s10562-019-02896-3

Zhu, Y. X., Murwani, I. K., Zhou, C. J., Kemnitz, E., and Xie, Y. C. (2003). Isotopic studies of Sn-Cr binary oxide catalysts for methane total oxidation. *Catal. Lett.* 85 (3-4), 205–211. doi:10.1023/A:1022197830984

Zuo, Z., Ramírez, P. J., Senanayake, S. D., Liu, P., and Rodriguez, J. A. (2016). Low-temperature conversion of methane to methanol on CeO_x/Cu_2O catalysts: Water controlled activation of the C-H bond. *J. Am. Chem. Soc.* 138 (42), 13810–13813. doi:10.1021/jacs.6b08668

Frontiers in Chemistry

Explores all fields of chemical science across the periodic table

Advances our understanding of how atoms, ions, and molecules come together and come apart. It explores the role of chemistry in our everyday lives - from electronic devices to health and wellbeing.

Discover the latest Research Topics

See more →

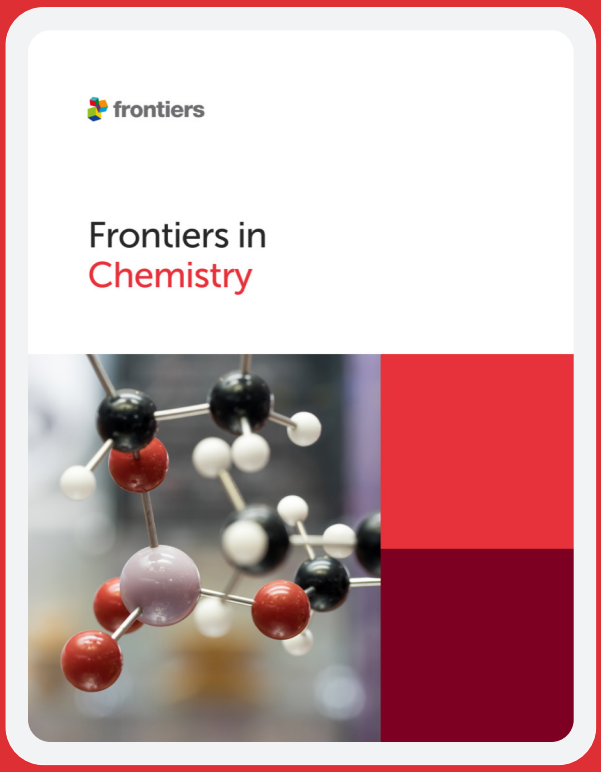

Frontiers

Avenue du Tribunal-Fédéral 34
1005 Lausanne, Switzerland
frontiersin.org

Contact us

+41 (0)21 510 17 00
frontiersin.org/about/contact